Zero mass jets for turbulent flow drag reduction

Feng Xie

Department of Mechanical Engineering
University of Sheffield

A thesis submitted in partial fulfilment of the requirements for the degree of
Doctor of Philosophy

Supervised by Professor Ning Qin

April 2019

I would like to dedicate this thesis to my loving wife and daughter.

Acknowledgements

I would like to sincerely thank my supervisor, Professor Ning Qin, for all of his advices, guidances, and supports. Not only his valuable experiences and thorough knowledge help me a lot, but also his scientific altitude will benefit me for the rest of my academic life. Thanks to him that I had the opportunity to undertake my PhD and work in an international cooperation project. This has expanded my horizons greatly.

I would also like to thank my second supervisor, Dr. Pierre Ricco, for his ideas and advices. He is both a teacher and a friend who encouraged me a lot when I got lost during my research.

I would like to thank Jose Daniel Pérez Muñoz who had worked on this project with me.

I would like to thank my friends, Benjamin L Hinchliffe, Alistair John, Guglielmo Vivarelli, MJR Hollom, and the others in rooms RD14 and RD12b for their friendship, and everything they have done for me.

I would like to acknowledge Hypervelocity Aerodynamics Institute, China aerodynamics research and development center for the financial support of my PhD study. I also like to thank the following for their help, Sen Liu, Xiang Xu, YanGuang Yang.

Abstract

Drag reduction has always been a very important research topic in aircraft design area. Over many decades, a lot of passive and active control methods have been developed to reduce drag. Since the friction drag takes a big percentage in the total drag of a commercial aeroplane which flies under a turbulent condition, the industry has inclined to reduce the friction drag in turbulent flow. Practical approaches are being found to be applied to the next generation of aeroplanes.

This research focuses on a novel method of active flow control that can be used to reduce friction drag in a fully developed turbulent flow. The method is named as 'zero mass jets' which can be achieved by using a pair of synthetic jets. Since it is new, the method needs to be checked whether it can obtain drag reduction or not. The fully developed turbulent channel flow at a low Reynolds number is a good case to investigate the above method. The geometry is simple to generate a structured mesh. The Reynolds number is low to do direct numerical simulations to obtain detailed flow structures and study the turbulence phenomena.

Direct numerical simulations are often carried out by high order solvers. In our group, an in-house solver has already been developed for many years. Various fluid topics were investigated using our solver, including open boundary layer flow, synthetic jets, flow separations, and aerofoil designs. The solver can do RANS and DES by solving the compressible Navier-Stokes equations with TVD schemes and unstructured meshes. In order to do DNS, a high order method is added in the solver called 'SHEFFlow' to reduce the numerical dissipation in this research.

The turbulent flow is directly simulated by SHEFFlow. Since the flow is turbulent and periodically oscillated by zero mass jets, the obtained data is also complicated to be analysed. Useful information should be figured out by statistic tools. A triple decomposition is employed to decompose the velocity fluctuations into periodic characters and purely turbulent quantities. The Reynolds shear stresses and kinetic energy are studied by quadrant analysis and power spectral density, respectively. Using various analysis methods, the turbulence flow controlled by zero mass jets is studied in detail.

This novel method of active flow control is approved to be able to significantly reduce the friction drag through the study of zero mass jets. It's proved that this method has the potential to be applied on an aeroplane to improve the performance in the future.

Table of contents

List of figures

List of tables

Nomenclature

Roman Symbols

$\boldsymbol{A}$	Vector of surface area
A	Area
a	Speed of sound
x	Streamwise direction or streamwise length
y	Wall-normal direction or wall-normal length
z	Spanwise direction or spanwise length
C	Sutherland's constant, 110.4
c	Chord length
C_f	Skin friction coefficients
C_p	Pressure heat capacity
d	Width of the slot
$\tilde{D}$	Difference of skin friction coefficients
DR	Level of gross drag reduction
E	Total energy per unit mass
E_k	Kinetic energy
$\boldsymbol{F}$	Vector of inviscid fluxes
f	Frequency

$\boldsymbol{G}$	Vector of viscous fluxes
H	Total enthalpy
k	Kinetic energy or wavenumber
L, l	Length
$\dot{m}$	Mass flow rate
Ma	Mach number
Ω	Control volume
p	Pressure
$\boldsymbol{Q}$	Vector of primitive variables
$\boldsymbol{q}$	Vector of heat fluxes
Q_1	First quadrant
Q_2	Second quadrant, ejection
Q_3	Third quadrant
Q_4	Fourth quadrant, sweep
Q_x	Flow rate in streamwise direction
R	Ideal gas constant, $287.04\,\mathrm{J\,kg^{-1}\,K^{-1}}$
Re	Reynolds number
Re_b	Reynolds number based on half channel-height and bulk velocity, $u_b\delta/\nu$
Re_τ	Reynolds number based on half channel-height and friction velocity, $u_\tau\delta/\nu$
Re_θ	Reynolds number based on the momentum thickness, $u_0\theta/\nu$
ρ_0	Freestream density, $\mathrm{kg\,m^{-3}}$
Sr	Strouhal number, $\sqrt{2\pi d^2/T\nu}$
T	Period or temperature
t	Physical time

u	Streamwise velocity, $\mathrm{m\,s^{-1}}$
u_0	Freestream velocity, $\mathrm{m\,s^{-1}}$
u_b	Bulk or mean velocity of a channel flow
$\overline{u_i u_i}$	Reynolds normal stresses
$\overline{u_i u_j}$	Reynolds shear stresses, $i \neq j$
$\boldsymbol{v}$	Vector of velocities
V	Arbitrary control volume
v	Wall-normal velocity, $\mathrm{m\,s^{-1}}$
$\boldsymbol{W}$	Vector of conserved variables
w, W	Spanwise velocity, $\mathrm{m\,s^{-1}}$
$\boldsymbol{x}$	Position vector

Greek Symbols

β	Jet angle
δ	Half channel-height
δ_{jet}	Height of the jet-exits
ε	Energy dissipation rate or a very small value
Γ	Preconditioning matrix
γ	Ratio of specific heats
κ	Thermal conductivity or Von Kármán constant
λ	Wavelength
λ_2	Lambda2 vortex criterion
μ	Dynamic viscosity, $\mathrm{Pa\,s}$
ν	Kinematic viscosity, $\mathrm{m^2\,s^{-1}}$
ϕ_{uu}	Energy spectrum of streamwise velocity fluctuations

φ	Phase time
π	$\simeq 3.14\ldots$
τ	Pseudo time
τ_s	Shear stress, Pa
τ_t	Turbulent or Reynolds shear stress, Pa
τ_v	Viscous shear stress, Pa
τ_w	Wall shear stress, Pa
θ	Momentum thickness, $\int_0^\infty \frac{\rho(y)u(y)}{\rho_0 u_0}\left(1-\frac{u(y)}{u_0}\right)dy$

Superscripts

L	Computations from left side of a face
R	Computations from right side of a face
inv	Inviscid
$'$	Total fluctuation
$''$	Purely turbulent fluctuation
$+$	normalization by wall units

Subscripts

x	Streamwise direction
y	Wall-normal direction
z	Spanwise direction
c	Channel centre
∞	Freestream
m, max	Maximum
min	Minimum
osc	Oscillation

rms	Root mean square
w	Channel wall
G	Global wall-normal distance
L	Local wall-normal distance

Other Symbols

$\overline{a}$	Time averaged value of a
$\widetilde{a}$	Periodic value of a
$\langle a \rangle$	Phase averaged value of a

Acronyms / Abbreviations

AOA	Angle of attack
CFD	Computational fluid dynamics
DES	Detached eddy simulation
DNS	Direct numerical simulation
HPC	High performance computing
JPDF	Joint probability density function
LES	Large eddy simulation
MUSCL	Monotonic Upwind Scheme for Conservation Laws
PSD	Power spectral density
RANS	Reynolds averaged Navier-Stokes simulation
RK	Runge-Kutta
SGS	Sub-grid scale
URANS	Unsteady Reynolds averaged Navier-Stokes simulation
ZMJ	Zero mass jets

Chapter 1

Introduction

"When I meet God, I am going to ask him two questions: Why relativity? And why turbulence? I really believe he will have an answer for the first."

– Werner Heisenberg

1.1 Background and motivations

Why turbulence? Why flow control? How to control a turbulent flow?

Werner Heisenberg said he could not answer the first question, and neither do I. The reason for the chaos in the flow is that the excessive kinetic energy in part of the fluid overcomes the damping effect of the fluid's viscosity. Turbulence often happens at high Reynolds number. In general terms, turbulence or turbulent flow means that many sizes of unsteady vortices interact with each other in the flow. Consequently, the drag is increased due to the friction effects.

A drag force usually arises from two components, including pressure drag and friction drag. The former one is related to the pressure differences over an object. The latter one is caused by the viscous effects between the fluid and a solid wall. When flow is at a high Reynolds number, the ratio of inertial forces to viscous forces is large, inducing turbulence in the boundary layer. Since commercial aeroplanes fly at a high Reynolds number, the skin-friction drag which is mostly turbulent drag takes about 50% of the total drag. An estimation by Walsh et al. [126] represents that 250 million of dollars per year can be generally saved by reducing around 10% of the friction drag for commercial aeroplanes. As the turbulent drag plays an important role in the friction drag, a huge saving in the fuel costs can be achieved by the turbulent drag-reduction. Reducing the fuel consumption is not only for saving money, but also for environment. Atmosphere is polluted by the jet exhausts, such as NO_x and

CO_2. Nitrogen oxides contributes to global warming in the lower atmosphere and damages the stratospheric ozone layer in the high altitude. Carbon dioxide emissions from aviation threaten government targets in terms of emissions growth. In Horizon 2020, the Clean Sky JTI, Europe focuses on the next generation of aeroplanes which will be more efficient, safer and greener. The price of airline tickets can also be reduced, increasing the competitiveness of air transport services.

Nowadays, the manufacture of aircraft surfaces is advanced. Smooth surfaces can be produced by industries, but some issues still cannot be avoided. In the actual situation, structures are joined by electric resistance spot and seam welding. Under some flying environment, the aeroplane is covered by ice. Both of these situations make the skin surfaces rough. Just smoothing the surfaces leaves marginal space for the improvement of reducing the skin friction. It is important to find a new method to reduce the skin friction in aerodynamic research.

My motivation is contributing my effect to a project in Horizon 2020 and finding an efficient flow control method for the reduction of turbulent friction.

1.2 Aims and objectives

This research aims to develop and investigate a novel method of active flow control, finding a new strategy to reduce the friction drag on wings or fuselages of aeroplanes in the future. The novel method is named as "Zero Mass Jets" (ZMJ) which uses a control device to manipulate the near-wall flow, as shown in figure 1.1. This research studies the flow physics of drag reduction in a turbulent channel flow using DNS.

A summary of the key objectives is listed below:

- The development of an in-house code for DNS - Since the flow structures controlled by the device in the near-wall region are very important to understand the mechanisms of drag reduction, a DNS code is needed to simulate the flow. Our group's code is for RANS or DES rather than DNS, so it needs to be improved.

- The investigation of simulation domain size - DNS is very "famous" for the consumption of computing resources. The size of computational domain is directly related to the mesh size. Due to the limited computing resources, a careful design of the domain size is crucial to obtain the desired results in time.

- The reduction of skin friction by zero mass jets - The flow control method is the first time to be used to achieve a reduction of skin friction. The drag-reduction capability of the control device should be validated by a simplified model.

- The mechanisms of drag reduction - Understanding the behaviour of zero mass jets is necessary to apply the control method in a practical situation.

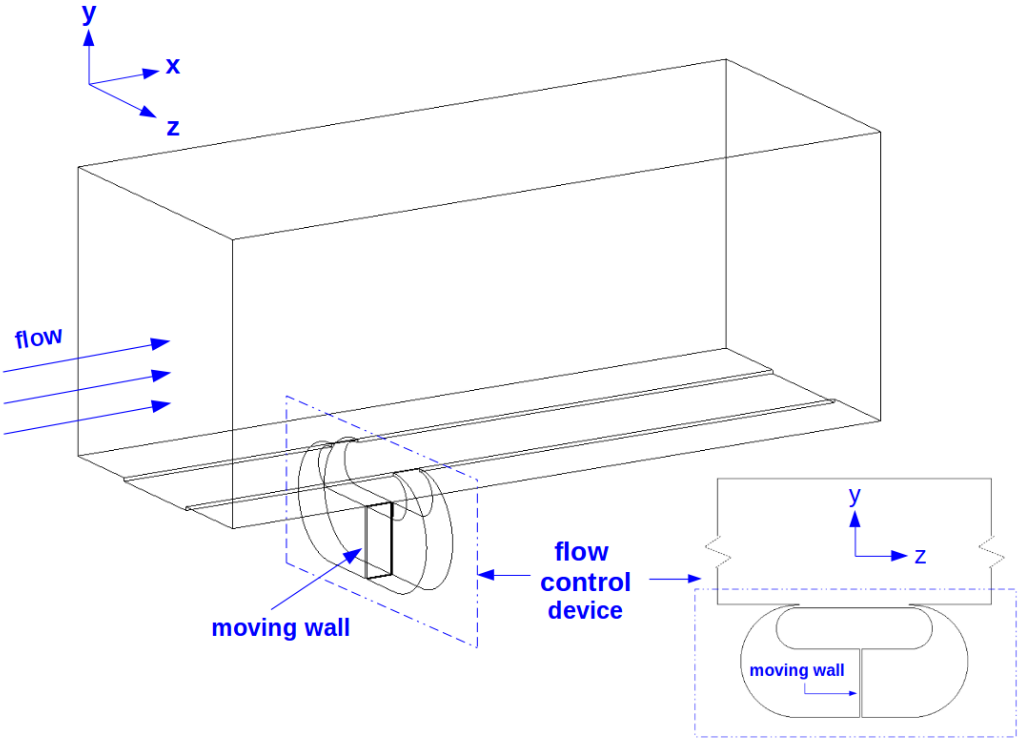

Figure 1.1 The physical model of the novel active-flow-control method

1.3 Outline

This thesis is organised as follows:

- Chapter 2 - Literature reviews of turbulent flow and flow control methods
- Chapter 3 - Computational methods
- Chapter 4 - Validations and verifications of the in-house code for the abilities of high oder and DNS.
- Chapter 5 - Analysis of drag reduction obtained by zero mass jets, comparing the results with off-jets and different jet angles
- Chapter 6 - Further investigations of the drag reduction by changing either the frequency or the speed of zero mass jets

- Chapter 7 - Conclusions

Chapter 2

Literature review

In this research, a unique flow control method is invented and used to reduce the friction drag in a fully developed turbulent channel flow at the Reynolds number $Re_\tau = 180$. The control method is to place Zero Mass Jets (ZMJ) on channel walls in a special way to oscillate the fluid in near-wall regions. Since turbulence phenomena near the wall are fundamental and useful for many engineering applications, DNS is employed to accurately capture the flow structures in near-wall regions. Given that turbulence flow and flow control methods are crucial topics in this research, so the past studies in these two categories will be reviewed in this chapter.

2.1 Turbulence flow

Over several decades of study, immense human and financial resources have been spent on understanding and analysing turbulence flow. Although the fundamental complexity of turbulence phenomena punctuates the progress with numerous controversies, some consensuses that concern many of the turbulent features in low-Reynolds-number canonical flows are increasing today. The canonical flows are often studied and compared, such as zero-pressure-gradient turbulent boundary layer flow, turbulent channel flow, and turbulent pipe flow.

2.1.1 Law of the wall

"Law of the wall" describes the universal mean-velocity profile near the wall in a fully developed turbulent flow. As shown in figure 2.1, the mean-velocity profile can be divided into three regions in a fully developed turbulent channel flow, including viscous sublayer, buffer layer and log-law region [86]. "Viscous sub-layer" is the nearest layer from the wall,

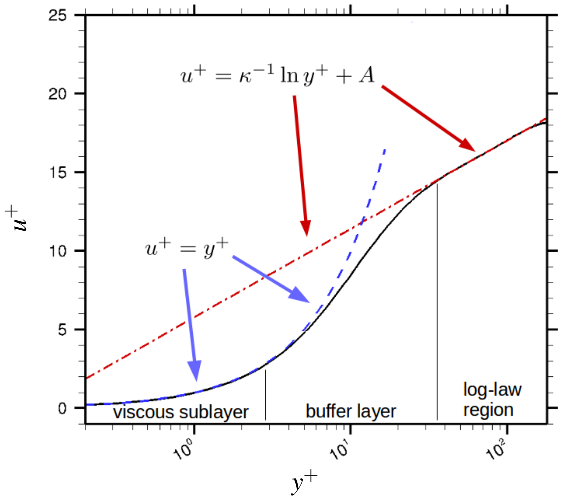

Figure 2.1 A sketch shows "Law of the wall" for a fully developed turbulent channel flow at $Re_\tau = 180$.

$y^+ < 5$, where is almost laminar flow because of the high viscosity. When $5 < y^+ < 30$, viscosity and turbulence are equally important in the second layer called "buffer layer". The third layer is called "log-law region", where turbulence dominates this layer in the region $y^+ > 30$. A log law function can describe the relation between the normalized mean velocity and the distances from wall.

2.1.2 Coherent motion

Robinson [98] defined the 'coherent motion' as *a three-dimensional region of the flow over which at least one fundamental flow variable (velocity component, density, temperature, etc.) exhibit significant correlation with itself or with another variable over a range of space and/or time that is significantly larger than the smallest local scales of the flow.* In turbulent research, "low-speed" and "high-speed" are often used as relative terms, referring to the streamwise-velocity fluctuations u' at that wall-normal position. When $u' > 0$, it is called high-speed. When $u' < 0$, it is named low-speed.

An idealized model of the vortices in turbulent boundary layers at low Reynolds numbers were proposed by Robinson [98] as well. The wake region was dominated by arch-like vortices. The quasi-streamwise vortices were common vortical structures in the buffer region. The log-law region has both types of vortices, as shown in figure 2.2.

Head and Bandyopadhyay [34] investigated the boundary-layer structures over the Reynolds-number range $500 < Re_\theta < 17500$ in the zero-pressure-gradient turbulent boundary-layer. Their studies showed hairpin vortices or vortex pairs in the wall region at high Reynolds

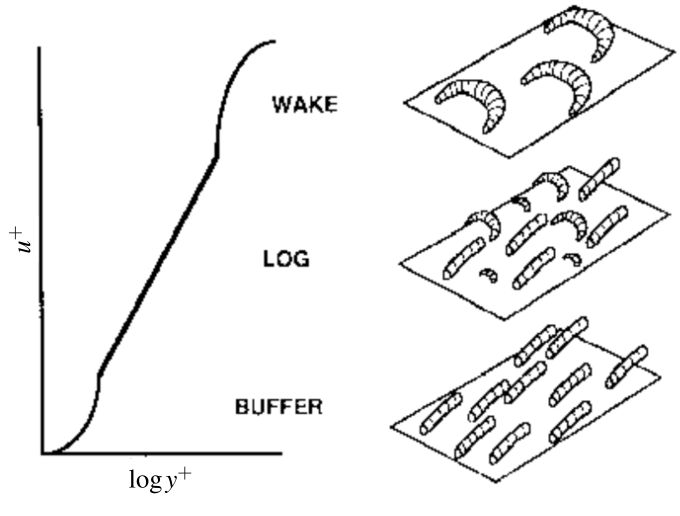

Figure 2.2 Idealized schematic of vortices corresponding to the different regions in law of the wall [98].

numbers ($Re_\theta > 2000$), and horseshoe vortices or vortex loops at low Reynolds numbers ($Re_\theta < 800$), as displayed in figure 2.3.

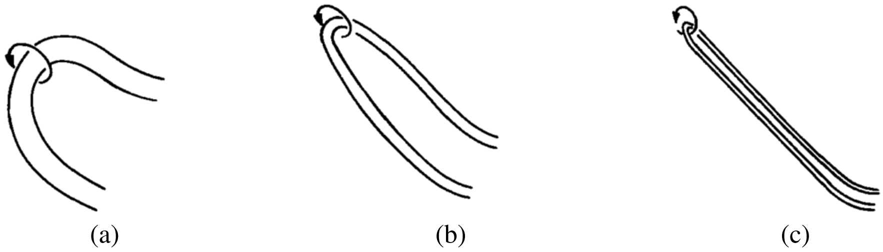
(a) (b) (c)

Figure 2.3 The features in outer region of turbulent boundary layer depends on different Reynolds numbers [34]. (a) vortex loops at very low *Re*; (b) elongated vortex-loops or horseshoe vortices at moderate *Re*; (c) hairpin vortices or vortex pairs at high *Re*.

Kim et al. [50] experimentally studied the process of turbulence production in a turbulent-boundary-layer flow. The term "busting" was used to describe the process of low-speed streaks lift-up, oscillation, and breakup. The low-speed streaks lose their coherence due to unstable interactions with the high-speed fluid. They found that the majority of turbulent kinetic energy in zone $0 < y^+ < 100$ was contributed from the busting process. Oldaker and Tiederman [84] proposed that the average transverse spacing of low-speed streaks in the viscous sublayer was related to the friction drag. The drag reduces when the spacing increases.

The variation of the spanwise streak spacing was experimentally found to be in a range of $20 \leqslant \lambda_z^+ \leqslant 200$ [62, 84]. Smith and Metzler [110] experimentally investigated the near-wall characteristics of the low-speed streaks in a turbulent-boundary-layer flow with a Reynolds-number range of $740 \leqslant Re_\theta < 5830$. They found that the non-dimensional spanwise spacing of low-speed streaks in the near-wall region, $y^+ \leqslant 30$, were statistically invariant with Reynolds number, showing a consistent mean value of $\overline{\lambda_z^+} = 100 \pm 20$. This value had been confirmed by other experiments [17, 35, 60]. The streamwise streak length could beyond $\lambda_x^+ > 1000$ [15].

2.1.3 Large-scale and small-scale structures

Iwamoto et al. [40] examined the relationship between the near-wall quasi-streamwise vortices and the large-scale outer-layer structures by simulating a turbulent channel flow at $Re_\tau = 1160$. The results represented that the vortices are located in the low-speed region, or between the low-speed and high-speed regions, as shown in figure 2.4.

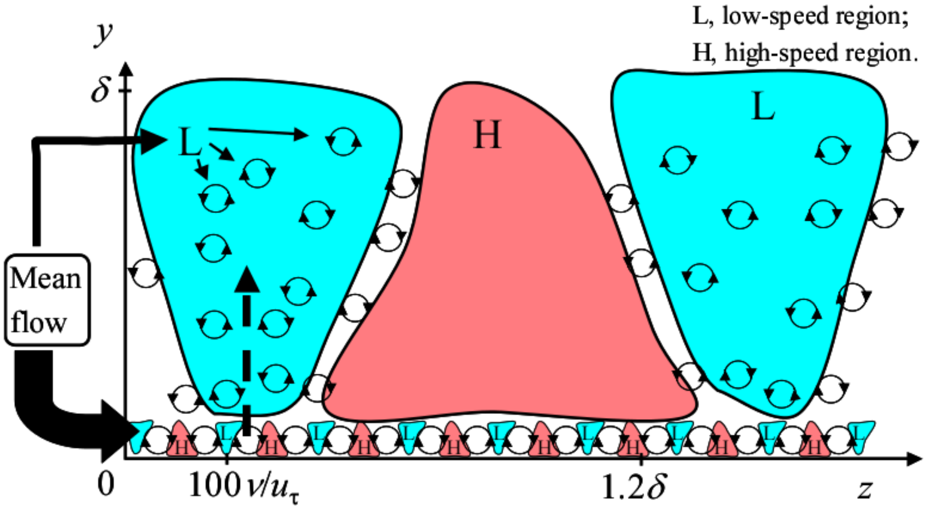

Figure 2.4 Conceptual diagram of energy flow between the near-wall vortices and the large-scale outer-layer structures [40].

Mathis et al. [72, 73] proposed a filter procedure to decompose the fluctuations into large and small scales with a certain filter length, comparing the amplitude modulations in turbulent-boundary-layer, pipe, and channel flows. The relationship of energy contained in large-scale and small-scale motions were investigated in detail using spectra analysis. The interactions between large-scale and small-scale motions were quantified by spectrally filtering small-scale component of the streamwise-velocity fluctuations with Hilbert transformation. An overview of the premultiplied streamwise energy spectra $k_x\phi_{uu}/u_\tau^2$ across the full height of the turbulent boundary layer is shown in figure 2.5.

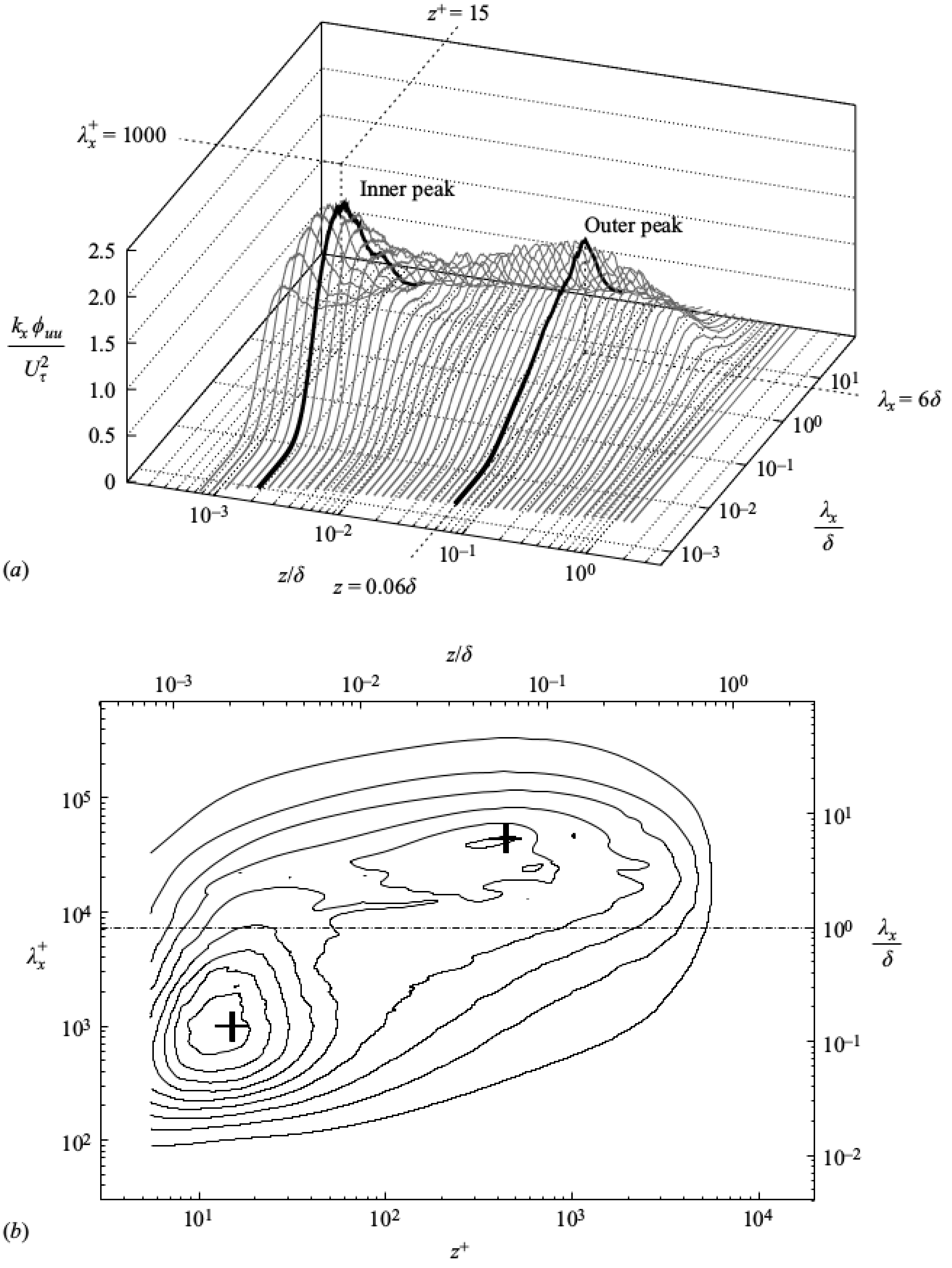

Figure 2.5 Overview of the pre-multiplied energy spectra of $k_x\phi_{uu}/U_\tau^2$ in a turbulent boundary layer flow at a high Reynolds number $Re_\tau = 7300$.

In the study of Mathis et al., the wall-normal direction was along with the z-axis. In figure 2.5a, a three-dimensional plot of spectrogram profiles shows the one-dimensional pre-multiplied energy spectra for all wall-normal locations. The contour view of the spectral surface is shown in figure 2.5b. According with reference [36], the first peak is referred as "inner peak" which has a fixed viscous coordinates ($z^+ = 15$, $\lambda_x^+ = 1000$). Kline et al. [54] suggested that the peak is the energetic signature due to the viscous-scaled near-wall cycle of elongated high-speed and low-speed streaks. The second peak found in the logarithmic region is referred as "outer peak". The location of this peak ($z/\delta = 0.06$, $\lambda_x = 6\delta$) is scaled in boundary-layer thickness suggested by Hutchins and Marusic [36]. It does not appear at low Reynolds numbers ($Re_\tau \lesssim 1700$) because the separation of scales is not sufficient and a diminishing strength exists at low Reynolds numbers [37]. The outer peak is the energetic signature of very large scale motions. Hutchins and Marusic [37] found that the magnitude of this peak is proportional to Reynolds number, when $k_x\phi_{uu}$ is scaled with u_τ.

The above methodology proposed by Mathis et al. [72] can be use to observe the bursting process of the large-scale and small-scale structures. Tang et al. [116] employed the method to decompose the fluctuations and examine the bursting process in a turbulent boundary layer. A cylinder roughness element was put on the smooth wall to investigate the influence of the element. They presented the average energy distribution with spectra analysis, as shown in figure 2.6. There was no obvious high energy contained in large-scale structures due to the relative low Reynolds number $Re_\tau = 980$. They used different filter lengths, $\lambda_x/\delta = 1.5$, 2, 3, 4 to decompose the instantaneous streamwise-velocity into the large and small scales. Figure 2.7 shows a case of the decomposition using a filter cut-off of $\lambda_x/\delta = 2$.

2.1.4 Effect of the computational domain size on direct simulation of turbulent channels

In a DNS of turbulent channel flow, it has found that the minimal boxes around $\lambda_x^+ \approx 250-350$ and $\lambda_z^+ \approx 85-110$ could maintain a "healthy" turbulence in the buffer region by Jiménez and Moin [42] and in the logarithmic layer by Flores and Jiménez [25]. The simulation result is only correct for the analysis of one-point statistics using the minimal boxes. These results are in good agreement with the streamwise and spanwise lengths of the mean streak reported in the experiments by Sankaran et al. [101] and Smith and Metzler [110]. The domain size should be wider than 3δ to obtain the healthy turbulence for the whole flow, where δ is the channel half-height [25]. The box size should not influence smaller-scale quantities such as the vorticities, as proposed by Lozano-Durán and Jiménez [68].

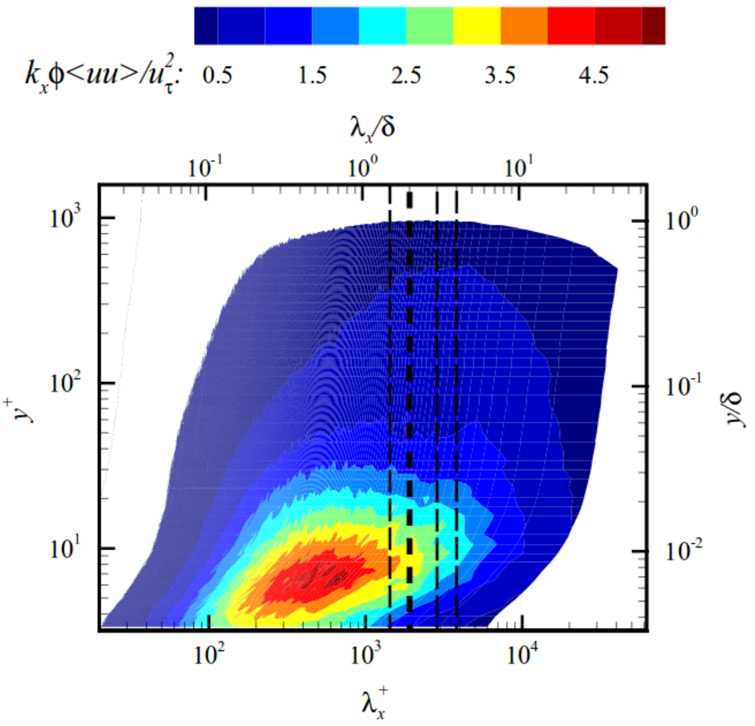

Figure 2.6 Pre-multiplied energy spectra of the streamwise velocity fluctuations, $k_x\phi_{uu}/u_\tau^2$, as a function of length scale and wall-normal heights [116].

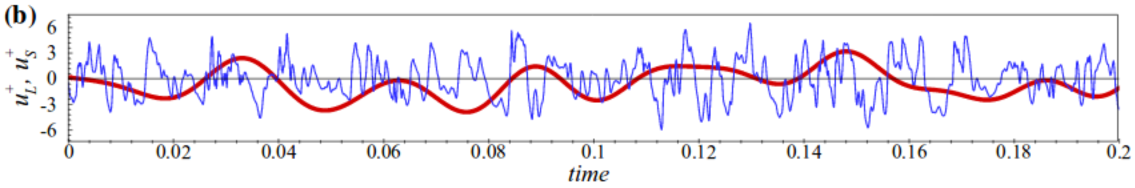

Figure 2.7 The large and small scales at the near-wall position $y^+ = 15$ [116]. The red line represents the large-scale fluctuations, and the blue line denotes the corresponding small-scale fluctuations.

It is still an open question that how large the computational domain has to be to accurately capture the large-scale structures of a turbulent channel flow. The premultiplied spectrum of the streamwise velocity obtained from the largest domains only contains about 70% of the total energy [68]. The maximum length of the streamwise streaks remains unknown.

2.1.5 Quadrant analysis

In the Reynolds-averaged Navier-Stokes (RANS) simulations, the quantities are decomposed into mean and fluctuating components. The Reynolds normal stresses and shear stresses are $\overline{u'_i u'_i}$ and $\overline{u'_i u'_j}$, respectively, as a result of Reynolds decomposition and averaging. According to the signs of the instantaneous $u'v'$, the fluid motions were classified into four categories, as shown in figure 2.8.

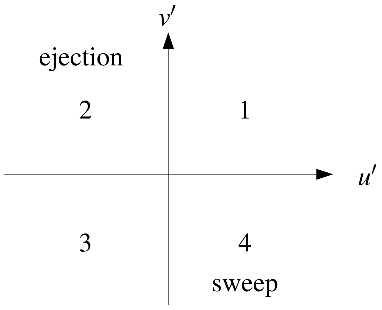

Figure 2.8 Categories of the instantaneous $u'v'$.

Corino and Brodkey [21] reported two main ones that are ejection ($u' < 0$, $v' > 0$) and sweep ($u' > 0$, $v' < 0$). In the turbulent channel flow, the Reynolds shear stress can be obtained from the joint probability density functions of velocity fluctuations by

$$\overline{u'v'} = \int_{-\infty}^{+\infty} \int_{-\infty}^{+\infty} u'v' P(u', v') du'v' \tag{2.1}$$

These four fluid-motions contribute to the Reynolds shear stress, so the physics of the generation of Reynolds shear stresses can be understood by quadrant analysis. The first quadrant analysis of Reynolds shear stress was carried out by Wallace et al. [124]. In reference [123], the history and evolution of quadrant analysis in turbulence research were reported in detail.

$P(u', v')$ is the joint probability density function of streamwise and wall-normal velocity fluctuations. As shown in figure 2.9, the points of (u', v') are obtained from the simulation results at a monitoring position. These points are put into the discretized domain and counted

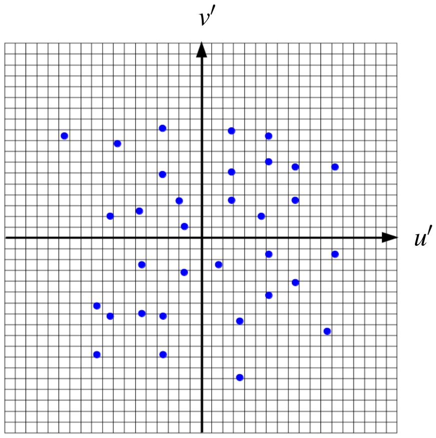

Figure 2.9 Calculation of the jPDFs for $P(u',v')$. A blue dot denotes a sample of (u',v') from the simulation results.

in every cells. The jPDFs for $P(u',v')$ in each cell can be calculated as

$$P(u',v') = N_{cell}/N_{total} \tag{2.2}$$

N_{cell} is the number of samples in each cell, and N_{total} is the total number of samples from the simulation results.

2.2 Flow control methods

At the beginning of twentieth century, the boundary layer theory was introduced by Ludwig Prandtl, which is a foundation to develop many flow control methods. One target of flow control is to reduce the drag of the wings, improving the aeroplane efficiency. In the boundary layer, fluid-motions play an important role in the drag, especially the viscous drag in a turbulent flow. Recently, the flow control methods can be divided into passive and active types due to the requirement of energy. The passive control does not need any energy input, but the active control needs external energy to manipulate flow. Based on the control loop, active control includes predetermined control and interactive control. The interactive control can be separated into feedforward control and feedback control. Figure 2.10 shows the classification [57]. The basics of flow control and some control practices are introduced in detail in book [28].

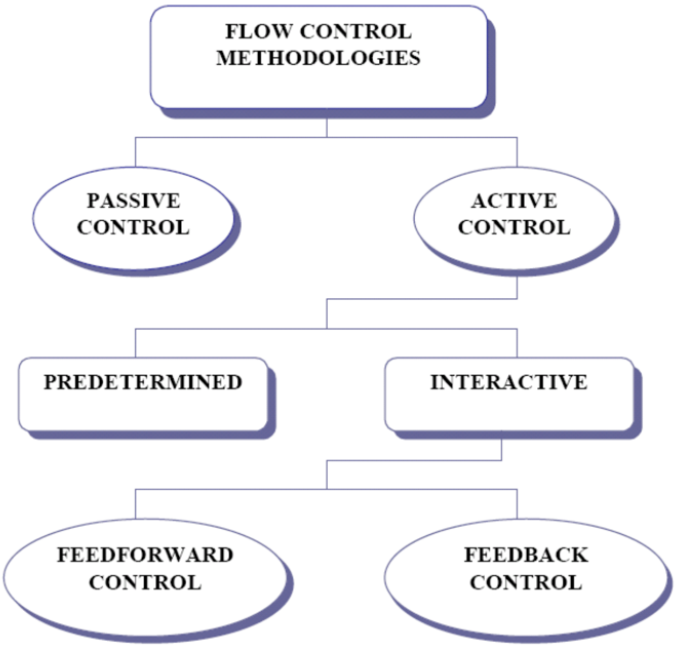

Figure 2.10 Classification of flow control methods [57]

2.2.1 Passive methods

External energy or auxiliary power is not always needed to achieve flow control. Some methods can control the development of the boundary layer and/or the interaction of the boundary layer with outer flow using some structural and morphological components, such as riblets, micro-textures, superhydrophobic surfaces, wavy surfaces, passive vortex generators and so on. Riblets, micro-textures and superhydrophobic surfaces are usually used to reduce drag. Flow separation is controlled by passive vortex generators. Since this research focuses on the drag reduction, the investigations and applications of riblets and micro-textures are reviewed in this section.

Riblets and micro-textures

In recent years, riblets and micro-textures have been used widely in aerospace, automotive and energy, as shown in figure 2.11. As one of the passive flow control methods, riblets and micro-texture can reduce drag approximately 6-10% in the turbulent flow. With featured surfaces, the turbulent boundary layers are controlled to reduce the skin friction, leading to drag reductions and saving fuel costs. Saravi and Cheng [102] gave a good review of drag reduction by riblets and micro-texture.

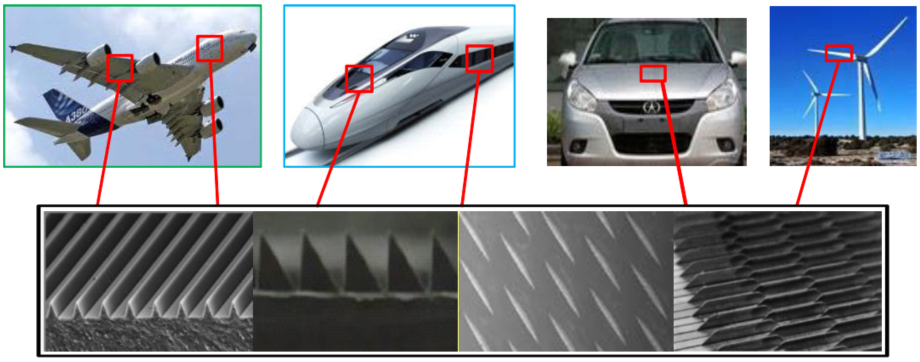

Figure 2.11 Riblets and Micro-texture applications in Aerospace, Automotive and Energy [102]

The riblet used in drag reduction is originally proposed by Michael Walsh and his group at NASA Langley Research Center [125, 126]. The wall was paved with symmetric v-groove riblets with the same height and spacing $15\nu/u_\tau$, reaching a reduction of 8% in skin friction. These riblets were longitudinally manufactured on the surfaces. The drag reduction by riblets can be considered as a roughness problem [117]. In the near-wall region, the characteristics of turbulence structures depend on the wall surface conditions, especially surface roughness. Peet et al. [85] increased the drag reduction by at least 50% by using sinusoidal-like rods, as displayed in figure 2.12. The wavelength was considered to be a key parameter that influences the performance of the riblets. Recently, Sareen et al. [103] applied riblet film on airfoils for wind turbines. This approach could reach a drag reductions up to 5%. An optimum riblet size of 62µm was found for a range of Reynolds numbers.

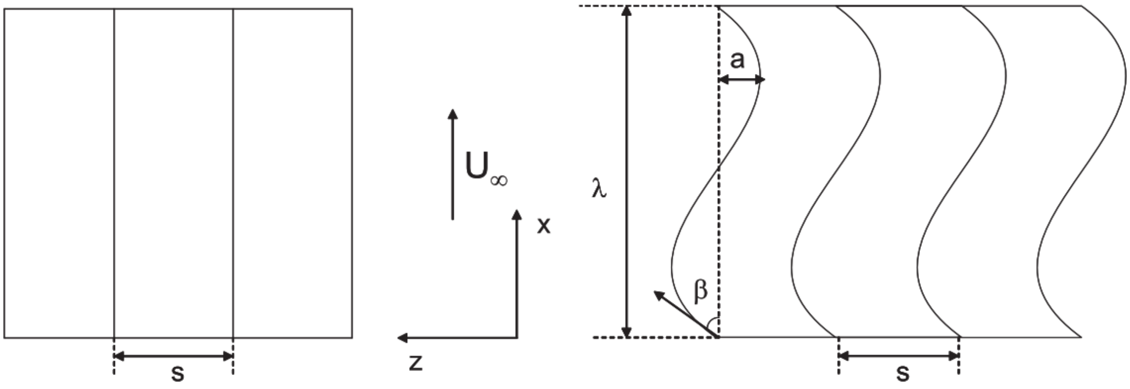

Figure 2.12 Straight riblets (left) and sinusoidal riblets (right) [85]. The flow is from bottom to top.

Many investigations have been carried out to study the physical mechanisms of the drag reduction by riblets. With experiments, Grek et al. [33] found that the point of laminar-turbulent transition is shifted downstream by the riblets, leading to drag reductions. Karniadakis and Choi [49] reviewed drag reductions by riblets and external forcing in wall-bounded flows. They found that the mechanism of drag reductions is the spanwise movement of longitudinal vortices which is passively forced by the riblets in the near-wall region. Jung et al. [44] Introducing small-scale streamwise vorticity near the wall to damp the lager streamwise vortices of the buffer layer can also reduce the drag. García-Mayoral and Jiménez [29] thought that the breakdown of the viscous regime is the key to have the drag-reduction effect. The physical mechanisms of drag reductions by riblets still need to be further investigated.

Riblets have been used in public, but it is not successful in the airline industry. The tests of drag reduction were good during the conducts, but the riblets are not durable, causing many issues. The riblets need big cost and labour to install, and a large part of profits is spent on the maintenance. Crucial structural inspections are affected by the riblets as well. Such significant drawbacks influence the promotion prospects of the riblets. However, materials and methods are developing, riblets are still a good flow control method to be considered.

2.2.2 Active methods

Active flow control methods have two advantages that passive methods do not have. Firstly, the methods can use small and localized energy-input to obtain large effects by introducing the control input at a high receptivity region. Secondly, the complex and dynamical processes can be controlled, such as the drag reductions in turbulent boundary layers by reducing the turbulent production. Active flow control is a powerful and effective way to reduce the turbulent drag and to control the flow separation. Many active methods have been developed for turbulent drag-reduction, including spanwise oscillating wall, rotating disks, plasma actuators, travelling waves, opposition control, and uniform wall blowing/suction. For the separation control, synthetic jet is a important method that must be mentioned.

Spanwise oscillating wall

Many experiments and numerical studies found that transient reductions of all turbulent quantities would happen when a spanwise pressure gradient was suddenly added into a two-dimensional turbulent boundary layer, such as the reports in references [16, 23, 78]. Johansson et al. [43] suggested that the turbulent drag reduction is caused by a flow phenomenon which presents as a streaky pattern. This influences the near-wall flow structures, leading to the reduction of near-wall turbulence production.

The group of Jung et al. [9, 44] firstly used DNS simulations to achieve sustained drag-reductions up to 40% of the friction drag by adding spanwise wall-oscillations into a planar turbulent channel flow. In their DNS cases, the channel walls oscillate in the spanwise direction with prescribed velocity $W_{wall} = 0.8(Q_x/2\delta)\sin(wt)$ and period $T^+_{osc} = 100$, where Q_x is the flow rate (per unit width) in the streamwise direction. $T^+_{osc} = T_{osc}u^2_\tau/\nu$ and δ is the half height of the channel. Laadhari et al. [59] carried out experiments and gained the same results as Jung. Figure 2.13 shows the experiment setup.

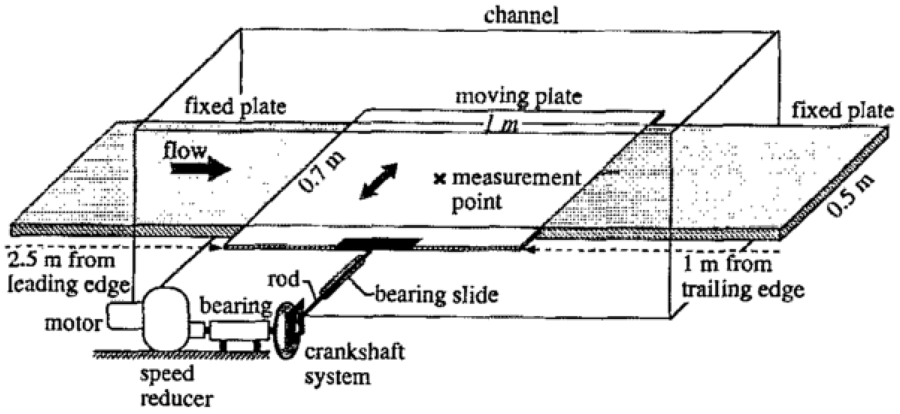

Figure 2.13 The experiment setup of spanwise wall oscillations [59].

Baron and Quadrio [12] fixed the period of wall oscillations at $T^+_{osc} = 100$ and found the best value of the oscillating amplitudes. The overall energy balance was first considered. Their study showed that using a low oscillating amplitude could give a positive overall energy balance, which means saving energy. Choi et al. [20] carried out experiments to investigate the mechanism of the turbulent drag reduction of spanwise wall oscillations. They conformed that the reductions have a strong connection with the spanwise vorticity generated by the periodic Stokes layer. Figure 2.14 shows the effects of spanwise wall oscillations on the longitudinal vortices in the near-wall region of the boundary layer. Moreover, they suggested that an improvement of drag reduction can be achieved by increasing the ratio of the spanwise-wall velocity to the freestream velocity of the boundary layer.

A key of drag reduction was noted by Choi et al. [19], which is the disturbance between the near-wall streamwise vortices and the walls. They also found the spanwise averaged velocity profiles are similar to the Stokes layer profiles. Moreover, Quadrio and Ricco [88] investigated the initial status of the oscillations before the flow is fully developed and assessed the wall oscillations [89]. They found that the net energy saving was up to 7.3% which is defined as $N_p = (P_{saved} - P_{spent})/P_0$, where P_{saved}, P_{spent}, and P_0 are the saved energy, the energy spent on the active control, and the energy used to drive the flow in an uncontrolled flow. A scaling parameter S is increased linearly with drag reduction, as explained in reference [96].

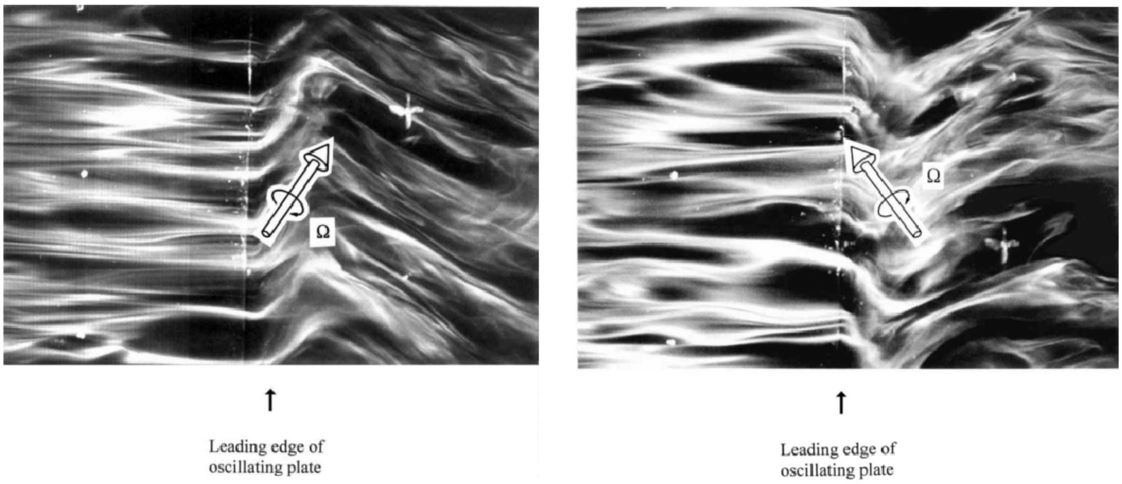

(a) moving upward

(b) moving downward

Figure 2.14 Flow visualization of longitudinal vortices in the near-wall region of the boundary layer with a wall oscillation. The flow is from left to right. [20]

The fundamental mechanisms of the drag reduction in a fully developed channel flow were revealed by Touber and Leschziner [118] using second-moment budgets, joint-probability-density functions, enstrophy, and energy-spectra maps. The Reynolds number was $Re_\tau = 500$. Period was $T^+ = Tu_\tau^2/\mu = 100$ and 200, where u_τ was the friction velocity in the unforced flow. The wall motion was described by

$$W(t) = W_m \sin\left[\frac{2\pi t}{T}\right] \tag{2.3}$$

The wall-velocity amplitude was $W_m^+ = W_m/u_\tau = 12$. They found that the turbulence contribution to the wall shear stress was disrupted by the spanwise distortions in the streak near-wall structures. When the Reynolds number increased, the actuation efficiency reduces due to a modulating 'top-to bottom' effect associated with large-scale outer-layer structures.

All of the above DNS studies used the geometry of a channel flow, but the experiments are carried out in the boundary-layer flow. Yudhistira and Skote [134] were the first to simulate the spanwise wall oscillations in the boundary-layer flow with DNS. Their research was further discussed in reference [108]. Their results were similar to the previous experimental results. Some further investigations of the spanwise oscillating wall have been done, such as the scaling of the velocity profile by Skote [109], qualitative correlations by Negi et al. [82], and the turbulence vorticity by Agostini et al. [7]. It is interesting that an illustration of the near-wall interactions were shown by Agostini et al. [7] during the drag-reduction or drag-increase interval of the actuation cycle.

Recently, experiments and simulations focus on the statistical characters of the correlation between the large-scale motion and the modulation [13, 71, 73, 106, 135]. Leschziner's group has investigated the spanwise oscillating wall in detail [2–6, 118].

Travelling waves

In the case of Jung et al. [44], the spanwise velocity of the walls was time dependent,

$$W_{wall} = W_m \sin(ft) \tag{2.4}$$

where f is the frequency of the spanwise oscillations and W_m is the maximum velocity of the wall. Quadrio et al. [92] converted it into a wavelength dependent oscillation,

$$W_{wall} = A\sin(\frac{2\pi}{\lambda_x}x) \tag{2.5}$$

where A is the maximum oscillation amplitude and λ_x is the streamwise wavelength. Viotti et al. [122] took advantage of this to analyse the energetic cost of the wall forcing. They also found an optimal streamwise wavelength which could significantly improve the energetic performance of passive flow control. Quadrio et al. [91] investigated the streamwise-travelling waves which were imposed by the spanwise wall velocity. The streamwise wavelength was useful to investigate the qualitative correlation. Both drag increase and reduction can be produced by the travelling waves. The backward-travelling waves always produce drag reduction [91]. A net energy saving is gained larger than 26%.

Uniform wall blowing/suction

Uniform wall blowing/suction is to impose a uniform wall-normal velocity on the wall, which was recently reviewed by Kornilov [55]. The original idea was to delay the flow transition from laminar to turbulence. This control method can be achieved by injection or suction of air through a permeable porous wall. The early experiments and simulations have been conducted for a turbulent boundary layer [41, 74, 77, 115].

To analyse the drag reduction quantitatively, a mathematical relation between skin-friction drag and Reynolds shear stresses named 'FIK identity' was derived by Fukagata et al. [26]. They found that the contribution of enhanced turbulence was decreased by the mean wall-normal convection. Fukagata et al. [27] studied a feedback-controlled turbulent channel flow at $Re_\tau = 640$ using DNS. By using FIK identity, they examined the contribution of drag reduction from damping the wall-normal velocity fluctuations. The fluctuations were classified into small scale and large scale by the spanwise wavelength $\lambda^+ = 300$. Their study reveals that more drag reduction could be achieved by the control of small scale fluctuations. The similar analysis was employed by Kametani and Fukagata [45] in their DNS study for applying the control method on a spatially developing turbulent boundary layer at low Reynolds number. Both uniform blowing and suction are investigated in the study which showed that the turbulent contribution of the friction drag was overwhelmed by the contribution of mean convection.

Kametani et al. [46] used wall resolved LES to investigate the controlling effects on the skin friction drag in a turbulent boundary layer at moderate Reynolds numbers up to $Re_\theta = 2500$. In their study, the Reynolds stresses were reduced by suction and increased by blowing. The control method could influence the fluctuation energy in the outer region. A spectral analysis was performed and showed that the energy was increased and decreased by blowing and suction, respectively. Kametani et al. [47] also separated the blowing region into several sections, finding that the large net-energy saving rates still could be achieved with spatially intermittent blowing regions. Mahfoze et al. [69] gained a net energy saving of 5% in their optimization.

In 1977, Schetz and Nerney [105] tested the blowing method on an axisymmetric model in a experiment, gaining reduction of the skin friction. Liu et al. [66] evaluated the blowing and suction method on a RAE2822 airfoil at Reynolds number $Re = 3.4 \times 10^6$, obtaining a drag reduction up tp 16%. The suction region was positioned at the leading edge to delay the transition from laminar to turbulent, and the blowing region was installed at the trailing edge to reduce the drag.

In a recent research, Noguchi et al. [83] studied the combination of uniform blowing and suction on a flat plate in detail. The global skin friction could be reduced by 44.1%. They found that the uniform blowing should be located upstream side of the turbulent region to obtain efficient effect of drag reduction. The blowing method was examined in a turbulent channel flow over a two-dimensional rough wall by Mori et al. [80]. Because the von Kármán constant was not changed by the method. They suggested that adding the roughness function term into Stevenson's formula could account the roughness effect for the log-law region. Eto et al. [24] experimentally investigated the blowing method on a Clark-Y airfoil at Reynolds number $Re = 1.5 \times 10^6$, different angles of attack $AOA = 0°, 6°$. Although the friction drag was reduced, the total drag was increased because of the pressure drag.

Synthetic Jets

Recently, the synthetic jet is one of the popular zero-net-mass-flux actuators, which has been intensively investigated on a wing. It can be used to reduce noise [10, 11, 14, 32, 70], to increase the lift-drag ratio or control flow separation of airfoils [1, 39, 53, 107, 111], to control the turbulence in boundary layers [61, 93, 94]. All of them are very useful to the airline industry. Figure 2.15 shows one kind of synthetic-jet device. The achievements and challenges of the synthetic jets are well reviewed by Glezer and Amitay [31] and Leschziner and Lardeau [63].

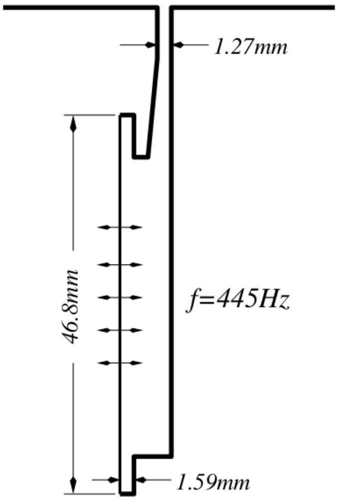

Figure 2.15 A kind of synthetic-jet device in a side view [100]

The synthetic jet was firstly simulated by Kral et al. [58] solving unsteady, two-dimensional, incompressible, and Reynolds-averaged Navier-Stokes equations. A suction/blowing type boundary condition was applied on the jet orifice instead of simulating the jet actuator. In their research, the development of the counter-rotating vortices simulated in the turbulent conditions are in agreement with experiments. They found that the pair of vortices under turbulent condition quickly diffuse and are not distinct beyond about one wavelength from the jet exit.

Rizzetta et al. [97] employed DNS to investigate the flow structures surrounding a synthetic-jet actuating device. By solving unsteady compressible Navier-Stokes equations, both the interior of the actuator cavity and the external jet flowfield were simulated. They studied two-dimensional and three-dimensional simulations, comparing with the experimental results. Due to limitations of computing resources, the three-dimensional simulations did not reproduce the exact experimental configuration. Because of the spanwise instabilities in the three-dimensional computations, the coherent vortex structures were broken, but the structures were maintained in the two-dimensional computations.

Mittal et al. [76] studied the interaction of synthetic jet with a flat plat boundary layer. The internal cavity flow and external flowfield are simulated in a simplified, two-dimensional configuration. Their investigation showed that the dynamics of the vortex structures were significantly influenced by the crossflow by comparing the jet with or without quiescent external flow. They also investigated the dynamics under different ratios V_{max}^{inv}/V_∞, where V_{max}^{inv} was the maximum velocity of inviscid jet and V_∞ was the freestream velocity. The vortex pairs formed at the jet lip could leave the boundary layer when the ratio $V_{max}^{inv}/V_\infty \approx 3$, but the vortex pairs could not penetrate out into the freestream when the ratio $V_{max}^{inv}/V_\infty \approx 0.67$. Since the high momentum fluid was injected into the boundary layer by these vortices, the boundary layer in the low ratio case is more resistant to separation than that in the high ratio case. Only if the crossflow velocity is significantly higher than the jet velocity, a large time averaged recirculation bubbles could be formed by the jet in the external boundary layer. Utturkar et al. [119] validated the jet formation criterion Re/Sr^2 for synthetic jet actuators by numerical simulations and experiments. The Reynolds number was based on the velocity scale which is defined as

$$U = \frac{1}{T}\frac{1}{A}\int_A \int_0^{T/2} u(t,y)dtdA \tag{2.6}$$

where A is the exit area, y is the cross-stream coordinate. T is the period, d is the width of the slot. They found that the jet formation depended on the Strouhal number $Sr = \sqrt{2\pi d^2/T\nu}$. Ravi et al. [95] studied the formation and evolution of three-dimensional synthetic jets using DNS. Three aspect ratios of the jet orifice are examined. The total momentum coefficient was found to be relatively insensitive to the aspect ratio.

By using DNS, Lee and Goldstein [61] simulated an array of two-dimensional synthetic jets with the internal cavity flow and the quiescent external flow. They investigated the effects of geometric parameters, such as the lip thickness and the lip geometry. When the lip thickness is greater than or equal to the slot width at $Re = 104.2$ and $Sr = 0.0628$, the boundary layer in the slit could become fully developed as in pipe flow. The device Reynolds number Re and Strouhal number Sr are based on the slot half-width and the maximum averaged jet velocity across the slot.

Kamnis and Kontis [48] examined different turbulence models, such as Spalart-Allmaras, $k-\varepsilon$ and $k-\omega$ models. The basic characteristics of the synthetic jet without cross-flow was predicted the best by the Spalart-Allmaras models. They did not simulate the internal cavity flow. A sinusoidal function was employed to simulate the jet velocity in the jet direction. A parabolic profile that was a function of radial distance across the orifice was used to describe the distribution of jet velocity. The parabolic profile could accurately predict the flow by physically correct forcing velocity. They also studied the effects of synthetic jet at different locations of NACA0015, showing the maximum lift change is at $x/c = 0.5$. The streamwise distance from the leading edge was x, and the chord length was c. A positive lift at zero degrees angle of attack could be produced by putting the synthetic jet near the leading edge.

Using a modified dynamic grid method, Xia and Qin [129] applied DES to simulate the synthetic jet with the internal cavity flow and quiescent external flow. Since a inflow/outflow boundary condition was used for the far field boundary, the simulation domain could be relatively small. This saved at least 30% computational costs. In order to improve the simulation, Qin and Xia [87] added a cubic-root filter in DES and used a hybrid centred-upwind flux scheme, gaining a better result compared with the standard method.

You et al. [133] employed Large-eddy simulation to predict the effects of synthetic jet on the turbulent flow separation over a wall-mounted hump. They used a dynamic subgrid-scale model was used to model the SGS stress tensor. The procedure of computing the Smagorinsky coefficient in the dynamic model was proposed by Germano et al. [30] and modified by Lilly [65]. A nondissipative, central-difference spatial discretization scheme was employed to retain the accuracy and predictive capability of the LES Mittal and Moin [75]. Using velocity boundary conditions, they introduced the synthetic jet into the external flow by the sinusoidal function as

$$U_{jet} = 6U_m \left[\frac{\xi}{d} - \left(\frac{\xi}{d} \right)^2 \right] \sin(2\pi f t) \tag{2.7}$$

where d was the slot width, $0 \leqslant \xi \leqslant d$, U_m was the peak bulk velocity of the jet, f was the jet frequency. The same approach was employed to replace simulating the detailed cavity flow by Rumsey et al. [100], Šarić et al. [104], and Capizzano et al. [18]. Such velocity boundary mostly did not affect the control effects. They claimed that their LES was consistently more accurate than the LES with a constant coefficient Smagorinsky model and dissipative numerics, implicit LES, DES, and URANS. They also investigated the control effects of synthetic jet on a NACA 0015, simulating the cavity flow [132]. The onset of flow separation was delayed, increasing the lift coefficient significantly.

The active separation control over a rounded ramp was examined by Dandois et al. [22] using DNS. They found two different modes, including vorticity-dominated and acoustic-dominated modes. The former one was observed in the low-frequency forcing case, reducing the separation length by 54%. The latter one was identified in the high-frequency forcing case. The separation length was increased by 43%. Stanek et al. [113, 114] presented that the low-frequency forcing increased the inviscid instability, but the high-frequency forcing weakened or cancelled the inviscid instability. This phenomena modified the mean flow through mixing, causing different statuses of separations.

Ishibashi and Miyaji [39] put a slot of a synthetic jet on the NACA 0012 airfoil. They found that the best practical angle was around 45° downstream which could suppress the flow separation and produce a highest lift-drag ratio with the synthetic jet. Abe et al. [1] investigated the effects of a synthetic jet installed on the leading edge of NACA0015 at

$Re = 63,000$ and $AOA = 12.0°$. They imposed the synthetic jets in two ways, including 'Cavity model' and 'Bc model'. The jet was directly simulated by a three-dimensional deforming cavity in 'Cavity model', and an artificial jet-profile was applied on the jet orifice in 'Bc model'. The spanwise disturbance induced by the synthetic jets were not always beneficial for the aerodynamic performance, even it was good for the turbulent transition. By using DNS, Zhang and Samtaney [136] compared the effects of three different frequencies on the flow-separation control, including the $f^+ = fC/U_0 = 0.5$, $f^+ = 1.0$, and $f^+ = 4.0$. A velocity profile that was parabolic and sinusoidal was applied on the jet slot. The lift-to-drag ratios were increased in all controlled cases.

A recent research done by Yao et al. [131] shows that it is possible to reduce the friction drag with spanwise opposed wall-jet forcing. They employed body forcing to obtain wall-jet in the near-wall region. The wall-jet can be produced by synthetic jets as well.

All of the investigations show that the synthetic jet is an effective method of active flow control. The jet slots were set normal to the freestream. The jets were vertically injected into the external flow. The drag of the airfoils was reduced due to the decrease of the pressure difference by suppressing the separation. There is no investigation of the synthetic jet by setting the jet slot along with the streamwise direction and the jet injected parallel with the wall. Can this synthetic jet be used to reduce the friction drag in that particular way? The question will be answered in this research.

Chapter 3

Methodologies

An in-house flow solver called SHEFFlow is developed to simulate the flow. It solves three dimensional, compressible Navier-Stokes equations with finite volume methods. The mesh is in unstructured file-format and is generated by Pointwise for the solver. In order to do DNS simulations, a high order MUSCL scheme is employed for the spatial accuracy in the CFD solver. A second order of time marching scheme is used to keep the time accuracy. At the beginning, DES was planed to do the investigation, but the flow structures could not be well resolved as the flow is modelled in the near-wall region, so DNS is the right tool to simulate the flow.

Before discussing the numerical details of SHEFFlow, some underlying assumptions should be announced. The speed of the fluid motion is much slower than the speed of light, so the study does not belong to the relativistic mechanics. The target fluid is an ideal gas, which is continuous, Newtonian and isotropic. SHEFFlow uses several numerical methods, including finite volume method, preconditioned Roe scheme, second order upwind scheme for spatial discretization, third and fifth order MUSCL schemes for spatial discretization, and dual time-step for temporal discretization. The parallel ability is achieved by using Open MPI.

3.1 Finite Volume Method

In CFD, the compressible Navier-Stokes equations can be solved with three types of methods, including finite difference method, finite volume method and finite element method. SHEFFlow uses finite volume method which is wildly employed in the industrial research. The computational domain is discretized into finite control-volumes based on the grid in the simulations.

The compressible Navier-Stokes equations consist of the conservation of mass, momentum, and energy equations, as expressed below in an integral form.

$$\frac{\partial}{\partial t}\int\int\int \boldsymbol{W} dV + \int\int [\boldsymbol{F}-\boldsymbol{G}]\cdot d\boldsymbol{A} = 0 \tag{3.1}$$

where, t is the time, V is an arbitrary control volume, $d\boldsymbol{A}$ is the vector of the differential surface area, $\boldsymbol{W}$ is the conserved variables, $\boldsymbol{F}$ and $\boldsymbol{G}$ are the inviscid and viscous fluxes, respectively. The variables and the fluxes are

$$\boldsymbol{W} = \left\{\begin{array}{c} \rho \\ \rho v_x \\ \rho v_y \\ \rho v_z \\ \rho E \end{array}\right\}, \quad \boldsymbol{F} = \left\{\begin{array}{c} \rho \boldsymbol{v} \\ \rho \boldsymbol{v} v_x + p\hat{\boldsymbol{i}} \\ \rho \boldsymbol{v} v_y + p\hat{\boldsymbol{j}} \\ \rho \boldsymbol{v} v_z + p\hat{\boldsymbol{k}} \\ \rho \boldsymbol{v} E + p\boldsymbol{v} \end{array}\right\}, \quad \boldsymbol{G} = \left\{\begin{array}{c} 0 \\ \boldsymbol{\tau}_{xi} \\ \boldsymbol{\tau}_{yi} \\ \boldsymbol{\tau}_{zi} \\ \boldsymbol{\tau}_{ij} v_j - \boldsymbol{q} \end{array}\right\}$$

where, $\rho, \boldsymbol{v}, E$, and p are the density, velocity, total energy per unit mass, and pressure of the fluid, respectively. The term $\tau_{ij} = \mu\left(v_{i,j} + v_{j,i} - \frac{2}{3} v_{k,k}\delta_{ij}\right)$ is the viscous stress tensor, $\boldsymbol{q} = -\kappa \frac{\partial T}{\partial \boldsymbol{x}}$ is the heat flux vector, and $\boldsymbol{x} = x\hat{\boldsymbol{i}} + y\hat{\boldsymbol{j}} + z\hat{\boldsymbol{k}}$ is the position vector. Total energy is related to the total enthalpy H by $E = H - p/\rho$, where $H = h + |\boldsymbol{v}|^2/2$ and $h = C_p T$. The ideal gas equation, $P = \rho RT$, plays the role of a constraint for the compressible Navier-Stokes equations. The ideal gas constant R is equal to $287.04\,\mathrm{J\,kg^{-1}\,K^{-1}}$. At the same time, the Sutherland's law is used to calculate the viscosity and thermal conductivity of the fluid, which is

$$\mu = \mu_0 \frac{T_0 + C}{T + C}\left(\frac{T}{T_0}\right)^{\frac{3}{2}} \tag{3.2}$$

Normally, the reference values of μ_0 and T_0 are from the ideal air at the sea level, which are $\mu_0 = 1.7894 \times 10^{-5}\,\mathrm{m^{-1}\,kg\,s^{-1}}$ and $T_0 = 288.15\mathrm{K}$. The Sutherland's constant $C = 110.4$. Moreover, for the ideal gas, the speed of sound a can be calculated by $a = \sqrt{\gamma RT}$ and the Mach number is $Ma = |\boldsymbol{v}|/a$.

According to equation 3.1, the Navier-Stokes equations can be solved by the volume and face integration. The grid architecture of SHEFFLow is unstructured and the primitive variables $\boldsymbol{Q}$ are located at the cell centre, where $\boldsymbol{Q} = [p, v_x, v_y, v_z, T]^T$. The conserved variables $\boldsymbol{W}$ are directly calculated from $\boldsymbol{Q}$, which is stored at the cell centre as well. The inviscid and viscous fluxes are at the face centre. The viscous flux $\boldsymbol{G}$ is obtained by the second order central difference scheme. The inviscid flux $\boldsymbol{F}$ is gained by Roe scheme which

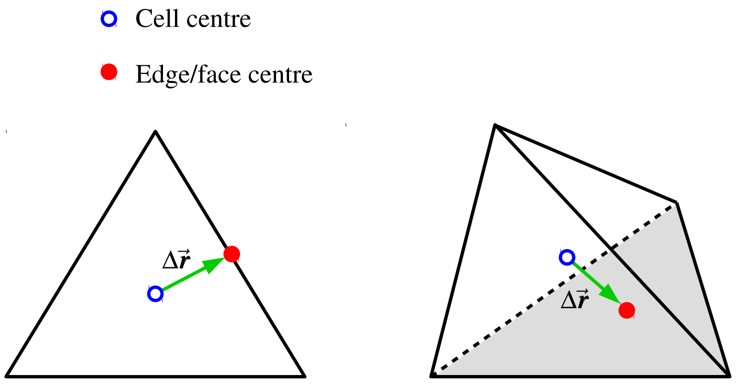

2D cell

3D cell

Figure 3.1 Illustration of the second order piecewise linear reconstruction. $\Delta\vec{\boldsymbol{r}}$ is the displacement vector from the cell centre to the edge/face centre.

is well known as Roe's approximate Riemann solver [99], as shown below.

$$\boldsymbol{F} = \frac{1}{2}(\boldsymbol{F}^R + \boldsymbol{F}^L) - \frac{1}{2}|B|\Delta\boldsymbol{W} \tag{3.3}$$

where $\boldsymbol{F}^R$ and $\boldsymbol{F}^L$ are the fluxes computed from the right $\boldsymbol{W}^R$ and left $\boldsymbol{W}^L$ of the face, and $\Delta\boldsymbol{W} = \boldsymbol{W}^R - \boldsymbol{W}^L$. The values at the cell centres from each side of the face can be directly given to $\boldsymbol{W}^R$ and $\boldsymbol{W}^L$ by using a first order upwinding scheme. The term $\frac{1}{2}(\boldsymbol{F}^R + \boldsymbol{F}^L)$ can be considered as the physical flux in a second order central difference form. The term $\frac{1}{2}|B|\Delta\boldsymbol{W}$ is an upwind term, introducing numerical dissipation to make the Roe scheme stable. The matrix B is the Jacobian $\partial\boldsymbol{F}/\partial\boldsymbol{W}$, which is evaluated at the Roe average state.

The accuracy of the values at the face centre for reconstructing the $\boldsymbol{W}^R$ and $\boldsymbol{W}^L$ is very important for the spatial accuracy. In order to increase the spatial accuracy, a second order piecewise linear reconstruction is employed in SHEFFlow, as shown in figure 3.1. The primitive variables are computed by

$$\boldsymbol{Q}_F = \boldsymbol{Q}_C + \nabla\boldsymbol{Q}\cdot\Delta\vec{\boldsymbol{r}} \tag{3.4}$$

where $\boldsymbol{Q}_F$ is the primitive variables at the face centre, $\boldsymbol{Q}_C$ is the primitive variables at the cell centre, and $\nabla\boldsymbol{Q}$ is the gradient in the cell. $\boldsymbol{W}^R$ and $\boldsymbol{W}^L$ are computed from $\boldsymbol{Q}_F$.

Using the divergence theorem, the gradient $\nabla\boldsymbol{Q}$ can be computed in a discrete form as

$$\nabla\boldsymbol{Q} = \frac{1}{V}\sum_{faces}\boldsymbol{Q}_a\cdot\boldsymbol{A} \tag{3.5}$$

$\boldsymbol{Q}_a$ is simply computed from the average values of $\boldsymbol{Q}_C^R$ and $\boldsymbol{Q}_C^L$ which are the primitive variables at the right and left side of the face.

$$\boldsymbol{Q}_a = \frac{1}{2}\left(\boldsymbol{Q}_C^R + \boldsymbol{Q}_C^L\right) \tag{3.6}$$

This is a traditional approach to have a second order accuracy for unstructured solvers, but the accuracy is not satisfied in this research.

3.2 High order MUSCL scheme

In order to improve the accuracy of SHEFFlow, a high order method is necessary to be added into the in-house code. Li et al. [64] used second order for the viscous term and fifth order for the inviscid term to study the feasibility of compressible direct numerical simulation at extremely low Mach numbers. The high order method for the inviscid term was the fifth-order MUSCL scheme proposed by Kim and Kim [52]. The limiter function was not used to avoid introducing extra dissipation and damaging the turbulent structures. In the i-direction, the fifth order MUSCL scheme without a limiter function is

$$\begin{aligned}\boldsymbol{Q}_{i+1/2}^L &= (2\boldsymbol{Q}_{i-2} - 13\boldsymbol{Q}_{i-1} + 47\boldsymbol{Q}_i + 27\boldsymbol{Q}_{i+1} - 3\boldsymbol{Q}_{i+2})/60 \\ \boldsymbol{Q}_{i-1/2}^R &= (-3\boldsymbol{Q}_{i-2} + 27\boldsymbol{Q}_{i-1} + 47\boldsymbol{Q}_i - 13\boldsymbol{Q}_{i+1} + 2\boldsymbol{Q}_{i+2})/60\end{aligned} \tag{3.7}$$

where i is the cell index. $i+1/2$ means the right face of the i_{th} cell, and $i-1/2$ means the left face of the i_{th} cell, as shown in figure 3.2. This can be extended to the other two directions.

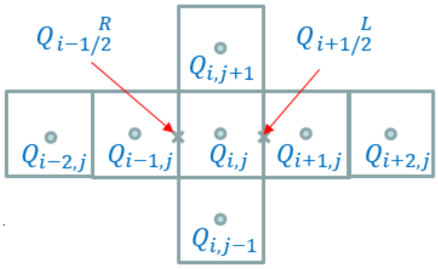

Figure 3.2 Illustration of the 5^{th} order MUSCL scheme.

In this study, the third order MUSCL is tested as well to check if it is accurate enough for this research. The third order MUSCL scheme without a limiter function is

$$\begin{aligned}\boldsymbol{Q}_{i+1/2}^L &= (-\boldsymbol{Q}_{i-1} + 5\boldsymbol{Q}_i + 2\boldsymbol{Q}_{i+1})/6 \\ \boldsymbol{Q}_{i-1/2}^R &= (2\boldsymbol{Q}_{i-1} + 5\boldsymbol{Q}_i - \boldsymbol{Q}_{i+1})/6\end{aligned} \tag{3.8}$$

Since this high order scheme is a structured method, it only works for the structured mesh in SHEFFlow. But SHEFFlow is an unstructured solver, the structured mesh is stored in an unstructured file-format. The cell stencils are adapted to satisfy the method.

3.3 Wall boundary condition

In SHEFFlow, wall boundary condition is adapted to satisfy the 5^{th} order MUSCL scheme. As shown in figure 3.3, three levels of ghost cells are employed to compute the fluxes near the wall. The values of primitive variables, $\boldsymbol{Q}^c$, in the simulation domain are computed and updated by solving the Navier-Stokes equations. The values of primitive variables, $\boldsymbol{Q}^g$, in the center of ghost cells are calculated as below to create a non-slipping isothermal wall.

$$\boldsymbol{Q}_i^{\boldsymbol{g}} = \left\{ \begin{array}{c} p_i^g \\ \boldsymbol{v}_i^g \\ T_i^g \end{array} \right\} = \left\{ \begin{array}{c} p_i^c \\ -\boldsymbol{v}_i^c \\ T_{wall} \end{array} \right\}$$

$$\boldsymbol{Q}_{i-1}^{\boldsymbol{g}} = \left\{ \begin{array}{c} p_{i-1}^g \\ \boldsymbol{v}_{i-1}^g \\ T_{i-1}^g \end{array} \right\} = \left\{ \begin{array}{c} p_{i-1}^c \\ -\boldsymbol{v}_{i-1}^c \\ T_{wall} \end{array} \right\}$$

$$\boldsymbol{Q}_{i-2}^{\boldsymbol{g}} = \left\{ \begin{array}{c} p_{i-2}^g \\ \boldsymbol{v}_{i-2}^g \\ T_{i-2}^g \end{array} \right\} = \left\{ \begin{array}{c} p_{i-2}^c \\ -\boldsymbol{v}_{i-2}^c \\ T_{wall} \end{array} \right\}$$

Where, $\boldsymbol{Q} = [p, \boldsymbol{v}, T]^T$, T_{wall} is the wall temperature.

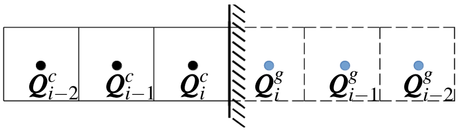

Figure 3.3 Illustration of wall boundary condition for the 5^{th} order MUSCL scheme.

3.4 Preconditioned Roe scheme

The pure Roe scheme is good with high Mach number, but it cannot deal well with the low Mach number, especially extremely low Mach number. There is a drawback buried in the matrix B. In Equation 3.3, the matrix B can be diagonalized into $|B| = M|\Lambda|M^{-1}$, where $\Lambda = \lambda(B) = diag(u, u, u, u+a, u-a)$. u is the flow velocity. a is the speed of sound. If the

Mach number is very low, it will have $u \ll a$. The eigenvalues are not in a same order. This influences the convergence and accuracy of the simulation results. In this study, the flow structures should be accurately captured in the near-wall region where the Mach number is relatively low. The preconditioned Roe scheme proposed by Weiss and Smith [128] is used to avoid this issue. The acoustic speeds of the system are altered to make all eigenvalues in the same order, so the convergence can be independent of Mach number.

In order to change the matrix B, the dependent variable in equation 3.1 is transformed from conserved variables $\boldsymbol{W}$ to primitive variables $\boldsymbol{Q}$.

$$\frac{\partial \boldsymbol{W}}{\partial \boldsymbol{Q}} \frac{\partial}{\partial t} \int\int\int \boldsymbol{Q} dV + \int\int [\boldsymbol{F} - \boldsymbol{G}] \cdot d\boldsymbol{A} = 0 \tag{3.9}$$

The Jacobian $\partial \boldsymbol{W} / \partial \boldsymbol{Q}$ is computed as

$$\frac{\partial \boldsymbol{W}}{\partial \boldsymbol{Q}} = \begin{bmatrix} \rho_p & 0 & 0 & 0 & \rho_T \\ \rho_p v_x & \rho & 0 & 0 & \rho_T v_x \\ \rho_p v_y & 0 & \rho & 0 & \rho_T v_y \\ \rho_p v_z & 0 & 0 & \rho & \rho_T v_z \\ \rho_p H - 1 & \rho v_x & \rho v_y & \rho v_z & \rho_T H + \rho C_p \end{bmatrix}$$

with

$$\rho_p = \left. \frac{\partial \rho}{\partial p} \right|_T, \quad \rho_T = \left. \frac{\partial \rho}{\partial T} \right|_p$$

The reasons for the choice of primitive variables $\boldsymbol{Q}$ as dependent variables are discussed by Weiss and Smith [128]. In our study, using the primitive variables $\boldsymbol{Q}$ is helpful for the implement of the high order MUSCL scheme in SHEFFlow.

Reference [128] represents the developing procedure of the preconditioned system in detail. After the procedure, the preconditioned system in conservation form is as the following.

$$\Gamma \frac{\partial}{\partial t} \int\int\int \boldsymbol{Q} dV + \int\int [\boldsymbol{F} - \boldsymbol{G}] \cdot d\boldsymbol{A} = 0 \tag{3.10}$$

Where

$$\Gamma = \begin{bmatrix} \Theta & 0 & 0 & 0 & \rho_T \\ \Theta v_x & \rho & 0 & 0 & \rho_T v_x \\ \Theta v_y & 0 & \rho & 0 & \rho_T v_y \\ \Theta v_z & 0 & 0 & \rho & \rho_T v_z \\ \Theta H - 1 & \rho v_x & \rho v_y & \rho v_z & \rho_T H + \rho C_p \end{bmatrix} \tag{3.11}$$

with

$$\Theta = \left(\frac{1}{U_r^2} - \frac{\rho_T}{\rho C_p}\right) \tag{3.12}$$

The reference velocity U_r is defined as:
For an ideal gas,

$$U_r = \begin{cases} \varepsilon c, & if\ |\boldsymbol{v}| < \varepsilon c \\ |\boldsymbol{v}|, & if\ \varepsilon c < |\boldsymbol{v}| < c \\ c, & if\ |\boldsymbol{v}| > c \end{cases} \tag{3.13}$$

For an incompressible fluid when the density is a constant,

$$U_r = \begin{cases} \varepsilon U_{\max}, & if\ |\boldsymbol{v}| < \varepsilon U_{\max} \\ |\boldsymbol{v}|, & if\ |\boldsymbol{v}| > \varepsilon U_{\max} \end{cases} \tag{3.14}$$

In the preceding expressions, $U_{\max}$ is the maximum velocity within the flowfield, and ε is a small number ($\sim 10^{-5}$) included to prevent singularities at stagnation points.

The resultant eigenvalues of the preconditioned system Eq.3.10 are given by

$$\lambda\left(\Gamma^{-1}\frac{\partial \boldsymbol{F}}{\partial \boldsymbol{G}}\right) = u, u, u, u' + c', u' - c' \tag{3.15}$$

where

$$\begin{aligned} u &= \boldsymbol{v} \cdot \hat{\boldsymbol{n}} \\ u' &= u(1-\alpha) \\ c' &= \sqrt{\alpha^2 u^2 + U_r^2} \\ \alpha &= (1 - \beta U_r^2)/2 \\ \beta &= \left(\rho_p + \frac{\rho_T}{\rho C_p}\right) \end{aligned}$$

3.5 Time marching Method

Since the time accuracy of the governing equations is destroyed by the preconditioning, a dual time-stepping procedure included to overcome the limitation is employed to solve unsteady flow. The dual time-stepping procedure can provide efficient and time-accurate solution for the preconditioned equations. In this study, a preconditioned pseudotime-derivative term is introduced into equation 3.1 as follows:

$$\frac{\partial}{\partial t}\int\int\int \boldsymbol{W}dV + \Gamma\frac{\partial}{\partial \tau}\int\int\int \boldsymbol{Q}dV + \int\int[\boldsymbol{F}-\boldsymbol{G}]\cdot d\boldsymbol{A} = 0 \tag{3.16}$$

where t denotes physical time, and τ is a pseudo time used in the time-marching method. The physical-time term is discretized in an implicit fashion by means of a three-point backwards difference which has second-order-accurate in time. The pseudo-time derivative is driven to zero by means of a multistage Runge-Kutta scheme (RK). When $\tau \rightarrow \infty$, equation 3.1 is recovered because the second term on the left-hand side of equation 3.16 vanishes.

The equation 3.16 can be rewritten as:

$$\frac{\partial \boldsymbol{W}}{\partial t} + \Gamma\frac{\partial \boldsymbol{Q}}{\partial \tau} + \boldsymbol{R} = 0 \tag{3.17}$$

where $\boldsymbol{R}$ is the spatial derivative terms of the residuals. The physical time derivative is discretized with a backward difference formula as,

$$\frac{\partial \boldsymbol{W}}{\partial t} = \frac{3\boldsymbol{W}^{n+1} - 4\boldsymbol{W}^{n} + \boldsymbol{W}^{n-1}}{2\Delta t} \tag{3.18}$$

Here n is the given physical time level. The primitive variable is known as $\boldsymbol{Q}_\tau$ at n, and $\boldsymbol{Q}_{\tau-\Delta\tau}$ at $n-1$. The conserved variables $\boldsymbol{W}^n$ and $\boldsymbol{W}^{n-1}$ are computed from $\boldsymbol{Q}_\tau$ and $\boldsymbol{Q}_{\tau-\Delta\tau}$, respectively. $\boldsymbol{W}^{n+1}$ is unknown in the equation because it is the next physical time level given by $\boldsymbol{Q}_{\tau+\Delta\tau}$. So $\boldsymbol{W}^{n+1}$ is replaced by $\boldsymbol{W}^{i+1}$. i stands for the current stage of RK scheme.

A typical stage of the multistage Runge-Kutta (RK) scheme for the pseudo-time derivative takes the form

$$\boldsymbol{Q}^{i+1} = \boldsymbol{Q}^{0} - \alpha_i\Delta\tau\Gamma^{-1}\left(\boldsymbol{R}^i + \frac{3\boldsymbol{W}^{i+1} - 4\boldsymbol{W}^{n} + \boldsymbol{W}^{n-1}}{2\Delta t}\right) \tag{3.19}$$

where α_i are the coefficients of the RK scheme. Let $\Delta\boldsymbol{Q} \equiv \boldsymbol{Q}^{(i)} - \boldsymbol{Q}^{(0)}$, it has

$$\Delta\boldsymbol{Q}^{i+1} = -\alpha_i\Delta\tau\Gamma^{-1}\left(\boldsymbol{R}^i + \frac{3\boldsymbol{W}^{i+1} - 4\boldsymbol{W}^{n} + \boldsymbol{W}^{n-1}}{2\Delta t}\right) \tag{3.20}$$

$$= -\alpha_i\Delta\tau\Gamma^{-1}\left(\boldsymbol{R}^i + \frac{3\boldsymbol{W}^{i+1} - 3\boldsymbol{W}^{i} + 3\boldsymbol{W}^{i} - 4\boldsymbol{W}^{n} + \boldsymbol{W}^{n-1}}{2\Delta t}\right) \tag{3.21}$$

$$= -\alpha_i\Delta\tau\Gamma^{-1}\left(\boldsymbol{R}^i + \frac{3\Delta\boldsymbol{W}^{i+1} + 3\boldsymbol{W}^{i} - 4\boldsymbol{W}^{n} + \boldsymbol{W}^{n-1}}{2\Delta t}\right) \tag{3.22}$$

By rearranging equation 3.22, a form can be obtained as follow.

$$\Gamma \Delta \boldsymbol{Q}^{i+1} + \frac{3\Delta\tau}{2\Delta t}\Delta \boldsymbol{W}^{i+1} = -\alpha_i \Delta\tau \left(\boldsymbol{R}^i + \frac{3\boldsymbol{W}^i - 4\boldsymbol{W}^n + \boldsymbol{W}^{n-1}}{2\Delta t} \right) \tag{3.23}$$

which can be transformed as

$$\left(\Gamma + \frac{3\Delta\tau}{2\Delta t}\frac{\partial \boldsymbol{W}}{\partial \boldsymbol{Q}} \right) \Delta \boldsymbol{Q}^{i+1} = -\alpha_i \Delta\tau \left(\boldsymbol{R}^i + \frac{3\boldsymbol{W}^i - 4\boldsymbol{W}^n + \boldsymbol{W}^{n-1}}{2\Delta t} \right) \tag{3.24}$$

In the RK scheme, it has $\boldsymbol{Q}^0 = \boldsymbol{Q}_\tau$, and $\boldsymbol{W}^0$ is computed from $\boldsymbol{Q}^0$. Both $\boldsymbol{W}^n$ and $\boldsymbol{W}^{n-1}$ are held constant. As $\tau \to \infty$ by m pseudo-time steps, $\boldsymbol{Q}_{\tau+\Delta\tau} = \boldsymbol{Q}^m$. The level of desired temporal accuracy determines the physical time step Δt. The stability condition of the RK scheme limits the pseudo-time step $\Delta\tau$.

3.6 Parallel computing

DNS is well known as high demanding for computing resources, so it is normally run on a high performance computing (HPC) system. The parallel efficiency of the solver is quite important for the simulation to obtain the results in an affordable time. SHEFFlow uses METIS for partitioning graphs of the mesh. Open MPI is employed for the parallel communication between partitions.

Chapter 4

Validations and Verifications

4.1 Two dimensional stationary vortex

High order methods are often used in DNS. SHEFFlow employs the high order MUSCL method to do DNS. In this section, the stationary vortex will be used to prove that SHEFFlow is a high order code with the MUSCL method.

In this case, the unsteady 2D Euler equations will be solved to simulate the 2D stationary vortex which is from reference [127]. Without viscosity in the flow, the vortex does not dissipate and keeps staying in the same position and status, but the CFD simulations have numerical dissipation. An error can be obtained by comparing the difference between the simulation results and the initial flow condition. By refining the mesh, the error will be different and show a trend which can be used to study the spatial order of numerical schemes.

The computational domain is a square with the dimensions of $L_x = L_y = 5$m, as displayed in figure 4.1. The flow is initialised by a uniform flow with a vortex sitting in the square centre (x_c, y_c). The fluid is an ideal gas with $\gamma = 1.4$ and $R = 287.15$. The parameters are

$$\begin{aligned}
&\rho_\infty = 1.225\mathrm{kg\,m^{-3}}, \quad T_\infty = 300\mathrm{K},\\
&P_\infty = \rho_\infty R T_\infty, \quad U_\infty = 0\mathrm{m\,s^{-1}},\\
&\Delta T = -\frac{\beta^2(\gamma-1)}{8\gamma\pi^2}\exp\left(1-r^2\right),\\
&\Delta u = -\frac{\beta}{2\pi}\exp\left(\frac{1-r^2}{2}\right)(y-y_0),\\
&\Delta v = \frac{\beta}{2\pi}\exp\left(\frac{1-r^2}{2}\right)(x-x_0),\\
&p_0 = P_\infty\left(1+\Delta T\right)^{\frac{\gamma}{\gamma-1}},\\
&T_0 = T_\infty\left(1+\Delta T\right),\\
&u_0 = U_\infty + \Delta u,\\
&v_0 = U_\infty + \Delta v
\end{aligned} \tag{4.1}$$

where, the variables with a subscript ∞ are the quantities for the uniform flow, and the variables with a subscript 0 are the quantities for the initial flow conditions. The vortex strength is $\beta = 5.0$, and the distance from the vortex centre is $r = \sqrt{(x-x_0)^2 + (y-y_0)^2}$.

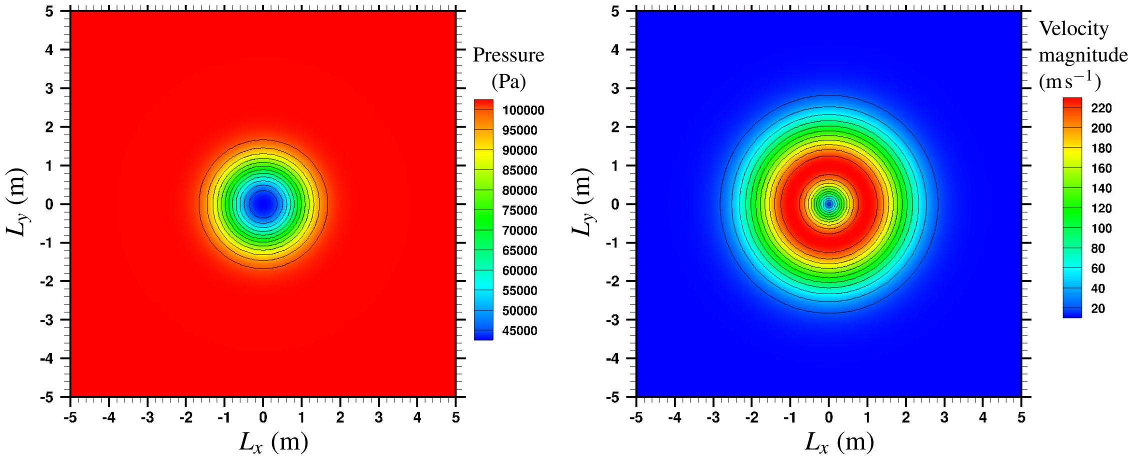

(a) Pressure (b) Velocity magnitude

Figure 4.1 Contours of the 2D stationary vortex for the initial conditions.

Four uniform meshes are used to test the spatial order of SHEFFlow, including 128^2, 256^2, 512^2 and 1024^2 cells in the simulations. The physical time step is $\Delta t = 0.5 \times 10^{-4}$s. The L_1 error of ρ is computed at the 4000 step. Because of the dissipation of the numerical scheme, the density in the centre of the computational domain is increased after 4000 steps,

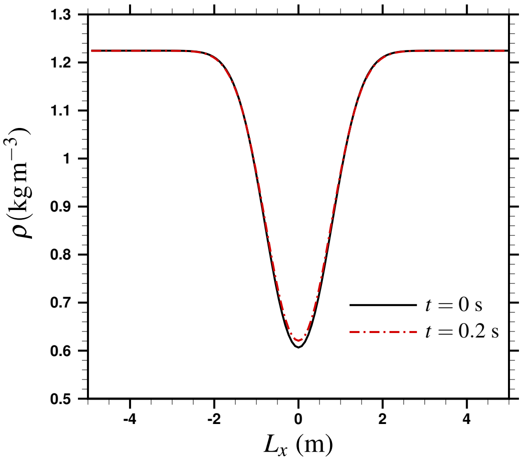

Figure 4.2 Comparison of the density curves at $t = 0$ s and $t = 0.2$ s, cutting along the central line of the computational domain.

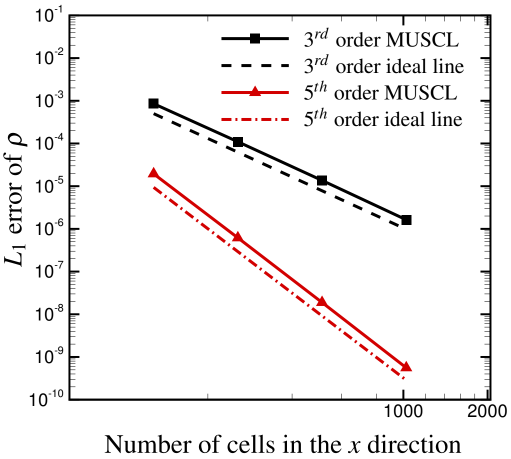

Figure 4.3 The study of 2D stationary vortex convergence, using the 3^{rd} and 5^{th} order MUSCL scheme.

as shown in figure 4.2. The L_1 error of ρ is computed by

$$L_1 \text{ error of } \rho = \sqrt{\frac{\sum_{N_x \times N_y} (\rho_0 - \rho_t)^2}{N_x \times N_y}} \tag{4.2}$$

where, N_x and N_y are the number of cells in the x-drection and y-direction, respectively. ρ_0 is the density in the initial flow condition, and ρ_t is the density at the time t of the simulation. In figure 4.3, the convergence study shows that the 3^{rd} and 5^{th} order MUSCL scheme can improve SHEFFlow to have the desired order.

4.2 Taylor-Green Vortex

To test the accuracy and the performance of the 5^{th} order MUSCL method in the DNS simulation, the DNS of Taylor-Green vertex at $Re = 1600$ is carried out. The geometry of this case is a periodic cubic with $-\pi L \ll x,y,z \ll \pi L$, including 8 vortices inside. The mesh is uniform in every direction. Periodic boundary conditions are applied in the simulation. The initial flow field can be described by the following equations.

$$\begin{aligned} u =& V_0 \sin\left(\frac{x}{L}\right)\cos\left(\frac{y}{L}\right)\cos\left(\frac{z}{L}\right), \\ v =& -V_0 \cos\left(\frac{x}{L}\right)\sin\left(\frac{y}{L}\right)\cos\left(\frac{z}{L}\right), \\ w =& 0, \\ p =& p_0 + \frac{\rho_0 V_0^2}{16}\left(\cos\left(\frac{2x}{L}\right)+\cos\left(\frac{2y}{L}\right)\right)\left(\cos\left(\frac{2z}{L}\right)+2\right). \end{aligned} \tag{4.3}$$

where, $p_0 = 105527.625\text{Pa}$, $\rho_0 = 1.225\text{kg}\,\text{m}^{-3}$, $V_0 = 24.11\text{m}\,\text{s}^{-1}$, $L = 0.001\text{m}$. The heat capacity ratio is $\gamma = 1.4$, and Prandtl number is $\text{Pr} = 0.71$. The value of the Reynolds number is defined as $Re = \frac{\rho_0 V_0 L}{\mu}$. The temperature is $T_0 = \frac{p_0}{R\rho_0}$ which is uniform for the initial flow field. An iso-surface of λ_2 is used to show the cores of the vortices in figure 4.4.

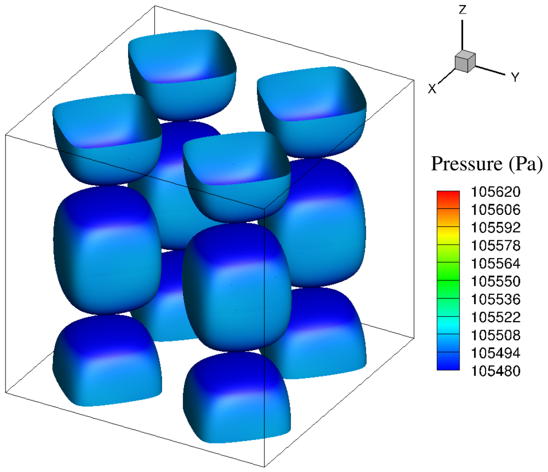

Figure 4.4 The iso-surface of λ_2 coloured by pressure for the initial flow field of Taylor-Green vortex.

The simulation duration is from 0 to $20t_c$, where $t_c = \frac{L}{V_0}$ is the characteristic convective time. Figure 4.5 displays the mesh sensitivity of SHEFFlow, using the 5^{th} order MUSCL method. When the mesh size is 256^3, the result is convergent and very close to the reference values. A tiny difference is found between the result of mesh 256^3 and the Spectral method

[67, 127] on the evolution of non-dimensional kinetic energy $E_k = \frac{1}{\rho_0 \Omega} \int_\Omega \rho \frac{\mathbf{v} \cdot \mathbf{v}}{2} d\Omega$ and kinetic energy dissipation rate $\varepsilon = -\frac{dE_k}{dt}$.

The 3^{rd} order of MUSCL method are tested with 256^3 grids as well. When the kinetic energy dissipation rate is high, the 3^{rd} order MUSCL method has bigger ε than the other two before the maximum dissipation. The maximum dissipation of the 3^{rd} order MUSCL method happens earlier than the other two, causing the kinetic energy of the 3^{rd} order MUSCL method is lower than that of the other two. After the maximum dissipation, the energy dissipation rate of the 3^{rd} order MUSCL method is smaller than that of the other two. After

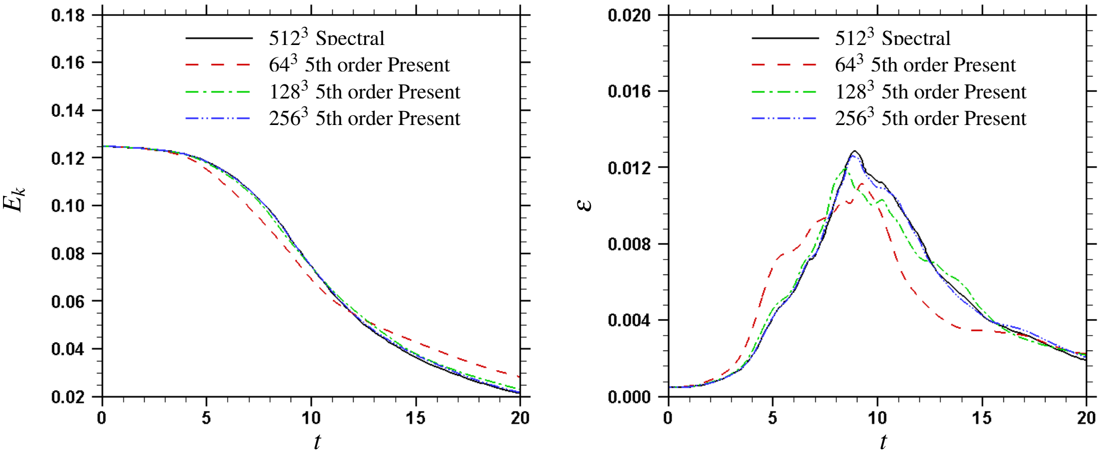

Figure 4.5 Mesh sensitivity

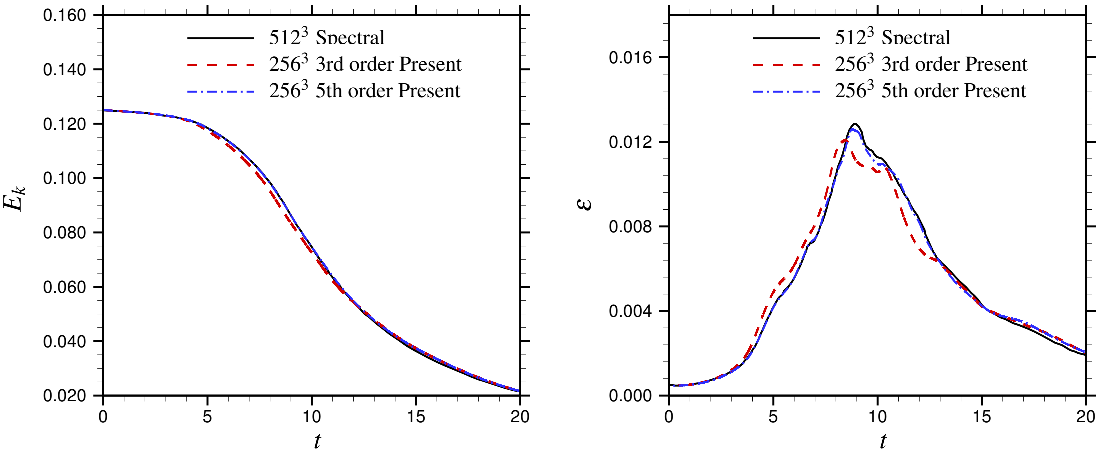

(a) (b)

Figure 4.6 Comparisons of non-dimensional kinetic energy E_k and energy dissipation rate ε between SHEFFlow and reference [127]. t is non-dimensionalized by $t_c = L/V_0$.

$t = 12.5$, the 3^{rd} order MUSCL method catches up with the other two, and the kinetic energy is similar among three methods.

In figure 4.7, the iso-surfaces of λ_2 at $t = 2.5, 8$ and 15 show the vortices structures gained by the 3^{rd} and 5^{th} order MUSCL methods before and after the maximum dissipation. An homogeneous isotropic turbulence is obtained from the simulation of the Taylor-Green vortex which creates small scales and follows a decay phase.

The validation of the Taylor-Green vortex proves that the 5^{th} order MUSCL method is able to produce a reasonable evolution of the kinetic energy and the kinetic energy dissipation rate. It is important to precisely simulate a turbulent flow. The 5^{th} order MUSCL method is better than the 3^{rd} order. It is necessary to use 5^{th} order for the later simulations rather than using the 3^{rd} order methods.

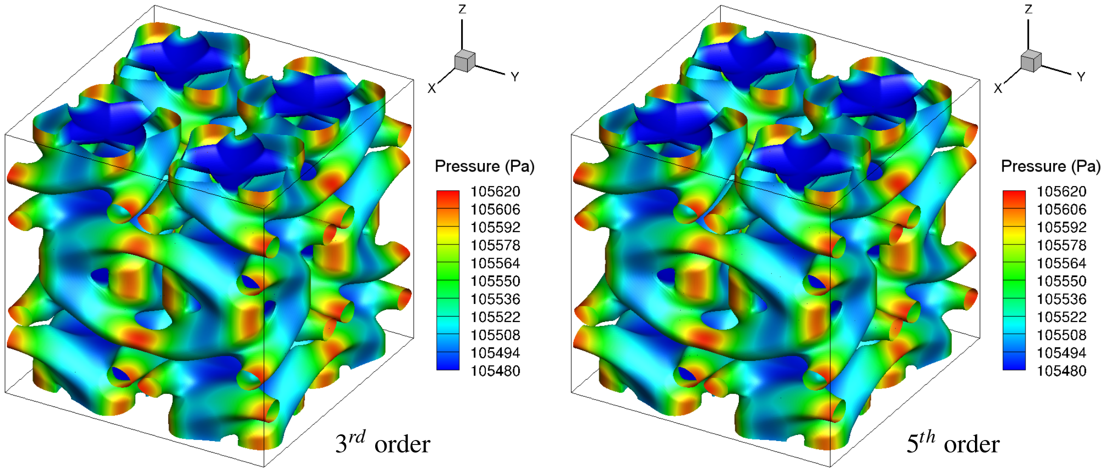

(a) $t = 2.5$

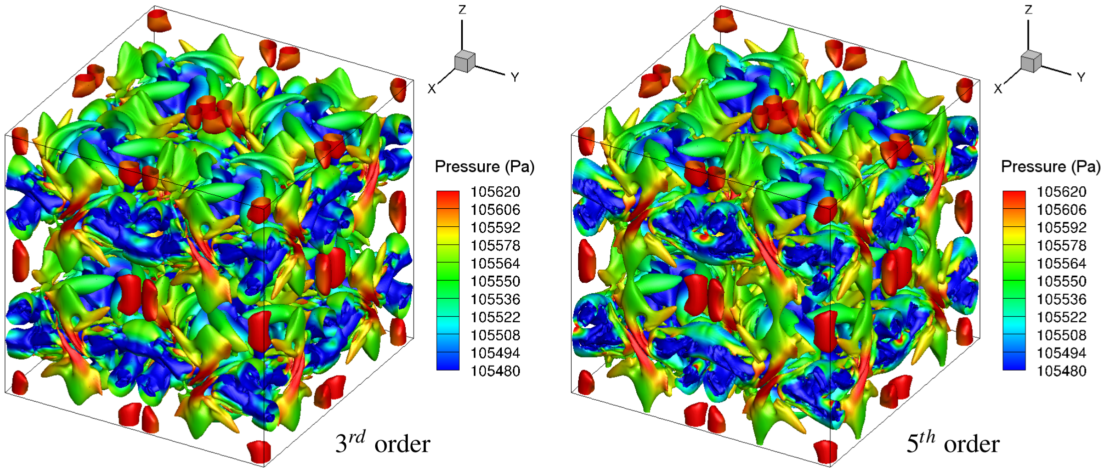

(b) $t = 8$

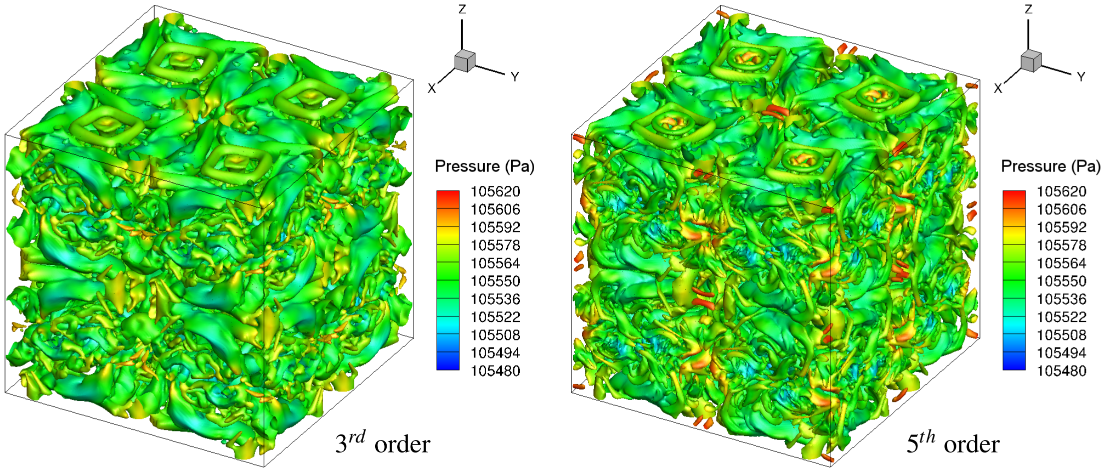

(c) $t = 15$

Figure 4.7 The iso-surface of λ_2 coloured by pressure at $t = 2.5, 8, 15$, simulated by SHEF-Flow with 256^3 grids and comparing the flow structures between the results of 3^{rd} order and 5^{th} order MUSCL scheme.

4.3 Fully developed turbulent channel flow

The channel flow is a good case to study the turbulent drag because of its simple geometry and boundary conditions. The unique flow control method will be applied in a channel to achieve the turbulent drag reduction. To make it clear, the channel without control is called **smooth channel**, and the other with control is called **controlled channel**.

4.3.1 Baseline case of the smooth channel

The fully developed turbulent channel flow shown in figure 4.8 is a classic case to validate the DNS ability of SHEFFlow. The results can be validated by the incompressible DNS data from reference [51] and their online database. For the boundary conditions, top and bottom are isothermal and no-slip wall conditions. Periodic conditions are applied in the streamwise and spanwise directions. The flow field is initialised by a parabolic velocity profile with random perturbations. The simulation parameters are listed in Table 4.1.

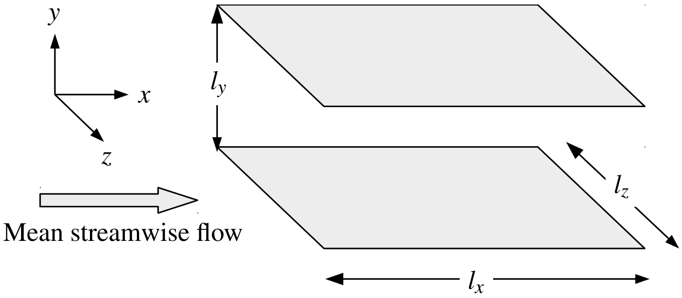

Figure 4.8 Schematic of the turbulent channel flow. The dimensions of the computational domain are l_x, l_y and l_z in the streamwise, wall-normal and spanwise directions, respectively.

Due to the wall friction and small numerical dissipation, the mass flux rate would decrease without driving force in the streamwise direction. To keep the mass flow rate, a background force is introduced through the pressure derivative with respect to x, which is $\partial p/\partial x$. The pressure gradient can be split into two parts as below.

$$\frac{\partial p}{\partial x} = \frac{\partial p_{mean}}{\partial x} + \frac{\partial p_{fluctuation}}{\partial x} \tag{4.4}$$

where $\partial p_{mean}/\partial x$ is the driving pressure gradient, and $\partial p_{fluctuation}/\partial x$ is the fluctuation of pressure gradient derived from the Navier-Stokes equations. A variable σ which is defined as $\sigma = \partial p_{mean}/\partial x$ is employed to keep the mass flow rate in the simulation. σ is calculated as

$$\sigma^{n+1} = \sigma^{n} - \frac{1}{\Delta t}(\dot{m}^{0} - 2\dot{m}^{n} + \dot{m}^{n-1}) \tag{4.5}$$

where $\dot{m}^0$ is the initial mass flux rate of the channel, $\dot{m}^n$ is the mass flux rate at the physical time step n, and Δt is the time of one physical time step.

The driving pressure gradient is related to the skin friction, following the below equation.

$$\frac{\partial p_{mean}}{\partial x} l_x l_y l_z = 2\tau_w l_x l_z \tag{4.6}$$

It can be simplified as

$$\frac{\partial p_{mean}}{\partial x} l_y = 2\tau_w \tag{4.7}$$

where

$$\tau_w = \rho u_\tau^2 \tag{4.8}$$

Substituting equation 4.8 into equation 4.7, it has

$$\frac{\partial p_{mean}}{\partial x} l_y = 2\rho u_\tau^2 \tag{4.9}$$

So, the target value of driving pressure gradient is

$$\frac{\partial p_{mean}}{\partial x} = \frac{2\rho u_\tau^2}{l_y} \tag{4.10}$$

Then,

$$u_\tau = \sqrt{\frac{l_y}{2\rho} \frac{\partial p_{mean}}{\partial x}} \tag{4.11}$$

Because the channel flow is initialized by a parabolic velocity profile, the initial mass flux rate can be obtain as

$$\dot{m}^0 = \int_0^{l_z} \int_{-l_y/2}^{l_y/2} u_c(1-(2y/l_y)^2) dydz/(l_y l_z) \tag{4.12}$$

where u_c is the velocity at the channel center. In the channel case, when $Re_\tau = 180$, it has $Re_c = 4200$. Re_τ and Re_c are defined as

$$Re_\tau = \frac{u_\tau \delta}{\nu}, \qquad Re_c = \frac{u_c \delta}{\nu} \tag{4.13}$$

where δ is half height of the channel. So, it has

$$\frac{u_\tau}{u_c} = \frac{Re_\tau}{Re_c} = \frac{180}{4200} = \frac{3}{70} \tag{4.14}$$

Then,

$$u_c = \frac{70u_\tau}{3} = \frac{70}{3}\sqrt{\frac{l_y}{2\rho}\frac{\partial p_{mean}}{\partial x}} \tag{4.15}$$

Substituting equation 4.15 into equation 4.12, the initial mass flux rate is related with the driving pressure gradient by

$$\dot{m}^0 = \int_{-l_y/2}^{l_y/2}\int_0^{l_z} \frac{70}{3}\sqrt{\frac{l_y}{2\rho}\frac{\partial p_{mean}}{\partial x}}\left(1-\left(\frac{2y}{l_y}\right)^2\right) dydz/(l_y l_z) \tag{4.16}$$

Table 4.1 Simulation parameters of the fully developed turbulent channel flow. Δx and Δz are the collocation resolutions parallel to the wall, using N_x and N_z cells. Δy_w is the first wall-normal grid spacing from the wall and Δy_c is the wall-normal grid spacing at the centre of the channel. N_y is the number of cells in the wall-normal direction.

Mean Mach number	0.211
Mean velocity	42.0 $\mathrm{m\,s^{-1}}$
Mean friction velocity	2.7 $\mathrm{m\,s^{-1}}$
Mean pressure	16065.05472 Pa
Mean temperature	110.0 K
$N_x \times N_y \times N_z$	$128 \times 128 \times 84$
Domain size ($l_x \times l_y \times l_z$)	$0.012566 \times 0.002 \times 0.0041888$ $\mathrm{m^3}$
Non-dimensional domain size	$4\pi \times 2 \times \frac{4}{3}\pi$
$\Delta x^+ \times \Delta(y_w^+ \sim y_c^+) \times \Delta z^+$	$17.67 \times (0.5 \sim 5.56) \times 8.98$

In this study, both dimensional and non-dimensional variables are used. The dimensional variables do not have any superscript. If the variables employ superscript +, it means the variables are non-dimensionalised in wall-units, which are defined as velocity $V^+ = V/u_\tau$, length $L^+ = \rho u_\tau L/\mu$ and time $T^+ = \rho u_\tau^2 T/\mu$. The validation is performed at $Re_\tau = 180$ based on the friction velocity u_τ and the half channel-height δ, using the physical time step $\Delta t^+ = 0.25$. The computational domain has $l_x/\delta = 4\pi$ and $l_z/\delta = 4\pi/3$ for the streamwise length and spanwise width, respectively. The mean velocity is 42.0 $\mathrm{m\,s^{-1}}$ and the mean pressure is 16065.05 Pa. The temperature is 110.0 K and the half channel-height is 0.001m. Moreover, the mesh resolution are $\Delta x^+ = 17.67$ and $\Delta z^+ = 8.98$ in the streamwise and spanwise directions, respectively. $\Delta y_w^+ = 0.5$ is the first wall-normal grid spacing from the walls and $\Delta y_c^+ = 5.56$ is the wall-normal grid spacing at the centre of the channel. The mesh has $128 \times 128 \times 84$ in the streamwise, wall-normal and spanwise directions respectively. In order to study the mesh convergence, two more meshes are tested. The resolutions of the two meshes are kept in the streamwise and spanwise direction, which are $\Delta x^+ = 17.67$ and

$\Delta z^+ = 8.98$. But the first wall-normal grid spacings are changed, which are $\Delta y_w^+ = 1.0$ and 2.0.

Figure 4.9b shows the history of friction coefficient from the initial flow-field to the fully developed turbulent status, using the mesh with $\Delta y_w^+ = 0.5$. At each physical time, the

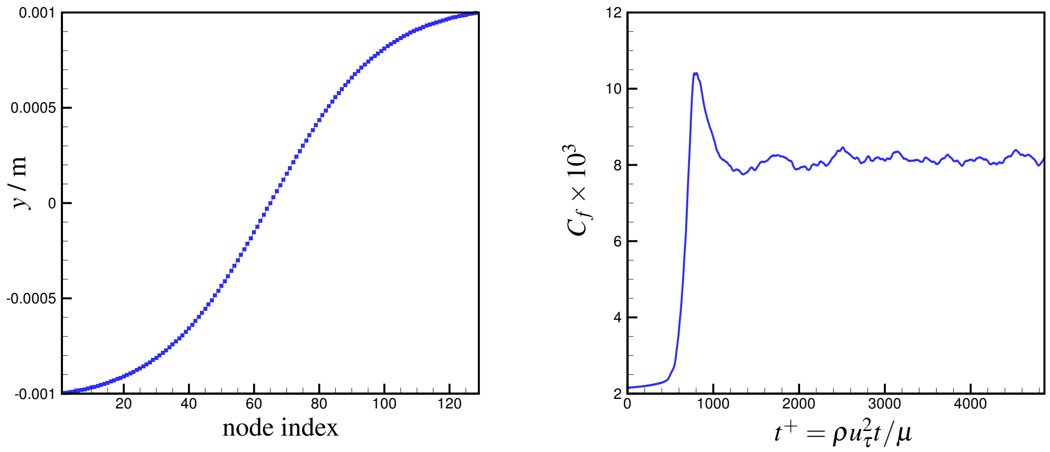

(a) The distribution of nodes in y direction.

(b) The history of friction coefficient from initial flow field to fully developed turbulent status.

Figure 4.9 The nodes distribution and the history of friction coefficients.

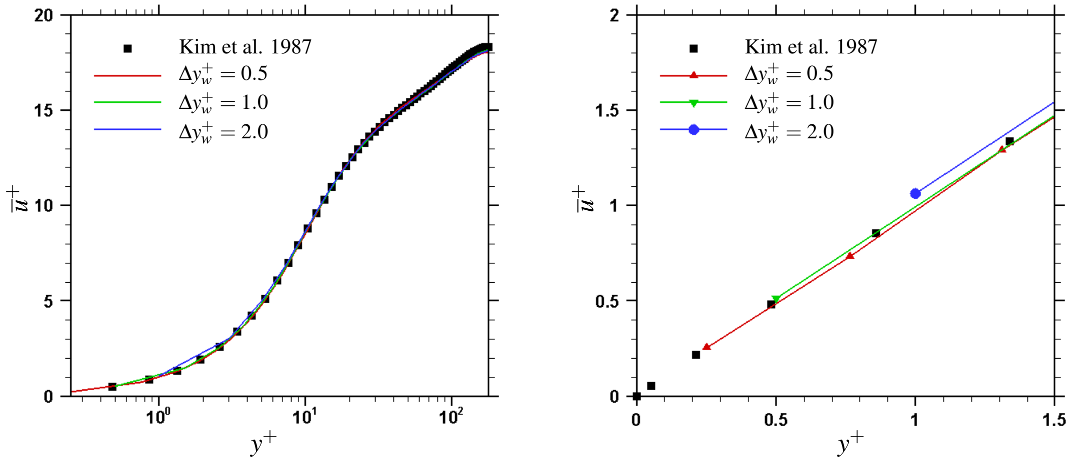

(a) From wall to the channel centre

(b) The values of several cells near wall

Figure 4.10 Comparisons of the mean streamwise velocity profiles.

friction coefficient is a space averaged value defined as

$$C_f = \frac{\int_0^{l_z}\int_0^{l_x} \tau_w dxdz}{l_x l_z} \times \frac{1}{\frac{1}{2}\rho u_b^2} \tag{4.17}$$

where u_b is bulk or mean velocity of the channel. In the non-dimensional duration from $t^+ = 2187$ to 4860, the time-averaged C_f is 8.16×10^{-3} compared to 8.18×10^{-3} which is from the DNS simulation of Kim et al. [51]. The difference is 0.24%. The time-averaged C_f are 8.32×10^{-3} and 8.51×10^{-3} for the meshes $\Delta y_w^+ = 1.0$ and 2.0, respectively. The differences are 1.7% and 4.0%. Figure 4.10 compares the mean streamwise velocity profiles of the three cases. It is hard to see the difference until zooming in the region of several cells near wall. Because the cell spacings of the coarse meshes are too coarse to accurately capture the velocity distribution, C_f is estimated bigger than the reference value. The result shows that it is reasonable to use the mesh of $\Delta y_w^+ = 0.5$.

Figures 4.11 and 4.12 show good agreements between the statistic results of SHEFFlow and reference [51], including the mean streamwise velocity, the root-mean-square of velocity fluctuations, shear stresses, streamwise spectra of velocities, and probability density function of velocities.

In this validation, by comparing the DNS results between SHEFFlow and Kim et al. [51] at $Re_\tau = 180$ or $Re_b = 2800$, it shows that SHEFFlow can accurately capture the turbulent structures and have the DNS ability to investigate the drag reduction of skin friction by using zero mass jets in the channel flow.

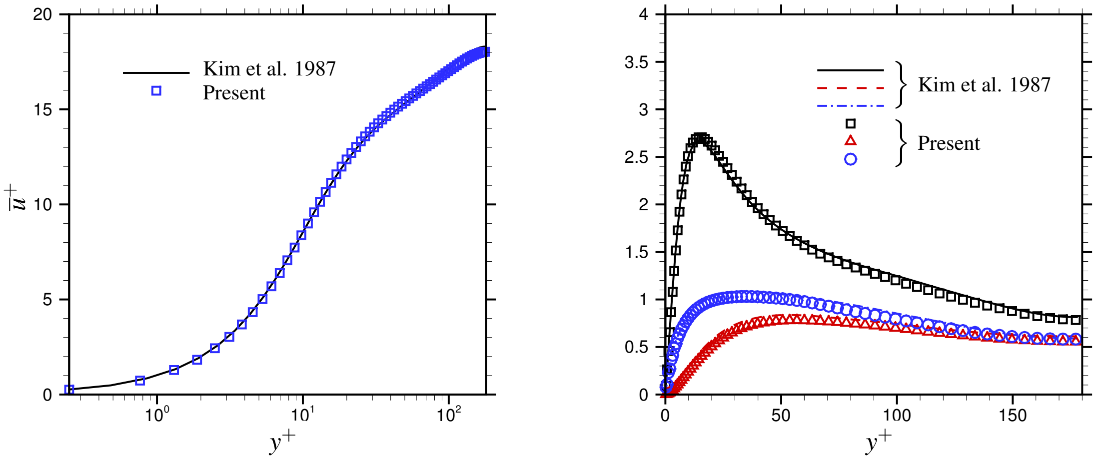

(a) The mean streamwise velocity profile.

(b) Root-mean-square velocity fluctuations normalized by the friction velocity: u'_{rms}/u_τ, ——, □; v'_{rms}/u_τ, - - - -, △; w'_{rms}/u_τ, -·-·-, ○.

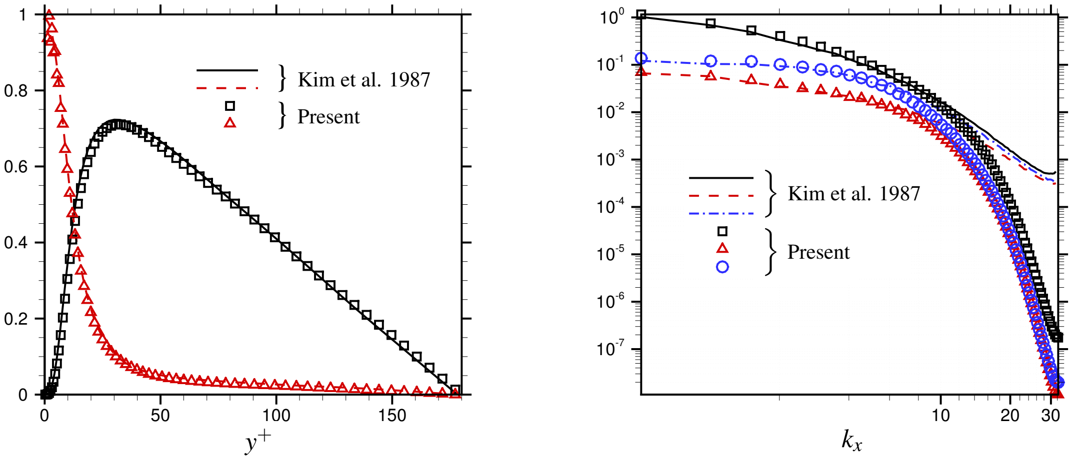

(c) Comparisons of the normalised viscous shear stress $\mu\frac{\partial\bar{u}}{\partial y}/\tau_w$, - - - -, △; and Reynolds shear stress $-\overline{u'v'}/u_\tau^2$, ——, □.

(d) Streamwise spectra for u, v, w at $y^+ = 30$ with E_{uu}, ——, □; E_{vv}, - - - -, △; E_{ww}, -·-·-, ○.

Figure 4.11 Comparisons of the flow quantities between SHEFFlow and Kim & Moin [51]

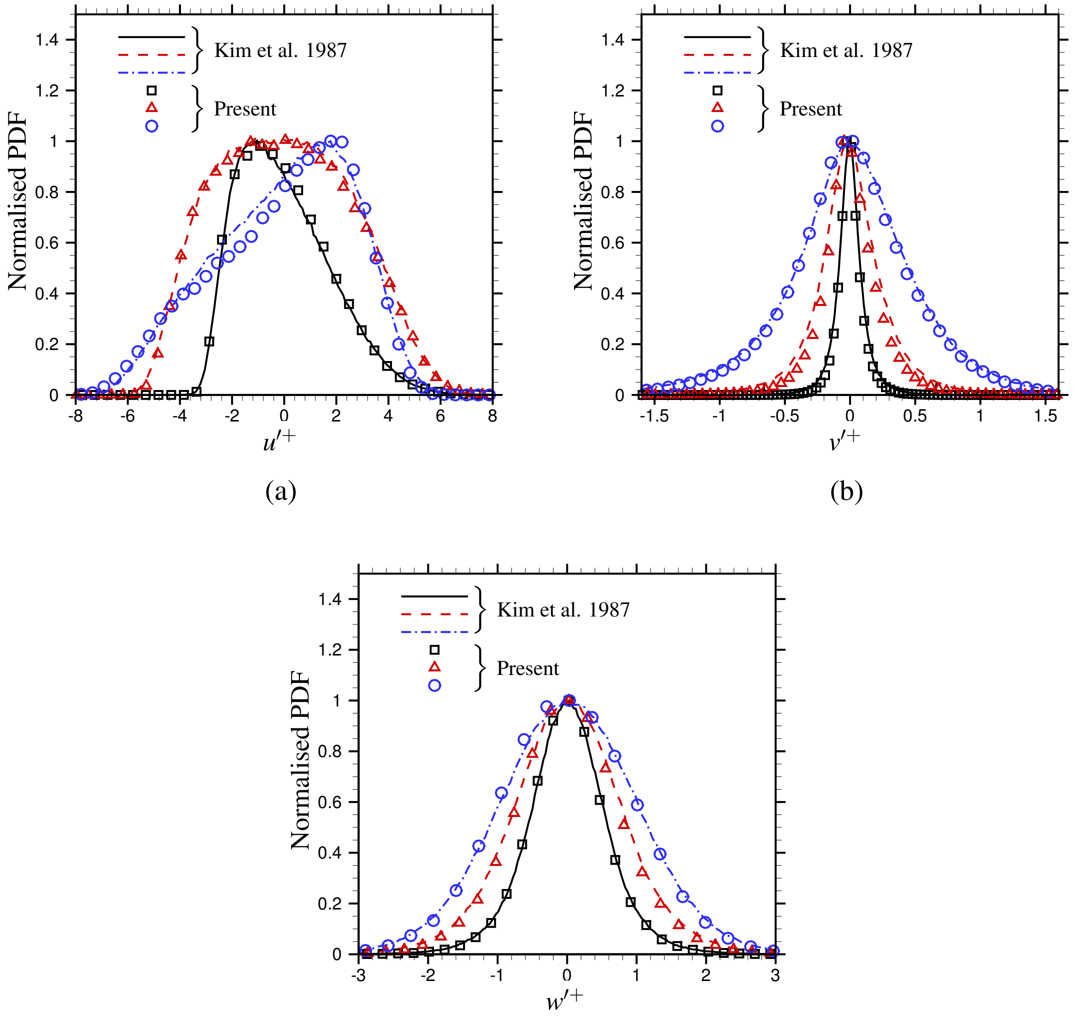

(a)

(b)

(c)

Figure 4.12 Comparisons of the normalised PDFs between SHEFFlow and Kim & Moin [51] at $y^+ = 5$, ——, □; $y^+ = 10$, - - - -, △; $y^+ = 20$, -·-·-, ○.

4.3.2 Sensitivity of computational domain size and mesh resolution

DNS highly demands computing resource which is not only the numbers of CPUs that can be used, but also the size of RAMs. The memory size would be a bottle neck for the simulation due to the big mesh size. If the mesh size is too big to be allocated into the memory, the simulation speed would be significantly dragged down. In our group, the computing resource is limited, so the computational domain size and mesh resolution should be carefully designed. The mesh size should be small enough to satisfy our high performance computer, and the computational domain and mesh resolution should be big and fine enough to have the high accuracy. It is not a job to find the smallest size of the simulation domain or to investigate the accuracy of the results influenced by the mesh resolution. The aim of this subsection is to find a reasonable computational domain size and mesh resolution to investigate the flow control method. The Zero Mass Jets which will be studied in the next chapter.

The computational domain size is the first step to be studied with the same mesh resolution as that in subsection 4.3.1. Several sizes of simulation domain are tested and shown in table 4.2, including the combination of $l_x/\delta = 4\pi, 3\pi, 2\pi$ and $l_z/\delta = 4\pi/3, 10\pi/9, 8\pi/9$. When the streamwise length l_x/δ is 4π or 3π, the skin friction coefficients are similar with the result of reference [51]. The absolute errors are smaller than 0.24%. When the streamwise length $l_x/\delta = 2\pi$, the results show that the skin friction coefficients are sensitive to the spanwise length l_z. Only when $l_z/\delta = 4\pi/3$, the result is acceptable and has a 0.12% difference with the reference [51]. It seems that the skin friction coefficient drops as the spanwise length becomes shorter. To keep the computational domain size as small as possible and obtain a reasonable skin friction coefficient, the best choice is case 7 among the cases with $l_x/\delta = 2\pi$ and $l_z/\delta = 4\pi/3$.

Table 4.2 The friction coefficients and errors for the different sizes of computational domain. The errors are computed from the difference between the results and the reference [51].

Cases	L_x/δ	L_z/δ	$C_f \times 10^{-3}$	Error (%)	Mesh size
1	4π	$4\pi/3$	8.16	−0.24	1,376,256
2	4π	$10\pi/9$	8.19	0.12	1,146,880
3	4π	$8\pi/9$	8.20	0.24	917,504
4	3π	$4\pi/3$	8.19	0.12	1,032,192
5	3π	$10\pi/9$	8.20	0.24	860,160
6	3π	$8\pi/9$	8.20	0.24	688,128
7	2π	$4\pi/3$	8.17	−0.12	688,128
8	2π	$10\pi/9$	8.15	−0.37	573,440
9	2π	$8\pi/9$	8.10	−0.98	458,752

In the previous simulations, the mesh resolution is $\Delta x^+ = 17.67$, $\Delta z^+ = 8.98$ and $\Delta y_c^+ = 5.56$, which is in the same order of the mesh used in reference [81]. Comparing with other DNS studies, the mesh resolution seems coarse, so a medium mesh is tested with the computational domain size $l_x/\delta = 2\pi$ and $l_z/\delta = 4\pi/3$. The previous mesh is called coarse mesh. The medium mesh is $\Delta x^+ = 8.84$, $\Delta z^+ = 4.49$ with double mesh points of the coarse mesh in the streamwise and spanwise directions. It is $\Delta y_w^+ = 0.2$ and $\Delta y_c^+ = 4.13$ in the wall-normal direction. In the non-dimensional duration $T_{total}^+ = 2250$, the time-averaged C_f with the medium mesh is 8.20×10^{-3} compared to 8.18×10^{-3} from the DNS result of reference [51]. The difference is 0.24%. The comparisons of the mesh resolutions and the results are shown in table 4.3.

Figure 4.13 shows the comparisons of the statistic data. The differences are small among the cases. This means all of them are satisfied to do the simulations of the smooth channel flow.

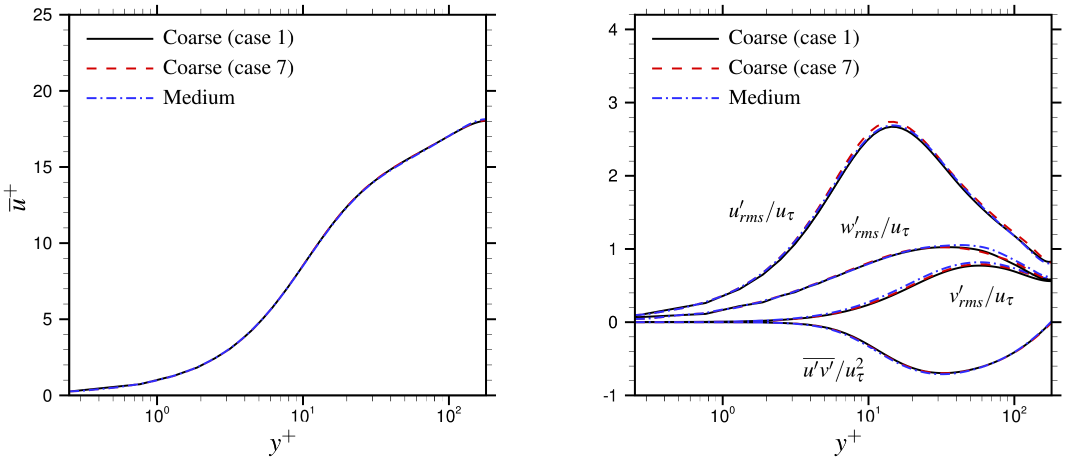

(a) streamwise velocity profiles

(b) Root-Mean-Square of fluctuations and Reynolds shear stresses.

Figure 4.13 The comparisons of statistic data from different simulation-domain size and mesh resolution.

Table 4.3 The friction coefficients and errors for the different mesh resolution. (The errors are computed from the difference between the results and the reference [51].)

Cases	Δx^+	Δz^+	Δy_w^+	Δy_c^+	Error (%)	Mesh size
Coarse (case 7)	17.67	8.98	0.5	5.56	-0.12	$64 \times 128 \times 84$
Medium	8.84	4.49	0.2	4.13	0.24	$128 \times 197 \times 168$

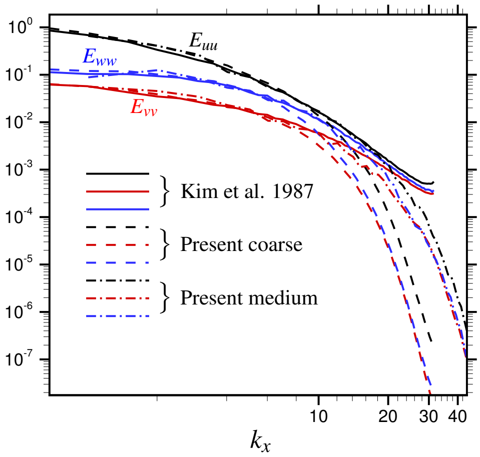

Figure 4.14 Comparisons of streamwise spectra for u, v, w at $y^+ = 30$ among the coarse mesh, the medium mesh and reference [51].

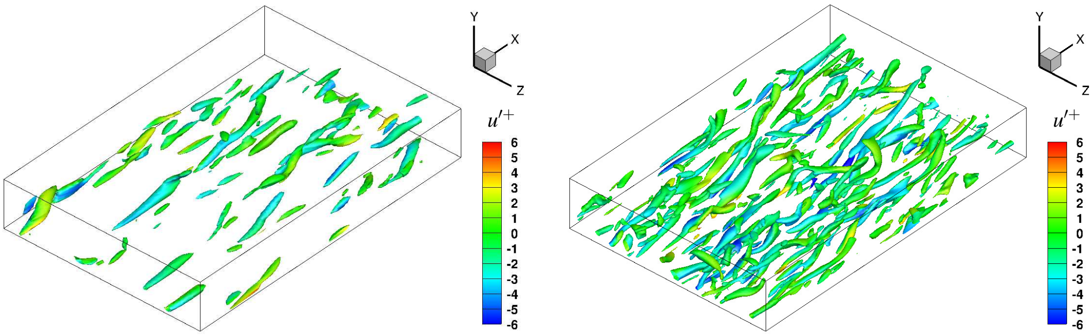

(a) The coarse mesh

(b) The medium mesh

Figure 4.15 Comparisons of flow structures between the coarse and medium mesh with the iso-surface of $\lambda_2 = -1$ coloured by u'^+, where $u'^+ = u'/u_\tau$, showing the bottom half of the channel.

Both the coarse and medium meshes can accurately obtain the kinetic energy when the wavenumber is small, but the kinetic energy dissipates early with the coarse mesh, as shown in figure 4.14.

Comparing the flow structures between the coarse and medium mesh in figure 4.15, the medium mesh can capture more details of the flow than the coarse mesh. The quantity of λ_2 is often used to show the core regions of vortices. More vortices are captured with the medium mesh. Because the numerical dissipation of the medium mesh is smaller than that of the coarse mesh, the vortices structures obtained by the medium mesh are kept better than that by the coarse mesh. The coarse mesh can be used to get the general quantity such as skin-friction, but it is better to use the medium mesh to capture the fine structures of the flow field.

4.3.3 Quadrant analysis of velocity fluctuations

Figure 4.16 presents the joint probability density function (JPDF), $P(u'^{+}, v'^{+})$, $P(u'^{+}, w'^{+})$ and covariance integrand, $u'^{+}v'^{+}P(u'^{+}, v'^{+})$, $u'^{+}w'^{+}P(u'^{+}, w'^{+})$ at $y^{+} = 20$ in the smooth channel. In figure 4.16a, the JPDF of (u'^{+}, v'^{+}) is a roughly elliptical shape. The major axis of the shape is inclined in the direction of Q2 and Q4, and the peak value happens in Q4 near the original point $(0,0)$. Figure 4.16b displays that the contributions of the Reynolds shear stresses dominantly come from Q2 and Q4. This is in a good agreement with reference [123]. The signs of u'^{+} and v'^{+} are opposite with each other, giving negative values to $\overline{u'v'}$. The peak values of $u'^{+}v'^{+}P(u'^{+}, v'^{+})$ are around $(-0.38, 0.25)$ and $(0.38, -0.25)$.

An interesting feature is that $P(u'^{+}, w'^{+})$ is symmetric with the w'^{+}-axis but asymmetric with the u'^{+}-axis, as displayed in figure 4.16c. The highest probability of (u'^{+}, w'^{+}) is in the negative part of u'^{+}. The big fluctuation of spanwise velocity is associated with negative fluctuation of streamwise velocity, and small fluctuation of spanwise velocity is accompanied with positive fluctuation of streamwise velocity. The contributions of $\overline{u'w'}$ are symmetric but the signs are opposite, so $\overline{u'w'}$ equals 0 in total.

In figures 4.16e and 4.16f, the shapes of contour-lines of $P(v'^{+}, w'^{+})$ are symmetric with the w'^{+}-axis but asymmetric with the u'^{+}-axis. This is similar as $P(u'^{+}, w'^{+})$. Because the wall-normal fluctuation v' is smaller than the streamwise fluctuation u', the area of $P(v'^{+}, w'^{+})$ is smaller than the area of $P(u'^{+}, w'^{+})$. It displays that small fluctuation of w'^{+} is associated with v'^{+}, and the big fluctuation of w'^{+} is accompanied with the positive v'^{+}. The highest value of $P(v'^{+}, w'^{+})$ is in the negative part of v'^{+}. The covariance integrand of $v'^{+}w'^{+}P(v'^{+}, w'^{+})$ is symmetric with w'^{+}-axis, making $\overline{v'w'}$ zero.

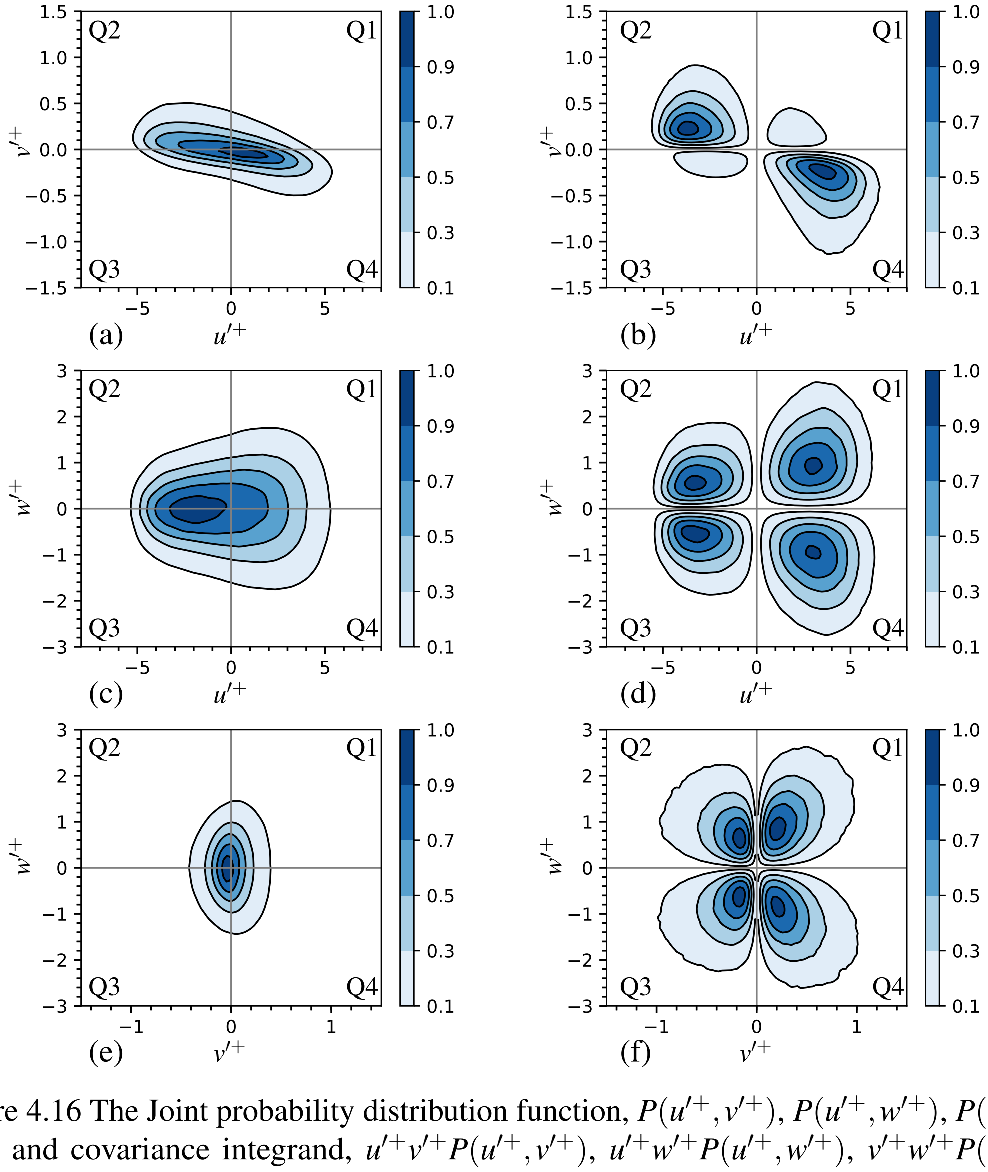

Figure 4.16 The Joint probability distribution function, $P(u'^+,v'^+)$, $P(u'^+,w'^+)$, $P(v'^+,w'^+)$ (left) and covariance integrand, $u'^+v'^+P(u'^+,v'^+)$, $u'^+w'^+P(u'^+,w'^+)$, $v'^+w'^+P(v'^+,w'^+)$ (right), at $y^+ \approx 20$, giving $10,30,50,70$ and 90% of the maximum probability level or covariance integrand.

4.4 Conclusions

In this chapter, the in-house code called SHEFFlow is validated and verified by three cases, including two-dimensional stationary vortex, Taylor-Green vortex, and also fully developed turbulent channel flow. Some of the conclusions are listed as below:

- The high order MUSCL scheme is successfully added into SHEFFlow which now has the desired order.
- The 3^{rd} order MUSCL is more dissipative than the 5^{th} order MUSCL. Since the numerical dissipation significantly influences the solver ability to capture the turbulence structures, it is better to use the 5^{th} order MUSCL.
- By using the 5^{th} order MUSCL, SHEFFlow can obtain the skin friction of a turbulent channel within a difference of 0.24% between our results and reference [51]. SHEFFlow is satisfied to accurately obtain the fluid statistics, including the mean streamwise velocity, the root-mean-square of velocity fluctuations, shear stresses, streamwise spectra of velocities, and probability density function of velocities.
- The computational domain size, $l_x/\delta = 2\pi$ and $l_z/\delta = 4\pi/3$, is able to accurately obtain the skin friction and fluid statistics of a turbulent channel flow at $Re_\tau = 180$. The mesh resolution, $\Delta x^+ = 8.84$, $\Delta z^+ = 4.49$, $\Delta y_w^+ = 0.2$ and $\Delta y_c^+ = 4.13$, is good to capture the cascade of kinetic energy and structures of flow field.
- The velocity data obtained by SHEFFlow can be used to do quadrant analysis.

Chapter 5

Drag reduction with Zero Mass Jets in turbulent channel flow

In this research, a unique flow control method is found to effectively reduce the friction drag in a fully developed turbulent channel flow with ZMJ. This research topic is new because the ZMJ is implemented in a special way which has not been investigated to gain the drag reduction by other research.

This chapter will present the investigation in the following sequence. The first section shows the geometry configurations of channel, parameters of ZMJ, and flow conditions. Secondly, drag reduction is obtained in the preliminary simulations by setting ZMJ properly. In the third section, mesh sensitivity is studied to find a reasonable mesh resolution for DNS. At the end, studying the simulation results reveals the averaged flow-fields, mechanisms of drag reduction, and turbulence phenomena.

5.1 Computational realization and flow conditions

In this research, the channel geometry is adapted to eject ZMJ from walls. To distinguish the geometries, the channel flow controlled by ZMJ will be called **controlled channel**. The classic channel flow that is shown in section 4.3 will be named **smooth channel**. Figure 5.1 shows the computational model of the controlled channel. 12 steps are evenly put on the walls in the controlled channel. The ZMJ comes out from the vertical sides of the steps. There are 6 steps on the top wall and 6 steps on the bottom wall. 12 pairs of ZMJ come out from the step-sides to obtain oscillating layers in the near-wall region. The step height is δ^+_{jet}, and the step width is L^+_{step}. For a pair of ZMJ, when one is blowing out fluid, the other is sucking in fluid, as shown on the left of figure 5.1. Since fluid is oscillating on the

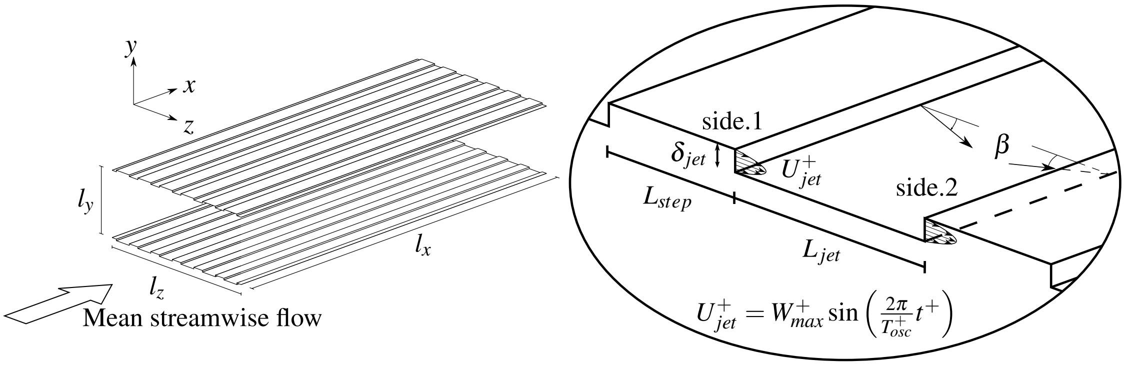

Figure 5.1 The schematic of the controlled channel with ZMJ. L_x^+, L_y^+ and L_z^+ are the streamwise, wall-normal and spanwise dimensions of the computational domain, respectively. The step length and the jet-exits height are in wall units based on the friction velocity of the smooth channel at $Re_\tau = 180$.

vertical sides of the steps, the step-sides serve as exits for ZMJ, so the step-sides will be called jet-exits as well. The term "jet-exits" is used interchangeably with "step-sides" in this research. There is a distance L^+_{jets} between a pair of ZMJ, and a jet angle β is against the incoming flow in the $x-z$ plane. When $\beta = 0°$, the jets follow with the spanwise direction at the jet-exits. The Reynolds number of ZMJ is low due to the small height of jet-exits and the low speed of the jets, so the ZMJ can be assumed as laminar flow and the velocity profiles of the ZMJ are parabolic. The fluid velocity at the jet-exits oscillates in a sinusoidal function, which is defined as

$$U^+_{jet} = W^+_{max} \sin\left(\frac{2\pi}{T^+_{osc}} t^+\right) \tag{5.1}$$

where, U^+_{jet} and W^+_{max} are the instantaneous velocity and the maximum velocity at the centre of the jet-exits, respectively. T^+_{osc} and t^+ are the period of the ZMJ and the physical time, respectively. Wall units means that length, velocity, and time are normalized by the viscous length ν/u_τ, friction velocity u_τ, and reference time ν/u_τ^2, respectively. If u_τ is not specified individually, u_τ is the friction velocity of the smooth channel at $Re_\tau = 180$. According to the previous works of spanwise oscillating walls [90], a saving in power can reach 39% with the maximum wall velocity $W^+_{wall,max} = 18$ and the oscillating period $T^+_{wall,osc} = 125$. It means that the period $T_{wall,osc} = 2.57 \times 10^{-4}$s, and the frequency is 3888Hz in this study. ZMJ was planned to emulate the similar mechanisms to the spanwise oscillating wall with the benefit of being more practical. Therefore, at the beginning of the design, time period of ZMJ is set to be $T^+_{osc} = 125$ and the maximum of the mean velocity of ZMJ is set to be $W^+_{mean,max} = 18$. Then, the maximum velocity at the centre of the jet-exits is $W^+_{max} = 27$ because the velocity profile is parabolic at the jet-exits. Figure 5.2 shows the velocity distribution at the centre of the jet-exits in a period of ZMJ. Four probes of the phase time are marked by (●) symbols in the figure. A pair of ZMJ comes out from two step-sides which are going to be called side.1 and side.2 in this research, as shown in figure 5.1. At side.1, the streamwise and spanwise velocities are $U^+_{side.1,x} = -U^+_{jet}\sin\beta$ and $U^+_{side.1,z} = U^+_{jet}\cos\beta$, respectively. At side.2, the streamwise and spanwise velocities are $U^+_{side.2,x} = U^+_{jet}\sin\beta$ and $U^+_{side.2,z} = U^+_{jet}\cos\beta$, respectively. This usage of ZMJ has not been investigated and used to reduce the skin friction in turbulent channel flow, especially in a DNS study.

When ZMJ is off, the boundary condition of jet-exits is assumed as slipping walls. It is computed as below:

$$\boldsymbol{Q}^{\boldsymbol{g}}_i = \left\{ \begin{array}{c} p^g_i \\ u^g_i \\ v^g_i \\ w^g_i \\ T^g_i \end{array} \right\} = \left\{ \begin{array}{c} p^c_i \\ u^c_i \\ v^c_i \\ -w^c_i \\ T^c_i \end{array} \right\}$$

$$\boldsymbol{Q}^{\boldsymbol{g}}_{i-1} = \left\{ \begin{array}{c} p^g_{i-1} \\ u^g_{i-1} \\ v^g_{i-1} \\ w^g_{i-1} \\ T^g_{i-1} \end{array} \right\} = \left\{ \begin{array}{c} p^c_{i-1} \\ u^c_{i-1} \\ v^c_{i-1} \\ -w^c_{i-1} \\ T^c_{i-1} \end{array} \right\}$$

$$\boldsymbol{Q}^{\boldsymbol{g}}_i = \left\{ \begin{array}{c} p^g_{i-2} \\ u^g_{i-2} \\ v^g_{i-2} \\ w^g_{i-2} \\ T^g_{i-2} \end{array} \right\} = \left\{ \begin{array}{c} p^c_{i-2} \\ u^c_{i-2} \\ v^c_{i-2} \\ -w^c_{i-2} \\ T^c_{i-2} \end{array} \right\}$$

When ZMJ is on, the boundary condition of jet-exits is assumed as below:

$$\boldsymbol{Q}^{\boldsymbol{g}}_i = \left\{ \begin{array}{c} p^g_i \\ \boldsymbol{v}^g_i \\ T^g_i \end{array} \right\} = \left\{ \begin{array}{c} p_b \\ \boldsymbol{v}_{pre} \\ T_{wall} \end{array} \right\}$$

$$\boldsymbol{Q}^{\boldsymbol{g}}_{i-1} = \left\{ \begin{array}{c} p^g_{i-1} \\ \boldsymbol{v}^g_{i-1} \\ T^g_{i-1} \end{array} \right\} = \left\{ \begin{array}{c} p_b \\ \boldsymbol{v}_{pre} \\ T_{wall} \end{array} \right\}$$

$$\boldsymbol{Q}^{\boldsymbol{g}}_{i-2} = \left\{ \begin{array}{c} p^g_{i-2} \\ \boldsymbol{v}^g_{i-2} \\ T^g_{i-1} \end{array} \right\} = \left\{ \begin{array}{c} p_b \\ \boldsymbol{v}_{pre} \\ T_{wall} \end{array} \right\}$$

where, p_b is the mean pressure in channel, $\boldsymbol{v}_{pre}$ is the prescribed velocity as discussed before, T_{wall} is the wall temperature. The meanings of rest variables are mentioned in subsection 3.3. Because it has $\rho = P/RT$, the density is prescribed at jet-exits as well. When ZMJ is on, the instantaneous mass flux of ZMJ is always fixed to be zero.

In this research, ZMJ periodically blows or sucks fluid in the channel flow. The periodic velocity of the fluid should be considered apart from the pure turbulent fluctuations of velocity, and mean velocity. Thus, velocities (u, v, w) can be decomposed into three components. For the streamwise velocity, u, the triple decomposition is adopted:

$$u = \overline{u} + \widetilde{u} + u'', \quad u' = \widetilde{u} + u'', \quad \langle u \rangle = \overline{u} + \widetilde{u} \tag{5.2}$$

where $\overline{u}$ is the time-averaged value, $\widetilde{u}$ is periodic velocity, u'' is the turbulent contribution of u or the pure turbulent fluctuation of u, u' is the total fluctuation of u, and $\langle u \rangle$ denotes the phase-averaged value.

The time average of u is computed by

$$\overline{u} = \frac{1}{t_2 - t_1} \int_{t_1}^{t_2} u dt \tag{5.3}$$

where, t_1 is the time when the channel flow is statistically convergent, and t_2 is the time when the sampling is finished.

The phase average of u can be computed by

$$\langle u \rangle = \frac{1}{M} \sum_{\varphi = t, i=1}^{M} u_i \tag{5.4}$$

where φ is the phase time of the jets in figure 5.2, and u_i is the i-th value of u at the phase time t. M is the number of samples which are at the same phase time between t_1 and t_2.

The Flow conditions and dimensions of the controlled channel are displayed in table 5.1. To make the controlled channel be able to compare with the smooth channel, the computational domain of the controlled channel has the same dimensions as the smooth channel in the streamwise and spanwise directions. The dimension in the wall-normal direction should take the steps into account because the steps are bulges on the walls. The bulges will influence the area of the streamwise cross-section, causing different Reynolds-number Re_b between the controlled channel and smooth channel. To have the same Re_b, it

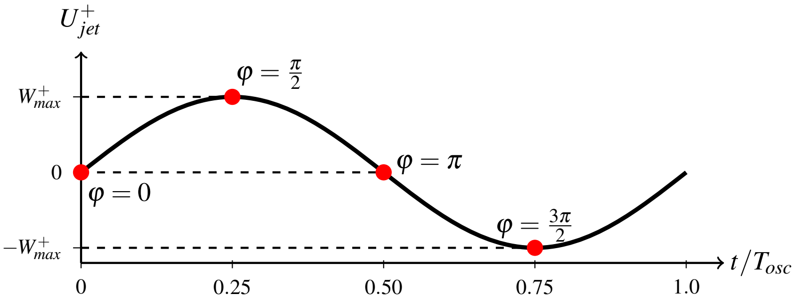

Figure 5.2 The velocity distribution in a period of the ZMJ. (U_{jet}^{+} is the normalised velocity of the jets, W_{max}^{+} is the maximum normalised-velocity of the jets, T_{osc} is the time period of the ZMJ and φ is the phase time of the ZMJ.)

Table 5.1 Flow conditions and dimensions of the controlled channel with $\delta_{jet}^{+} = 2$. The Reynolds number is based on the friction velocity of the smooth channel in section 4.3.

Re_τ	180
Re_b	2800
Mean Mach number Ma_b	0.211
Mean velocity U_b	$42.0\,\mathrm{m\,s^{-1}}$
Mean pressure P_b	16065.1 Pa
Mean temperature T_b	110.0 K
Mean density ρ_b	$0.509\,\mathrm{kg\,m^{-3}}$
Reference length δ	0.001m
$(l_x \times l_y \times l_z)/\delta$	$2\pi \times 1.987 \times \frac{4}{3}\pi$
$\left(\delta_{jet} \times L_{step} \times L_{jet}\right)/\delta$	$0.011 \times 0.199 \times 0.499$
Number of devices N_d	12
step height δ_{jet}	1.1×10^{-5} m

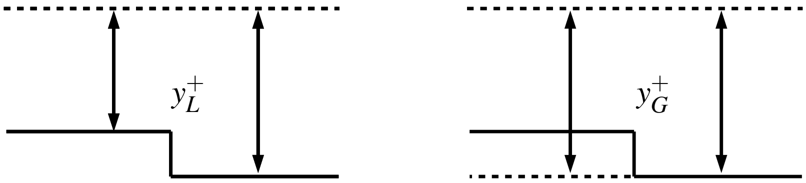

Figure 5.3 The illustration of y_L^+ and y_G^+.

should satisfy below equation.

$$l_{y.smooth} \times l_{z.smooth} = l_{y.controlled} \times l_{z.controlled} + 12\delta_{jet} \times L_{jet} \tag{5.5}$$

where, $l_{y.smooth}$ and $l_{z.smooth}$ are the wall-normal and spanwise dimensions of the smooth channel, respectively; $l_{y.controlled}$ and $l_{z.controlled}$ are the wall-normal and spanwise dimensions of the controlled channel, respectively; $l_{y.controlled}$ also is the wall-normal distance between the top and bottom surfaces of the steps. δ_{jet} and L_{jet} are defined in figure 5.1. Because the controlled channel and smooth channel have the same mass flux in the streamwise direction, the mean streamwise-velocity U_b can be the same with the same areas. The mass flux are fixed to be a constant, employing the method introduced in section 4.3.

Because of the steps, two kinds of y^+ which are y_L^+ and y_G^+ will be employed in the data analysis, as displayed in figure 5.3. y_L^+ is the local y^+ and is the wall-normal distance away from the local wall. y_L^+ is suitable to compare the profiles with a real wall-distance. No extra length outside the computational domain is taken into account. y_G^+ is the global y^+ and is the wall-normal distance away from the wall between a pair of ZMJ. y_G^+ will be employed in the 2-D contours of the cross-section to compare the results in a global view.

The flow field has following characters.

- The flow field can be divided into 12 sections based on the geometry pattern of the controlled channel. Each sections is statistically same as the others.
- The flow field is statistically symmetric in the wall-normal direction between top and bottom sections.
- The flow field in a streamwise cross-section is statistically same as that in the other streamwise cross-sections.

Because of the characters, the space average of the flow field can be done as the process shown in figure 5.4. From stage 1 to stage 2, the flow field is space-averaged into a pair of sections. The flow field of the top section is mirrored to the flow field of the bottom section, taking an average from stage 2 to stage 3. At the last stage, the bottom flow field is averaged into the streamwise cross-section.

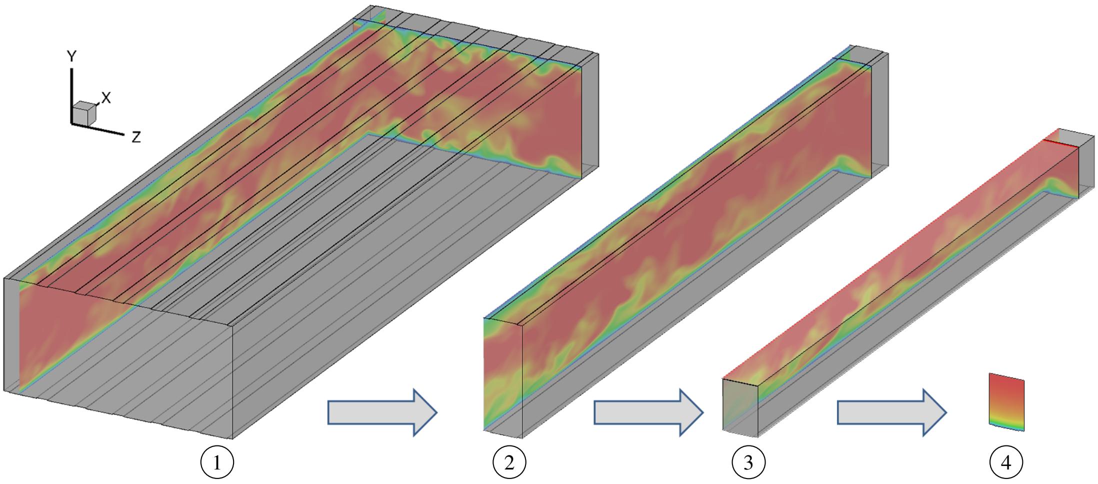

Figure 5.4 The space-averaged process.

In this thesis, the skin friction coefficients are computed by

$$C_f = \frac{\int_0^{l_x}\int_0^{l_z} \tau_w dxdz}{l_x l_z} \times \frac{1}{\frac{1}{2}\rho_b U_b^2} \tag{5.6}$$

where, τ_w is the wall shear stress at local. ρ_b and U_b are the parameters of the flow conditions in table 5.1.

5.2 Preliminary Simulations

To test whether the ZMJ can achieve a drag reduction or not, a coarse mesh which is similar as the coarse mesh of the smooth channel in section 4.3 is used. The mesh can be divided into two parts, including main channel part and jets part. The main channel part is the region between the horizontal wall of the bottom steps to the horizontal wall of the top steps. The jets part is the region between the pair of ZMJ, and is below or above the horizontal wall of the steps. For the main channel part, the mesh resolution is $\Delta x^+ = 17.67$, $\Delta z^+ = 8.97$, $\Delta y_c^+ = 7.028$ and $\Delta y_w^+ = 0.2$. For the jets part, the mesh is uniform in the wall-normal direction with $\Delta y^+ = 0.2$. The mesh resolution of the jets part is the same as that of the main channel part in the streamwise and spanwise directions.

The level of gross drag reduction (DR) compares the drag coefficients between the controlled channel and the smooth channel, which is defined as

$$DR(\%) = 100\frac{C_{f,smooth} - C_{f,controlled}}{C_{f,smooth}} \tag{5.7}$$

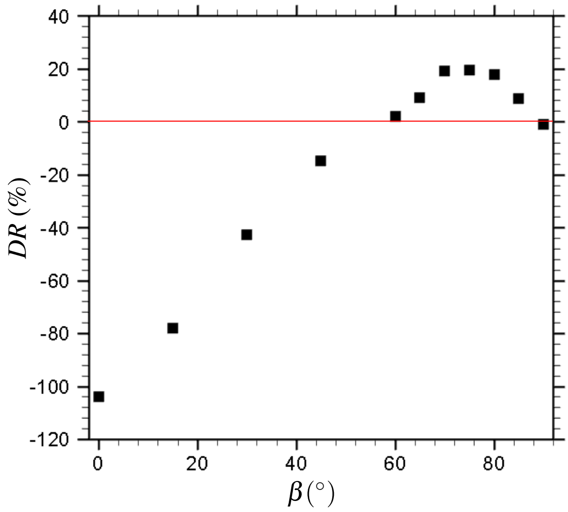

Figure 5.5 Correlation between β and the level of gross drag reduction with the coarse mesh.

When the value of the drag reduction is negative, it means that the drag is increased.

The drag reduction is obtained in the preliminary simulations, as shown in figure 5.5. It indicates that ZMJ can obtain positive drag reduction between $\beta = 60^\circ$ and $\beta = 85^\circ$. From $\beta = 70^\circ$ to $\beta = 80^\circ$, the values of the drag reduction are similar. The maximum value of gross drag reduction is 19.7%, when $\beta = 75^\circ$. The drag can be increased by ZMJ as well. When $\beta = 0^\circ$, the drag is increased 104.0%, giving the maximum drag coefficient in the results. When the jet angle is between 0° and 60°, the drag behaviour is almost linear. When $\beta = 90^\circ$, ZMJ has little influence because ZMJ does not inject any fluid into main flow.

5.3 Mesh sensitivity

In the previous section 5.2, the jet angle $\beta = 75^\circ$ gives the biggest drag reduction, but the general trend of the skin friction is estimated by the ’coarse’ mesh. In section 4.3, it has been proved that the skin friction can be accurately predicted for the smooth channel by using the coarse mesh, but ZMJ in the controlled channel would introduce some extra flow-structures into the flow field. The length scales of the extra flow-structures may be smaller than the length scales of the flow-structures in the smooth channel, causing the turbulent flow is not fully resolved in the controlled channel with the coarse mesh. The accuracy of the skin friction predicted by the coarse mesh maybe not high enough for the controlled channel. A mesh sensitivity investigation needs to be done with the case of the controlled channel. In this section, the best case of drag reduction which has the jet angle $\beta = 75^\circ$ is chosen to study the mesh sensitivity.

The baseline mesh for the study of mesh sensitivity would start from a mesh resolution which is similar to the resolution of the medium mesh in section 4.3. Figure 5.6 displays how the mesh refined in the spanwise direction. Table 5.2 shows the mesh resolutions and skin-friction coefficients for the investigation of mesh sensitivity.

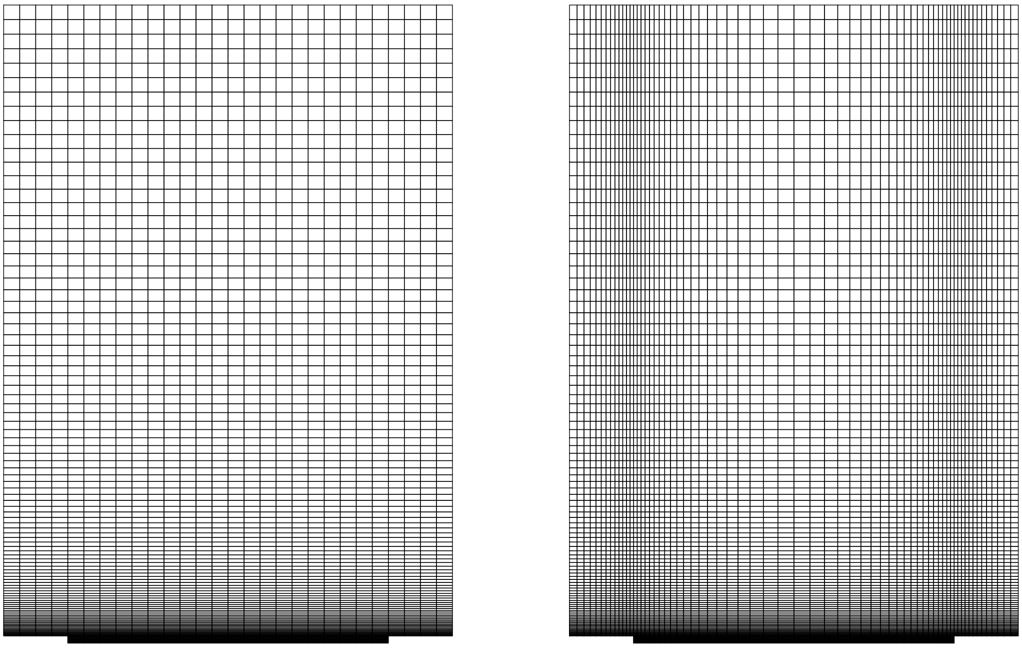

(a) Baseline

(b) C1

Figure 5.6 The meshes in the study of mesh sensitivity, viewing a section in the streamwise direction.

Table 5.2 The mesh resolutions and skin-friction coefficients for the study of mesh sensitivity.

Case	Δx^+	Δz^+_{min}	Δz^+_{max}	Δy^+_w	Δy^+_c	$C_f \times 10^{-3}$
Baseline	8.84	4.49	4.49	0.2	4.09	6.92
A	4.42	4.49	4.49	0.2	4.09	6.89
B	8.84	4.49	4.49	0.1	4.06	6.88
C1	8.84	1.00	4.49	0.2	4.09	7.18
C2	8.84	0.50	3.80	0.2	4.09	7.32
C3	8.84	0.20	3.97	0.2	4.09	7.34

To study the mesh sensitivity, the baseline mesh is refined in three directions. Cases A, B and C are refined in the streamwise, wall-normal and spanwise directions, respectively. The skin-friction coefficient of case C1 is very different from that of the baseline case, giving two more cases to find the convergent mesh. Comparing the results between the baseline case and

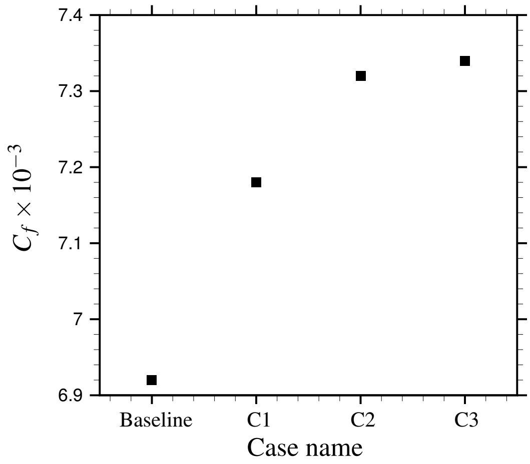

Figure 5.7 Comparison of the skin friction coefficients with different mesh refinements in the spanwise direction when the jet angle is 75°.

case A, the difference of the skin frictions is 0.43%. The difference is 0.58% between the baseline case and case B. Both of the differences are small and acceptable, showing that the mesh resolutions $\Delta x^+ = 8.84$, $\Delta y_w^+ = 0.2$ and $\Delta y_c^+ = 4.09$ are fine enough to obtain the skin friction. However, the results of the skin friction are very different between the baseline case and case C1, which means that the mesh resolution of the baseline case is not fine enough in the spanwise direction. As the mesh is refined in the spanwise direction, figure 5.7 shows a convergent trend of the skin frictions. The C_f difference which is computed by equation 5.8 starts from 3.6% to 0.27% by refining the spanwise mesh. This means that the mesh of case C2 is fine enough to study the drag reduction with ZMJ.

$$\begin{aligned}
\tilde{D}_{C1.vs.Baseline} &= \frac{C_{f.C1} - C_{f.baseline}}{C_{f.C1}} = 3.6\% \\
\tilde{D}_{C2.vs.C1} &= \frac{C_{f.C2} - C_{f.C1}}{C_{f.C2}} = 1.9\% \\
\tilde{D}_{C3.vs.C2} &= \frac{C_{f.C3} - C_{f.C2}}{C_{f.C3}} = 0.27\%
\end{aligned} \tag{5.8}$$

In conclusion, the mesh resolution of case C2 is fine enough to resolve the flow near the jet-exits, so the DNS results simulated with the mesh of case C2 should be reasonable and reliable. From now on, the simulations are going to use the mesh resolution of case 2.

5.4 Results when ZMJ is off

To obtain the initial turbulent flow for the simulations, a case is carried out with ZMJ off in the controlled channel. This case is named as "case ZMJ(off)". When the turbulent flow of this case is statistically convergent, the flow field is employed as the initial flow field for the simulations which have ZMJ on. In order to distinguish the cases, when ZMJ is on with a jet-angle of β, the case will be called "case ZMJ(β)". When the simulations are statistically convergent again, the results are used to study the mechanisms of drag reduction by ZMJ. The simulation result of case ZMJ(off) can be used to study the step effects. Vanderwel and Ganapathisubramani [120] found that large-scale secondary flow is directly related to the spanwise spacing of the steps. When the spacing is similar to boundary layer thickness, the secondary vortices are maximumly strengthened. Hwang and Lee [38] systematically changed the pitch and width of the steps. In their results, when the pitch increases or when the width decreases, the strength of the vortices increases. The formation of secondary flows are demonstrated by Vanderwel et al. [121], using both experiments and numerical simulations. They found that a non-homogeneous distribution of mid-size vortices causes the secondary flows. This study focuses on the ZMJ. By comparing the flow field between ZMJ off and on, the jet effects can be completely separated out.

In case ZMJ(off), the skin friction coefficient of the controlled channel is 8.20×10^{-3}. The value is 0.24% bigger than that of the smooth channel which is 8.18×10^{-3} in the reference [51]. This means that the steps have small influence on the skin friction, comparing to the influence of ZMJ.

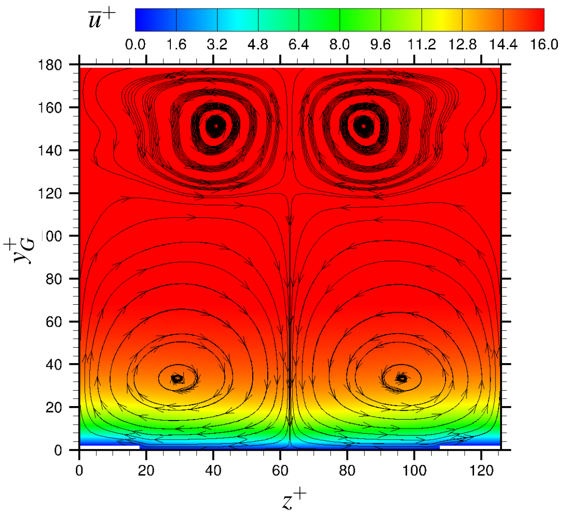

Figure 5.8 The contours of time and space averaged streamwise-velocity $\overline{u}^+$, showing the streamlines of $(\overline{w}^+, \overline{v}^+)$.

Because of the steps, the fluid is squeezed into the middle of each sections, causing the top of the fluid is turned upward and the bottom of the fluid is brought downwards, as shown in figure 5.8. There are four vortices which are clearly shown by the streamlines of $(\overline{w}^{+}, \overline{v}^{+})$ in the time and space averaged flow field. As the motion of the averaged flow, the viscous sublayer is compressed in the middle of each sections, and is expanded in the both sides of each sections in the near-wall region.

To show the differences between the smooth channel and the controlled channel without jets, the time and space averaged streamwise-velocity-profiles are compared in figure 5.9. Three spanwise positions are chosen for the controlled channel, including $z^{+} = 0$, 18.5 and 63 which are located at the left side of each sections, the left jet-exits and the middle of each sections, respectively. In the sides and middle of each sections, the profiles of the controlled channel are almost the same as the profile of the smooth channel. The steps significantly influence the velocity profile near the jet-exits. Zooming in the viscous layer, the gradient of the streamwise velocity is reduced by the jet-exits, and the gradient is slightly reduced in the sides of each sections. Note that the gradient is increased in the middle of each sections. It can be seen that the velocity profile of $z^{+} = 18.5$ is wavy at $y_L^{+} = 2$ because the flow is suddenly changed at the sharp corner of the steps.

The gradient of the streamwise velocity is increased between the pair of ZMJ, but decreased on the steps and near the jet-exits. The skin friction is related to the gradient by $\tau_w = \mu \partial u / \partial y$. Overall, the steps only influence a small region near the jet-exits, and the effects are balanced in other places. Therefore, the skin friction of the controlled channel without jets is similar as that of the smooth channel.

The Reynolds stresses are associated with the skin friction, which has already been discussed in reference [27]. The Reynolds normal stresses can be computed by $\overline{u'u'} = u'^{2}_{rms}$, $\overline{v'v'} = v'^{2}_{rms}$ and $\overline{w'w'} = w'^{2}_{rms}$, so the trends should be similar between the Reynolds normal stresses and the root-mean-square of the velocity fluctuations.

The root-mean-square of the velocity fluctuations in three directions is shown in figure 5.10. In figure 5.10a, all of the contours of the velocity fluctuations are z-symmetric in a section. The peak locations of fluctuations are lifted up by the steps, and the values of the fluctuations in the sides of each sections are higher than that in the middle of each sections. Figure 5.10b shows that the jet-exits reduce the fluctuations of the streamwise and spanwise velocity, but increase the wall-normal velocity fluctuations near the sharp corner of the steps. Except the profile of the controlled channel at $z^+ = 18.5$ and below $y_L^+ = 10$, the profiles are close to each other. This means that the step influence is rapidly dissipated from the regions near the jet-exits to other flow region, leaving little influence in the outer flow region.

Figure 5.11 displays that $-\overline{u'v'}$, $\left|\overline{u'w'}\right|$, $\left|\overline{v'w'}\right|$ are $z-$symmetric in a section. The sign of $-\overline{u'v'}$ is the same in the left and right parts of each sections, but the signs of $\overline{u'w'}$, $\overline{v'w'}$ are opposite. This indicates that the face integrations of $\overline{u'w'}$, $\overline{v'w'}$ are 0 in a section. The reason is that the averaged flow is z-symmetric, as shown in figure 5.8. The velocity fluctuations of u', v' and w' are statistically symmetric in the streamwise, wall-normal and spanwise directions, respectively. The signs of u' and v' do not change in the left and right parts of each sections, but the sign of w' is opposite.

Cutting the contour plots of figure 5.11a along with $z^+ = 0$, 18.5, 63 and comparing the profiles with the profiles of the smooth channel, figure 5.11b shows that the peak values of $-\overline{u'v'}$ at $z^+ = 0$, 18.5 are higher than that of the smooth channel. Among all of the profiles, the peak value is the lowest at $z^+ = 63$ which locates in the middle of each sections. At

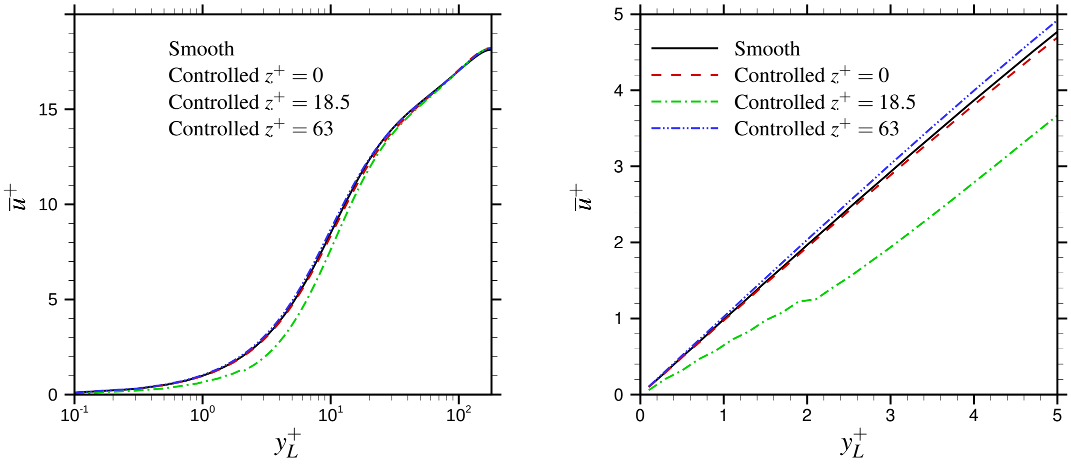

(a) streamwise velocity profiles

(b) streamwise velocity profiles, zooming in the viscous layer.

Figure 5.9 Comparisons of time and space averaged streamwise-velocity-profiles for the smooth channel and case ZMJ(off).

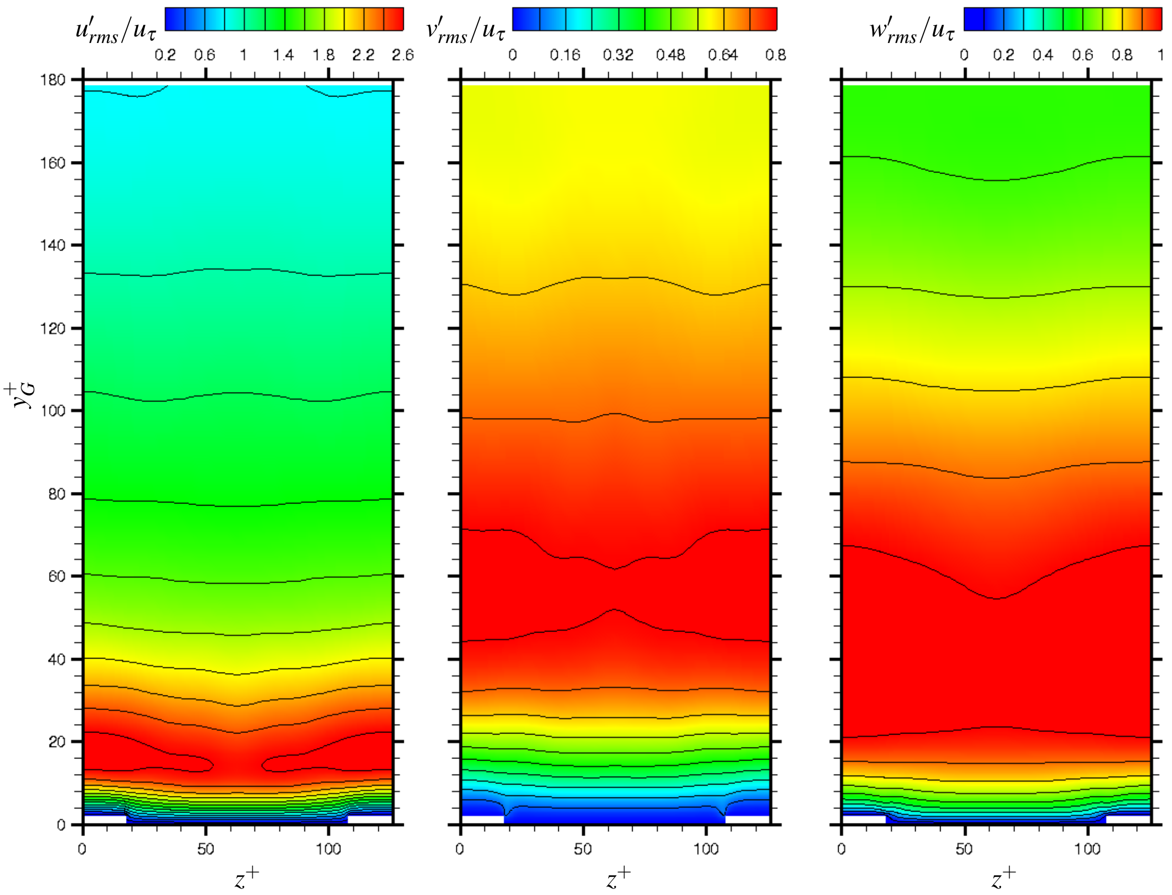

(a) Contours of case ZMJ(off) in a section.

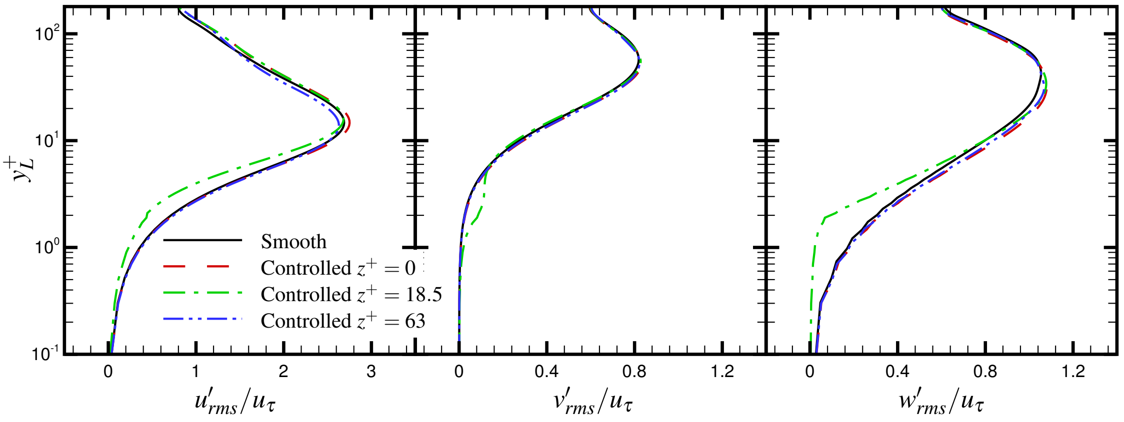

(b) Comparisons of profiles between the smooth channel and case ZMJ(off).

Figure 5.10 The root-mean-square of the velocity fluctuations in three directions.

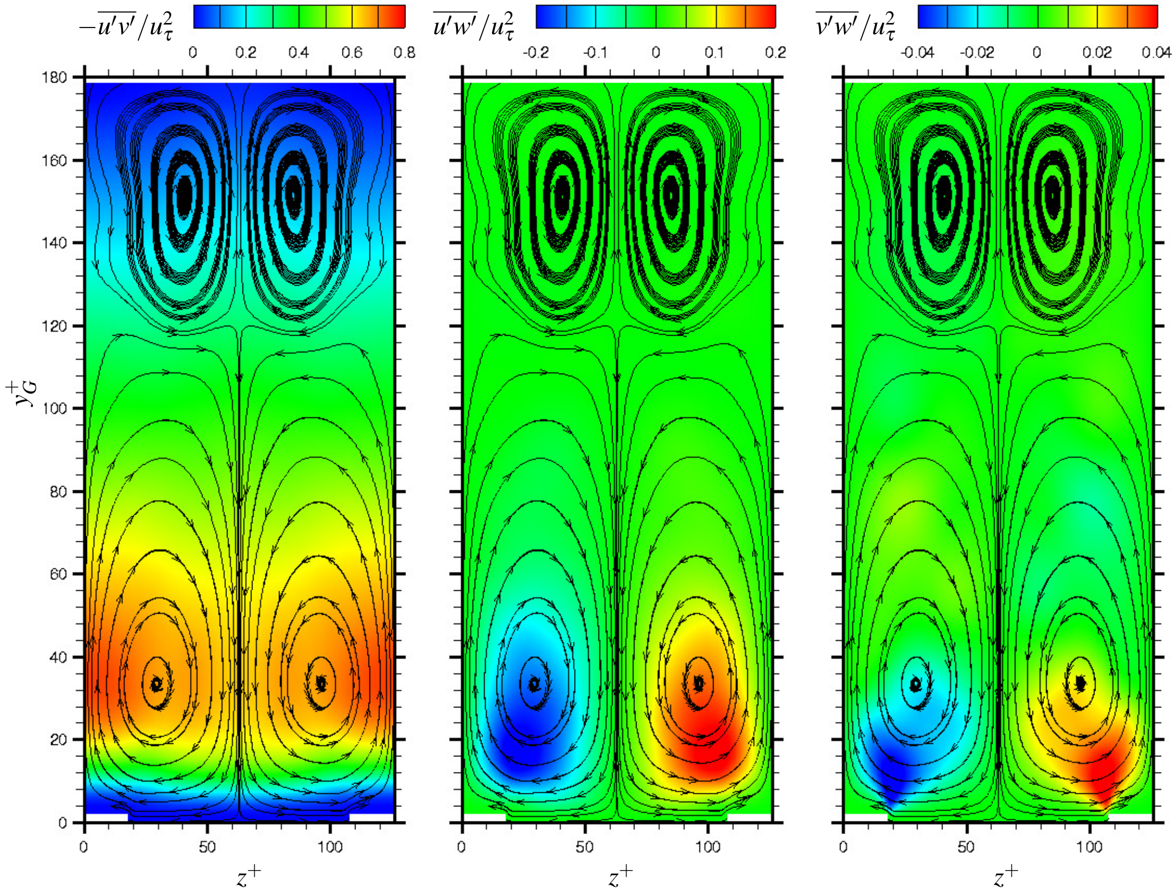

(a) Contours of case ZMJ(off) in a section.

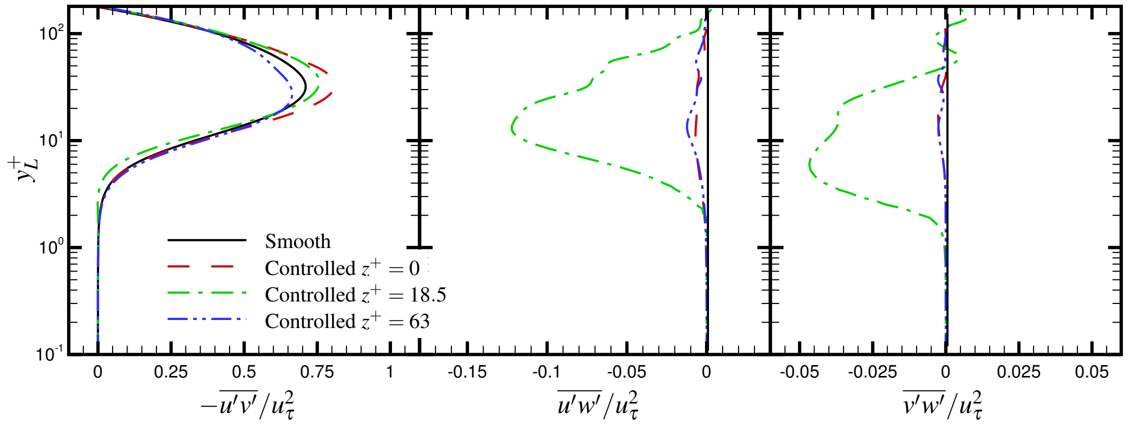

(b) Comparisons of profiles between the smooth channel and case ZMJ(off).

Figure 5.11 The Reynolds shear stresses

$z^+ = 18.5$, the peak values of $\overline{u'w'}/u_\tau^2$ and $\overline{v'w'}/u_\tau^2$ are -0.12 and -0.047, respectively. $\overline{u'w'}$ and $\overline{v'w'}$ are not zero in the controlled channel due to the steps. If the position is far from the steps, the influence of the steps is small. If the position is close to the steps, the velocity fluctuations are small. So, the peak values of $\overline{u'w'}$ and $\overline{v'w'}$ appear between the step corners and vortex cores, as shown in figure 5.11a.

In order to understand the influence from the steps, probability density function is used to analyse the velocity fluctuations at the positions $y_L^+ = 20$ and $z^+ = 0$, 18.5, 63, as shown in figure 5.12. All the PDF values are normalised by the peak value of each curve. In figure 5.12a, the normalized PDF of streamwise-velocity fluctuation, $P(u'^+)$, is biased to the positive part with a peak at $u'^+ = 2$, indicating that the averaged flow are driven downstream in the streamwise direction. This is similar to the phenomenon in a smooth channel, as shown in figure 4.12a. The skewness of $P(u'^+)$ is expected to be negative. Kim et al. [51] found negative skewness of $P(u'^+)$ at $y^+ = 20$ as well. The skewness is related to the sweep and ejection motions.

The fluctuation ranges of the streamwise velocity are almost the same at the different spanwise positions. The distribution of the streamwise velocity fluctuation is the most concentrated at the centre of each sections, so that u'_{rms} is the smallest. The distributions of $P(v'^+)$ and $P(w'^+)$ are almost symmetric and similar at the different spanwise positions. An interesting phenomenon is that, at $(y_L^+ = 20, z^+ = 18.5)$ where is above the jet-exits, $P(w'^+)$ is a bit biased to the negative part. The negative bias of w'^+ indicates that the averaged flow are weakly driven from the centre of each sections to the sides of each sections.

In figure 5.13, joint probability density function and covariance integrand are employed to study the contributions of the Reynolds shear stresses at the position $(y_L^+ = 20, z^+ = 18.5)$. This can be compared with figure 4.16 to show the effects of the steps. In case ZMJ (off), the areas of the shapes formed by the contour lines of 10% level are larger than that in the smooth channel. This means that all of the velocity fluctuations at the position are increased by the steps. In figures 5.13a and 5.13b, the highest value of $P(u'^+, v'^+)$ is in Q4 $(u'^+ > 0, v'^+ < 0)$ which is the zone of sweeping movement. The contours of $u'^+v'^+P(u'^+, v'^+)$ show that the contributions for $\overline{u'v'}$ are mainly from Q2 and Q4. The peak value of the contributions in Q4 is higher than that in Q2. The contributions are little from Q1 and Q3. The contour lines of $P(u'^+, w'^+)$ and $P(v'^+, w'^+)$ are biased to the negative w'^+, which are different from the contour lines for the smooth channel. The highest values of $u'^+w'^+P(u'^+, w'^+)$ and $v'^+w'^+P(v'^+, w'^+)$ are in Q4, giving negative values to $\overline{u'w'}$ and $\overline{v'w'}$. Figures 5.13a, 5.13c and 5.13e show that flow status $(u'^+ > 0, v'^+ < 0, w'^+ < 0)$ has the highest probability at the position $(y_L^+ = 20, z^+ = 18.5)$.

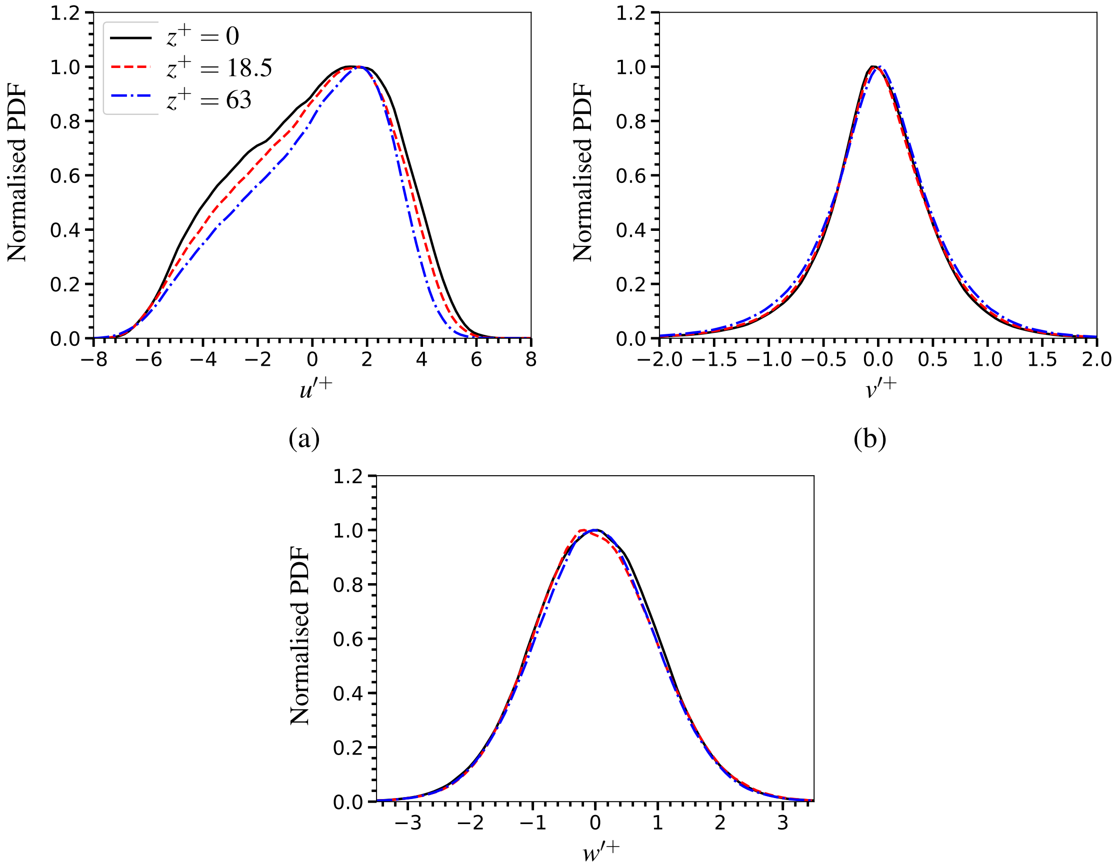

(a)

(b)

(c)

Figure 5.12 The PDFs of velocity fluctuations at the positions $y_L^+ = 20$ and $z^+ = 0$, 18.5, 63 in case ZMJ (off).

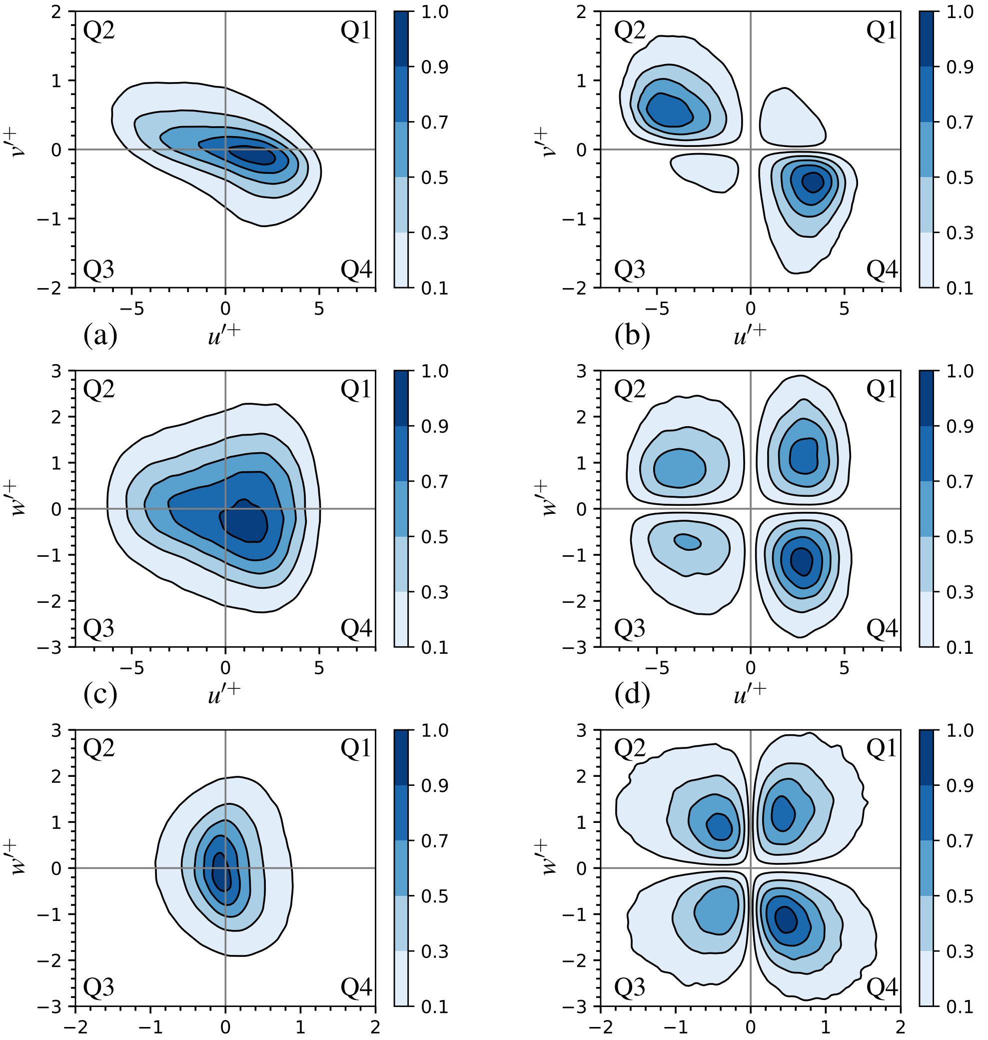

Figure 5.13 The Joint probability density function, $P(u'^+,v'^+)$, $P(u'^+,w'^+)$, $P(v'^+,w'^+)$ (left) and covariance integrand, $u'^+v'^+P(u'^+,v'^+)$, $u'^+w'^+P(u'^+,w'^+)$, $v'^+w'^+P(v'^+,w'^+)$ (right), at ($y_L^+ = 20, z^+ = 18.5$), giving $10, 30, 50, 70$ and 90% of the maximum probability level or covariance integrand.

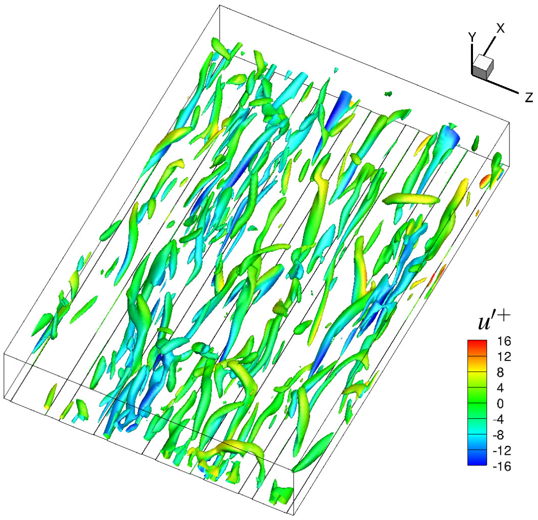

Figure 5.14 The iso-surfaces of $\lambda_2^+ = -1$ coloured by the fluctuations of the streamwise velocity u'^+ in case ZMJ(off), .

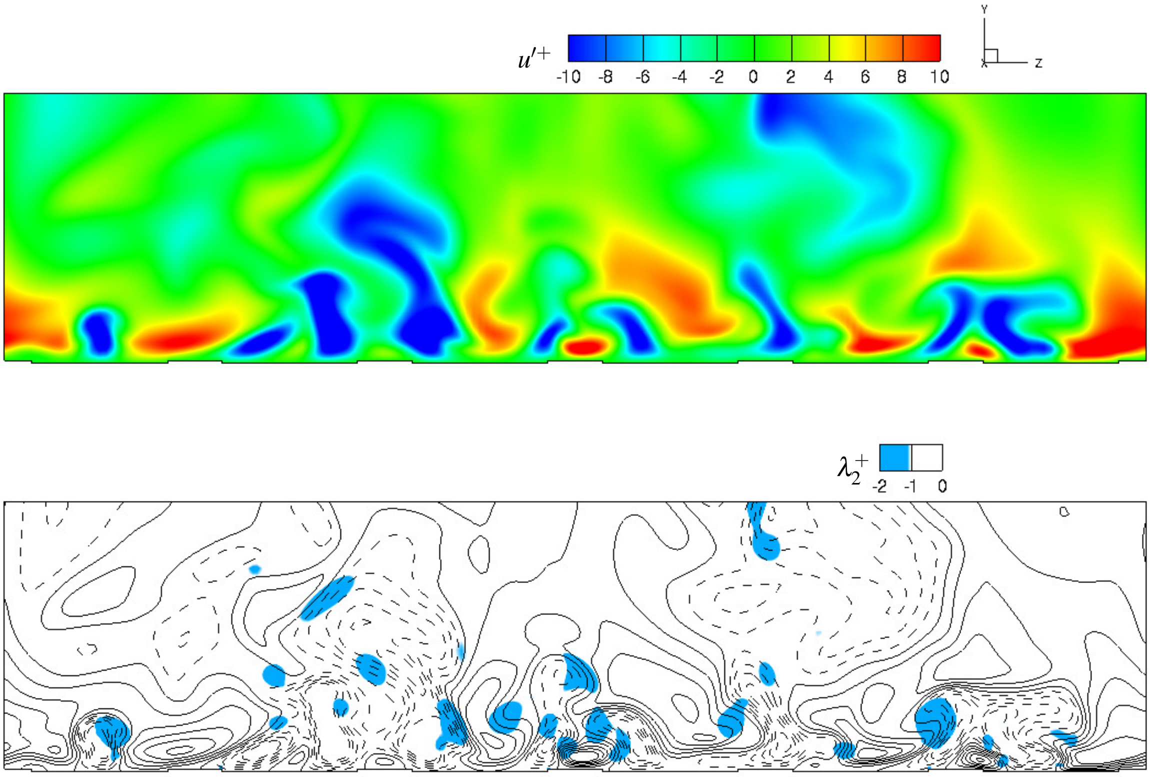

Figure 5.15 In case ZMJ(off), the contours of u'^+ (top) and the regions of $\lambda_2^+ < -1$ (bottom) in the $y-z$ plane at $x^+ = 5$. In the bottom contour plot, the contour lines are corresponding to the top contours of u'^+. The solid lines are the positive values and the dashed lines are the negative values.

Figure 5.14 shows the iso-surfaces of $\lambda_2^+ = -1$ coloured by the streamwise-velocity fluctuations in case ZMJ(off). The iso-surfaces show the near-wall flow structures in the controlled channel, which have high proportion in the low-speed regions $u'^+ < 0$. To compare the height of the jet-exits with the turbulence structures, the contour plot of u'^+ clearly shows the low-speed and high-speed regions in the $y-z$ plane at $x^+ = 3$ in figure 5.15. The contour lines on the bottom are corresponding to the top contour plot of u'^+. The blue regions are the vortex regions where $\lambda_2^+ < -1$. From figure 5.15, it is noticed that the vortices are located in the low-speed regions, or between the low-speed and high-speed regions. The step height is much smaller than most of the length-scales of the flow structures, so the steps only have limited influence on the flow structures in case ZMJ(off).

5.5 Time averaged results

In section 5.2, figure 5.5 shows that the optimal jet-angle β is 75° which has been used to study the mesh sensitivity. It is proved that the mesh resolution of case C2 is able to obtain the reliable result for the controlled channel with $\beta = 75^\circ$ and $\delta_{jet}^+ = 2$. By using the same mesh, two more simulations under different jet angles are carried out, including $\beta = 0^\circ$ and 60°. The aim of simulating $\beta = 0^\circ$ and 60° is to analyse the mechanisms of the drag reduction. The case ZMJ($\beta = 0^\circ$) can give the reason why the drag is increased. The case ZMJ($\beta = 60^\circ$) is a case between the best and worst case for the drag reduction according to figure 5.5.

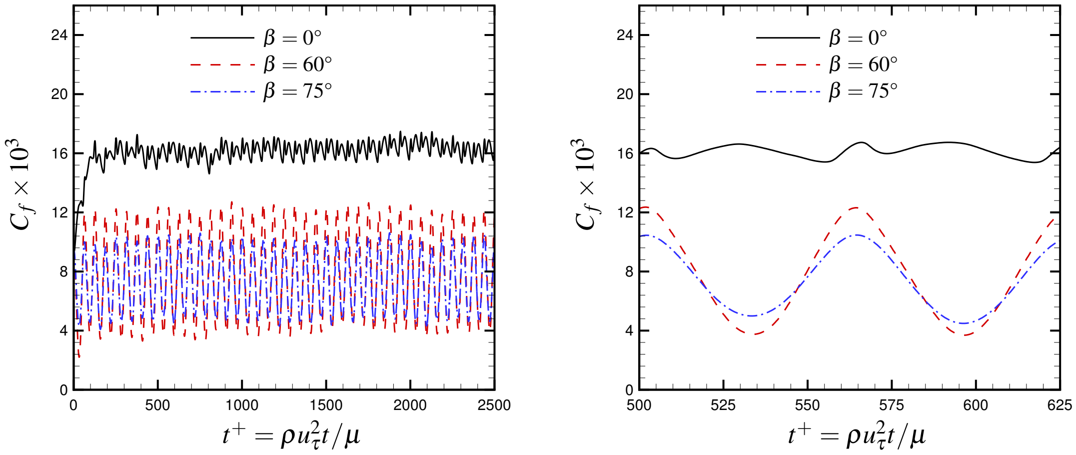

(a) The whole history

(b) One period

Figure 5.16 The evolutions of skin friction coefficients with different jet angles.

Different evolutions of skin friction coefficients with $\beta = 0°$, $60°$ and $75°$ are shown in figure 5.16. Considering the velocity characters of ZMJ, the jet effects at phase time φ are symmetric with that at phase time $(\varphi + \pi)$ in the spanwise direction. This gives the same effects to the skin friction in the streamwise direction. It means that the time period of skin friction is the half period of ZMJ. So, there are two cycles of skin friction in one period of ZMJ. Zooming in one period, the skin frictions are strongly influenced by ZMJ, showing big fluctuations. When $\beta = 0°$, the skin friction has four local peaks in one period. There are two local peaks in one period when $\beta = 60°$ and $\beta = 75°$. The frequencies of the skin-friction fluctuations are related to the jet frequency. The time averaged C_f are 16.23×10^{-3}, 7.82×10^{-3} and 7.32×10^{-3}, when $\beta = 0°$, $\beta = 60°$ and $\beta = 75°$, respectively. The figure shows that the fluctuating amplitude of C_f is the smallest when $\beta = 0°$, and it has the biggest C_f. The case ZMJ($\beta = 75°$) has the smallest C_f. The fluctuating amplitude of C_f in case ZMJ($\beta = 75°$) is smaller than that in case ZMJ($\beta = 60°$). It indicates that the fluctuating amplitude is not linear from $\beta = 0°$ to $\beta = 75°$. The levels of gross drag reduction for all of the three cases are shown in figure 5.17. The level of gross drag reduction is 10.5% in case ZMJ($\beta = 75°$).

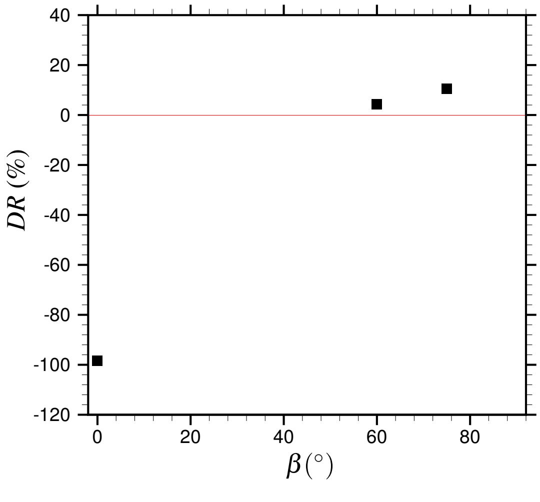

Figure 5.17 Levels of gross drag reduction with different β by using the mesh of case C2.

To study the fluctuation pattern of the skin friction coefficients, Fast Fourier Transform is employed to analyse the evolutions, as shown in figure 5.18. According to figure 5.18a, three of the jet angles have a frequency of 7776Hz, and $\beta = 0°$ has three more dominant frequencies including 15552, 23328 and 31104Hz. It confirms that the ZMJ is the dominant contribution to the flow in the controlled channel. The reason why the frequency of the skin friction doubles the jet frequency is that the influence of the jet-exits in a pair are symmetric

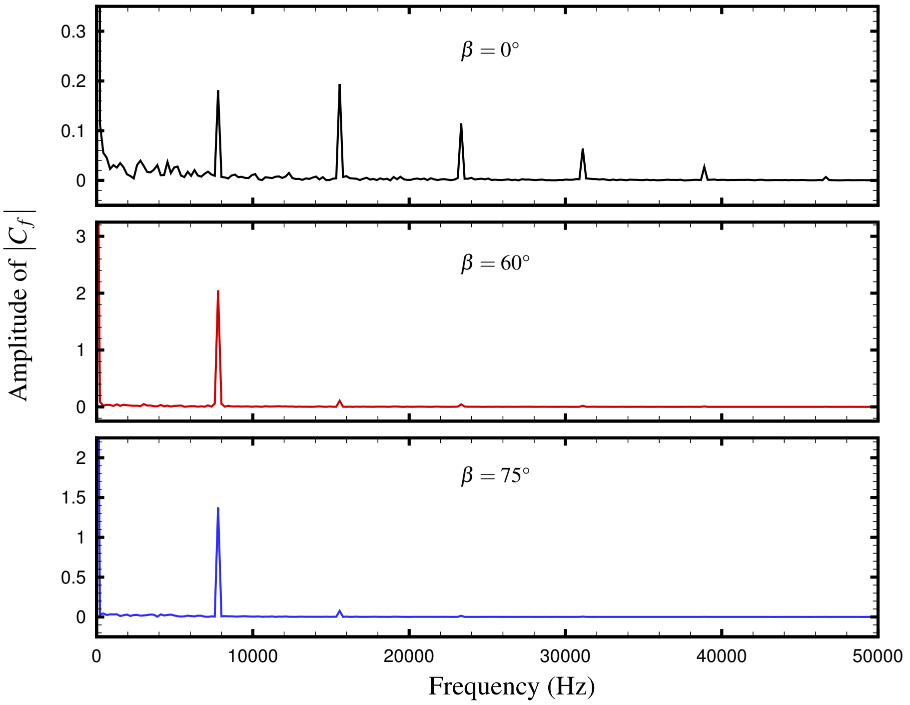

(a) The regular plots of the amplitude show the dominant frequency.

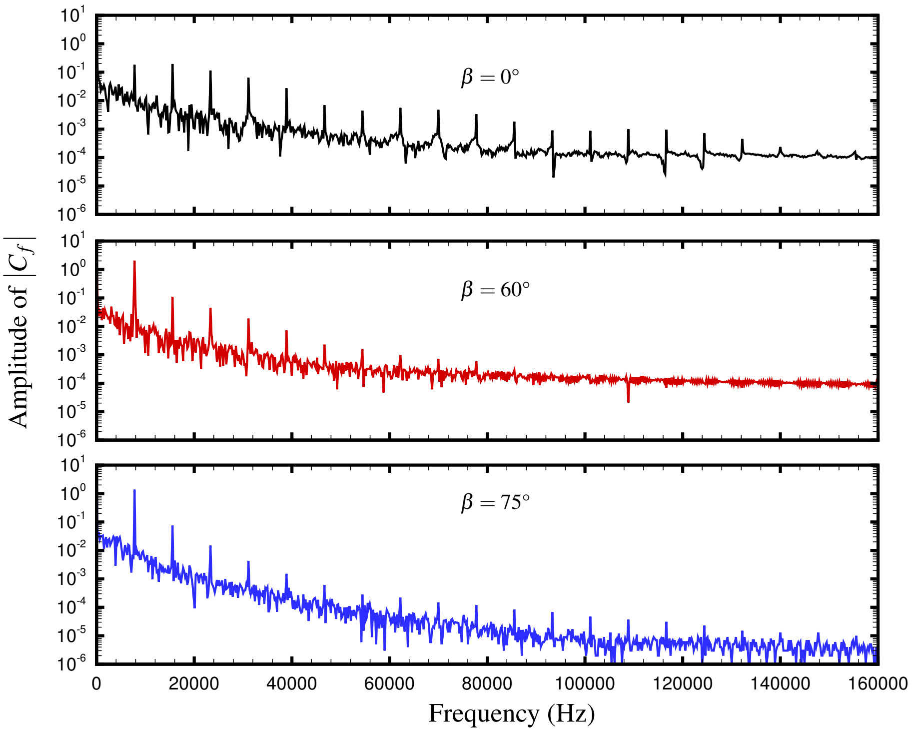

(b) The Logarithm plots of the amplitude show all frequency.

Figure 5.18 The Fast Fourier Transform of C_f evolutions with different jets angles.

with each other in the phase time. When the jet velocity reaches the maximum and minimum values at the phase time $\varphi = \pi/2$ and $\varphi = 3\pi/2$, respectively, the influence is symmetric in the streamwise direction. The skin friction is computed from the integration of the friction force in a section, so the skin friction is the same at $\varphi = \pi/2$ and $\varphi = 3\pi/2$. The time period of the skin friction is half of ZMJ, which means the frequency of the skin friction is doubled by the symmetric effect of ZMJ.

Figure 5.18b shows the amplitude of $\left|C_f\right|$ in log-scale. All three cases have the same peaks at the same frequencies with a gap of 7776Hz. The amplitudes of $\left|C_f\right|$ decrease fast and are overshadowed by the noise, when $\beta = 60°$ and $\beta = 75°$. It means that the strength of the fluctuations at the other frequencies is related to the jet speed in the spanwise direction, except 7776Hz. By reducing the jet speed in the spanwise direction, the strength of the fluctuations can be decreased. The jet in the spanwise direction creates a series of frequencies. The amplitude of $\left|C_f\right|$ at 7776Hz depends on a combination effect of the jet in the spanwise and streamwise directions, which is the biggest when $\beta = 60°$. Also, the amplitude of C_f is the largest when $\beta = 60°$ in the evolutions.

It is hard to understand the mechanisms of the drag reduction from the instantaneous flow field, because the flow is turbulent and the quantities are fluctuating. Therefore, the statistic analysis is used to examine the effects of ZMJ by averaging the flow field in time and space, and the averaging process is introduced in section 5.1.

By averaging the flow field in time and space, the induced flow by ZMJ is shown in figure 5.19. In a section, the averaged flow field is symmetric in the spanwise direction. In each case, a pair of averaged vortices are created by either the steps or the jets, shown clearly by the cross-flow streamlines. The vortex cores are brought down by the ZMJ. In case ZMJ(off), the left vortex rotates clockwise and the right vortex rotates anti-clockwise, bringing the fluid downward to the walls in the middle of each sections and upward away from the walls in the both sides of each sections. On the other hand, the rotating directions of the vortices in case ZMJ(on) are opposite from that in case ZMJ(off), because the fluid in the near-wall region is controlled to move in the opposite directions. The ZMJ works like the synthetic jets which blow out the fluid near the exits.

Using the averaged flow field of case ZMJ($\beta = 0°$) as an example, a zooming zone near the jet-exits is displayed in figure 5.20. The maximum value of time and space averaged spanwise-velocity is away from the jet-exits boundary. That is because the averaged value of the spanwise velocity of ZMJ is zero due to the zero-mass character of the jet-exits boundary, and the ZMJ works like a synthetic jet. The synthetic jet can induce the flow to move outwards of the jet-exits, but keep the velocity is zero at the jet-exits boundary [56]. Depending on the distribution of the spanwise velocity, the region can be divided into three

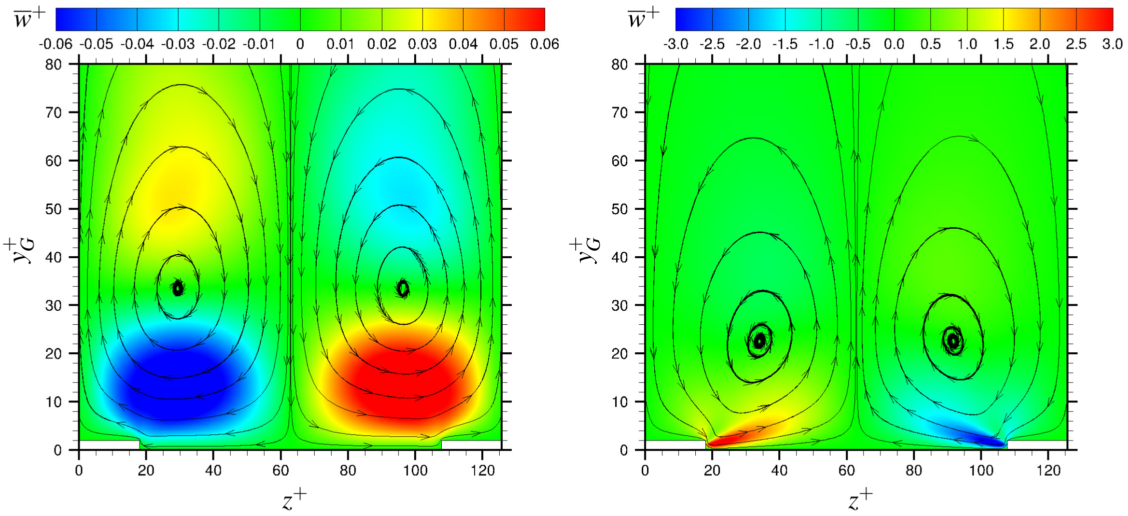

(a) ZMJ off

(b) ZMJ on, $\beta = 0°$

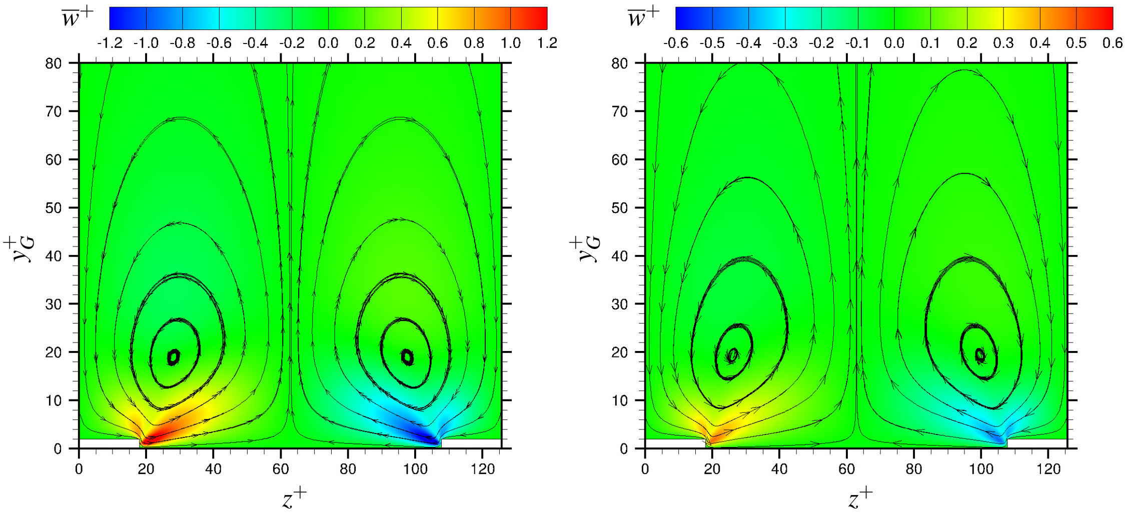

(c) ZMJ on, $\beta = 60°$

(d) ZMJ on, $\beta = 75°$

Figure 5.19 Contours of time and space averaged spanwise-velocity $\overline{w}^+$ in cross-stream ($y-z$ plane) view, showing the streamlines of the induced flow $(\overline{w}^+, \overline{v}^+)$.

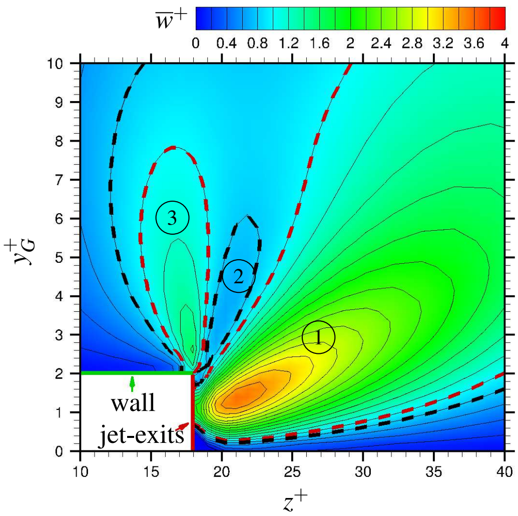

Figure 5.20 Contours of time and space averaged spanwise-velocity $\overline{w}^+$ in the zooming region near the jet-exits. The red dashed lines are $\overline{w}^+ = 1.0$, and The black dashed lines are $\overline{w}^+ = 0.8$.

zones, as shown in figure 5.20. The spanwise velocity in zones ①, ③ is higher than 1.0, and zone ② is a region where the velocity is lower than 0.8. The flow moves right and up in zone ①, and the flow moves right and down in zones ②, ③. Figure 5.19b shows that the shape of the vortices are not smooth near the step corners and have bulges towards the step corners. From zone ③ to zone ②, the fluid moves downwards to the jet-exits at the step corners. The ratio of the wall-normal velocity to the spanwise velocity increases, so the spanwise velocity drops. From zone ② to zone ①, the fluid is accelerated by ZMJ, so the spanwise velocity is increased.

Following the cutting lines in figure 5.21a, the profiles of time and space averaged velocity $\overline{w}^+$ in the near-wall region are displayed in figure 5.21. Figures 5.21b and 5.21c represent that the spanwise-velocity are strongly influenced by ZMJ when the locations are at $z^+ = 17, 20$, and the peak values of the spanwise velocity locate at $y_L^+ \approx 1.5$. Looking at the spanwise-velocity along the lines $y_G^+ = 1$ and $y_G^+ = 3$ in figures 5.21d and 5.21e, the maximum values are not at the jet-exits. This has been explained in the previous paragraph. The time and space averaged spanwise-velocity is zero in the middle of each sections, and the velocity is oscillating near the step corners. As expected, all the peak values are inversely proportional to the jet angle β.

Figure 5.22 shows the contours of time and space averaged streamwise-velocity in the cross-stream ($y-z$ plane) view. When ZMJ is on, the contour lines are lifted up between the jet-exits due to the effects of ZMJ, but the contour lines are brought down in region above the steps. Near the jet-exits, the gradient of $\overline{u}^+$ is increased when the jet angle is 0°, but the

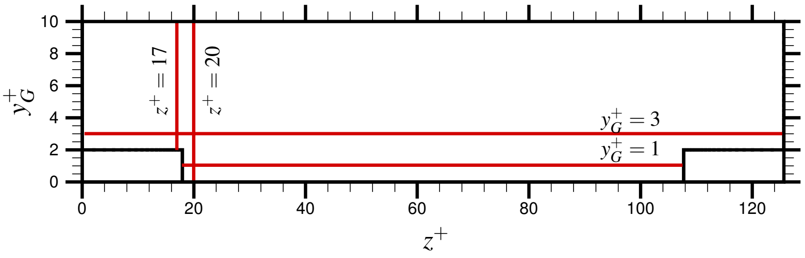

(a) The cutting lines.

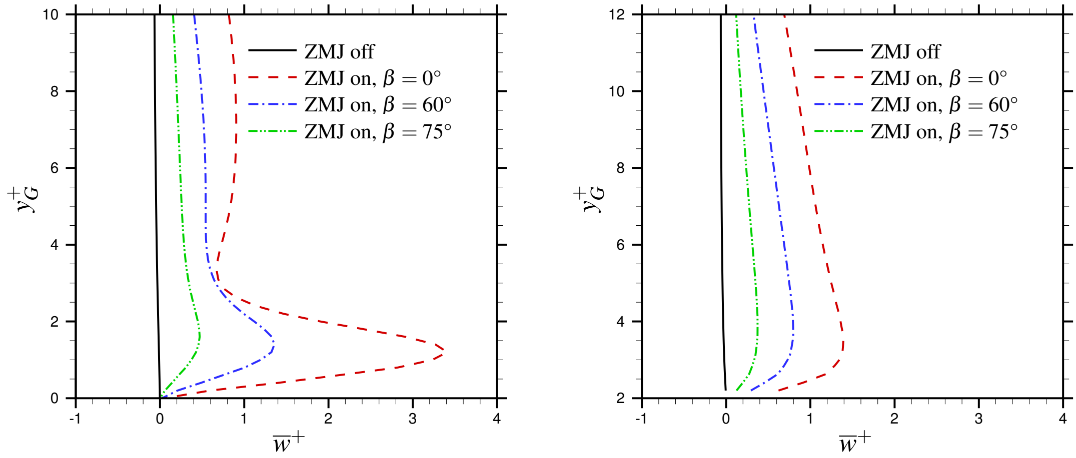

(b) $z^+ = 20$

(c) $z^+ = 17$

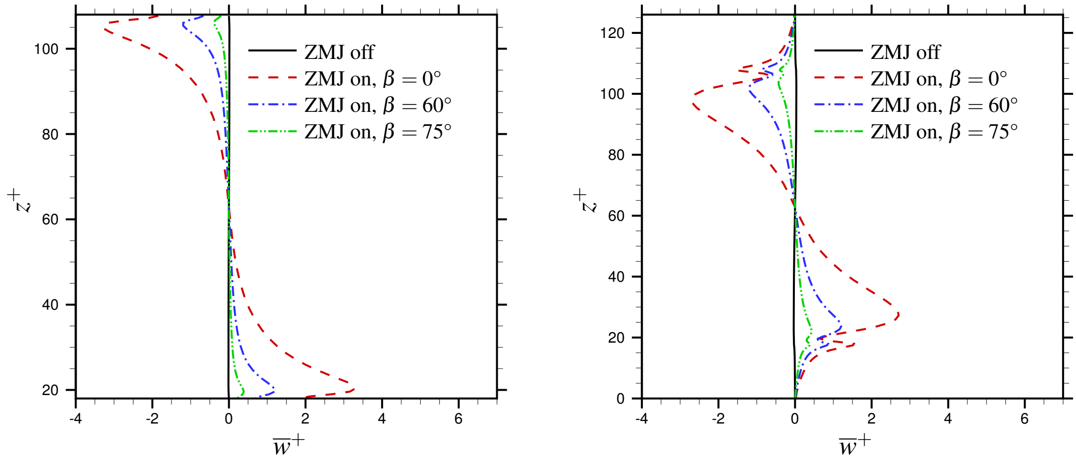

(d) $y_G^+ = 1$

(e) $y_G^+ = 3$

Figure 5.21 Comparisons of time and space averaged spanwise-velocity profiles in the near-wall regions.

gradients are decreased when the jet angles are 60° and 75°. The reason is that ZMJ can produce countering jets in the streamwise direction when $\beta = 60°, 75°$. The countering jets reduce the streamwise velocity of the main flow near the jet-exits.

Profiles of time and space averaged streamwise-velocity in the near-wall regions are displayed in figure 5.23. The cutting lines are shown in figure 5.23a. Taking the periodic character into account, $z^+ = 0.1$ is near the side of each sections. Figures 5.23b and 5.23c show that the near-wall gradients of $\overline{u}^+$ are increased by the jets in region above the steps. When the jet angle increases, the velocity gradients decrease. This means that the gradients are proportional to the spanwise jet-velocity in region above the steps. Comparing figure 5.23b and figure 5.23c, when the jet angles are the same, the velocity gradients at $z^+ = 0.1$ are smaller than that at $z^+ = 17$. This indicates that the gradients increase from the sides of each sections to the jet-exits.

In figure 5.23d, because of the countering jets near the jet-exits, the velocity gradients near wall are negative when $\beta = 60°$ and 75°, giving negative skin frictions near the jet-exits. The absolute value of the velocity gradient when $\beta = 60°$ is higher than that when $\beta = 75°$. The reason will be discussed later with figure 5.25. Not liking $\beta = 60°$ or 75°, the velocity gradient when $\beta = 0°$ is increased by the jets at $z^+ = 20$. This will be revealed by studying the phase averaged results. Figure 5.23e shows that the influence of the velocity gradients in the near-wall regions is relatively small between the pair of ZMJ.

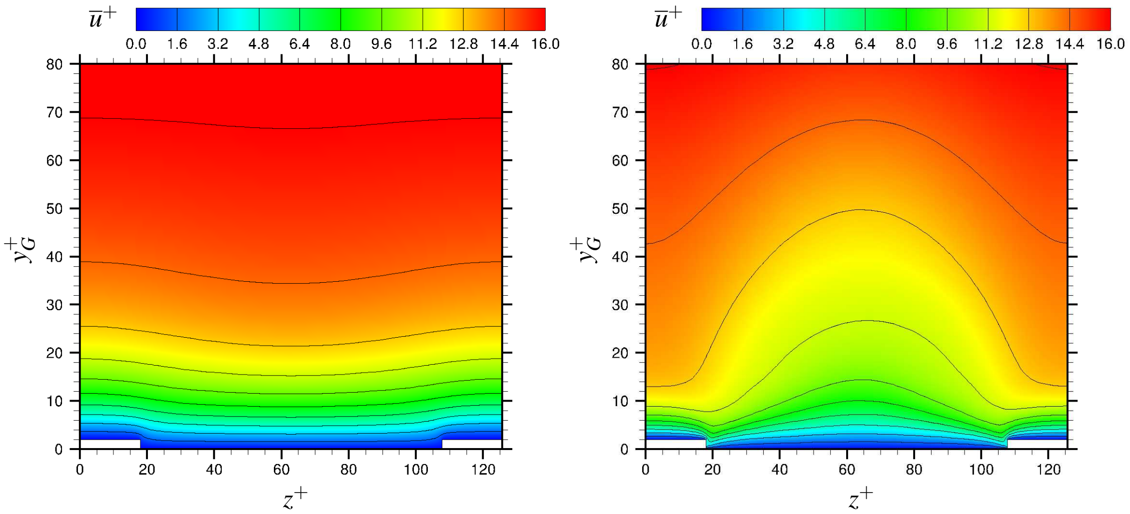

(a) ZMJ off

(b) ZMJ on, $\beta = 0°$

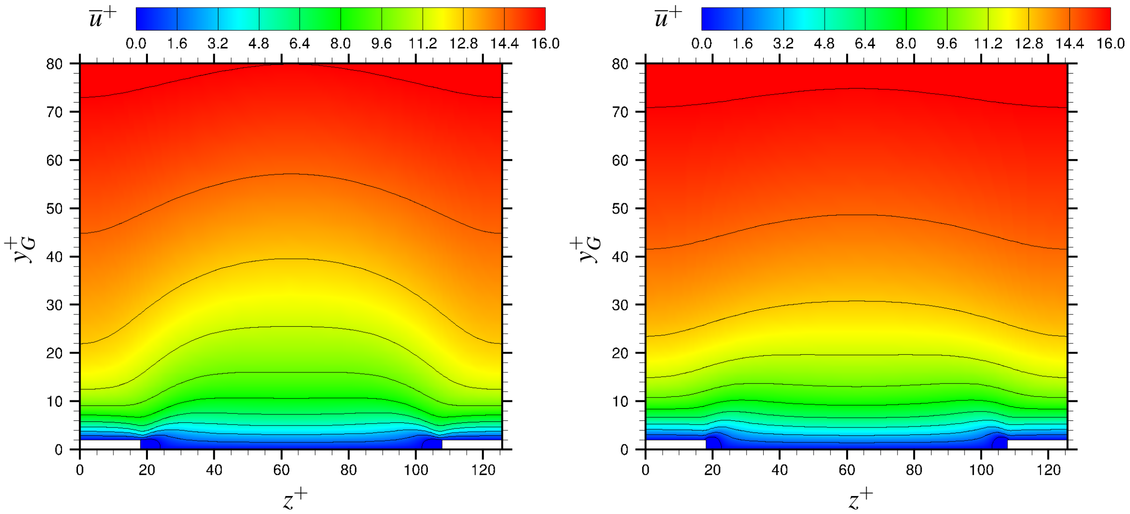

(c) ZMJ on, $\beta = 60°$

(d) ZMJ on, $\beta = 75°$

Figure 5.22 Cross-stream ($y - z$ plane) view of time and space averaged streamwise-velocity $\overline{u}^+$ with contours.

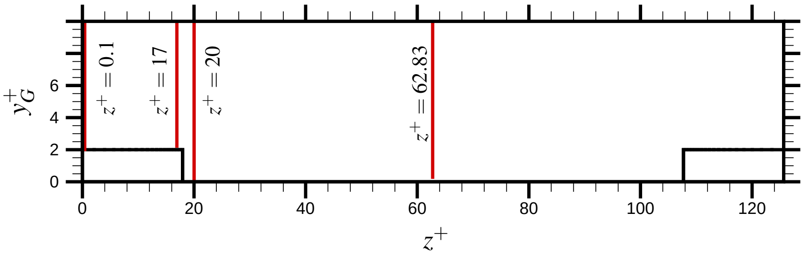

(a) The cutting lines.

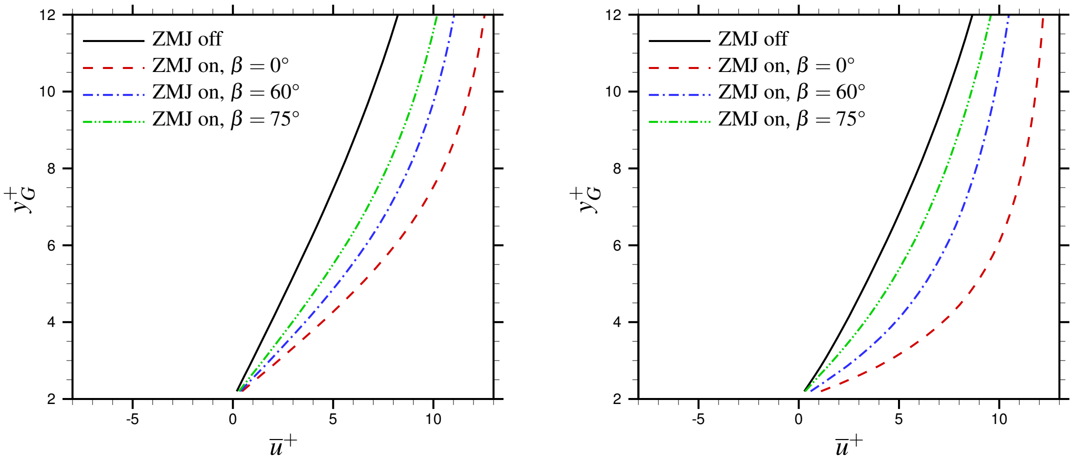

(b) $z^+ = 0.1$ (c) $z^+ = 17$

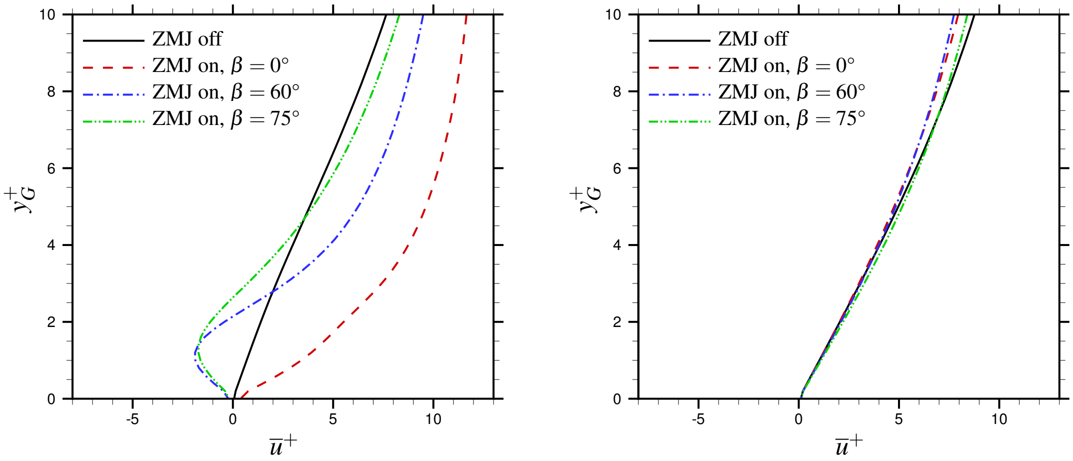

(d) $z^+ = 20$ (e) $z^+ = 62.83$

Figure 5.23 Comparisons of the time and space averaged streamwise-velocity profiles in the near-wall regions.

Figure 5.24 shows the time and space averaged skin-friction-coefficients in the controlled channel. To show a whole picture of the averaged skin-friction-coefficients, the range of C_f in figure 5.24a includes the maximum and minimum values that occur near the jet-exits. As discussed before, the gradients of the streamwise velocity near the jet-exits are significantly influenced by ZMJ. Because the skin friction coefficients are related to the gradients, the coefficients are affected by ZMJ as well. The influence of ZMJ dissipates fast away from the jet-exits, showing spikes near the jet-exits, as shown in figure 5.24a. The steps are not wide enough to eliminate the influence, so the skin frictions in region above the steps in case ZMJ(on) are bigger than that in case ZMJ(off). The distance between the pair of ZMJ is much longer than the step width, so the influence in the middle of each sections is much smaller than that in the sides of each sections, as shown in figure 5.24b.

It is no doubt that the mean skin-friction-coefficient for a whole channel in case ZMJ($\beta = 0°$) is bigger than that in case ZMJ(off), because the skin friction coefficients in case ZMJ($\beta = 0°$) are always bigger than that in case ZMJ(off) at the same spanwise positions. The mean C_f when $\beta = 60°$ and $75°$ are more complicated than that when $\beta = 0°$. Although the skin-friction-coefficients when $\beta = 60°$ are smaller than that when $\beta = 75°$ between the pair of ZMJ, the C_f of case ZMJ($\beta = 60°$) is much bigger than that of case ZMJ($\beta = 75°$) in region above the steps. So the mean C_f for a whole channel when $\beta = 60°$ is bigger than that when $\beta = 75°$.

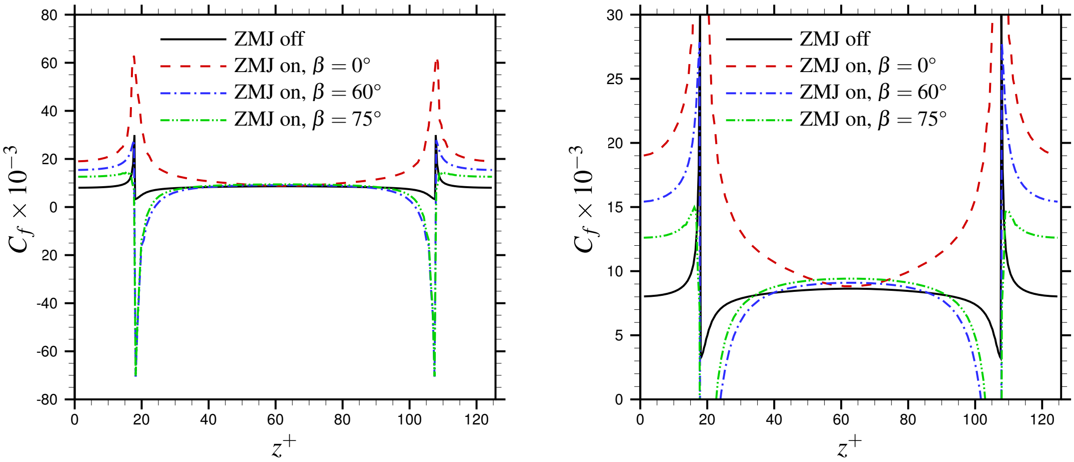

(a) Whole rang of C_f (b) Narrow range of C_f

Figure 5.24 Comparisons of time and space averaged skin-friction-coefficients.

In figure 5.24b, by narrowing the range of C_f, the C_f distributions show that C_f in region above the steps decreases when the jet angle β increases. The C_f of case ZMJ($\beta = 0°$) is always bigger than that of case ZMJ(off). C_f is decreased by ZMJ near the jet-exits when

$\beta = 60°$, $75°$. The effect of drag reduction between the pair of ZMJ when $\beta = 60°$ is slightly better than that when $\beta = 75°$. The C_f is proportional to β in the middle of each sections, but the C_f is inversely proportional to β in region above the steps.

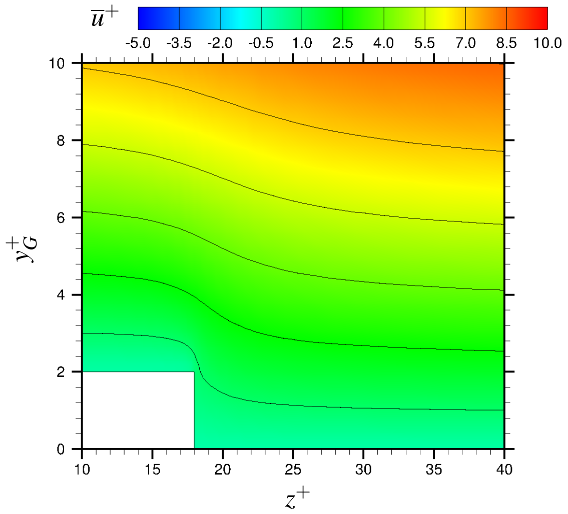

(a) ZMJ off

(b) ZMJ on, $\beta = 0°$

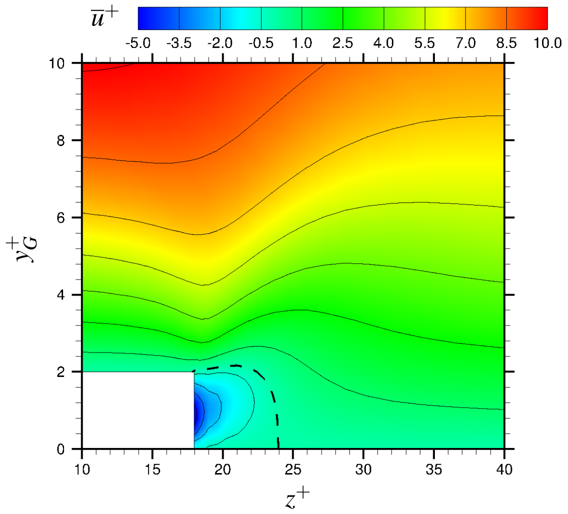

(c) ZMJ on, $\beta = 60°$

(d) ZMJ on, $\beta = 75°$

Figure 5.25 Contours of time and space averaged streamwise-velocity in the cross-stream ($y-z$ plane) view, zooming in the regions near the jet-exits. The black dashed line is $\overline{u}^+ = 0$.

Figure 5.25 shows contours of time and space averaged streamwise-velocity $\overline{u}^+$ in the cross-stream view near the left jet-exits with the same contour levels. The contour lines in region above the steps in case ZMJ(on) are more clustered than that in case ZMJ (off). The case ZMJ($\beta = 0°$) is the most clustered among $\beta = 0°$, $60°$, $75°$. From the figures, it can be observed that the high velocity fluid is brought down by ZMJ. When $\beta = 0°$, the fluid speed near the jet-exits is increased by ZMJ. However, when $\beta = 60°$, $75°$, the fluid speed is reduced near the jet-exits because of the countering jets. The black dashed lines show the regions where the averaged streamwise-velocity is negative. The region when $\beta = 60°$ is wider than that when $\beta = 75°$ in the spanwise direction, but the region when $\beta = 60°$ is shorter than that when $\beta = 75°$ in the wall-normal direction.

Figure 5.26 represents that ZMJ not only influences the viscous sublayer but also the buffer layer and log-law region. As discussed in section 5.4, the ZMJ influence on the velocity profiles is limited near the jet-exits, when the jets are off in the controlled channel.

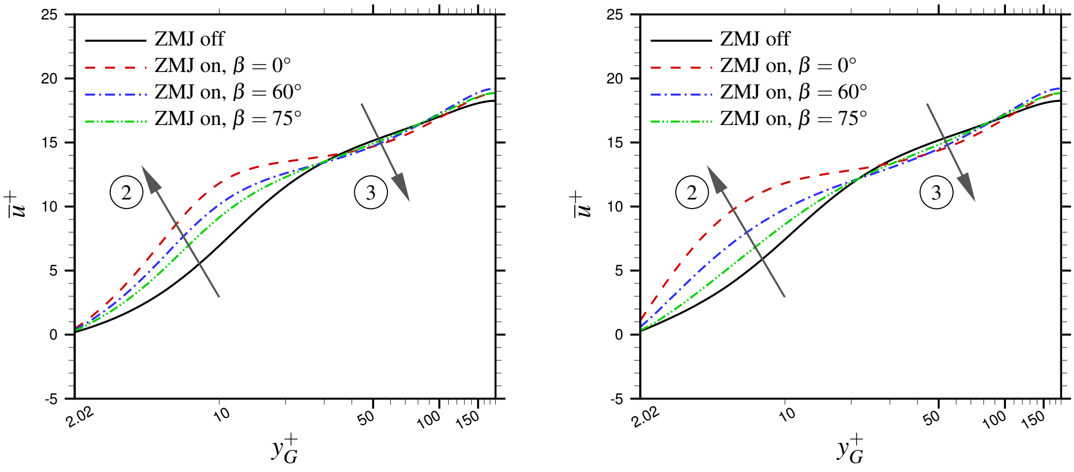

(a) $z^+ = 0.1$

(b) $z^+ = 17$

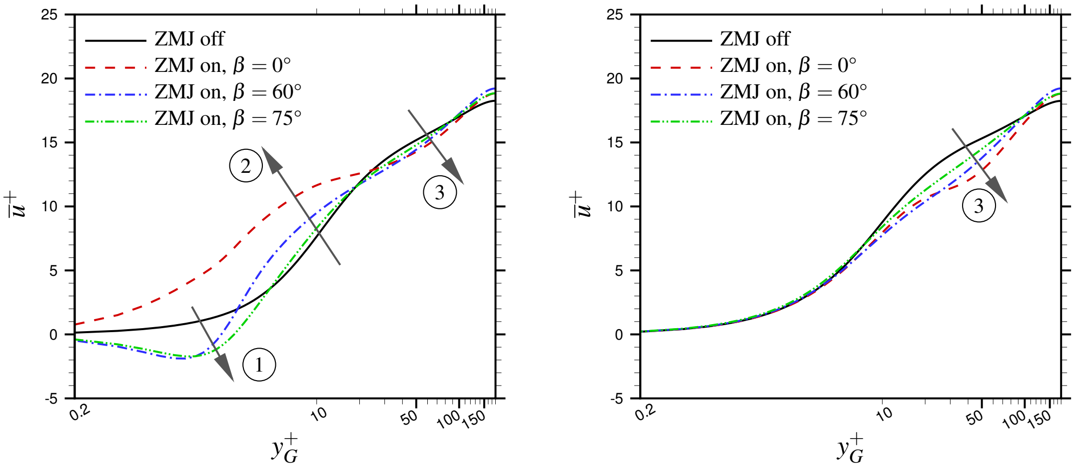

(c) $z^+ = 20$

(d) $z^+ = 62.83$

Figure 5.26 Comparisons of time and space averaged streamwise-velocity profiles at different spanwise positions, covering the height ranges of a half channel.

Therefore, when the jets are on, the influences on the streamwise-velocity profiles in the buffer region and log-law region are given by ZMJ.

Figure 5.26c compares time and space averaged streamwise velocity $\overline{u}^+$ profiles near the left jet-exits, showing the profiles are shifted by ZMJ at three positions ①, ② and ③. The shift ① is because of the countering jets created by ZMJ, as discussed before. Figures 5.26a, 5.26b and 5.26d display that the shift ① does not appear in region above the steps and in the middle of each sections. To understand the shifts ② and ③, it is better to go back and look the flow movements in figure 5.19. The flow is driven up in the middle of each sections, and is brought down at the sides of each sections. The upwards movements in the middle of each sections bring the fluid of low velocity from the wall to the channel centre, reducing the streamwise velocity in the log-law region and creating the shift ③. The downwards movements in region above the steps take the fluid of high velocity from the channel centre towards the steps, increasing the streamwise velocity and creating the shift ②. The strengths of shifts ② ③ depend on the spanwise averaged-velocity of ZMJ, so case ZMJ($\beta = 0°$) shifts the most. The shift ③ in the middle of each sections is the strongest and extends the influence to the sides of each sections. Since the jets flow out from the jet-exits and move obliquely upward in the spanwise direction, ZMJ is too weak to influence the viscous sublayer in the middle of each sections, so there is not shift ① at $z^+ = 62.83$. The buffer layer mainly merges the velocity between the viscous sublayer and log-law region, so the shift ② does not exist in the middle of each sections.

During the simulation, the mass flux of controlled channel should be a constant. The initial mass-flux of the controlled channel is equal to initial mass-flux of the smooth channel .

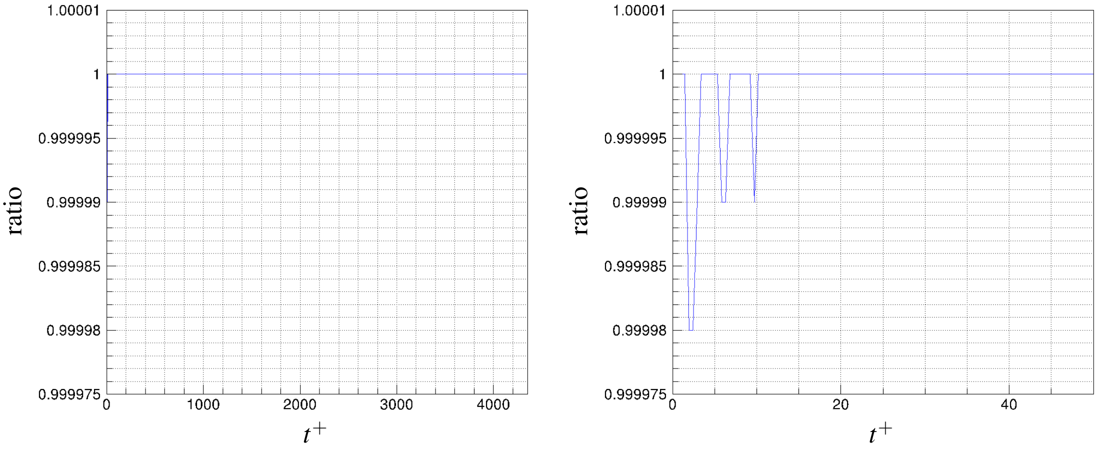

(a) Whole time

(b) Beginning time

Figure 5.27 History of the ratio of instantaneous mass-flux to initial mass-flux.

Figure 5.27 shows that the instantaneous mass-flux is smaller than initial mass-flux at the beginning steps, but the maximum difference is 0.002%. This means that the mass flux can be considered as a constant in the simulations.

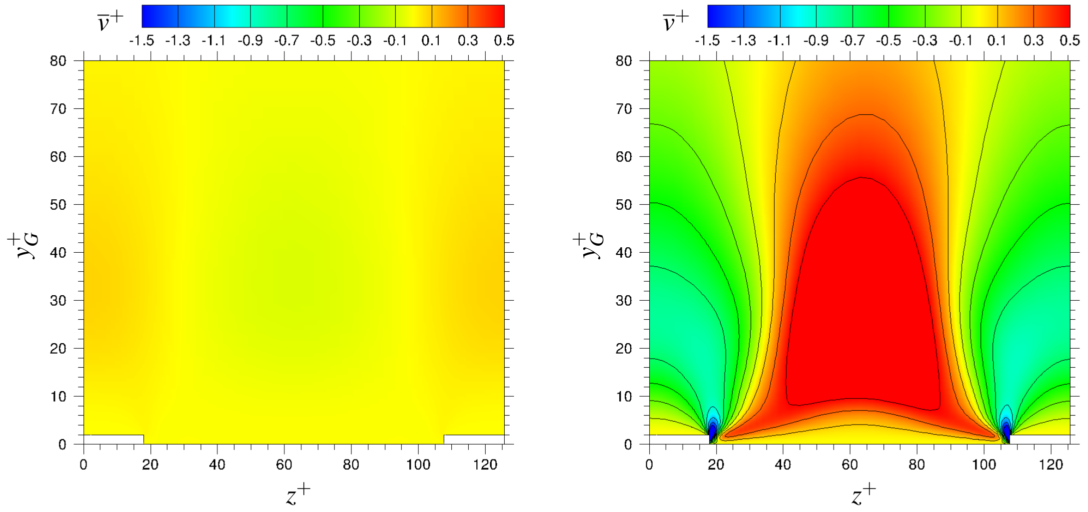

(a) ZMJ off

(b) ZMJ on, $\beta = 0°$

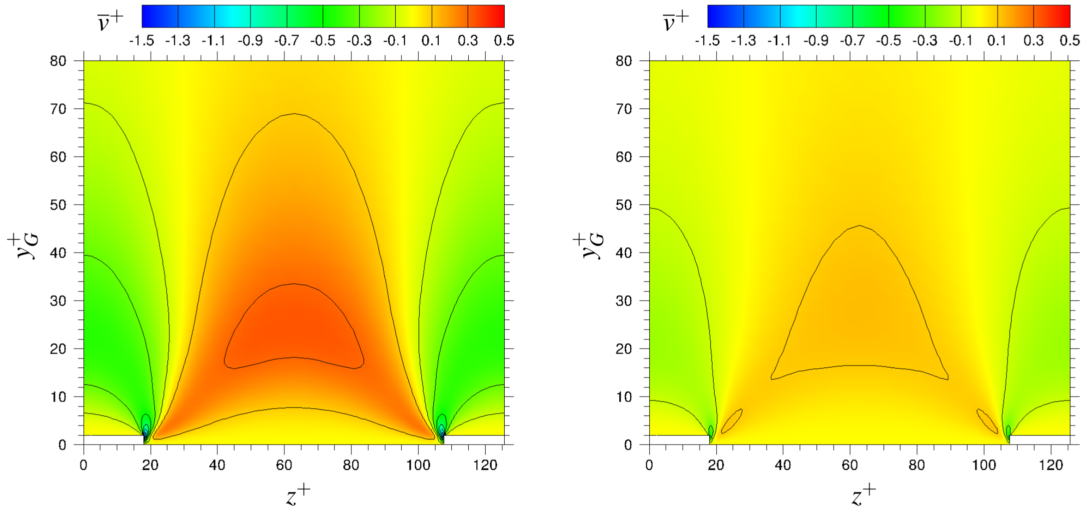

(c) ZMJ on, $\beta = 60°$

(d) ZMJ on, $\beta = 75°$

Figure 5.28 Cross-stream ($y-z$ plane) view of time and space averaged wall-normal-velocity $\overline{v}^+$ with contours.

The contour plots of time and space averaged wall-normal velocity are shown in figure 5.28. When ZMJ is on, the wall-normal velocity is positive in section middle and is negative in section sides. The maximum value happens in section middle and minimum value is near jet-exits. Comparing cases ZMJ(on), the maximum value of case ZMJ($\beta = 0°$) is the biggest. Case ZMJ($\beta = 75°$) has the smallest value. Looking at both figures 5.19 and 5.28, it shows that the wall-normal velocity is related to the spanwise jet-velocity. High spanwise jet-velocity induces high wall-normal velocity.

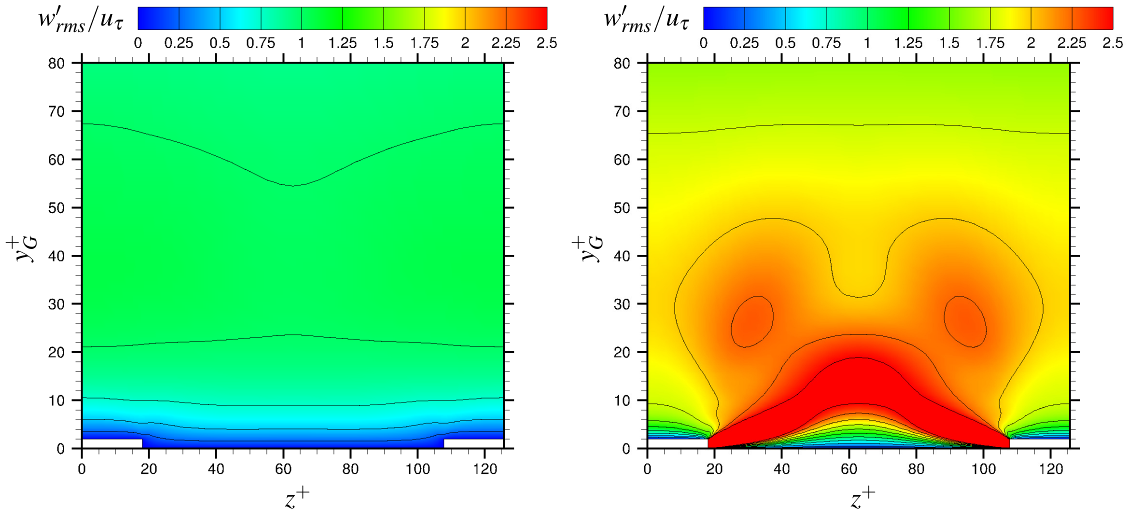

(a) ZMJ off

(b) ZMJ on, $\beta = 0°$

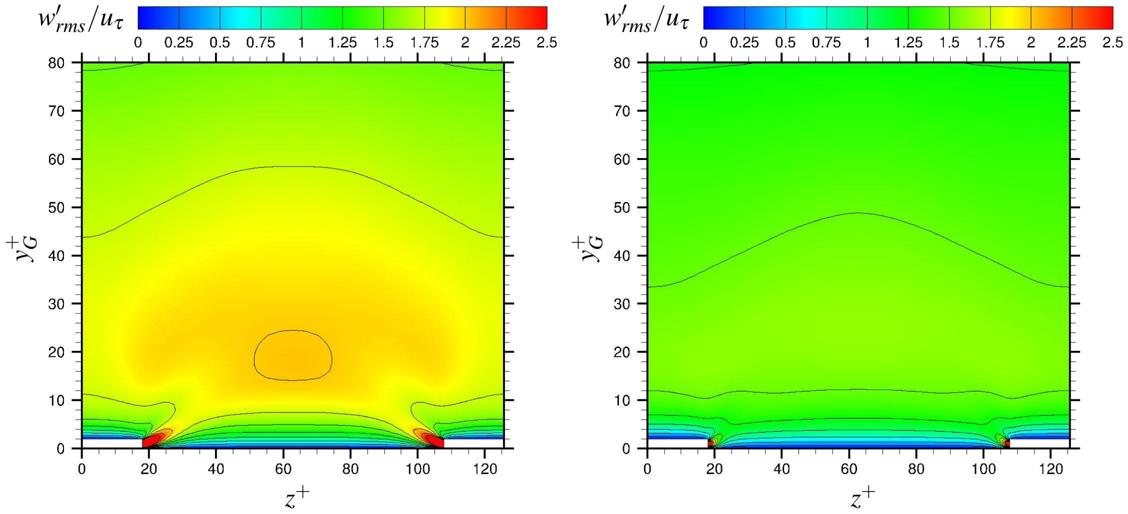

(c) ZMJ on, $\beta = 60°$

(d) ZMJ on, $\beta = 75°$

Figure 5.29 Contours of w'_{rms}/u_τ in the cross-stream ($y-z$ plane) view.

Figures 5.29, 5.30 and 5.31 represent the contours of the root-mean-square of w'/u_τ, v'/u_τ and u'/u_τ in the cross-stream ($y-z$ plane), respectively. These figures show the influence of ZMJ on the velocity fluctuations. In the controlled channel, the total velocity-fluctuations contain the periodic velocity and the pure turbulent fluctuation. Because the periodic velocity generated by ZMJ is treated as additional fluctuations for the time averaged results, the total velocity-fluctuations are strengthened by ZMJ, comparing to the case ZMJ(off). The fluctuating source is ZMJ at the jet-exits, and the fluctuating energy dissipates from the jet-exits to the channel centre, so the largest total velocity-fluctuations are at the jet-exits. Because ZMJ has periodic character, the fluctuations of time averaged results are symmetric in the spanwise direction.

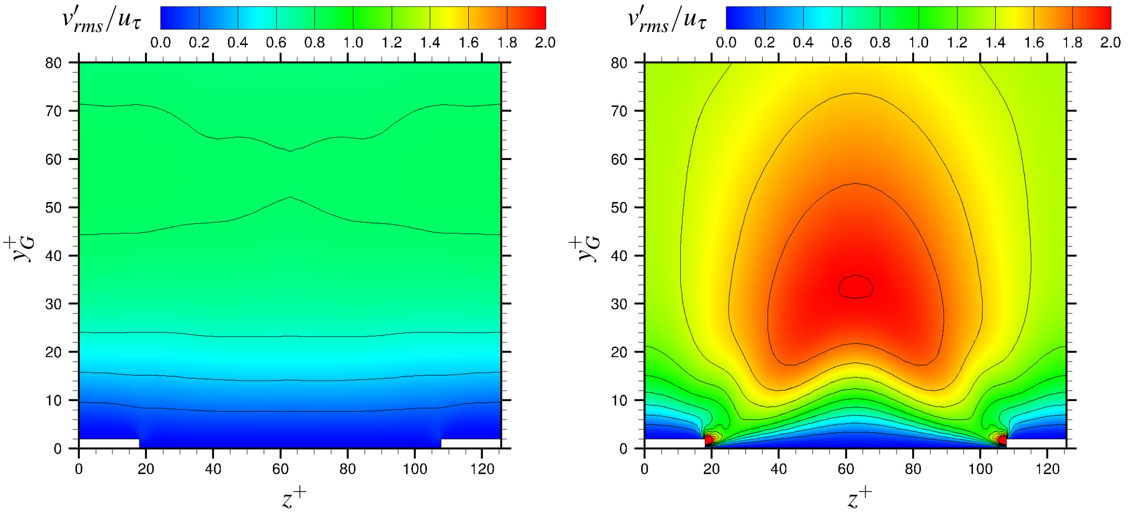

(a) ZMJ off (b) ZMJ on, $\beta = 0°$

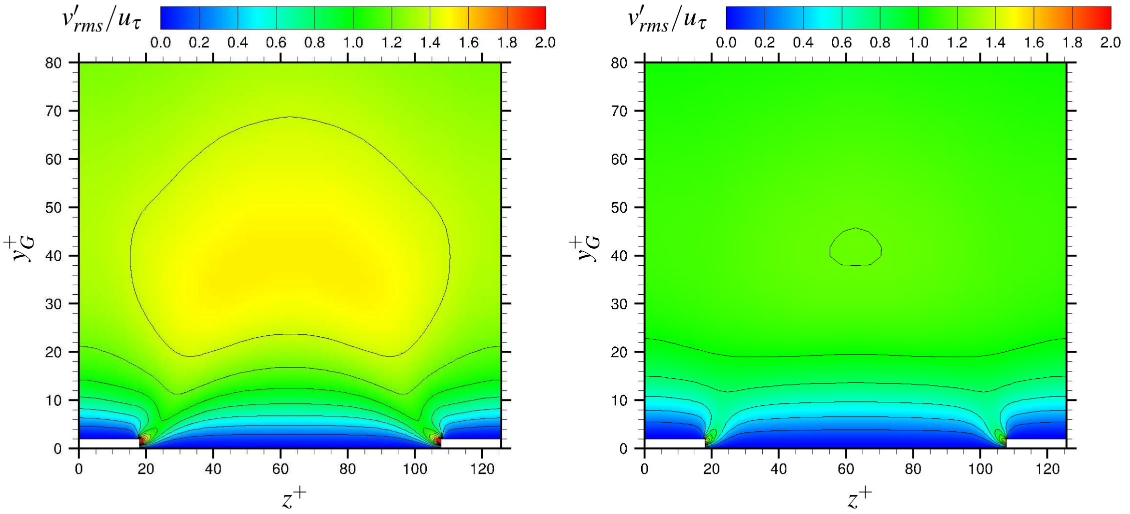

(c) ZMJ on, $\beta = 60°$ (d) ZMJ on, $\beta = 75°$

Figure 5.30 Contours of v'_{rms}/u_τ in the cross-stream ($y - z$ plane) view.

In figure 5.29, the spanwise-velocity fluctuations are mainly caused by the periodic spanwise-velocity of ZMJ, so the peak value of w'_{rms}/u_τ reduces from $\beta = 0°$ to $\beta = 75°$ due to the decrease of the fluctuating amplitude of $\widetilde{w}$. Looking at figure 5.19, the wall-normal velocity is related to the spanwise velocity. This means that the maximum fluctuating amplitude of v is proportional to that of w. So the peak value of v'_{rms}/u_τ is the largest when $\beta = 0°$ among $\beta = 0°$, 60° and 75°. Because the left and right flow-streams meet in the

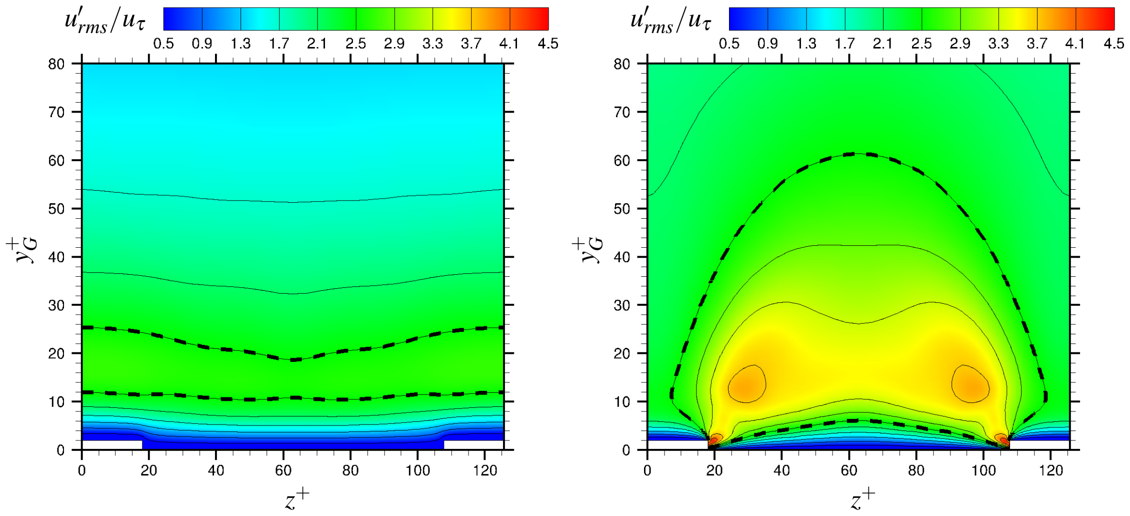

(a) ZMJ off

(b) ZMJ on, $\beta = 0°$

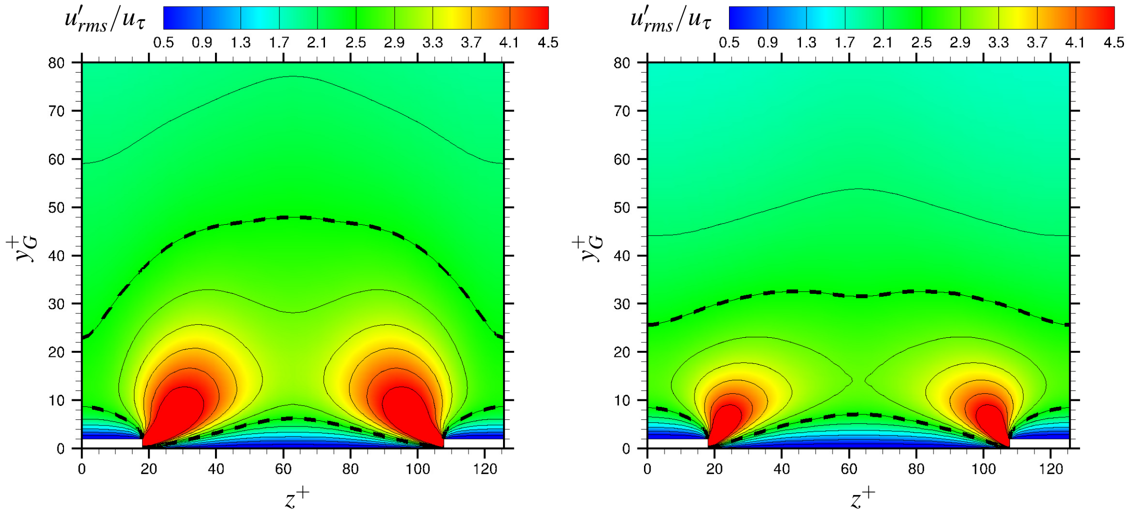

(c) ZMJ on, $\beta = 60°$

(d) ZMJ on, $\beta = 75°$

Figure 5.31 Contours of u'_{rms}/u_τ in the cross-stream ($y - z$ plane) view. The black dashed lines are $u'_{rms}/u_\tau = 2.5$.

middle of each sections, the influence of the wall-normal velocity is strengthened there. So there is a local peak in the middle of each sections, as displayed in figures 5.30b, 5.30c and 5.30d.

The streamwise-velocity fluctuation is the combined effects of the periodic velocity in three directions. The spanwise and wall-normal periodic velocities can shift the streamwise velocity and influence the streamwise-velocity fluctuations. This interaction between the periodic velocities will be discussed in the next section using the phase averaged results.

Figure 5.31b shows four local peaks in the contours plots. Two peak are at the jet-exits and two peaks are away from the jet-exits. Because ZMJ makes streamwise periodic-velocity at the jet-exits, two peaks at the jet-exits are directly generated by the oscillating jets in the streamwise direction. Away from the jet-exits, ZMJ oscillates the fluid in the streamwise direction relatively weak comparing to the region near the jet-exits, and the streamwise velocity-fluctuations are not mainly from the oscillating jets. The two peaks away from the jet-exits are mainly caused by the periodic fluid-motions in the spanwise and wall-normal directions.

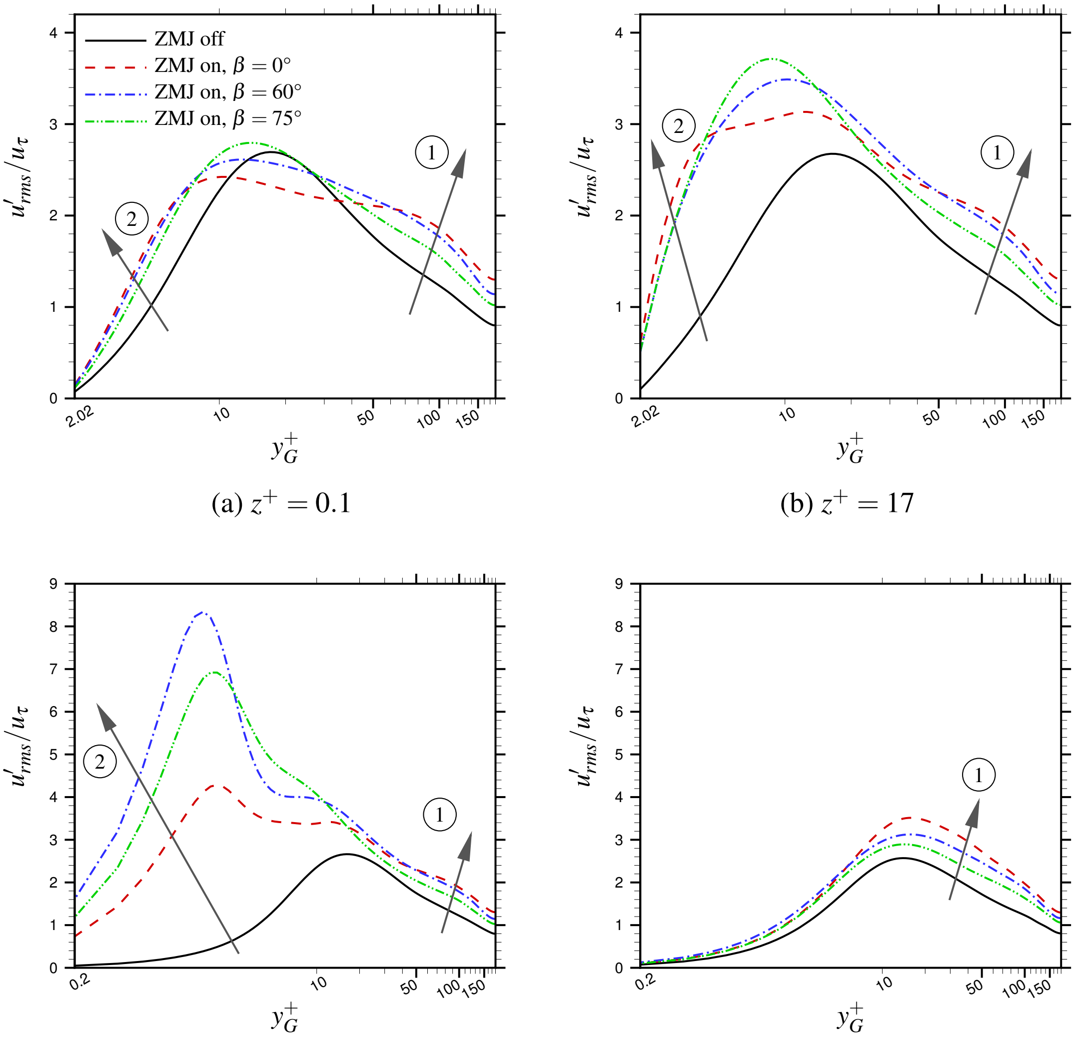

(a) $z^+ = 0.1$

(b) $z^+ = 17$

(c) $z^+ = 20$

(d) $z^+ = 62.83$

Figure 5.32 Comparisons of u'_{rms}/u_τ profiles at different spanwise positions, covering the height ranges of a half channel. Note, to clearly show the profile differences, the ranges of u'_{rms}/u_τ are different between (a),(b) and (c),(d).

When the jet angle changes from 0° to 60°, the spanwise and wall-normal periodic-velocities decrease, so the strength of streamwise-velocity fluctuations caused by the periodic fluid-motions in the spanwise and wall-normal directions decreases. However, the amplitude of the streamwise velocity at the jet-exits increases, so the strength of the oscillating jets is increased in the streamwise direction. This increases the strength of streamwise-velocity fluctuations at the jet-exits. The jets influence on the streamwise-velocity fluctuations is spread to the regions away from the jet-exits as well, and overtakes the influence from the spanwise and wall-normal periodic-motions. This phenomenon is shown in figure 5.31c.

When the jet angle is 75°, region where is $u'_{rms}/u_\tau > 4.5$ shrinks comparing figure 5.31c and figure 5.31d. The reason is that the spanwise strength of ZMJ drops due to the decrease of the jet spanwise-velocity. Although the streamwise-velocity fluctuations are increased at the jet-exits, the strength is not strong enough to keep the spread of the streamwise-velocity fluctuations as the same to case ZMJ($\beta = 60°$). Therefore, the area of region $u'_{rms}/u_\tau > 4.5$ when $\beta = 75°$ is smaller than that when $\beta = 60°$.

The region of $u'_{rms}/u_\tau > 2.5$ is crossed out by the black dashed lines in figure 5.31. The region area mainly depends on the positions of the upper dashed lines which are away from the jet-exits. The upper dashed lines are influenced by the spanwise strength of ZMJ. When the spanwise strength decreases, the middle of the upper dashed line drops its height, but the sides of the upper dashed line increase their heights.

Figure 5.32 compares the u'_{rms}/u_τ profiles at different spanwise positions. There are two shifts ① and ② in the viscous sublayer and log-law region, respectively. The buffer layer connects the viscous sublayer and log-law region. Shift ① is away from the jet-exits. The fluctuating strength of the streamwise velocity depends on the spanwise strength of ZMJ in that height ranges. The fluctuating strength increases from $\beta = 75°$ to 0° for all spanwise positions.

Shift ② is different from shift ①. The trend of the fluctuating strength is not the same at the different spanwise positions. In figure 5.32a, the shift ② is caused by the periodic motions of fluid in the viscous sublayer. The periodic motions depends on the spanwise strength of ZMJ, so case ZMJ($\beta = 0°$) has the biggest u'_{rms}/u_τ among the cases. Figure 5.32c compares the profiles of u'_{rms}/u_τ in the viscous sublayer to study shift ② near the jet-exits. In that region, the streamwise-velocity fluctuations u' are dominated by the streamwise periodic-velocity $\widetilde{u}$. Both the streamwise and spanwise periodic-velocity of ZMJ on the jet-exits boundary can decide the value of $\widetilde{u}$. Case ZMJ($\beta = 0°$) has the smallest $\widetilde{u}$ when ZMJ is on. Even case ZMJ($\beta = 0°$) has the biggest $\widetilde{w}$, the jet-exits cannot blow out big $\widetilde{u}$, so u'_{rms}/u_τ is the smallest for case ZMJ($\beta = 0°$). Comparing cases ZMJ($\beta = 60°$) and ZMJ($\beta = 75°$) for shift ② in figure 5.32c, the situation of case ZMJ($\beta = 75°$) is the opposite to that of case ZMJ($\beta = 0°$). Case ZMJ($\beta = 75°$) has bigger $\widetilde{u}$ than case ZMJ($\beta = 60°$) at the jet-exits, but $\widetilde{w}$ of case ZMJ($\beta = 75°$) is smaller than that of case ZMJ($\beta = 60°$). The jet-exits do not have enough spanwise strength to spread $\widetilde{u}$, so u'_{rms}/u_τ of case ZMJ($\beta = 75°$) is smaller than that of case ZMJ($\beta = 60°$). The shift ② in figure 5.32b is the status between the statuses at spanwise positions $z^+ = 0.1$ and $z^+ = 20$. Figure 5.32d shows that the streamwise-velocity fluctuations of cases ZMJ($\beta = 0°$), ZMJ($\beta = 60°$) and ZMJ($\beta = 75°$) almost dissipate to be in the same level in the viscous sublayer when the locations is in the middle of each sections. Even the fluctuations dissipate, the fluctuating levels in case ZMJ(on) are still higher than that in case ZMJ(off), because the flow is disturbed by ZMJ when ZMJ is on.

In figures 5.33, 5.34 and 5.35, the periodic velocity and pure turbulent fluctuations are separated from the total velocity fluctuations to study their contributions. There are some phenomenons among them. The root mean square of periodic velocity is the highest at the jet-exits, and becomes smaller and smaller away from the jet-exits. For the root mean square of pure turbulent fluctuations, the zones of high values are near wall but not on the jet-exits. When the jet angle becomes bigger, the zone of high influence becomes smaller. The periodic velocities from a pair of jet-exits interacts with each other when the jet angle is zero degree, but they are independent when the jet angle is 75 degrees. The strength of pure turbulent velocity are the strongest when the jet angle is zero degree, and is the weakest when the jet angle is 75 degrees.

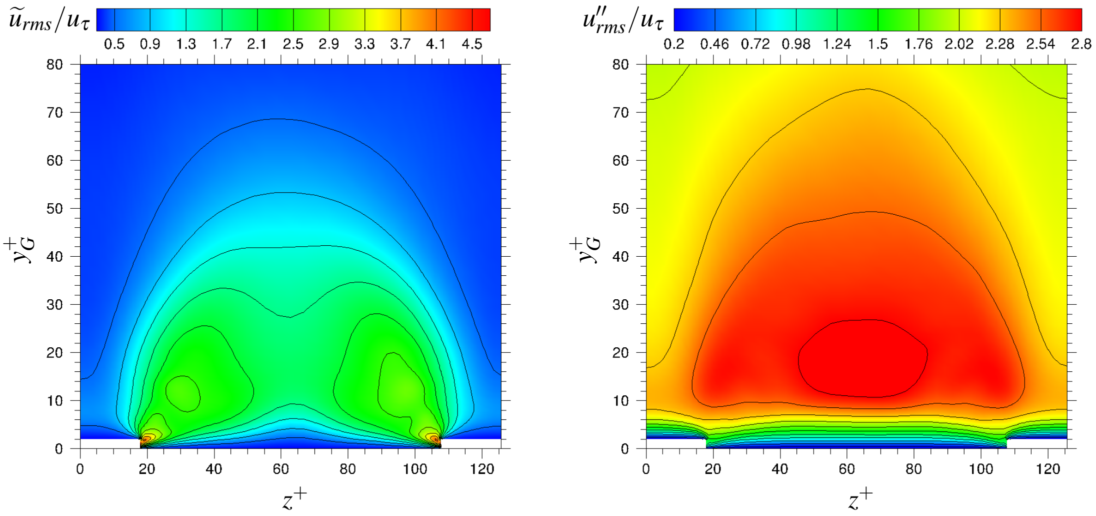

(a) ZMJ on, $\beta = 0°$, $\widetilde{u}_{rms}/u_\tau$ (b) ZMJ on, $\beta = 0°$, u''_{rms}/u_τ

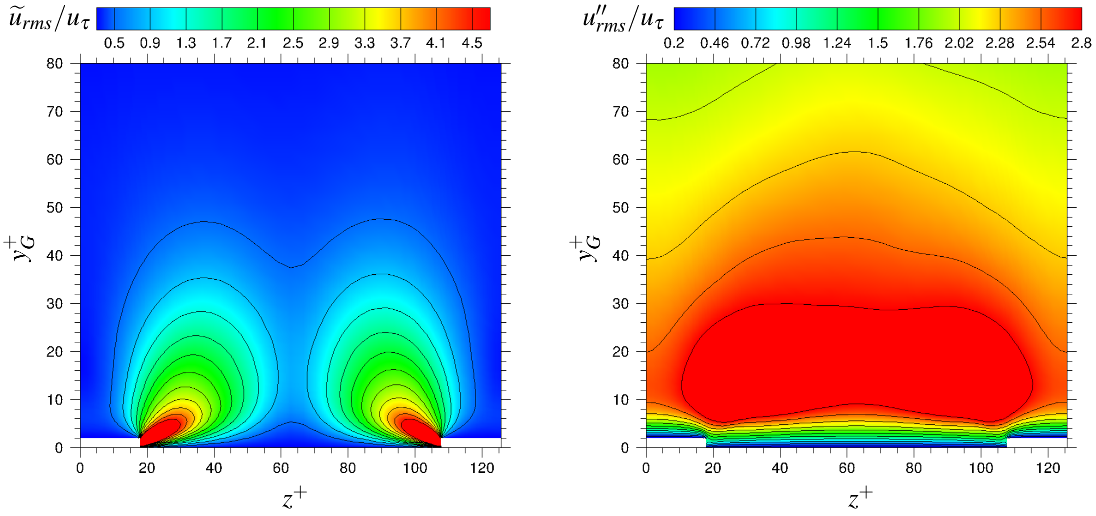

(c) ZMJ on, $\beta = 60°$, $\widetilde{u}_{rms}/u_\tau$ (d) ZMJ on, $\beta = 60°$, u''_{rms}/u_τ

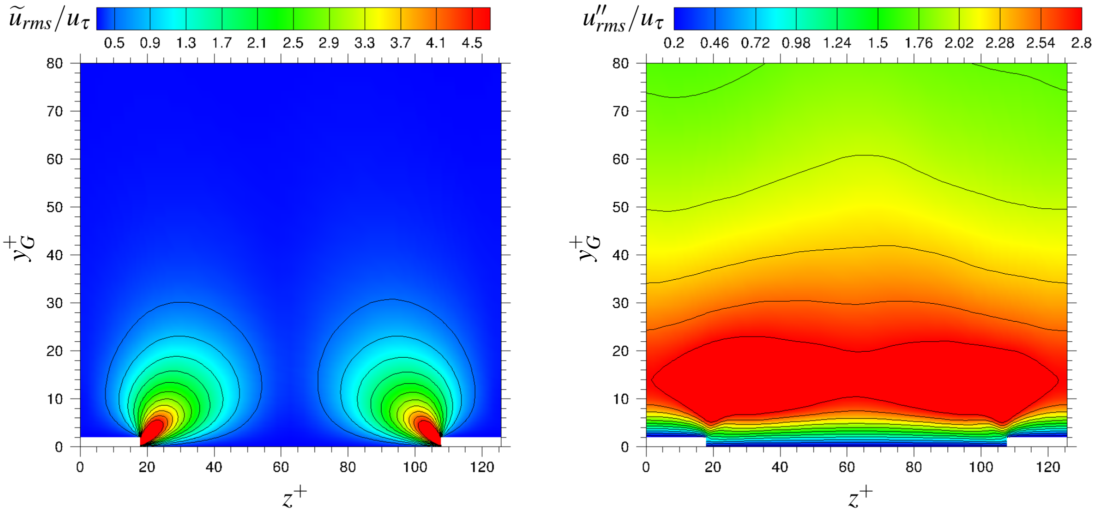

(e) ZMJ on, $\beta = 75°$, $\widetilde{u}_{rms}/u_\tau$ (f) ZMJ on, $\beta = 75°$, u''_{rms}/u_τ

Figure 5.33 The root mean square of streamwise-velocity fluctuations in the cross-stream ($y - z$ plane) view, including periodic velocity $\widetilde{u}$ and pure turbulent fluctuations u''.

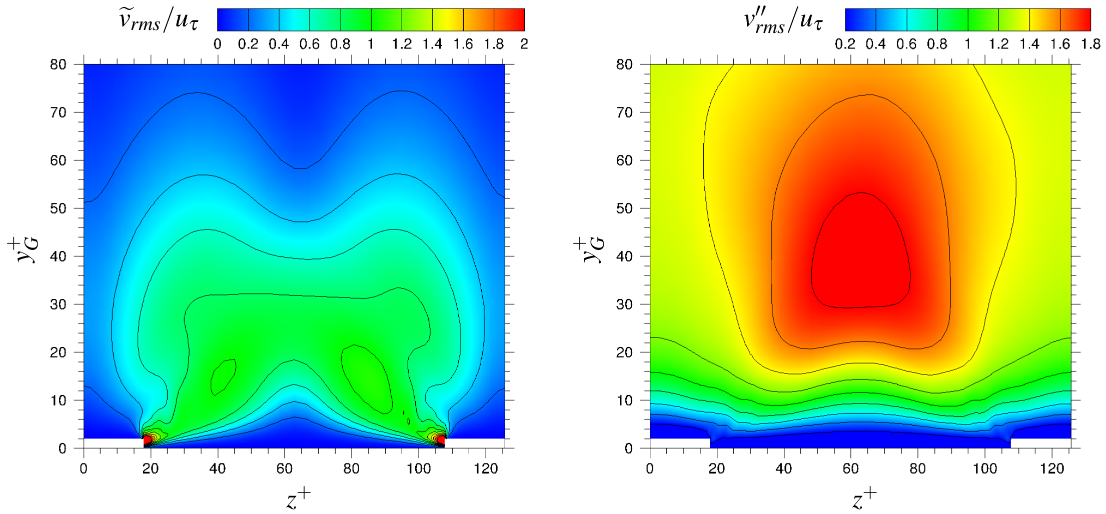

(a) ZMJ on, $\beta = 0^\circ$, $\widetilde{v}_{rms}/u_\tau$ (b) ZMJ on, $\beta = 0^\circ$, v''_{rms}/u_τ

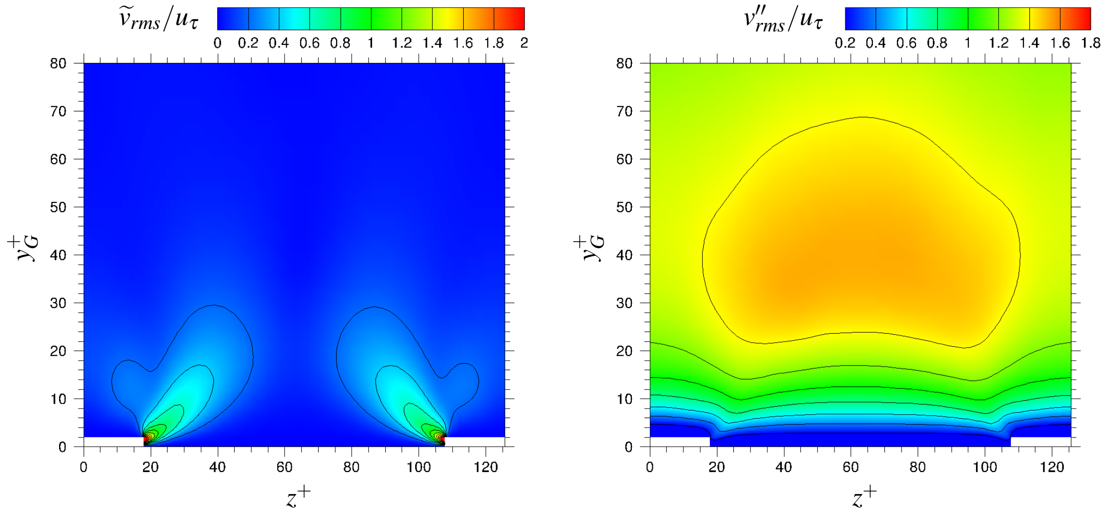

(c) ZMJ on, $\beta = 60^\circ$, $\widetilde{v}_{rms}/u_\tau$ (d) ZMJ on, $\beta = 60^\circ$, v''_{rms}/u_τ

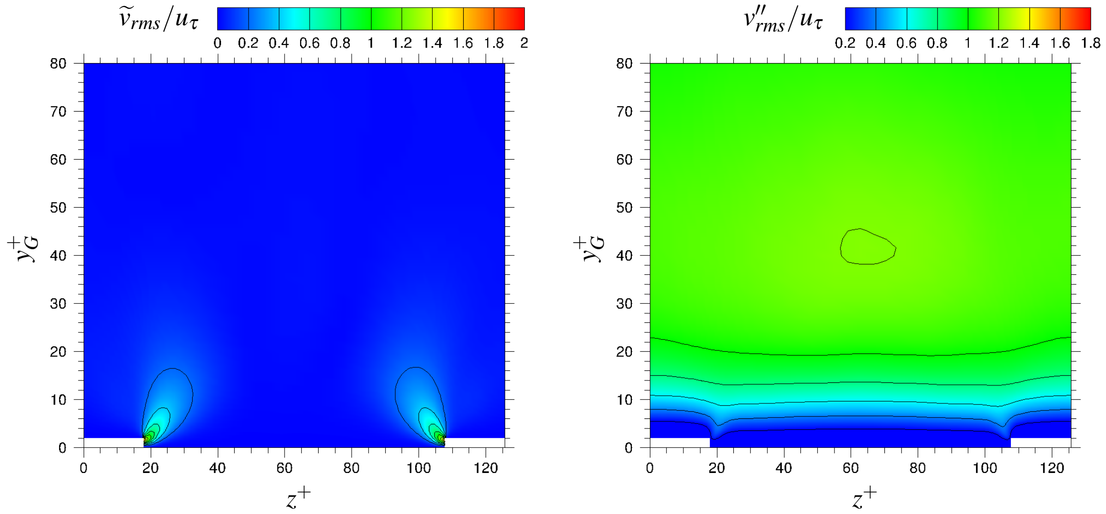

(e) ZMJ on, $\beta = 75^\circ$, $\widetilde{v}_{rms}/u_\tau$ (f) ZMJ on, $\beta = 75^\circ$, v''_{rms}/u_τ

Figure 5.34 The root mean square of wall-normal-velocity fluctuations in the cross-stream ($y - z$ plane) view, including periodic velocity $\widetilde{v}$ and pure turbulent fluctuations v''.

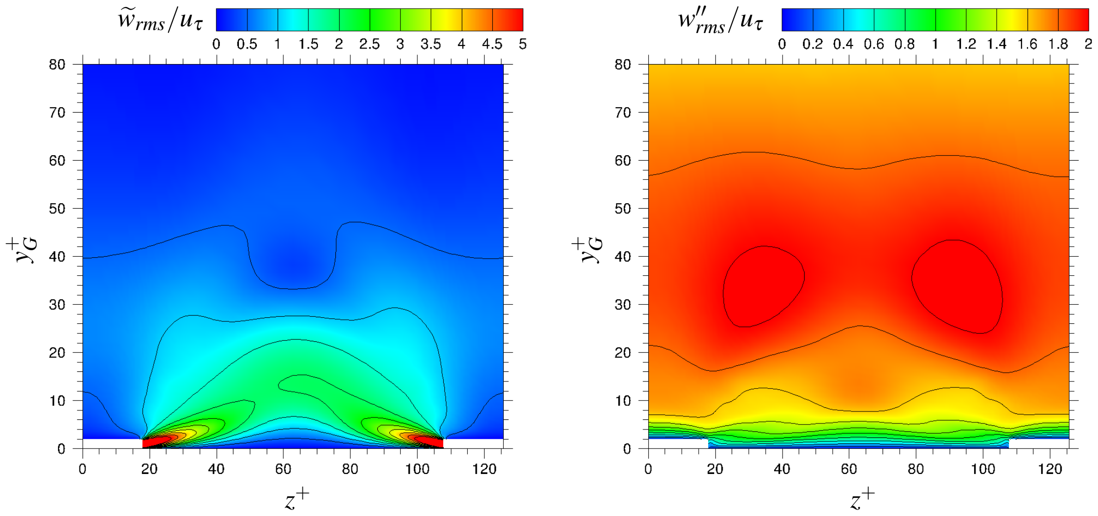

(a) ZMJ on, $\beta = 0°$, $\widetilde{w}_{rms}/u_\tau$

(b) ZMJ on, $\beta = 0°$, w''_{rms}/u_τ

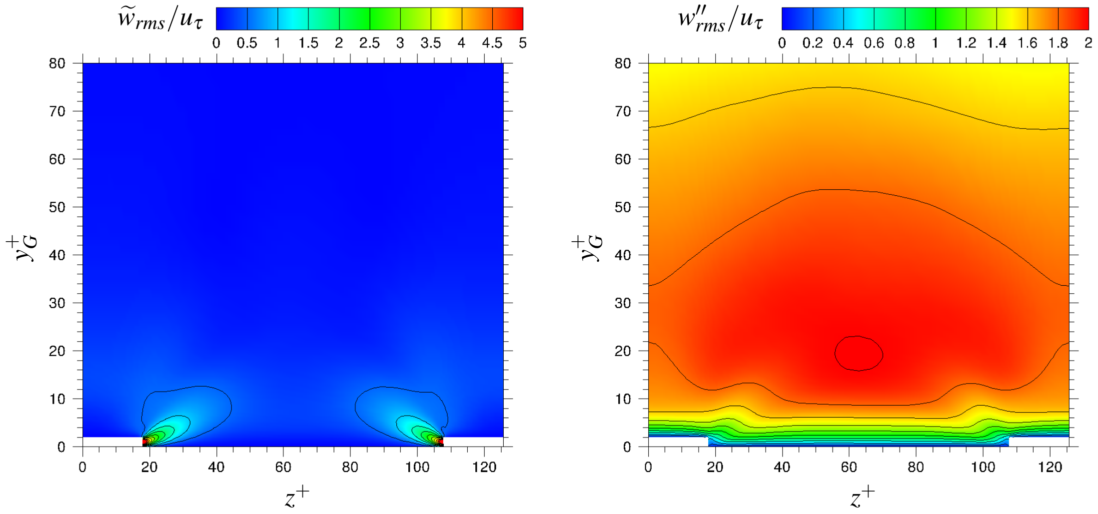

(c) ZMJ on, $\beta = 60°$, $\widetilde{w}_{rms}/u_\tau$

(d) ZMJ on, $\beta = 60°$, w''_{rms}/u_τ

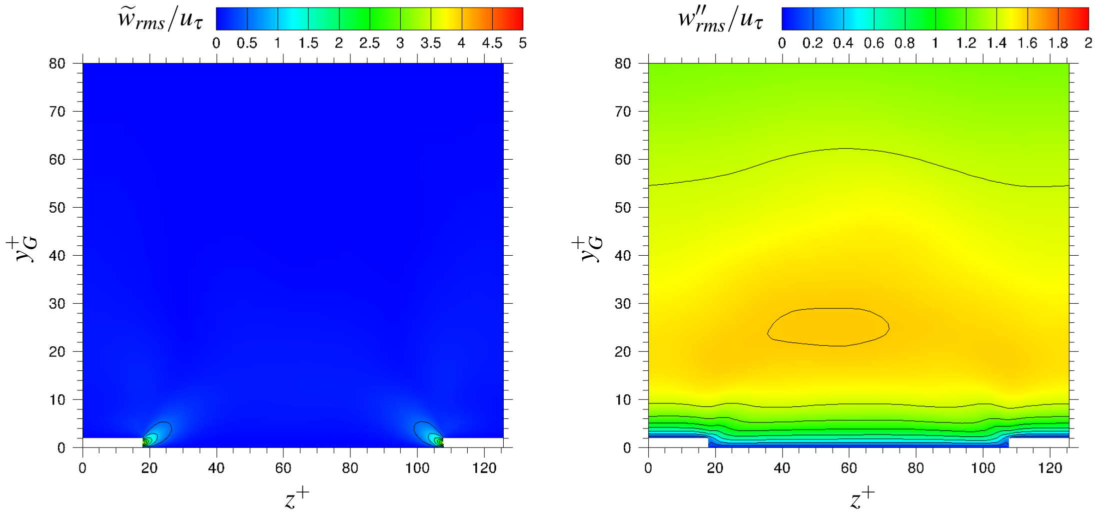

(e) ZMJ on, $\beta = 75°$, $\widetilde{w}_{rms}/u_\tau$

(f) ZMJ on, $\beta = 75°$, w''_{rms}/u_τ

Figure 5.35 The root mean square of spanwise-velocity fluctuations in the cross-stream ($y-z$ plane) view, including periodic velocity $\widetilde{w}$ and pure turbulent fluctuations w''.

Figures 5.36, 5.37 and 5.38 show the contour plots of the Reynolds shear stresses $\overline{u'w'}$, $\overline{v'w'}$ and $\overline{u'v'}$ which are nondimensionalized by u_τ^2. These compare cases ZMJ(off) and ZMJ($\beta = 0°$, $60°$, $75°$). As shown in the figures, the contour lines of $\overline{u'w'}$ and $\overline{v'w'}$ are z-symmetric. The left and right signs of the quantity values are opposite. The z-symmetric reason has been discussed in the section 5.4. When the jet-angle increases, the regions of high values shrink to the jet-exits due to the decrease of the spanwise jet-speed. From the figures, the signs of the $\overline{u'w'}$ or $\overline{v'w'}$ above the jet-exits are the opposite to that near the jet-exits. The reason is that the signs of w' are the opposite in the left and right parts of a section, and the

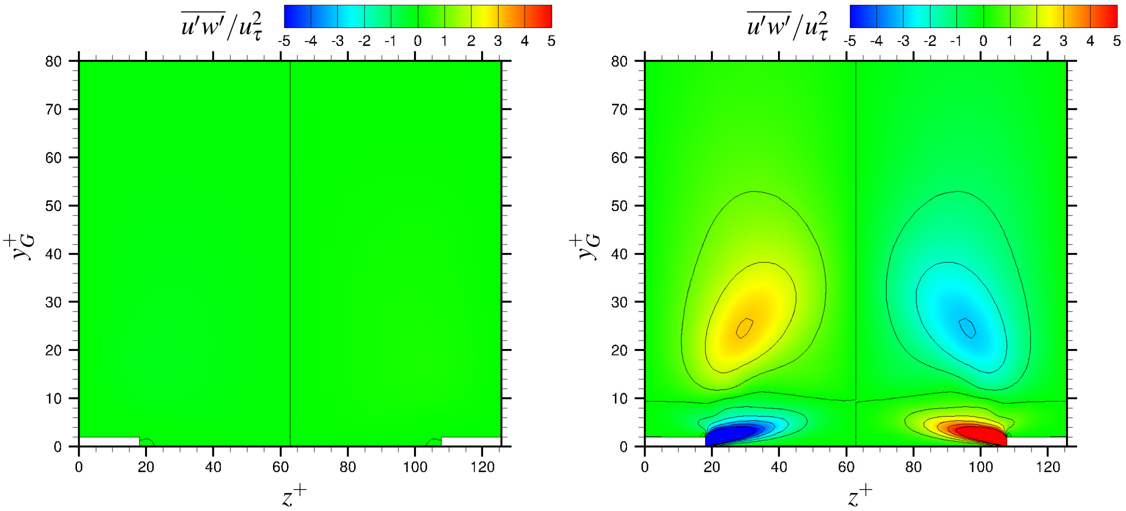

(a) ZMJ off

(b) ZMJ on, $\beta = 0°$

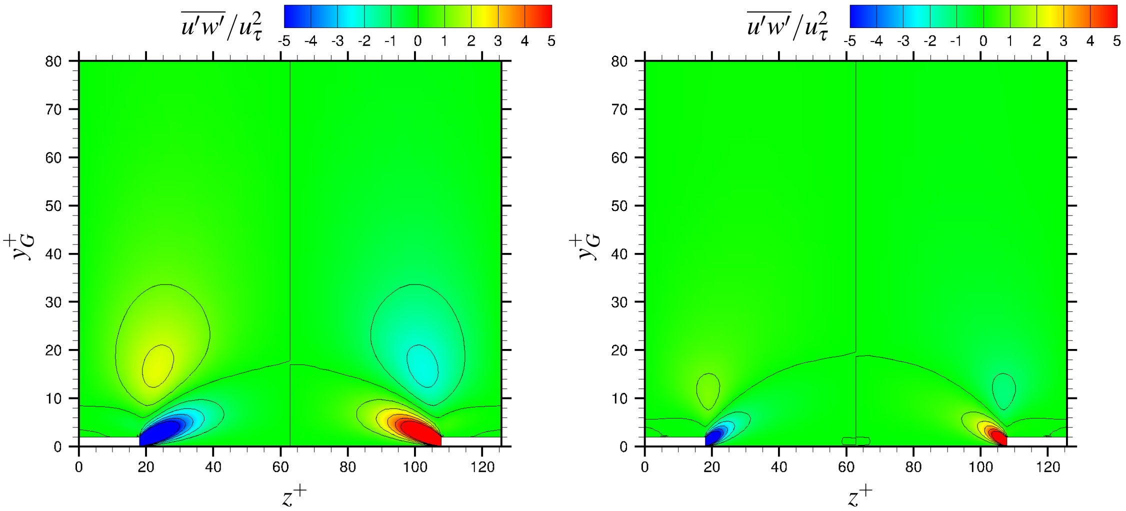

(c) ZMJ on, $\beta = 60°$

(d) ZMJ on, $\beta = 75°$

Figure 5.36 Contours of $\overline{u'w'}/u_\tau^2$ in the cross-stream ($y - z$ plane) view.

signs of u' and v' are the same. Since the integrations of $\overline{u'w'}$ and $\overline{v'w'}$ are zero in a section, the time averaged influences of $\overline{u'w'}$ and $\overline{v'w'}$ should be zero for a whole channel.

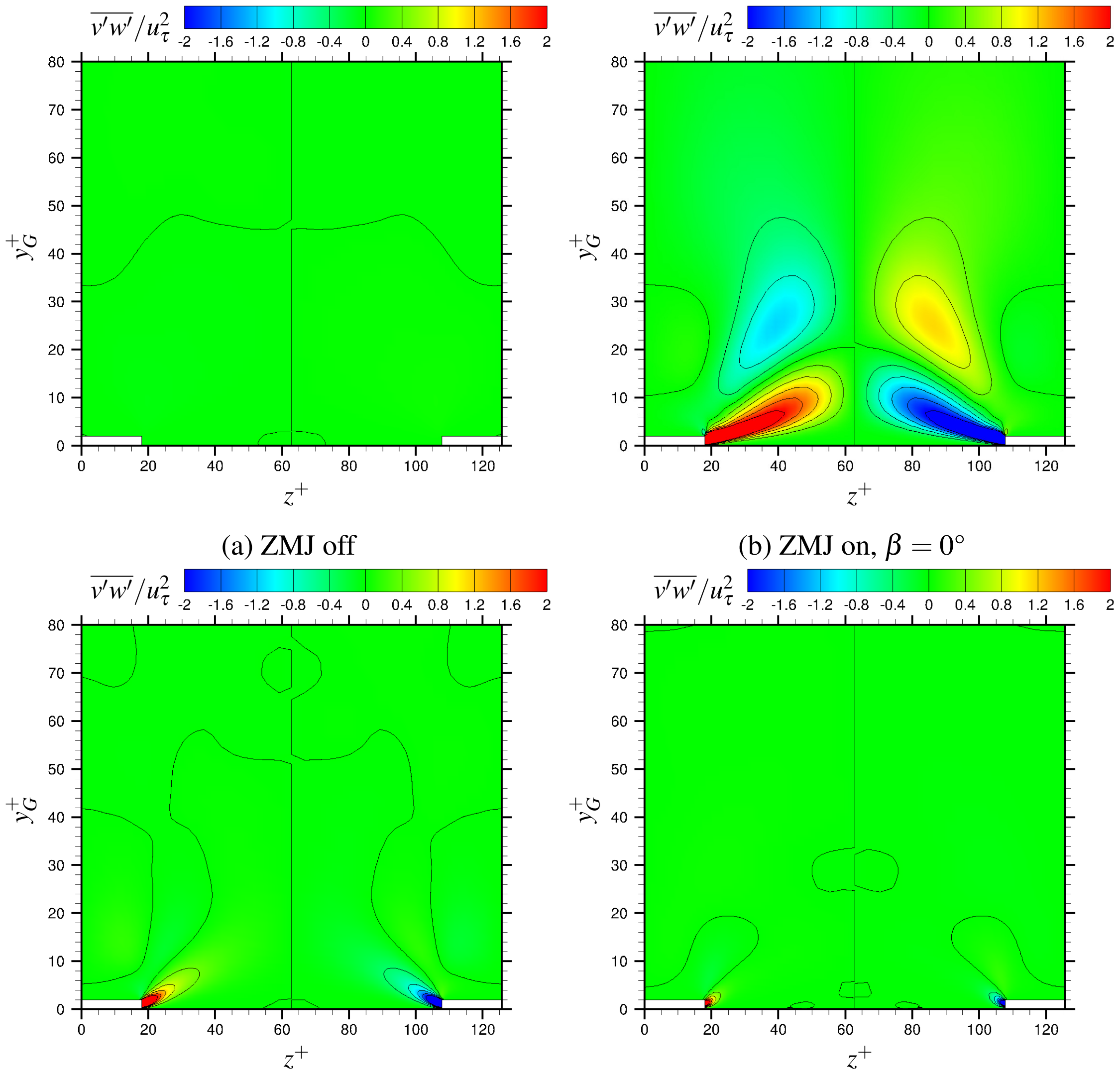

(a) ZMJ off

(b) ZMJ on, $\beta = 0°$

(c) ZMJ on, $\beta = 60°$

(d) ZMJ on, $\beta = 75°$

Figure 5.37 Contours of $\overline{v'w'}/u_\tau^2$ in the cross-stream ($y - z$ plane) view.

As shown in figure 5.38, the Reynolds shear stress $\overline{u'v'}$ cannot be cancelled in the time averaged results, which is unlike $\overline{u'w'}$ and $\overline{v'w'}$. Because the integration of $\overline{u'v'}$ cannot be zero in a section. Comparing the cases ZMJ(off) and ZMJ(on), ZMJ significantly changes the distribution of $\overline{u'v'}$. According to the FIK analysis [27], the increase of Reynolds shear stress would increase the friction drag in the flow. Therefore, if here was no other reason to reduce the friction drag in the controlled channel, the friction drag would not be reduced. In the controlled channel, the countering jets created by ZMJ can reduce the friction drag, so there is a possibility to overcome the increased drag caused by the increase of the Reynolds shear stress. In figure 5.38, the case ZMJ($\beta = 0°$) has the largest Reynolds shear stress in the centre of each sections. When the jet angle β increases, the Reynolds shear stress decreases, the strength of the countering jets increases. When $\beta = 75°$, the friction drag can be decreased by ZMJ.

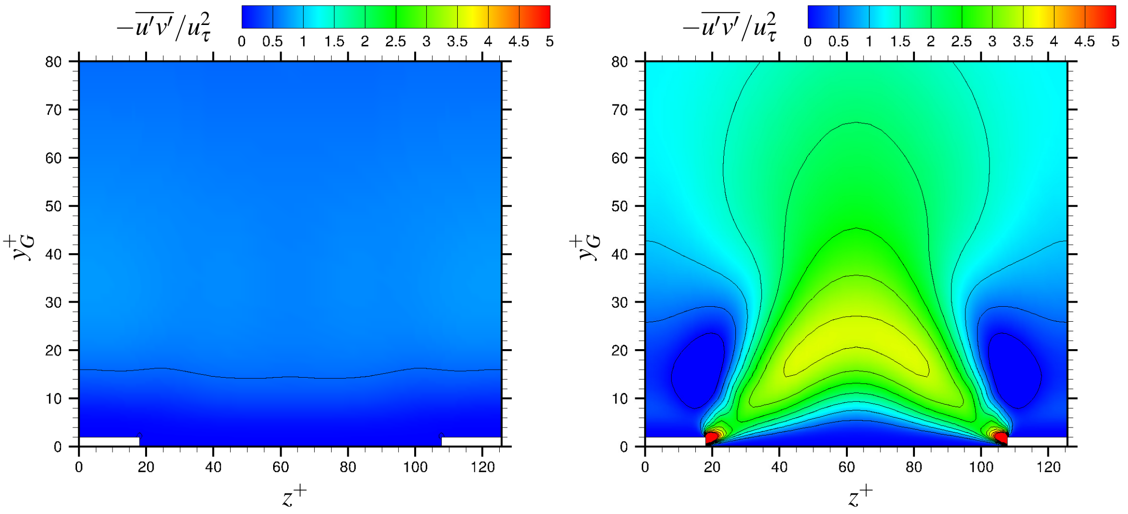

(a) ZMJ off

(b) ZMJ on, $\beta = 0°$

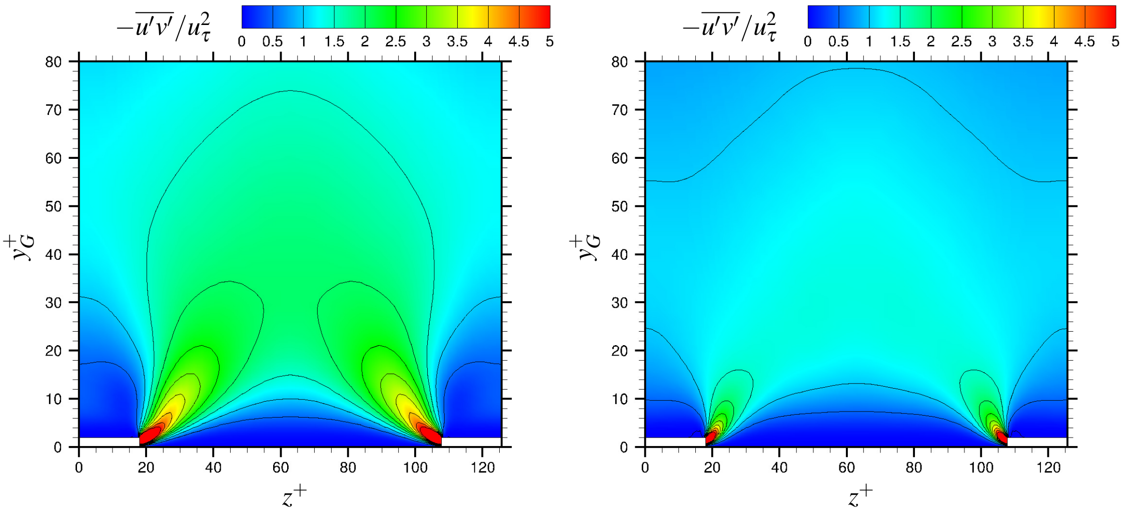

(c) ZMJ on, $\beta = 60°$

(d) ZMJ on, $\beta = 75°$

Figure 5.38 Contours of $-\overline{u'v'}/u_\tau^2$ in the cross-stream ($y-z$ plane) view.

Figure 5.39 compares the profiles of the Reynolds shear stress $-\overline{u'v'}$ at different spanwise positions. There are three shifts ①, ②, ③. Shift ① makes case ZMJ($\beta = 0°$) have the largest $-\overline{u'v'}$ among the cases. In contrast, Shift ② causes that the smallest $-\overline{u'v'}$ is in case ZMJ($\beta = 0°$). As shown in figure 5.36c, case ZMJ($\beta = 60°$) has the biggest $-\overline{u'v'}$ in the viscous sublayer near the jet-exits due to shift ③. The reason of shift ③ is the same as that explained for the shift ② in figure 5.32c.

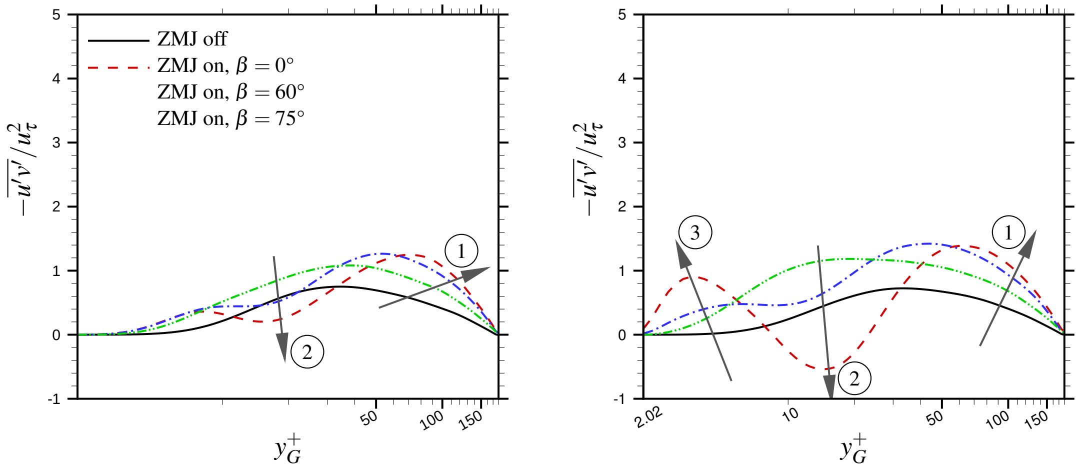

(a) $z^+ = 0.1$ (b) $z^+ = 17$

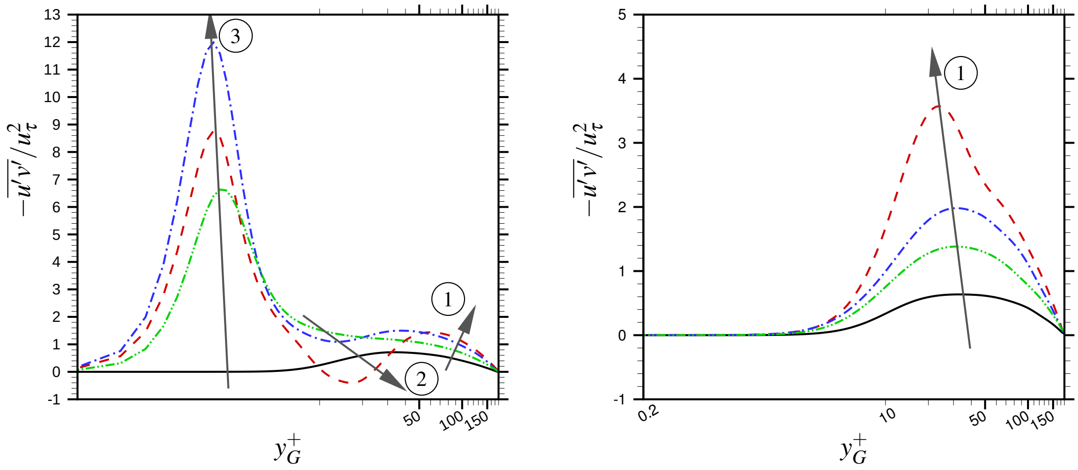

(c) $z^+ = 20$ (d) $z^+ = 62.83$

Figure 5.39 Comparisons of $-\overline{u'v'}/u_\tau^2$ profiles at different spanwise positions, covering the height ranges of a half channel. Note, to clearly show the profile differences, the ranges of $-\overline{u'v'}/u_\tau^2$ is different in (c).

The joint probability density function (JPDF) $P(u'^+, v'^+)$ and covariance integrand $u'^+v'^+P(u'^+, v'^+)$ are used to study the Reynolds shear stress $\overline{u'v'}$ at the position ($y_L^+ = 30$, $z^+ = 20$), as displayed in figure 5.40. The left figures show that all highest values of the JPDF are in the same quadrant that is Q4. The JPDF distributions are expanded by ZMJ. Since case ZMJ($\beta = 0°$) has the strongest spanwise-strength of ZMJ to enlarge the fluctuating ranges of u'^+ and v'^+, case ZMJ($\beta = 0°$) has the largest area of region $P(u'^+, v'^+) > 10\%$ among the cases. When the jet angle β is from 0° to 75°, the shape of JPDF distribution is twisted anticlockwise. The inclined angle of the distribution reduces. This means that the level of cross-correlation between u'^+ and v'^+ reduces. So case ZMJ($\beta = 0°$) has the strongest correlation between u'^+ and v'^+ at ($y_L^+ = 30$, $z^+ = 20$). The right figures show that the ejections and sweeps dominate the contributions for the Reynolds shear stress $\overline{u'v'}$. The comparison of the covariation integrands shows that the sweeps becomes more important when the jet angle is from $\beta = 0°$ to 75°. The right figures also displays that the position of the highest value of $u'^+v'^+P(u'^+, v'^+)$ becomes closer to the original point $(u'^+ = 0, v'^+ = 0)$, when the jet angle increases. This causes that the integration of $u'^+v'^+P(u'^+, v'^+)$ becomes smaller, reducing the value $-\overline{u'v'}$. The consequence is shift ① in figure 5.39d.

Figure 5.41 shows $P(u'^+, v'^+)$ and $u'^+v'^+P(u'^+, v'^+)$ at the position $(y_L^+ = 20, z^+ = 0.1)$. There is a JPDF difference between the cases ZMJ(off) and ZMJ(on). The highest probability happens in Q4 quadrant in case ZMJ(off), but the highest probability is in Q1 quadrant in case ZMJ(on). The reason is that the flow moves downwards at that position in case ZMJ(off), but the flow moves upwards in case ZMJ(on), as shown in figure 5.19. The downward and upward motions bias v' to be negative and positive, respectively. When the jet angle β increases from 0° to 75°, the strength of the upward motions reduces, so the position of the highest moves closer to the axis of $v'^+ = 0$ in Q1 quadrant $(u'^+ > 0, v'^+ > 0)$. The value of $u'^+v'^+$ is positive in Q1 quadrant, giving positive contributions to $\overline{u'v'}$. When the jet angle increases, the level of covariance integrand becomes smaller in Q1 quadrant. This causes the increase of $-\overline{u'v'}$, resulting with shift ② in figure 5.39a.

In figure 5.42, $P(u'^+, v'^+)$ and $u'^+v'^+P(u'^+, v'^+)$ show the flow status at the position $(y_L^+ = 1, z^+ = 20)$. Comparing the cases ZMJ(off) and ZMJ(on), the ranges of the velocity fluctuations in case ZMJ(on) are significantly larger than that in case ZMJ(off) due to the periodic velocities near the jet-exits. The ejections and sweeps which are caused by ZMJ almost dominate all the fluid motions when ZMJ is on. The case ZMJ($\beta = 60°$) has the largest area of the JPDF region $P(u'^+, v'^+) > 10\%$ among all the cases, resulting with the largest value of $-\overline{u'v'}$. When ZMJ blows out fluid from the jet-exits, the fluid is driven upwards and the streamwise velocity is reduced, giving the ejections in Q2 quadrant. When the jet sucks in fluid, the wall-normal velocity is negative and the streamwise velocity is increased, creating the sweeps in Q4 quadrant. Therefore, ZMJ creates large Reynolds shear stress near the jet-exits. The strengths of the periodic velocities control the peak value of $-\overline{u'v'}$, giving shift ③ in figure 5.39c.

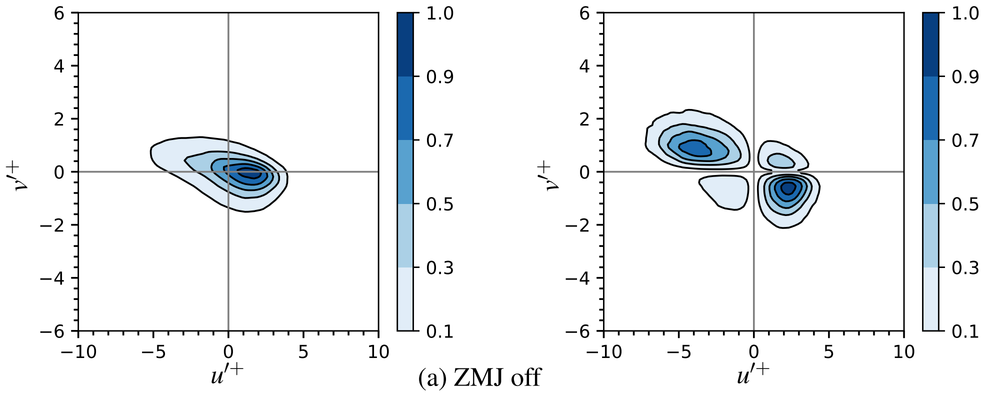

(a) ZMJ off

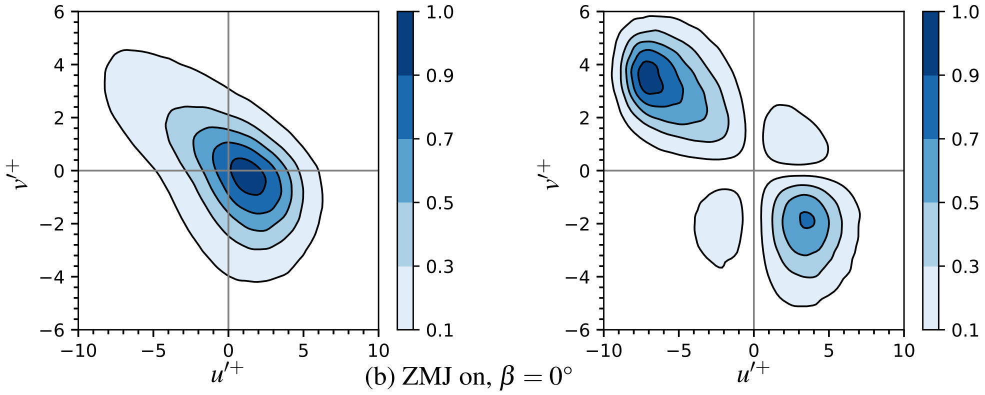

(b) ZMJ on, $\beta = 0°$

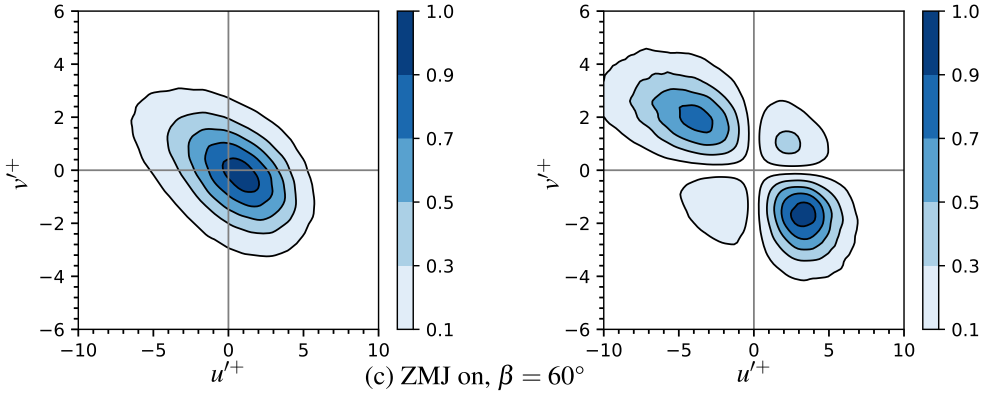

(c) ZMJ on, $\beta = 60°$

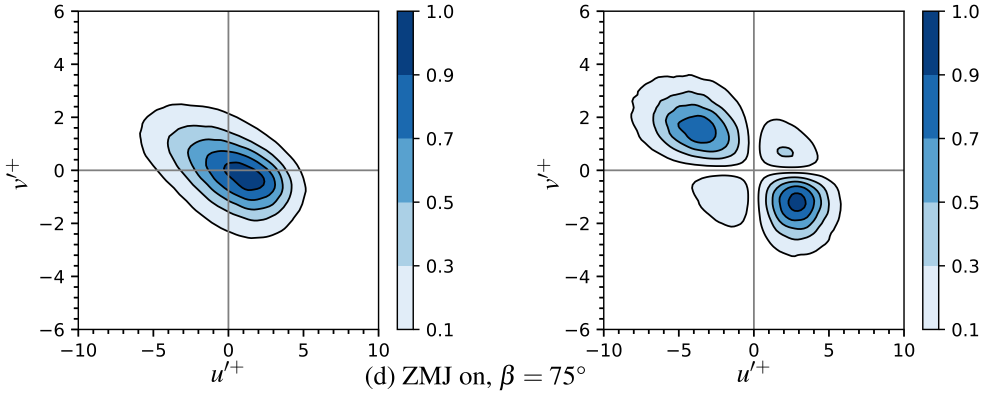

(d) ZMJ on, $\beta = 75°$

Figure 5.40 The joint probability density function $P(u'^+, v'^+)$ (left) and covariance integrand $u'^+ v'^+ P(u'^+, v'^+)$ (right) at $(y_L^+ = 30, z^+ = 62.83)$, giving $10, 30, 50, 70$ and 90% of the maximum probability level or covariance integrand.

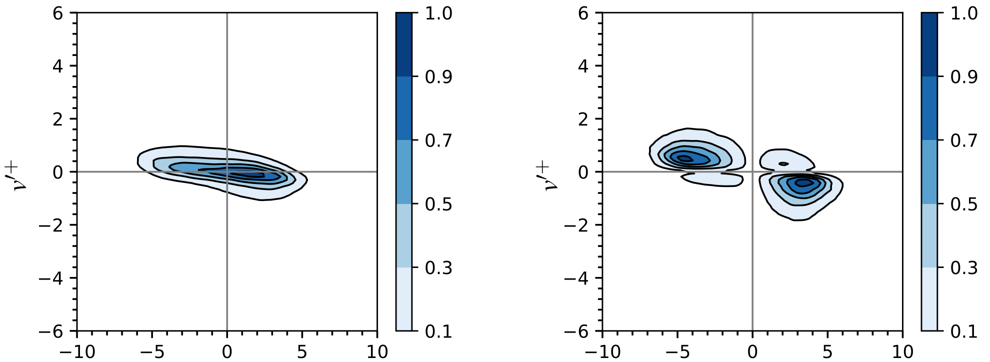

(a) ZMJ off

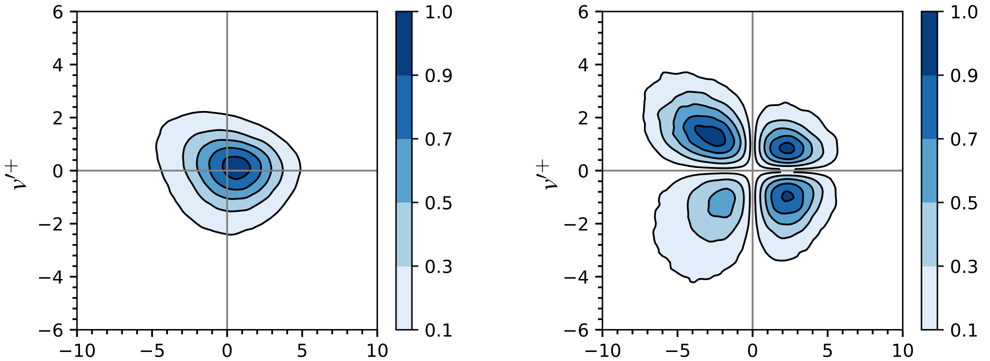

(b) ZMJ on, $\beta = 0°$

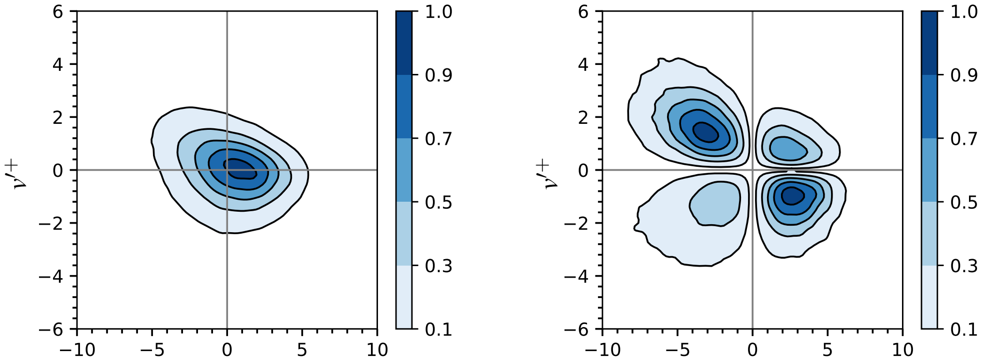

(c) ZMJ on, $\beta = 60°$

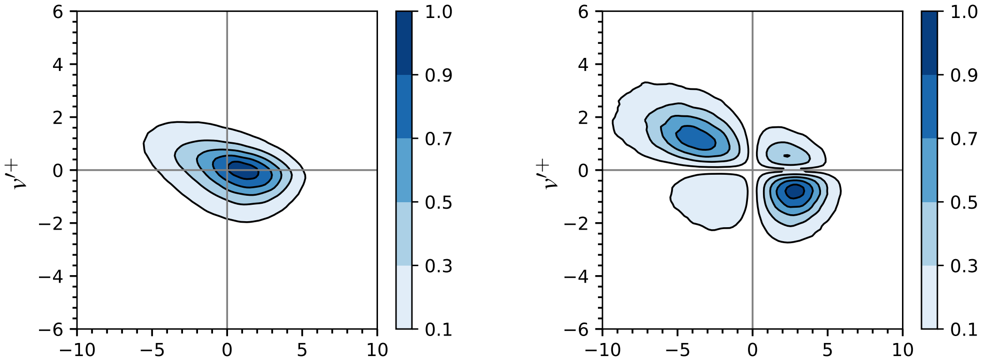

(d) ZMJ on, $\beta = 75°$

Figure 5.41 The joint probability density function $P(u'^+, v'^+)$ (left) and covariance integrand $u'^+ v'^+ P(u'^+, v'^+)$ (right) at $(y_L^+ = 20, z^+ = 0.1)$, giving $10, 30, 50, 70$ and 90% of the maximum probability level or covariance integrand.

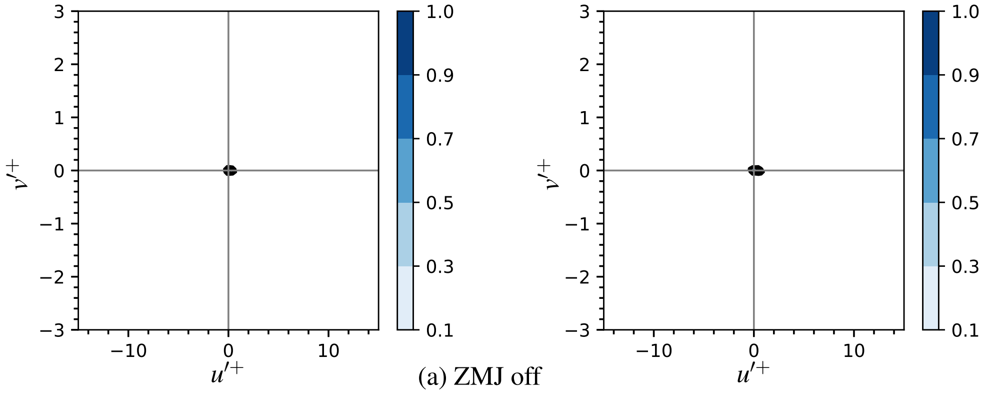

(a) ZMJ off

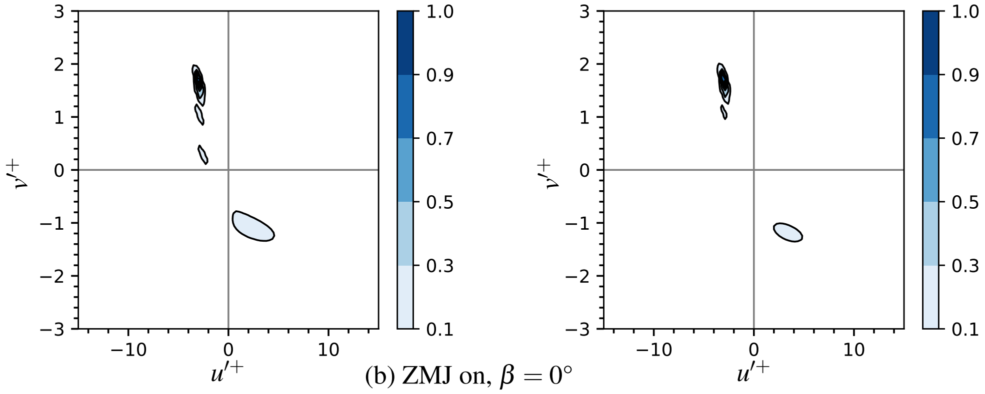

(b) ZMJ on, $\beta = 0°$

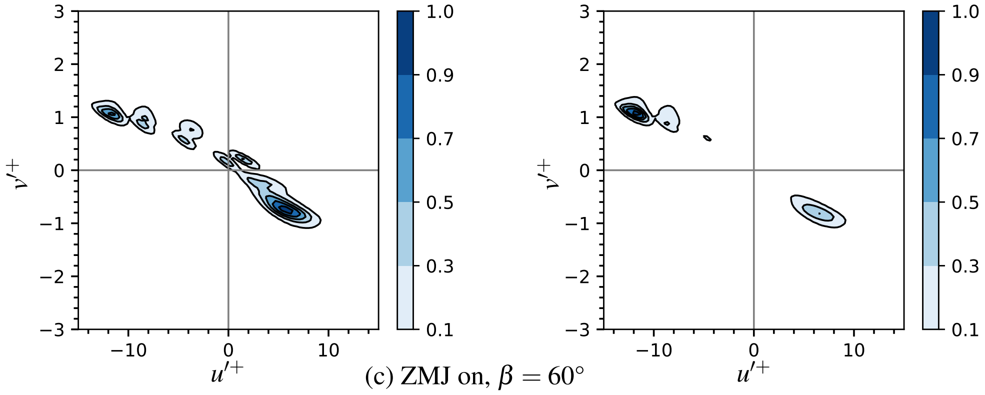

(c) ZMJ on, $\beta = 60°$

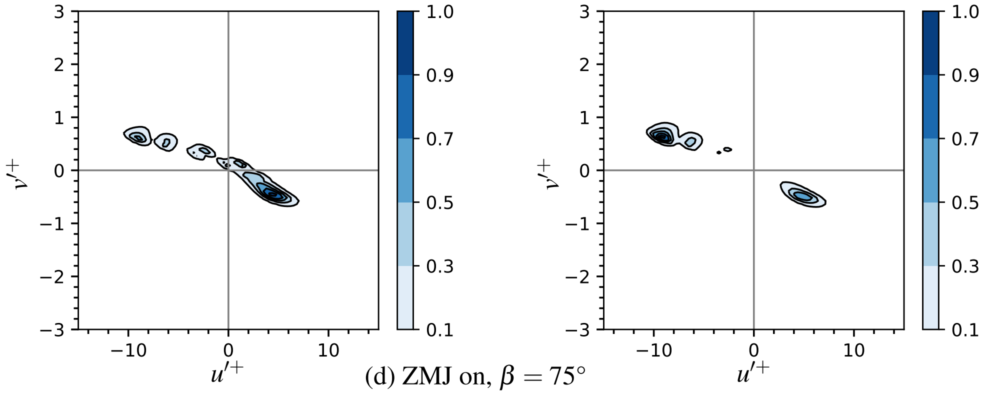

(d) ZMJ on, $\beta = 75°$

Figure 5.42 The joint probability density function $P(u'^+, v'^+)$ (left) and covariance integrand $u'^+ v'^+ P(u'^+, v'^+)$ (right) at $(y_L^+ = 1, z^+ = 20)$, giving $10, 30, 50, 70$ and 90% of the maximum probability level or covariance integrand.

From the previous study, it is noticed that the time-averaged profiles of the streamwise velocity $\overline{u}^+$ are quite different at different spanwise positions due to the different effects of ZMJ. The time-averaged profiles of the Reynolds shear stress $\overline{u'v'}/u_\tau^2$ are in the same situation. To study the differences, case ZMJ($\beta = 75°$) is employed as an example. Figure 5.43 shows all profiles of time and space averaged streamwise-velocity at different spanwise positions in the same plot. Three spanwise positions are highlighted, including $z^+ = 0$, $z^+ = 18.25$ and $z^+ = 62.83$. These positions are in the sides of each sections, jet-exits, and the middle of each sections, respectively. Figure 5.43a shows that, the upper and lower profiles under $y_G^+ < 5$ are at $z^+ = 62.83$ and $z^+ = 18.25$, respectively. The smallest value is

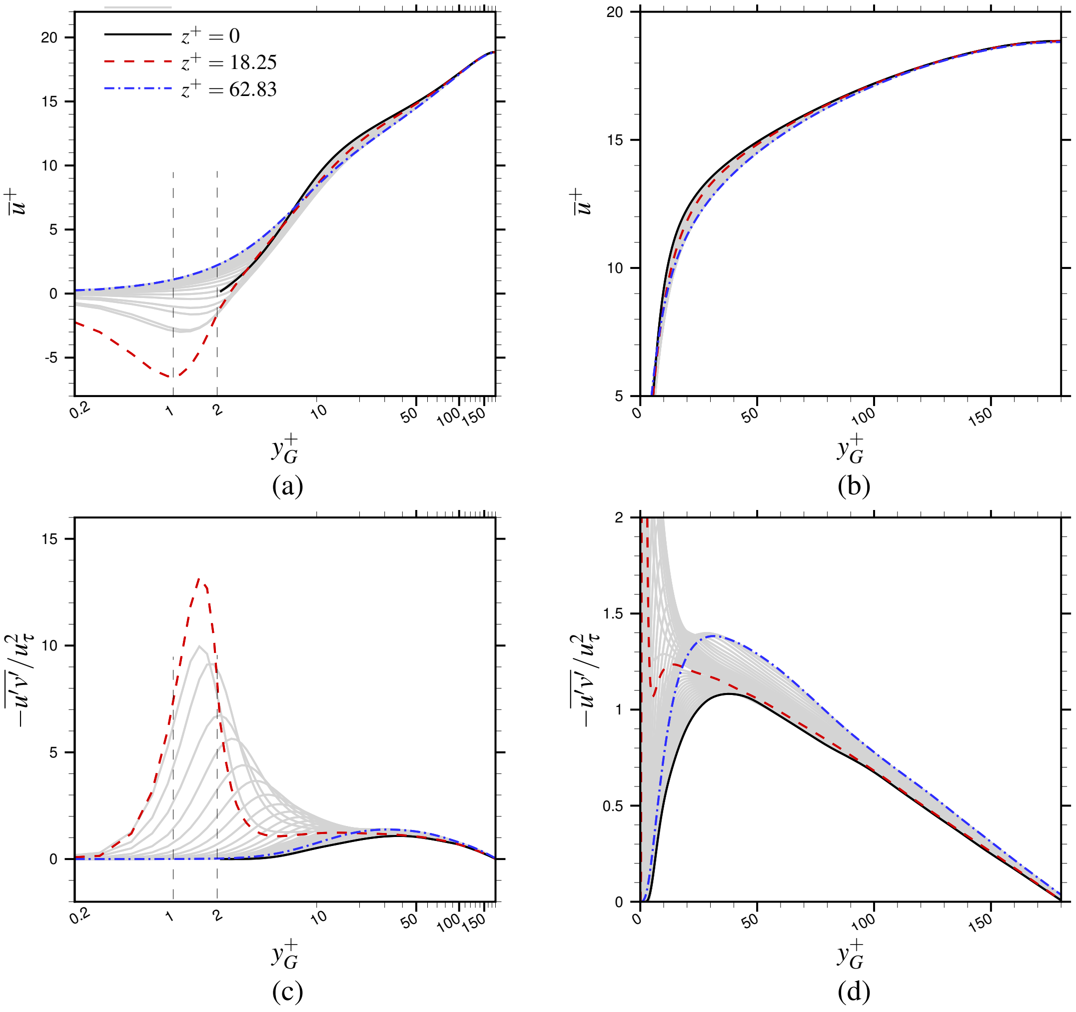

(a)
(b)
(c)
(d)

Figure 5.43 The profiles are displayed at different spanwise positions in case ZMJ($\beta = 75°$). The left figures are in inner-scale units to show the viscous sublayer, and the right figures are in outer-scale units to show the log-law regions. The grey lines are at the other spanwise positions which are not listed in the line legend.

at $(y_G^+ = 1, z^+ = 18.25)$ which is the closest coordinate of the cell centre to the middle of the left jet-exits. In the buffer layer, the profiles at $z^+ = 0$ and $z^+ = 62.83$ are the upper and lower profiles, respectively. Looking at figure 5.43b, it is interesting to notice that the profiles are almost the same above $y_G^+ > 80$. This means that the ZMJ effects on the streamwise velocity profiles are almost the same in the log-law regions.

In figure 5.43c, the highest value of all the nondimensionalized Reynolds shear stresses $-\overline{u'v'}/u_\tau^2$ is between $y_G^+ = 1$ and 2. The reason is that the velocities fluctuate the strongest between $y_G^+ = 1$ and 2, as shown in figure 5.44. As said before, the total velocity fluctuation contains the periodic velocity and the pure velocity fluctuation. The largest periodic velocity may happen at $y_G^+ = 1$ near the jet-exits, but the largest value of pure velocity fluctuation does not appear at $y_G^+ = 1$. When the wall distance increases, the pure velocity fluctuation in the viscous sublayer increases. Therefore, the highest values of the total velocity fluctuations should always locate above $y_G^+ = 1$. Figures 5.43c and 5.43d show that the profiles of the Reynolds shear stress can be divided into two parts, according to the difference among the profiles. The difference is big in the viscous sublayer, but it is relatively small in the log-law region. The reason also can be found from figure 5.44. The strength of velocity fluctuations are very different in the viscous sublayer, but it is almost the same in the log-law region. Figure 5.43c shows the upper and lower profiles in the viscous layer are at $z^+ = 18.25$ and 0, respectively. Figure 5.43d represents that the upper and lower profiles are at $z^+ = 62.83$ and 0, respectively. This means that the Reynolds shear stress has two local peaks which are near the jet-exits and the middle of each sections.

In figure 5.45, it compares the logarithmic profiles of the averaged streamwise-velocity and shows the ZMJ effects among different cases. The profile is computed by averaging all the velocity profiles at the different spanwise positions into one profile, considering the weights of the cell width in the spanwise direction. To compare the velocity gradients, the averaged velocities and the wall distance are in wall units by using the same friction velocity u_τ. The friction velocity is obtained from the result of the smooth channel. Because of the steps, there are jumps in the profiles at $y_G^+ = 2$. In figure 5.45a, the gradient of the averaged velocity in case ZMJ($\beta = 0°$) is the highest in the viscous sublayer among the cases. In the buffer layer, the velocity in case ZMJ($\beta = 0°$) is the highest among all cases, comparing at the same height. Zooming in the profiles near the channel centre, figure 5.45b shows that all profiles are in logarithmic distributions. This indicates that the log-law region is still existed when ZMJ is on. ZMJ changes the gradients of the time-averaged velocities near the channel centre.

In the turbulent modelling, the Von Kármán constant κ is a very important parameter. κ is treated as a universal constant and equals 0.41 in the Spalart-Allmaras model [112]. In

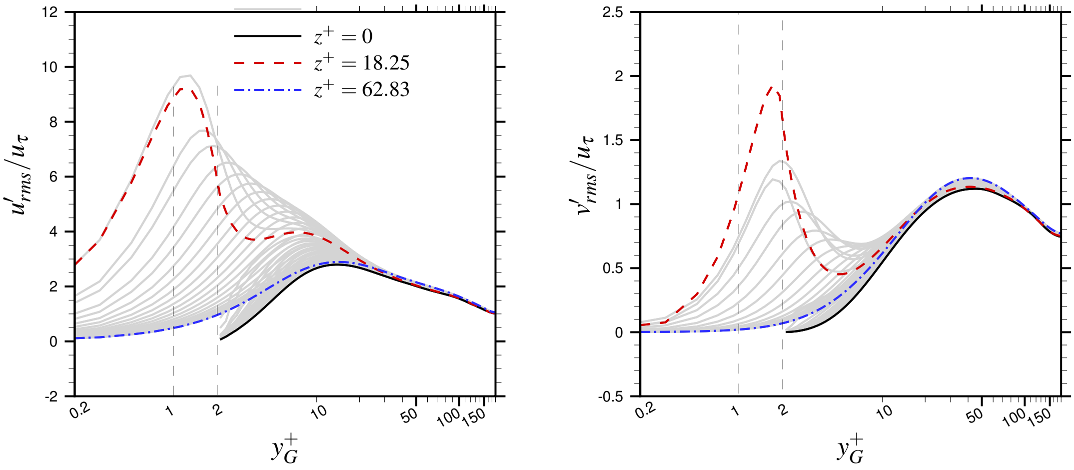

(a) (b)

Figure 5.44 In case ZMJ($\beta = 75°$), the profiles of the root-mean-square of the streamwise and wall-normal velocity-fluctuations are shown at the different spanwise positions, including $z^+ = 0$, 18.25, 62.83. The grey lines are at the other spanwise positions which are not listed in the line legend.

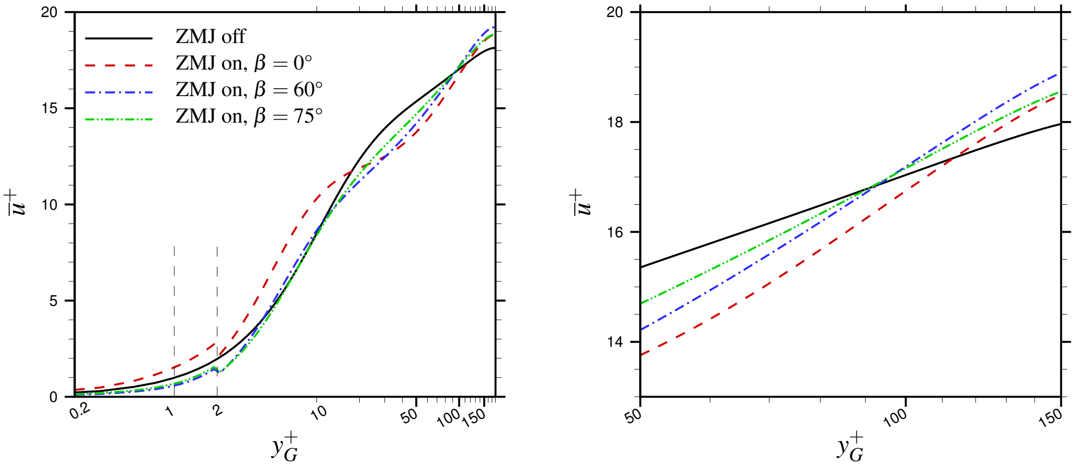

(a) (b)

Figure 5.45 The logarithmic profiles of the averaged streamwise-velocity which are nondimensionalized by the friction velocity u_τ obtained from the smooth channel. (a) shows the profiles across the half channel, and (b) zooms in regions near the jet-exits.

law of the wall, the Von Kármán constant is related to the velocity gradient in the log-law region. If a RANS simulation would like to model the ZMJ effects, the Von Kármán constant should be taken care of, because the velocity profiles are twisted by ZMJ in the log-law region. To obtain the right values of the Von Kármán constant for the time-averaged flow in the controlled channel, the local friction velocity $u_{\tau.l}$ is used to nondimensionalize the averaged velocities and the wall distance in wall units. $u_{\tau.l}$ is directly obtained from the results of the controlled channel. The velocity distribution of the controlled channel in the log-law region can be expressed as

$$u^{+} = \kappa^{-1} \ln y^{+} + A \tag{5.9}$$

where κ is the Von Kármán constant, A is a constant.

Figure 5.46 shows the universal velocity profile in the fully developed channel flow at $Re_{\tau} = 180$. A log-law line is drawn along with the part of the velocity profile in the log-law region. A vertical line is drawn at $y^{+} = 1$. In order to obtain the values of κ and A, three points are put on the log-law line. Points 1 and 2 are in the log-law region of the velocity profile. Point 3 is at the cross of the log-law line and the vertical line. The coordinates of the three points are assumed as (y_1^{+}, u_1^{+}), (y_2^{+}, u_2^{+}) and (y_3^{+}, u_3^{+}).

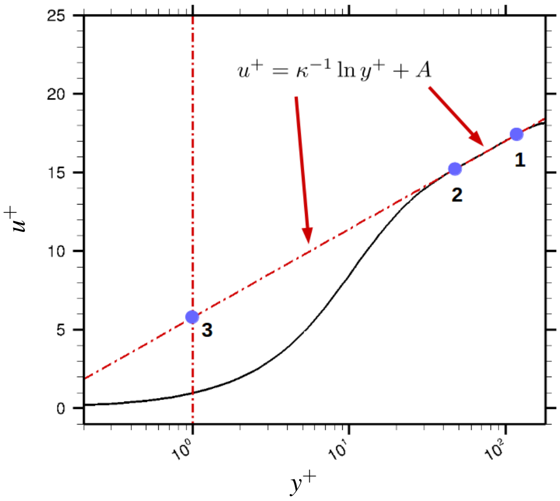

Figure 5.46 The universal velocity profile in the fully developed channel flow at $Re_{\tau} = 180$.

Using the coordinates of points 1 and 2, it is able to compute the value of κ as below,

$$\kappa = \frac{\ln y_1^{+} - \ln y_2^{+}}{u_1^{+} - u_2^{+}} \tag{5.10}$$

The value of A can be obtained from the coordinate of point 3. Because the point 3 is on the vertical line at $y^+ = 1$, it has

$$y_3^+ = 1 \tag{5.11}$$

so,

$$\ln y_3^+ = 0 \tag{5.12}$$

Substituting equation 5.12 into equation 5.9, the value of A can be computed by

$$A = u_3^+ \tag{5.13}$$

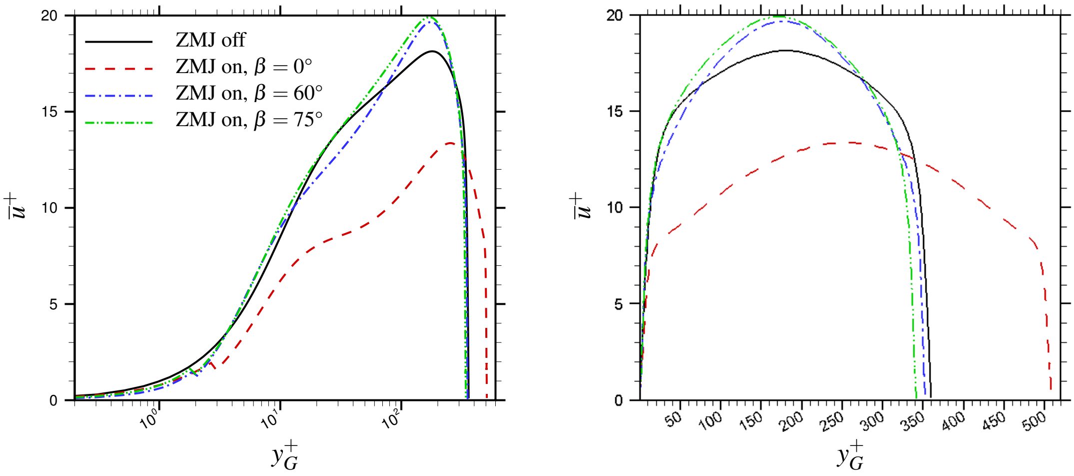

(a) logarithmic scale (b) linear scale

Figure 5.47 Profiles of the averaged streamwise-velocity which are nondimensionalized by the local friction-velocity $u_{\tau,l}$.

Table 5.3 The values of the parameters in the general logarithmic equation 5.9.

ZMJ	β	κ	A
off	–	0.41	5.8
on	0°	0.31	−4.1
on	60°	0.22	−3.2
on	75°	0.26	0.7

Figure 5.47 compares the profiles of the averaged streamwise-velocity. The entire channel height is covered in the plots so that the velocity is zero on both ends. The ZMJ effects on the velocity profiles in the log-law region are different from the effects caused by the oscillating

walls [8]. In the cases of oscillating walls, the velocity profiles are shifted in the log-law region with different periods, and none of the profiles is crossed with the original velocity profile. In the ZMJ cases, the profile of case ZMJ($\beta = 60°$) in the log-law region is crossed with the profile of case ZMJ(off). The values of the parameters in equation 5.9 are listed in table 5.3. This would be very useful for the RANS simulations.

In this study, the flow is simulated by a compressible solver. Density is a variable in the simulation. Figure 5.48 shows the contour plots of time averaged density. The density is high near wall. The levels of density variation is 0.65% in case ZMJ(off). The levels are

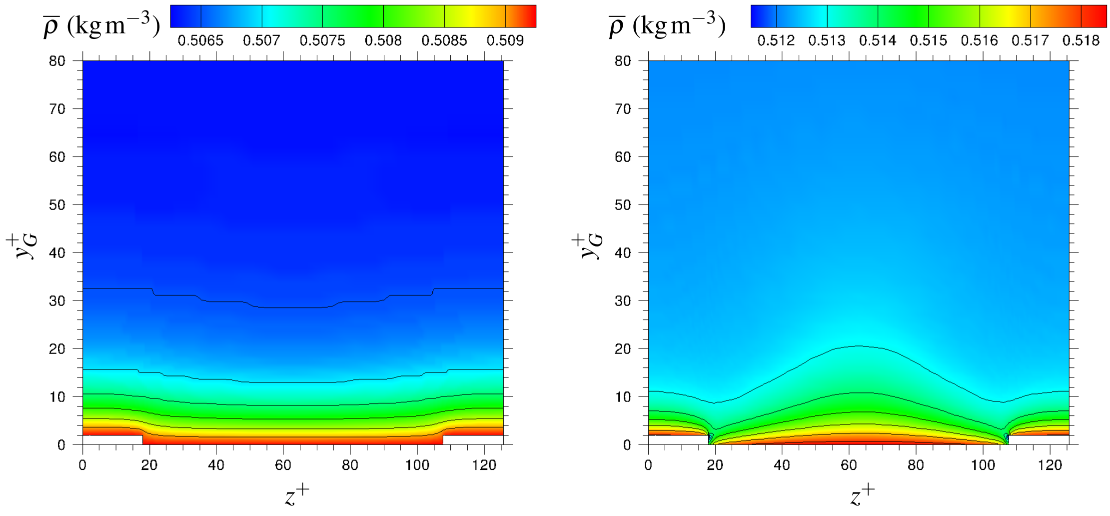

(a) ZMJ off

(b) ZMJ on, $\beta = 0°$

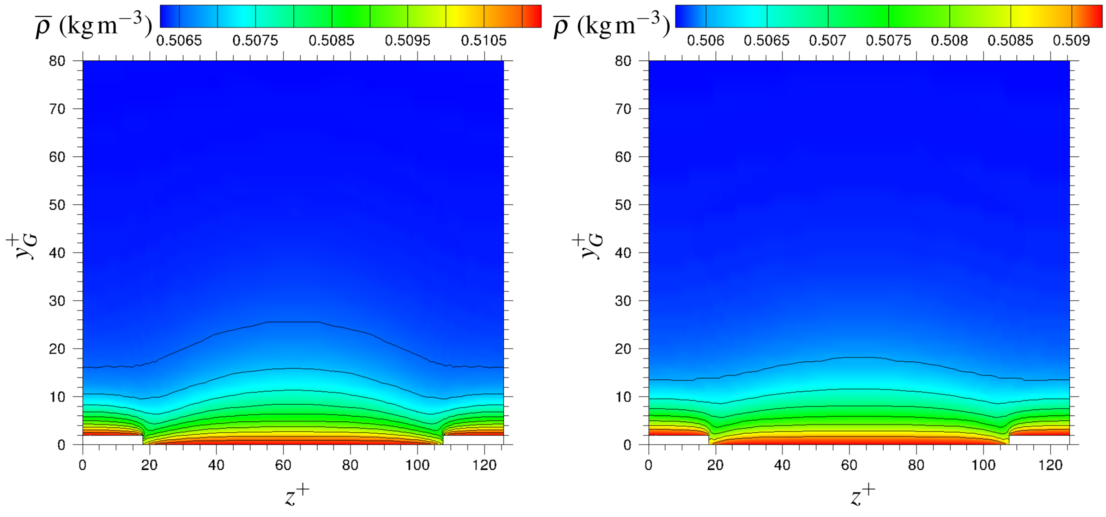

(c) ZMJ on, $\beta = 60°$

(d) ZMJ on, $\beta = 75°$

Figure 5.48 Contours of time averaged density in the cross-stream ($y - z$ plane) view. The contour levels are different in each plot.

1.43%, 1.10% and 0.88% for cases ZMJ($\beta = 0°$, 60° and 75°), respectively. This shows that the density variation is proportionally increased by the spanwise strength of ZMJ. The compressibility effect is low in the data.

5.6 Phase averaged results

In the previous section, the time-averaged flow-fields are studied in details. The time effects of ZMJ are $z-$symmetric. In this section, the phase-averaged flow-fields should not be $z-$symmetric, because the effects from the left and right sides of a pair of ZMJ are phase shifted. When one side of the jets blows out fluid, the other side of the jets sucks in fluid. The flow-field have periodic characters because the jet velocity of ZMJ is in a sinusoidal function which is periodic.

In case ZMJ(off), the phase and space averaged flow-field in a section should be the same as the time and space averaged results, because there is no asymmetrical perturbation in the spanwise direction. The phase-averaged results with ZMJ on can be compared with the time-averaged results with ZMJ off to study the periodic characters. In this section, cases $\beta = 0°$, 60° and 75° will be investigated and compared, using the phase-averaged results to study the mechanisms of the turbulent drag-reduction in details.

The oscillating characters of the flow-field is strongly related to ZMJ, so the results are phase-averaged depending on the period of ZMJ. All the simulations of cases ZMJ(on) are initialized by the same and convergent result which is from case ZMJ(off). To make sure the sampling number for the phase average is big enough, the simulations computed 20 periods. The control method is very efficient. As shown in figure 5.16, the transition of the flow is finished in 2 periods, so it is reasonable to start the phase average after 2 periods.

Going back to figure 5.2, it represents that the jet velocity reaches the peak values at the phase time $\varphi = \pi/2$ or $3\pi/2$. The minimum skin frictions happen at these two phase time, as shown in figure 5.16b. Using phase and space average, the overview of the skin-friction distributions in a period is shown in figure 5.49. In the 3D figures, each profiles corresponds to the spanwise distributions of skin friction coefficients at each phase time. The 2D figures put the profiles together to show the exact values of the coefficients.

As shown in the 3D figures, the skin frictions are significantly influenced near the jet-exits which are at z=18 and 107.66. In the following analysis, the jet-exits at z=18 and 107.66 are called left jet-exits and right jet-exits, respectively. From $\varphi = 0$ to π, the fluid is blown out at the left jet-exits and is sucked in at the right jet-exits. In contrast, from $\varphi = \pi$ to 2π, the fluid is sucked in at the left jet-exits and is blown out at the right jet-exits. The skin friction is reduced near the blowing jet-exits and is increased near the sucking jet-exits. The drag cannot

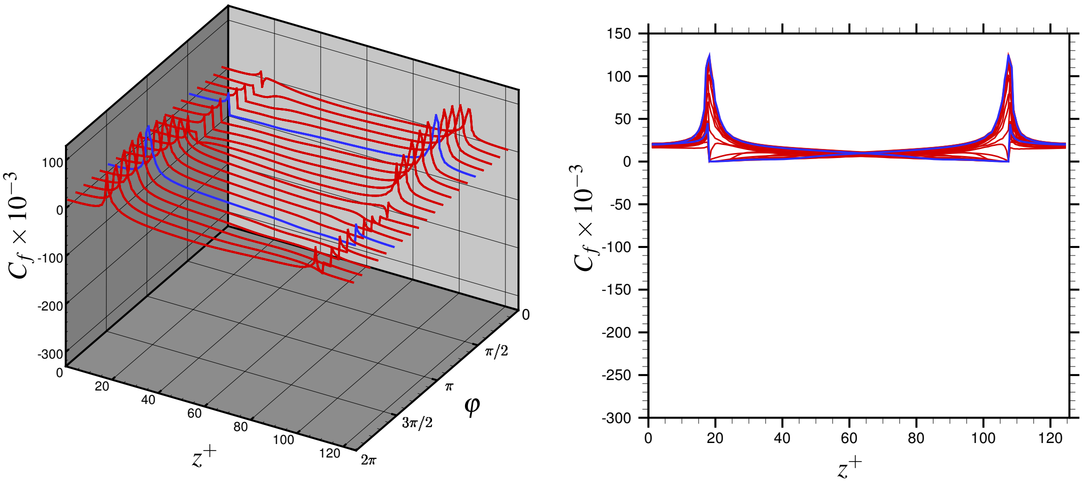

(a) 3D, $\beta = 0°$ (b) 2D, $\beta = 0°$

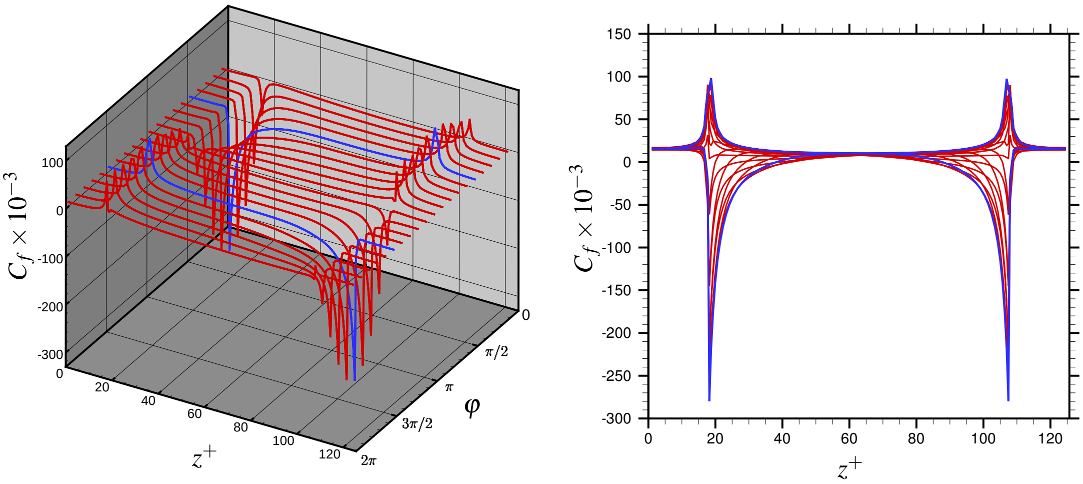

(c) 3D, $\beta = 60°$ (d) 2D, $\beta = 60°$

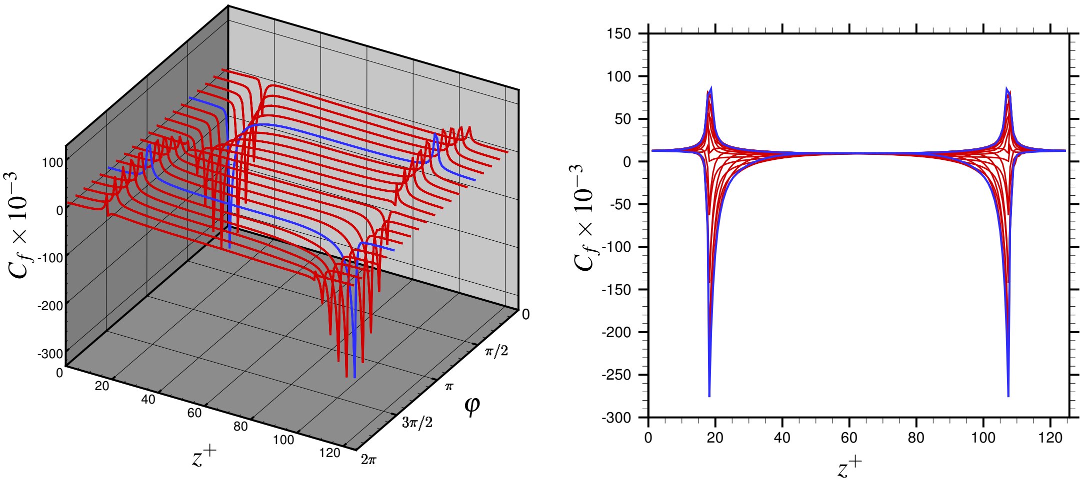

(e) 3D, $\beta = 75°$ (f) 2D, $\beta = 75°$

Figure 5.49 The phase and space averaged skin-friction-coefficient distributions in 3-dimensional and 2-dimensional. The blue lines denote the phase time φ is at $\pi/2$ or $3\pi/2$.

be reduced below zero, when $\beta = 0°$. However, the drag can be significantly decreased to be negative, when $\beta = 60°, 75°$. It can be observed that the peak values happen at $\varphi = \pi/2$ and $3\pi/2$. Looking at the positive peaks in the 2D figures, the value of the peak is proportional to the spanwise strength of ZMJ. Checking the negative peaks in the 2D figures, case $\beta = 60°$ has the lowest value of the peak. An interesting phenomenon found from the 2D figures is that the absolute peak values of the decreased skin-frictions are much bigger than the peak values of the increased skin-frictions, so it is possible to obtain a drag reduction overall.

Figure 5.50 shows phase and space averaged flow-fields near wall at $\varphi = \pi/2$, comparing the streamwise and spanwise velocities among the cases ZMJ(on). The phase-averaged flow-fields are different from the time-averaged flow-fields. The areas of the region $|w^+| > 5$ are different between the left and right jet-exits, showing that the blowing side can influence larger area than the sucking side. At $\varphi = \pi/2$, the fluid of low or negative velocity is blown out from the left jet-exits and reduces the fluid velocity. The width of the region $u^+ < 0$ is proportional to the spanwise strength of ZMJ. When the fluid is blown out from the left jet-exits, it can be observed from figures 5.50b, 5.50d, 5.50f that the fluid moves right and upwards. Near the right jet-exits, the streamwise velocity is increased by ZMJ, and the high velocity fluid is brought downwards.

In figure 5.49f, it is observed that the skin friction is significantly influenced at the spanwise position $z^+ = 20$ which is a typical position to be examined. Figure 5.51 shows the phase and space averaged streamwise-velocity at the spanwise position $z^+ = 20$ in a period. The left figures are the contour plots of the streamwise velocity by treating the phase time as a variable in the x-axis. The right figures display all streamwise-velocity profiles at different phase time in a single plot to show the exact values. The contour plots show that it is impossible to reduce the phase-averaged streamwise-velocity to be negative when $\beta = 0°$, because the minimum jet-speed is only zero in the streamwise direction. The velocities of cases ZMJ($\beta = 60°$) and ZMJ($\beta = 75°$) can be negative in the near-wall regions, when the phase time is between $\pi/10$ and π, as shown in figures 5.51c and 5.51e. The difference of the velocity profiles are huge in the viscous sublayer and buffer layer as shown in the left figures, but the difference in the log-law region is relatively low.

The influence of ZMJ has a delaying effect on the velocity, depending on the distance between the position and the jet-exits. The longer the distance is, the stronger the delaying effect is, because the flow needs time to propagate the influence from the jet-exits. That is why there is a inclined wave of the contour lines biasing to the side of the big phase-time in the contour plots, when the phase time is between 0 and π. The inclined angle of the wave becomes smaller, when the jet angle increases from 0° to 75°. The delaying effect makes the velocity profiles wavy in the buffer layer, as shown in the profile plots.

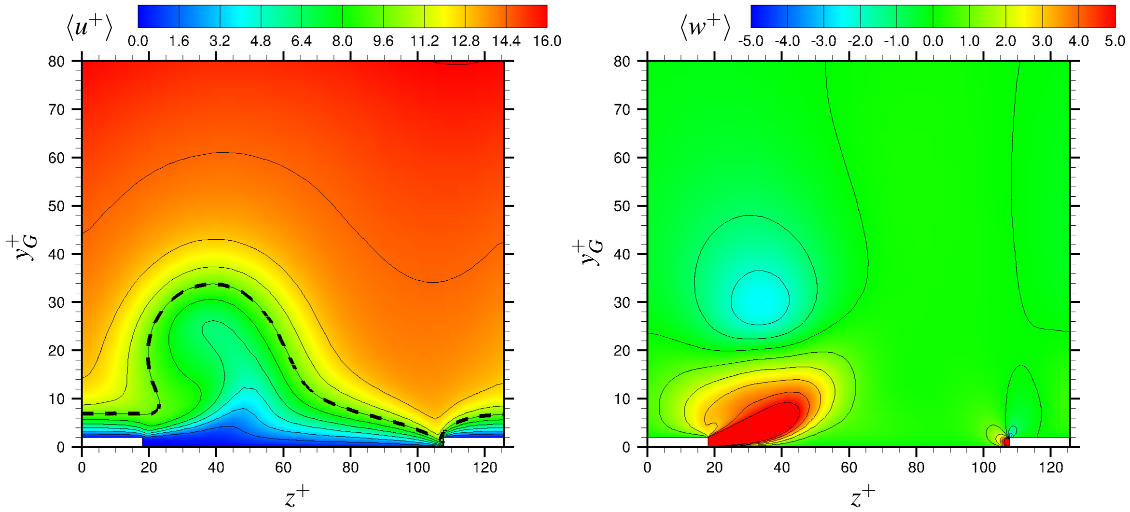

(a) Streamwise velocity $\langle u^+ \rangle$, $\beta = 0°$

(b) Spanwise velocity $\langle w^+ \rangle$, $\beta = 0°$

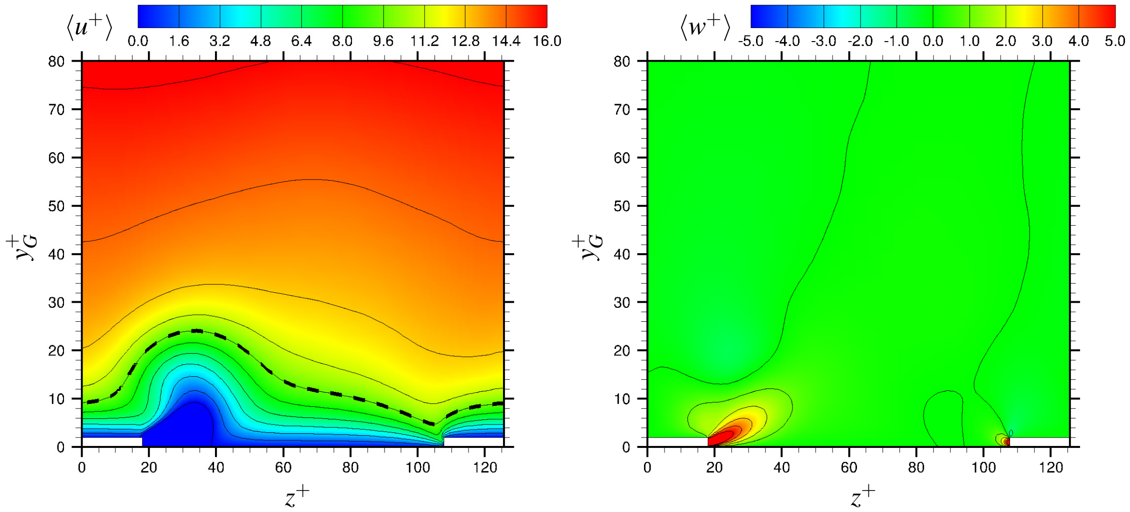

(c) Streamwise velocity $\langle u^+ \rangle$, $\beta = 60°$

(d) Spanwise velocity $\langle w^+ \rangle$, $\beta = 60°$

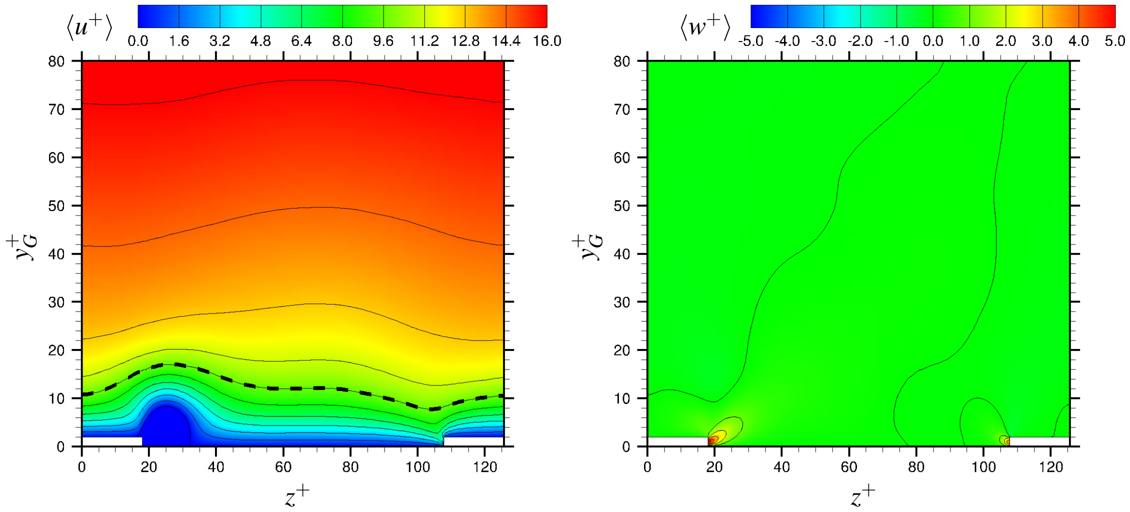

(e) Streamwise velocity $\langle u^+ \rangle$, $\beta = 75°$

(f) Spanwise velocity $\langle w^+ \rangle$, $\beta = 75°$

Figure 5.50 Contours of phase and space averaged velocities in the cross-stream ($y - z$ plane) view, including $\langle u^+ \rangle$ and $\langle w^+ \rangle$, when the phase time $\varphi = \pi/2$ with $\beta = 0°$, $60°$, $75°$. The dashed lines denote $\langle u^+ \rangle = 9.6$.

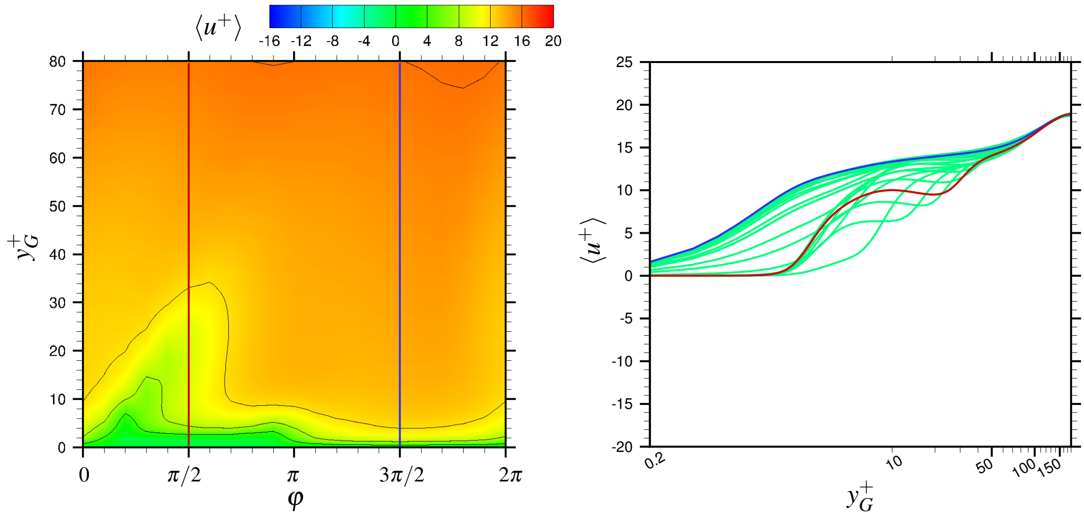

(a) The contours of $\beta = 0°$ (b) The profiles of $\beta = 0°$

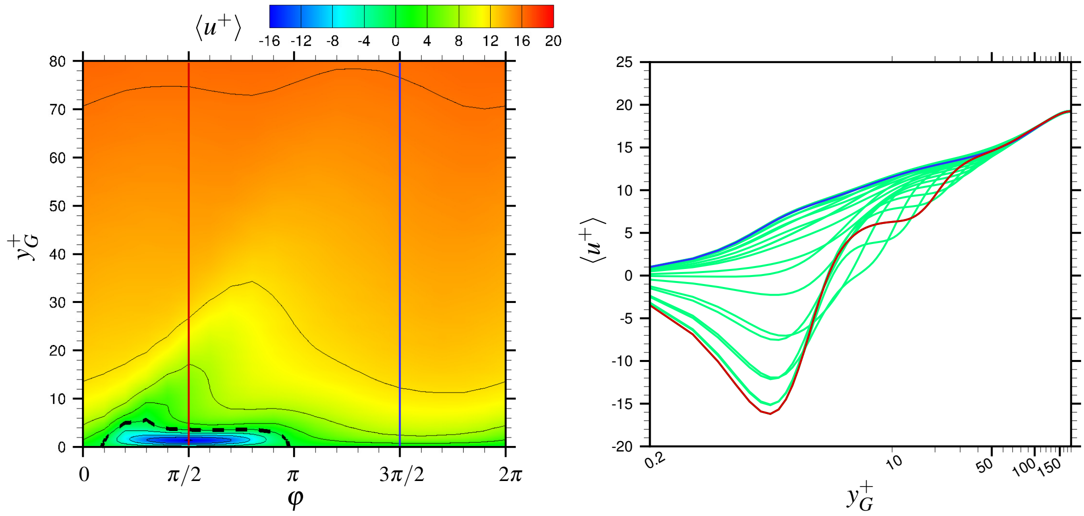

(c) The contours of $\beta = 60°$ (d) The profiles of $\beta = 60°$

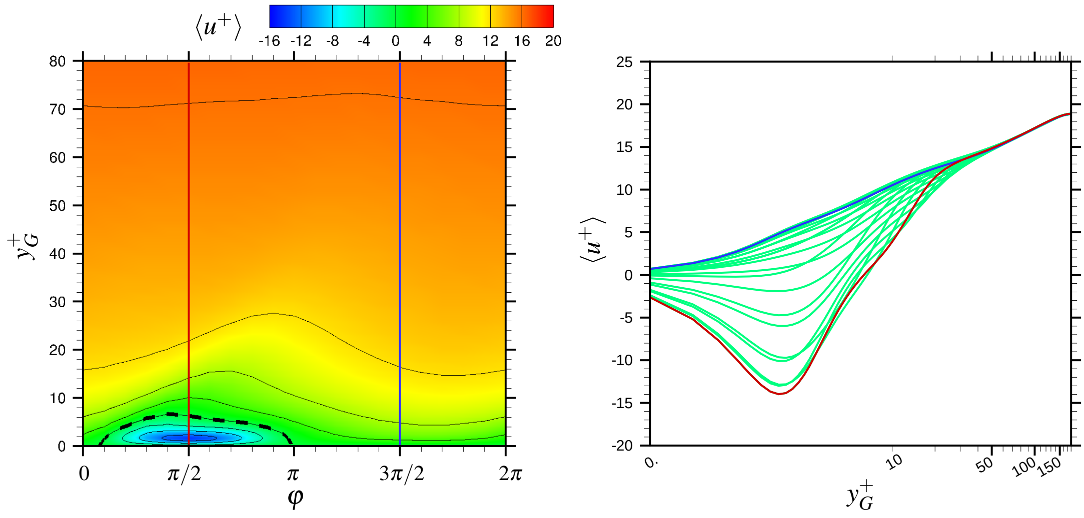

(e) The contours of $\beta = 75°$ (f) The profiles of $\beta = 75°$

Figure 5.51 The contours and profiles of phase and space averaged streamwise-velocity at the spanwise position $z^+ = 20$. The black dashed lines denote $\langle u^+ \rangle = 0$. The red and blue solid lines are at $\varphi = \pi/2$ and $3\pi/2$, respectively, responding to the red and blue velocity-profiles in the right figures.

The ZMJ increases the Reynolds shear stresses in the channel flow. According to the FIK method [27], the friction drag is proportional to the Reynold shear stresses. When the jet angle increases, the Reynold shear stresses reduce. The contouring jet produced by ZMJ can reduce the friction drag as well. Therefore, there is a possibility to obtain a positive drag reduction with a proper jet angle in the controlled channel flow. To study the ZMJ effects, it is important to check the Reynolds shear stresses given by the pure turbulent velocity-fluctuations.

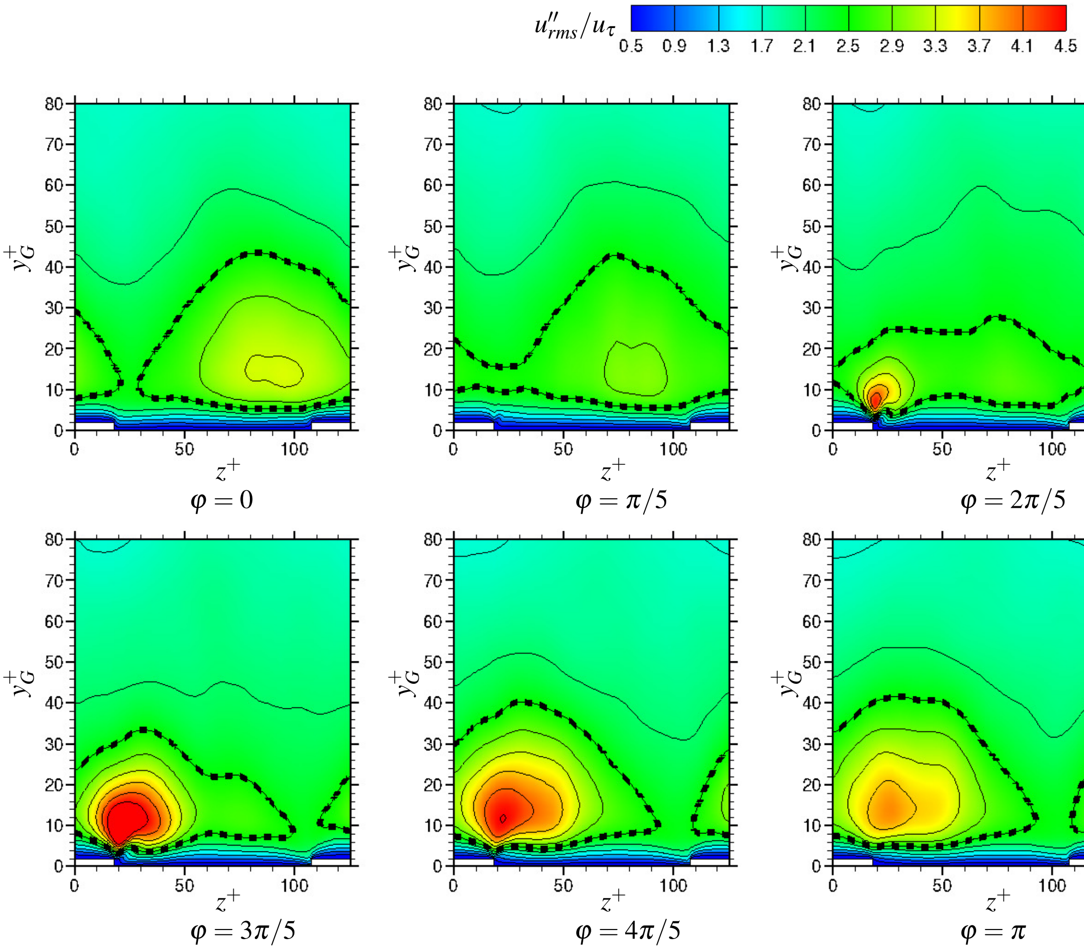

Figure 5.52 Contours of u''_{rms}/u_τ in the cross-stream ($y-z$ plane) view at different phase time φ in case ZMJ($\beta = 75°$). The dashed lines denote $u''_{rms}/u_\tau = 2.5$. The left jet-exits is blowing and the right jet-exits is sucking during $0 \leq \varphi \leq \pi$.

Case ZMJ($\beta = 75°$) is helpful to study the pure turbulent velocity-fluctuations when ZMJ can have positive drag-reduction. Figure 5.52 represents the development of the root-mean-square of the pure fluctuation u''/u_τ in a half period $0 \leq \varphi \leq \pi$. During the other half period $\pi \leq \varphi \leq 2\pi$, the contour plots are symmetric with that shown in figure 5.52. Comparing with the contours of u'_{rms}/u_τ in figure 5.31d, the contours of u''_{rms}/u_τ is not symmetric at any phase time. The peaks of u''_{rms}/u_τ locate away from the jet-exits. On the blowing side, when the jet speed increases, the peak value of u''_{rms}/u_τ grows. When the jet speed decreases, the peak value becomes smaller. That means the amplitude of the pure turbulent velocity-fluctuations depends on the speed of the blowing jet. On the sucking side, the fluctuations are sucked into the jet-exits and removed from the flow during the half period $0 \leq \varphi \leq \pi$.

Figure 5.53 shows the root mean square of the pure turbulent fluctuations of the streamwise velocity u'' at the spanwise position $z^+ = 20$ in contours and profiles, displaying like $\langle u^+ \rangle$ in figure 5.51. The profiles of u''_{rms}/u_τ at the different phase time are compared with u'_{rms}/u_{tau}. Figure 5.53a displays that the peak value happens at $y_G^+ = 9.2$ and $\varphi = 6\pi/5$. The phase time of the peak is latter than the phase time when ZMJ reaches its maximum speed. Because ZMJ needs time to propagate the effects, which is similar to the delaying effect of the streamwise velocity in figure 5.51e. When the phase time is between 0 and π, the pure turbulent velocity-fluctuations do not fluctuate strong below $y_G^+ = 2$, but the fluctuations sharply increase from $y_G^+ = 2$ to $y_G^+ = 8$. When the fluid is blown out from the jet-exits, the fluid expands upwards. The sharp corners which locate between the step walls and the jet-exits are obstacles for the flow, disturbing the flow and generating vortices. The vortices make the velocity fluctuate. The flow is dominated by the jet below the sharp corners. According to the flow direction, the jet does not interact with the sharp corners. ZMJ only

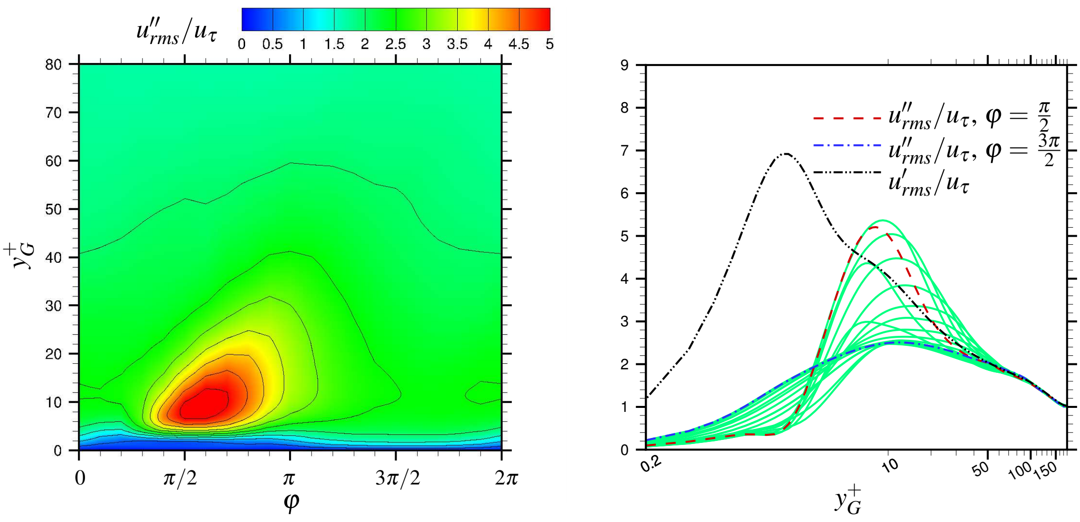

(a) (b)

Figure 5.53 The contours or profiles of the root mean square of the streamwise velocity fluctuations for case ZMJ($\beta = 75°$) at the spanwise position $z^+ = 20$. The profiles include the pure turbulent fluctuations u'' and the total fluctuations u' which are nondimensionalized by the friction velocity u_τ based on the smooth channel. The green lines are the profiles at the phase time except $\varphi = \pi/2, 3\pi/2$.

creates the periodic velocity and does not have much pure turbulent fluctuations. That is why the location of the sharp corner separates the regions of high and low u'' near the blowing side. When the fluid is sucked in, the high fluctuating fluid is continuously brought downwards and sucked in to the jet-exits. The profiles are relatively smooth near the sucking side. Figure 5.53b indicates that the pure turbulent velocity-fluctuations u'' only contributes little to the total velocity-fluctuations u' when the position is lower than the steps $y_G^+ < 2$. u' is mainly increased by u'' when it is higher than the steps. This means that the disturbance of the steps is a important reason for the increase of the turbulent intensity in the controlled channel.

The contour plots of u''_{rms}/u_τ for case ZMJ($\beta = 0°$) in the $y-z$ plane are shown in figure 5.54. The differences of u''_{rms}/u_τ between cases ZMJ($\beta = 0°$) and ZMJ($\beta = 75°$) are studied to find the connection between the jet angle β and the pure turbulent velocity-fluctuations

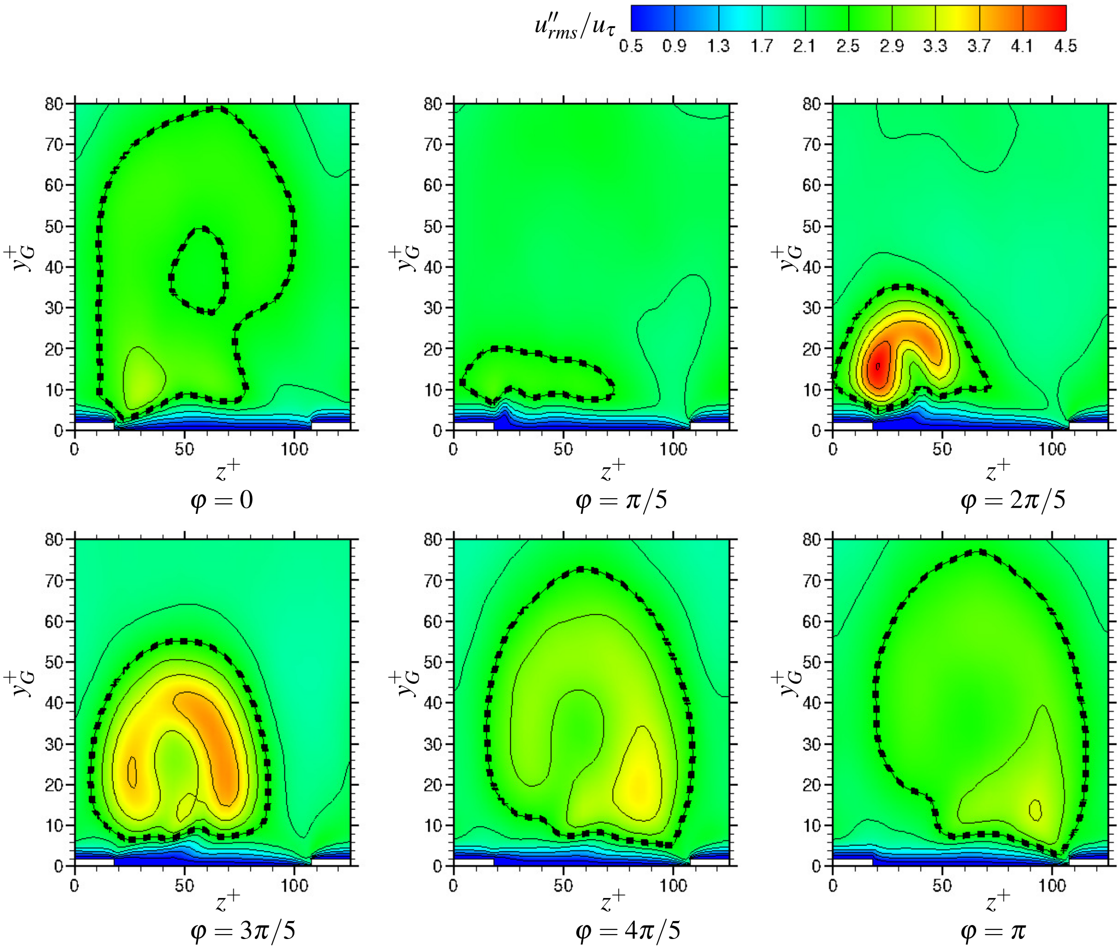

Figure 5.54 Contours of u''_{rms}/u_τ in the cross-stream ($y-z$ plane) view at the different phase time φ for case ZMJ($\beta = 0°$). The dashed lines denote $u''_{rms}/u_\tau = 2.5$. The left jet-exits is blowing and the right jet-exits is sucking during $0 \leq \varphi \leq \pi$.

u''. By comparing figures 5.52 and 5.54, it reveals two differences. Firstly, the highest height of region $u''_{rms}/u_\tau = 2.5$ among all the phase time in case ZMJ($\beta = 0°$) is higher than that in case ZMJ($\beta = 75°$) because the spanwise velocity of ZMJ in case ZMJ($\beta = 0°$) is bigger than that in case ZMJ($\beta = 75°$). Secondly, the peak value of the pure turbulent velocity-fluctuations among all of the phase time in case ZMJ($\beta = 0°$) happens earlier than that in case ZMJ($\beta = 75°$). The pure turbulent fluctuations of the streamwise velocity are caused by the combined perturbations from the streamwise and spanwise velocities of ZMJ. In the region which is between $y_G^+ = 10$ and $y_G^+ = 20$, u'' mainly depends on the perturbation strength from the spanwise velocity of ZMJ. The fluctuations of case ZMJ($\beta = 0°$) increase faster than that of case ZMJ($\beta = 75°$) in that region. After the spanwise velocity of ZMJ reaches the peak, the fluctuations propagate further. The amplitudes of the fluctuations reduce due to the decrease of the perturbation strength. In the region which is between $y_G^+ = 10$ and $y_G^+ = 2$, the perturbation from the streamwise velocity of ZMJ determines u''. Because the streamwise velocity of case ZMJ($\beta = 0°$) is not disturbed stronger than that of case ZMJ($\beta = 75°$), u''_{rms}/u_τ of case ZMJ($\beta = 0°$) is smaller than that of case ZMJ($\beta = 75°$).

There are some similarities between cases ZMJ($\beta = 0°$) and ZMJ($\beta = 75°$) as well. The fluctuations are generated by the blowing jet-exits and eliminated by the sucking jet-exits. The turbulent intensity is increased by ZMJ. The flow has very strong periodical characters determined by the periodical characters of ZMJ.

Figure 5.55a shows the contour plots of u''_{rms}/u_τ at the spanwise position $z^+ = 20$ for case ZMJ($\beta = 0°$). When $\beta = 75°$, the peak value happens at $\varphi = 3\pi/5$. When $\beta = 0°$, the peak value happens at $\varphi = 2\pi/5$. The peak value of u''_{rms}/u_τ in case ZMJ($\beta = 0°$) is smaller than that in case ZMJ($\beta = 75°$). Because there is no countering jet in the streamwise direction in case ZMJ($\beta = 0°$), so the fluctuating amplitude of the streamwise velocity is smaller than that of case ZMJ($\beta = 75°$). The spanwise velocity of ZMJ in case ZMJ($\beta = 0°$) increases faster than that in case ZMJ($\beta = 75°$). This causes that case ZMJ($\beta = 0°$) blows out more mass in the spanwise direction than case ZMJ($\beta = 75°$) at the same phase time. The fluid which is in region above the steps when $\beta = 0°$ gets active earlier than that when $\beta = 75°$. This can be observed from figure 5.54 as well.

Figure 5.55b compares the profiles of u''_{rms}/u_τ between cases $\beta = 0°$ and 75° at different critical phase time. The profiles are near the left jet-exits at the spanwise position $z^+ = 20$. The left jet-exits blows at $\varphi = \pi/2$ and sucks at $\varphi = 3\pi/2$. In the region $y_G^+ < 2$, the fluctuations u'' at $\varphi = \pi/2$ is smaller than that at $\varphi = 3\pi/2$. The difference of the fluctuations u'' between two phase time in case ZMJ($\beta = 0°$) is bigger than that in case ZMJ($\beta = 75°$). The reason is that the fluid when $\beta = 0°$ can be blown out or sucked in more than that when $\beta = 75°$. At $\varphi = \pi/2$, when $\beta = 0°$ is quieter than that when $\beta = 75°$, because case

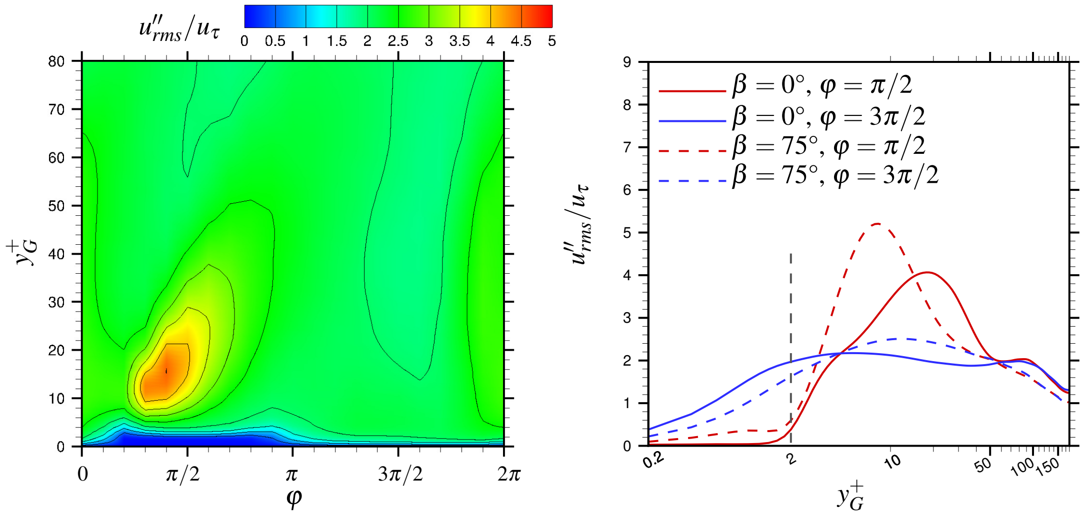

(a) (b)

Figure 5.55 (a) Contours of u''_{rms}/u_τ when ZMJ is on with $\beta = 0°$ at the spanwise position $z^+ = 20$, varying the phase time. (b) Comparisons of u''_{rms}/u_τ profiles among the cases, including the different jet angles $\beta = 0°$, $75°$, and phase time $\varphi = \pi/2$, $3\pi/2$.

ZMJ($\beta = 0°$) blows out larger amount of quiet jets. At $\varphi = 3\pi/2$, when $\beta = 0°$ is noisier than that when $\beta = 75°$, because case ZMJ($\beta = 0°$) brings larger mount of the noisy fluid in region above the steps. The phenomenon is different in the region $y_G^+ > 2$. At $\varphi = \pi/2$, the peak value of case ZMJ($\beta = 0°$) is smaller than that of case ZMJ($\beta = 75°$). Because the fluctuations are from the streamwise perturbations of ZMJ. The perturbations of case ZMJ($\beta = 0°$) is weaker than that of case ZMJ($\beta = 75°$). At $\varphi = 3\pi/2$, the fluctuations are brought down from the fluid in region above the steps. The amplitude of the fluctuations is relatively low in case ZMJ($\beta = 0°$), so the peak value of case ZMJ($\beta = 0°$) is smaller than that of case $\beta = 75°$.

Based on the previous discussion, it can be expected that some vortices are generated by ZMJ from the blowing side. To confirm the guess, figure 5.56 shows the vortices based on the phase and space averaged flow-field in the $y - z$ plane for two jet angles $\beta = 0°$, $75°$. When the fluid is blown out, a small vortex is generated from the blowing jet-exits and expends to its maximum size at $\varphi = \pi$. The existed vortex is sucked into the sucking jet-exits. In the turbulent environment, the averaged vortices are the mean of many small vortices which produce the velocity fluctuations. That is why the turbulent intensity is always increased by ZMJ. The difference between cases ZMJ($\beta = 0°$) and ZMJ($\beta = 75°$) is that case ZMJ($\beta = 0°$) can eliminate the existed vortex but case ZMJ($\beta = 75°$) cannot. The core height of the existed vortex in case ZMJ($\beta = 0°$) is higher than that in case ZMJ($\beta = 75°$), resulting with the height difference of the vortex cores in the time and space averaged results.

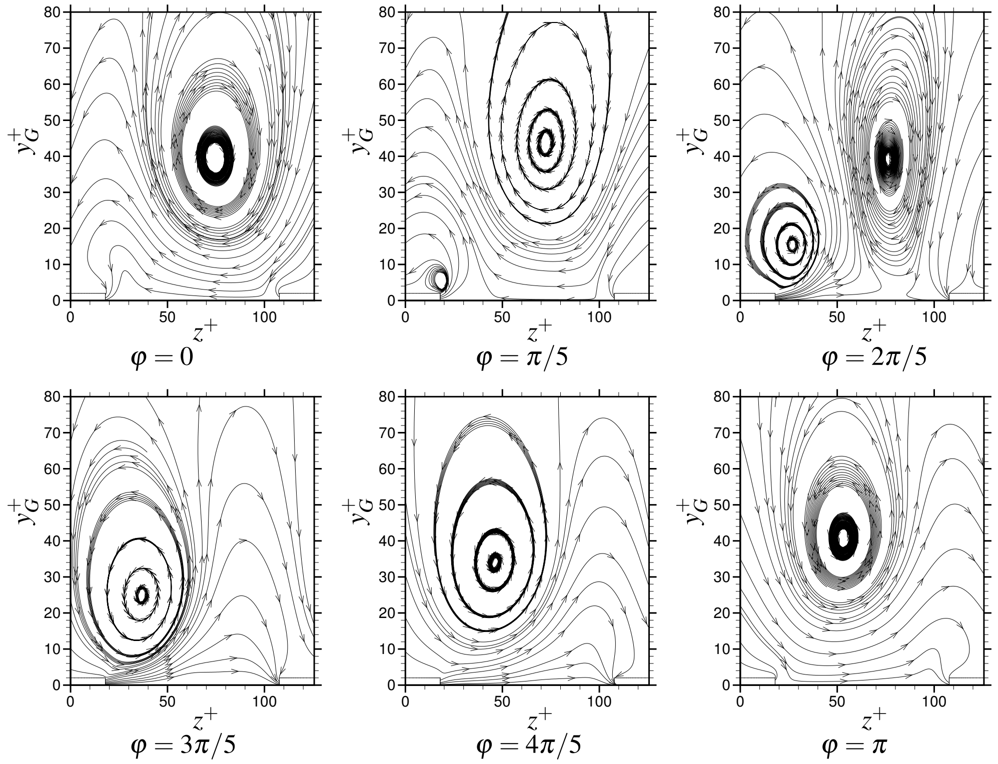

(a) $\beta = 0°$

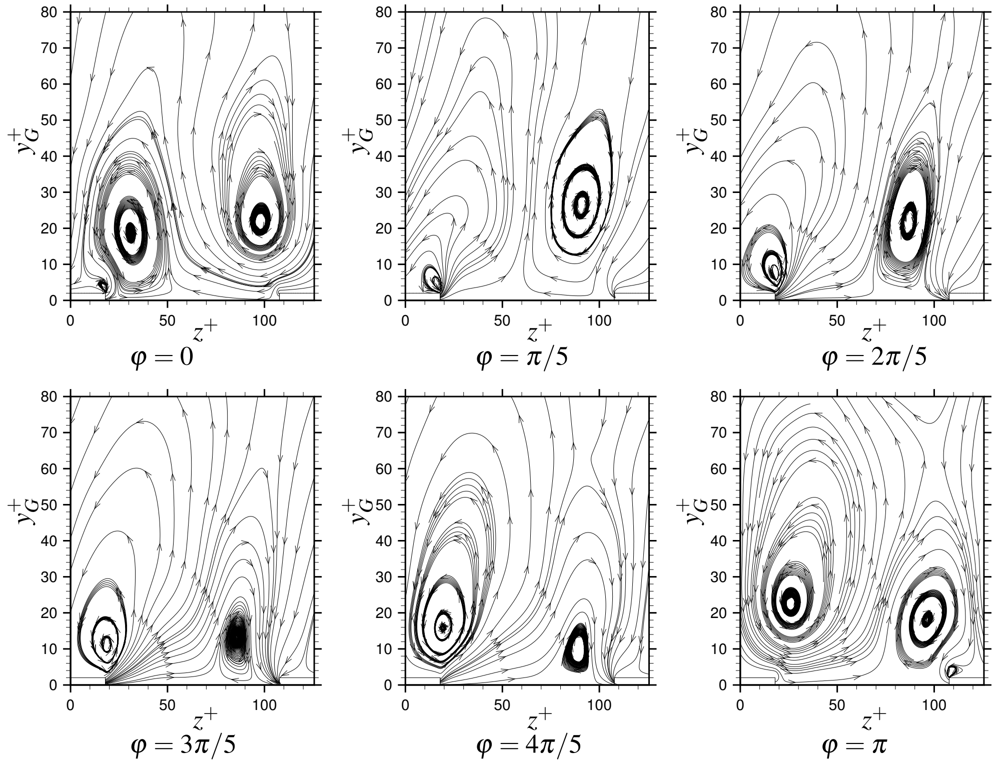

(b) $\beta = 75°$

Figure 5.56 Streamlines of the induce flow $(\langle w^+\rangle, \langle v^+\rangle)$ in the cross-stream $(y - z$ plane) view at different phase time φ for cases ZMJ($\beta = 0°$, $75°$).

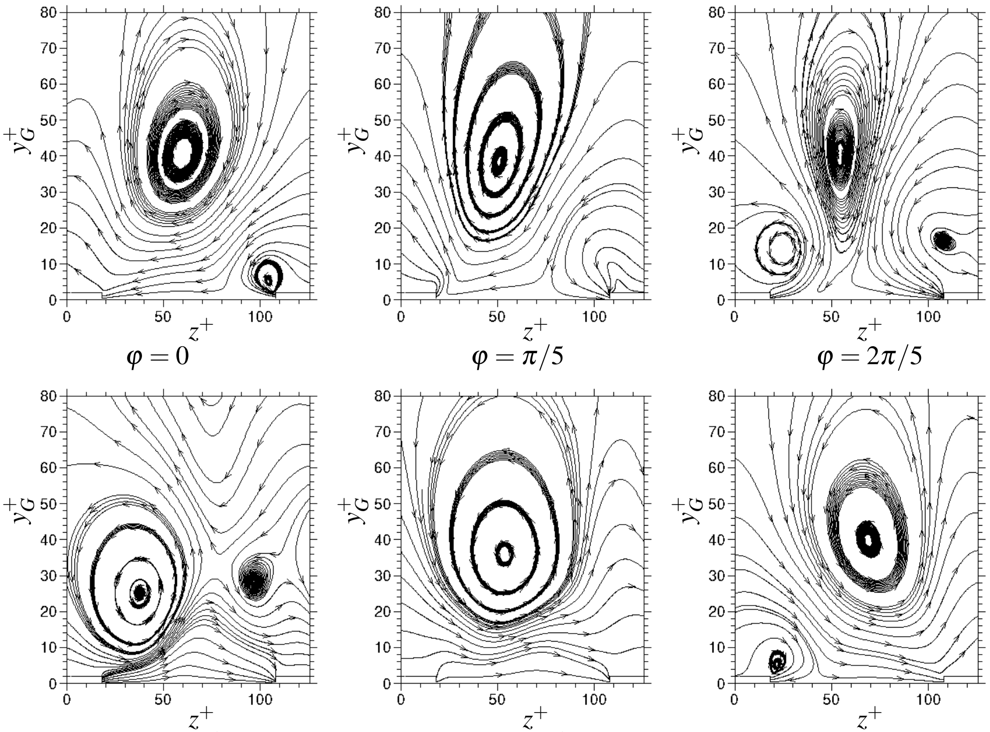

$\varphi = 0$ $\varphi = \pi/5$ $\varphi = 2\pi/5$

$\varphi = 3\pi/5$ $\varphi = 4\pi/5$ $\varphi = \pi$

(a) $\beta = 0°$

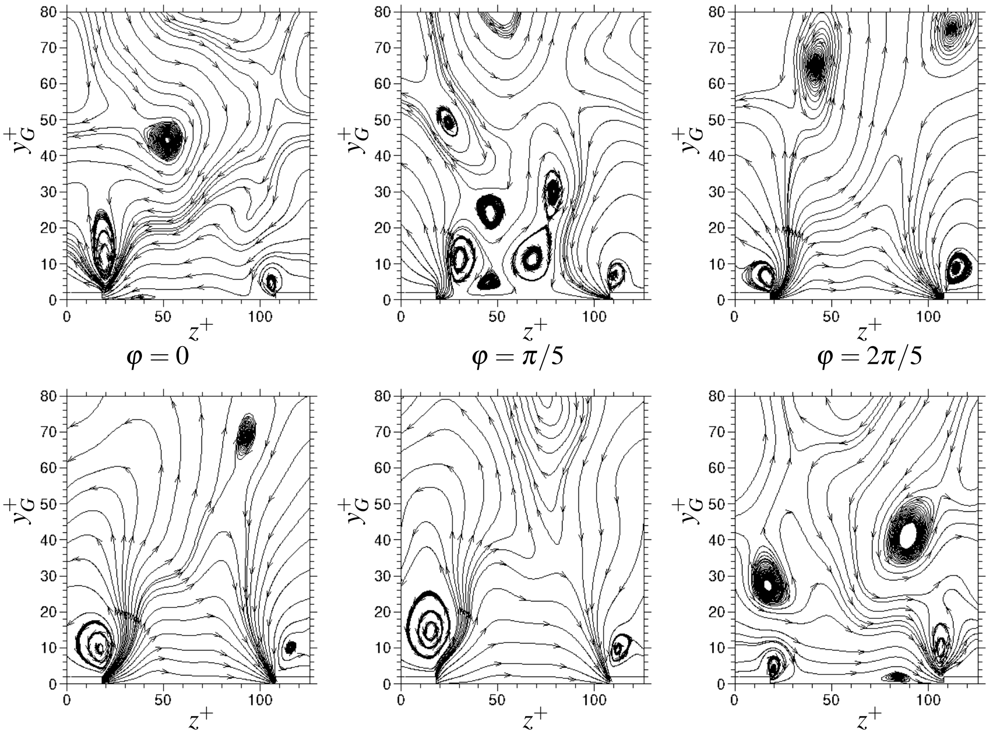

$\varphi = 0$ $\varphi = \pi/5$ $\varphi = 2\pi/5$

$\varphi = 3\pi/5$ $\varphi = 4\pi/5$ $\varphi = \pi$

(b) $\beta = 75°$

Figure 5.57 Streamlines of the induce flow $(\widetilde{w}^+, \widetilde{v}^+)$ in the cross-stream ($y - z$ plane) view at different phase time φ for cases ZMJ($\beta = 0°$, 75°).

Figure 5.57 shows the vortices induced by the periodic velocities, $(\widetilde{w}^+, \widetilde{v}^+)$. The vortices are generated by the blowing jet-exits and sucked in to the sucking jet-exits. In case ZMJ($\beta = 0°$), the large-scale vortex induced by the periodic velocities is similar to that created by the phased averaged flows. The large-scale vortex is formed by the blowing jets. But the small-scale vortex acts differently from the small-scale vortices in the phase averaged results. In case ZMJ($\beta = 75°$), the scales of vortices induced by the periodic velocities are smaller than that generated by the phased averaged flows. It is hardly to form large-scale vortex. At phase time $\varphi = \pi/5$ and π, when the vortex which created by blowing jet-exits leave the jet-exits, it is broken into small-scales vortices.

Figure 5.58 shows the contour plots of the Reynolds shear stress $-\langle u''v''\rangle/u_\tau^2$ given by the pure turbulent fluctuations. The Reynolds shear stress is nondimensionalized by

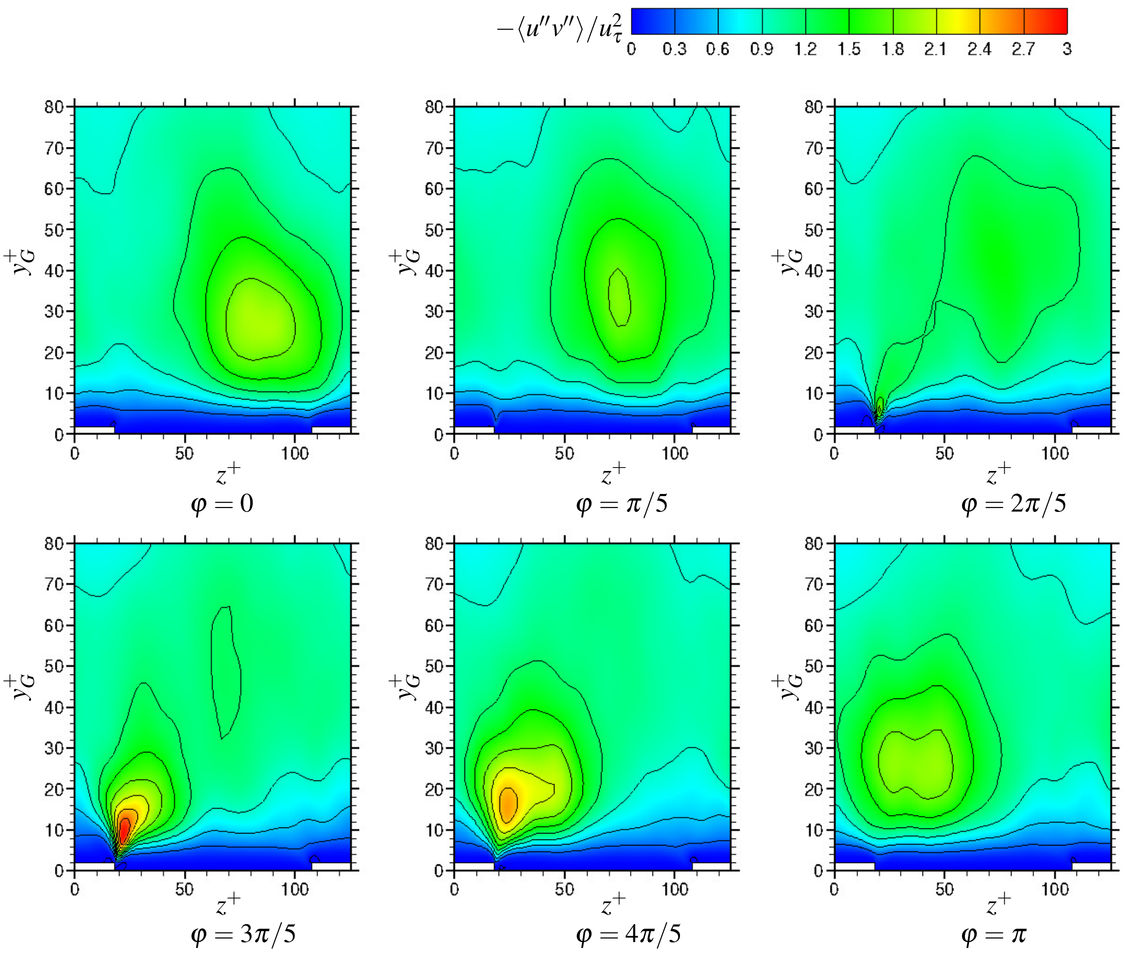

Figure 5.58 Contours of $-\langle u''v''\rangle/u_\tau^2$ in the cross-stream ($y - z$ plane) view at different phase time φ for case ZMJ($\beta = 75°$). The left jet-exits is blowing and the right jet-exits is sucking during $0 \leq \varphi \leq \pi$.

u_τ^2 which is based on the friction velocity of the smooth channel. The figure displays the results of case ZMJ($\beta = 75°$) at different phase time $\varphi = 0$, $\pi/5$, $2\pi/5$, $3\pi/5$, $4\pi/5$, π. In the figure, it indicates that the high Reynolds shear stress $-\langle u''v''\rangle/u_\tau^2$ is generated by the blowing jet-exits. The Reynolds shear stress increases and expends from $\varphi = 0$ to $3\pi/5$, and reaches its peak at $\varphi = 3\pi/5$ in the figure. After $\varphi = 3\pi/5$, the Reynolds shear stress keeps expending and begins to dissipate. When the phase time is between π and 2π, the contour plots are symmetric with that in the figure. The fluid with high Reynolds shear stress on the left sides is sucked into the left jet-exits and keeps dissipating. After a period, the new generated $\langle u''v''\rangle/u_\tau^2$ will be added into the left part of the flow. Comparing figure 5.58 and 5.38d, the Reynolds shear stress $\langle u''v''\rangle$ contributes little to $\overline{u'v'}$ near the jet-exits, and is the main contribution for $\overline{u'v'}$ away from the jet-exits. The reason is that the periodic velocities dominates the fluctuations near the jet-exits, and are weak away form the jet-exits.

Figure 5.59 displays the contour plots of $-\langle u''v''\rangle/u_\tau^2$ for case ZMJ($\beta = 0°$). The contour levels are different from case ZMJ($\beta = 75°$) to clearly show the distributions of $-\langle u''v''\rangle/u_\tau^2$. It is interesting to notice that the blowing jet-exits generate both positive and negative regions of $-\langle u''v''\rangle/u_\tau^2$ when $\beta = 0°$. This is different from case ZMJ($\beta = 75°$) which only produces positive $-\langle u''v''\rangle/u_\tau^2$. The negative $-\langle u''v''\rangle/u_\tau^2$ in these phase-averaged results creates two negative regions of $-\overline{u'v'}/u_\tau^2$ in the time-averaged results in figure 5.38b. The region of negative $-\langle u''v''\rangle/u_\tau^2$ is closer to the jet-exits than the positive region of $-\langle u''v''\rangle/u_\tau^2$. It seams that the positive region is pushed away from the jet-exits by the negative region. When the jet-exits changes the status from blowing to sucking, the fluid with negative $-\langle u''v''\rangle/u_\tau^2$ will be sucked in earlier than the fluid with positive $-\langle u''v''\rangle/u_\tau^2$. The influenced region when $\beta = 0°$ is stronger than that when $\beta = 75°$, expended to the log-law region. The peak value of the positive $-\langle u''v''\rangle/u_\tau^2$ in case ZMJ($\beta = 0°$) is larger than that in case ZMJ($\beta = 75°$). This can explain why the former Reynolds shear stress is higher than the latter one.

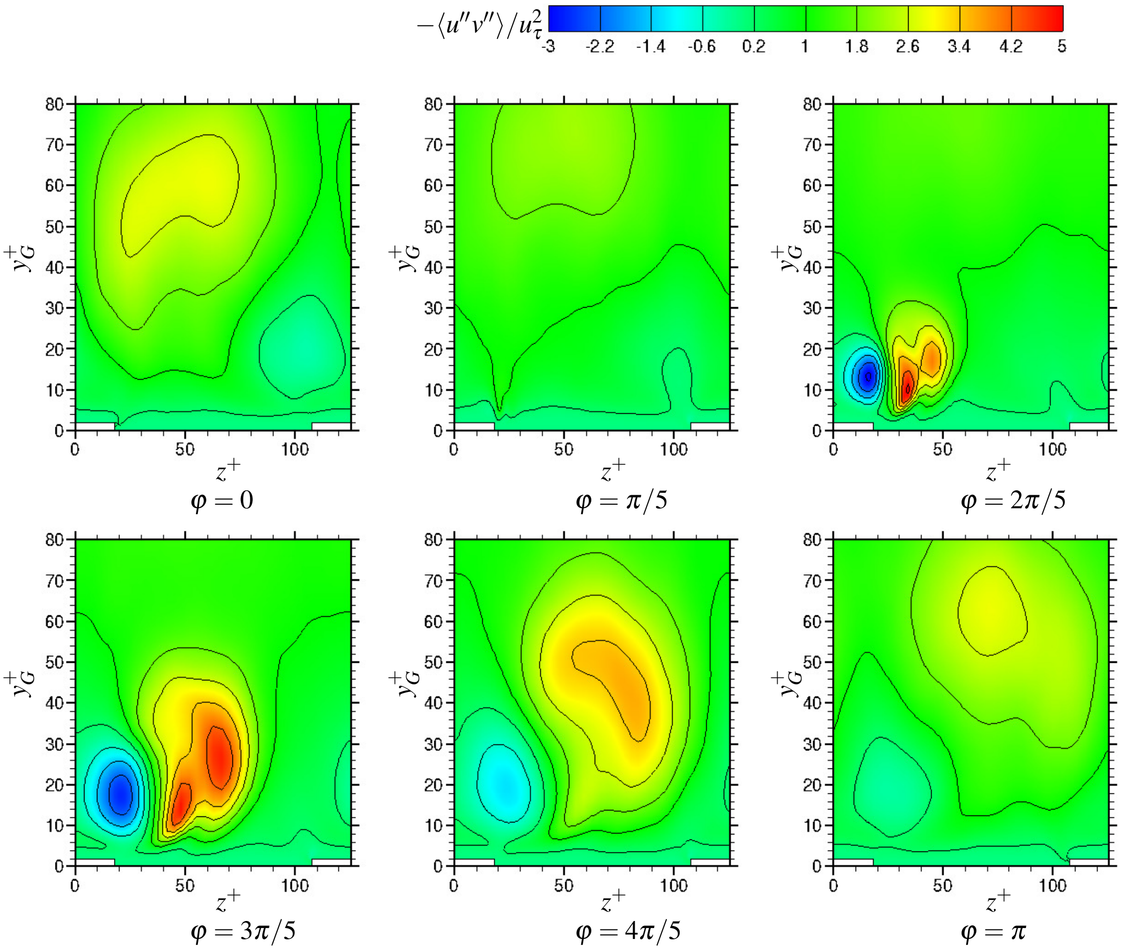

Figure 5.59 Contours of $-\langle u''v''\rangle/u_\tau^2$ in the cross-stream ($y-z$ plane) view at different phase time φ for case ZMJ($\beta = 0°$). The left jet-exits is blowing and the right jet-exits is sucking during $0 \leq \varphi \leq \pi$.

As the above discussion, the distributions of the Reynolds shear stress are very different between cases ZMJ($\beta = 0°$, $75°$). In order to clear show the difference, figure 5.60 compares $-\langle u''v''\rangle/u_\tau^2$ using the same contour levels at the phase time $\varphi = \pi/2$.

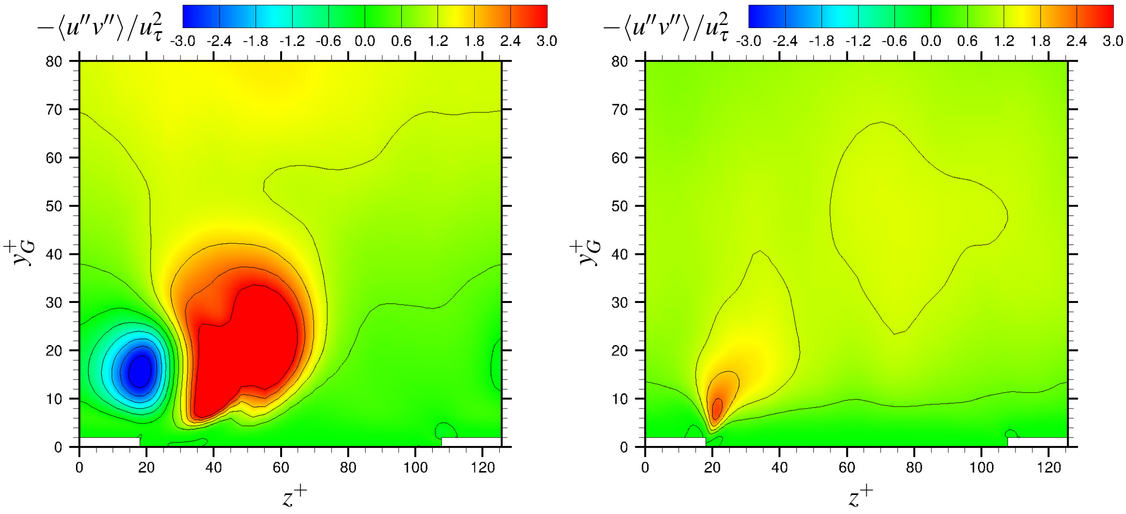

(a) $\beta = 0°$ (b) $\beta = 75°$

Figure 5.60 Contours of $-\langle u''v''\rangle/u_\tau^2$ at $\varphi = \pi/2$, comparing cases ZMJ($\beta = 0°$, $75°$).

As discussed before, case ZMJ($\beta = 0°$) has both positive and negative regions, but case ZMJ($\beta = 75°$) only has one positive region. To understand the reason, it is better to study the contributions of the Reynolds shear stress $\langle u''v''\rangle/u_\tau^2$ using the joint probability density functions and covariance integrand. Two positions are chosen to be investigated at the phase time $\varphi = \pi/2$. One position is at $(y_G^+ = 20, z^+ = 20)$ where is in the negative region when $\beta = 0°$. The other one is at $(y_G^+ = 20, z^+ = 50)$ where is in the positive region. At this phase time, the jet velocities of ZMJ reach their maximum, disturbing the flow the strongest.

The comparisons of the JPDF and covariance integrand between cases ZMJ($\beta = 0°$) and ZMJ($\beta = 75°$) at the phase time $\varphi = \pi/2$ are shown in figure 5.61. When ZMJ is on with $\beta = 0°$, the contributions of the Reynolds shear stress mainly come from Q1 and Q3 quadrants. The signs of $u''v''$ in the quadrants are always positive at the point $(y_G^+ = 20, z^+ = 20)$. The highest probability of $P(u''^+, v''^+)$ is in Q1 quadrant $(u''^+ > 0, v''^+ > 0)$. The contributions for the Reynolds shear stress $\langle u''v''\rangle$ is the highest from Q3 quadrant $(u''^+ < 0, v''^+ < 0)$. Therefore, the value of $-\langle u''v''\rangle/u_\tau^2$ is negative at the position $(y_G^+ = 20, z^+ = 20)$, when $\beta = 0°$. Under the same jet angle, at the position $(y_G^+ = 20, z^+ = 50)$, the pure turbulent velocity-fluctuations (u'', v'') mainly appear in Q2 quadrants. This indicates that the fluid tends to move upwards in the wall-normal direction and backwards in the streamwise direction. As expected, the most contribution for $\langle u''v''\rangle$ is from Q2 quadrant which gives

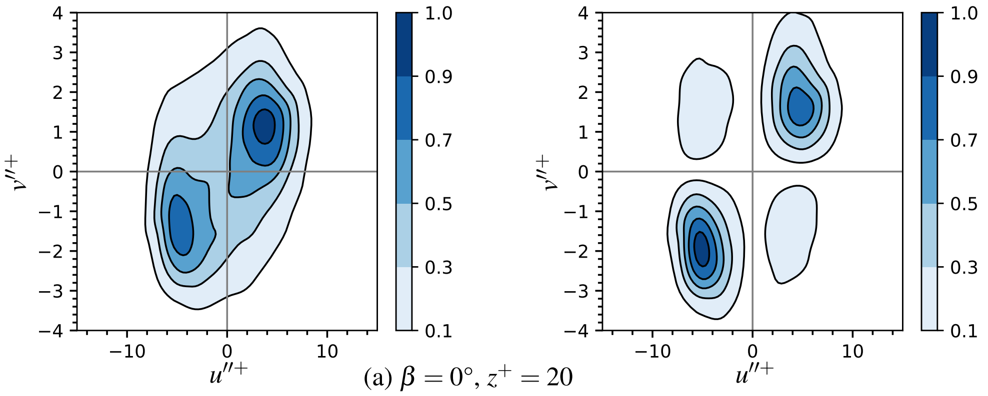

(a) $\beta = 0°$, $z^+ = 20$

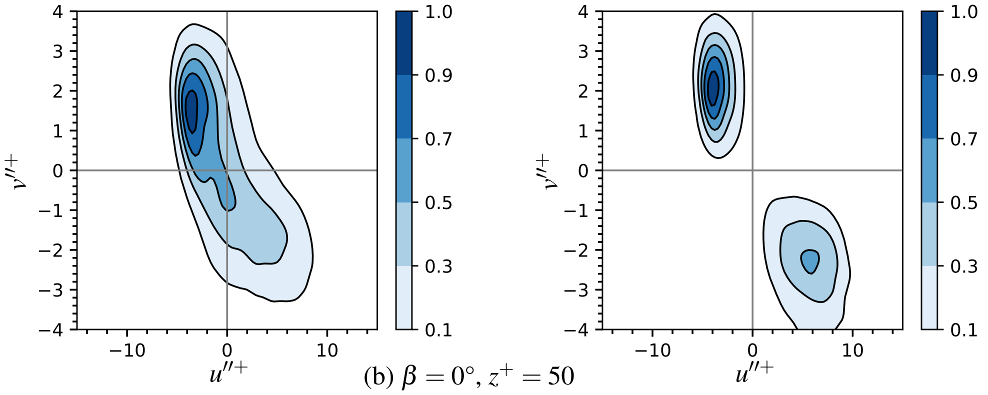

(b) $\beta = 0°$, $z^+ = 50$

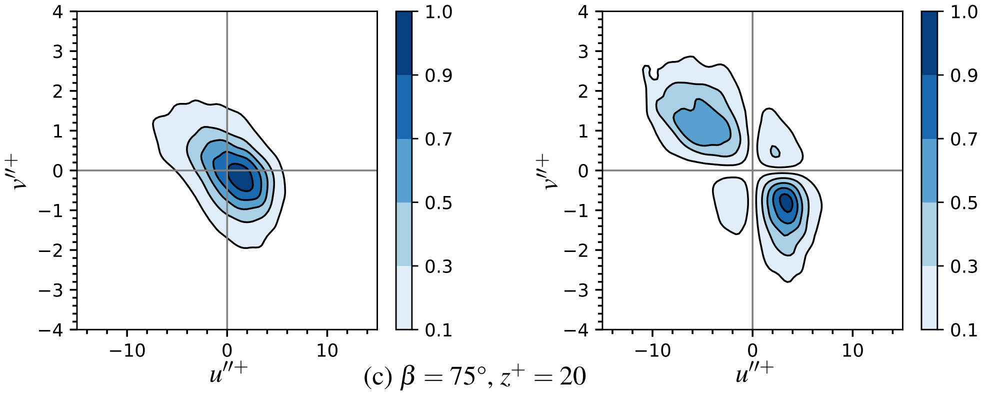

(c) $\beta = 75°$, $z^+ = 20$

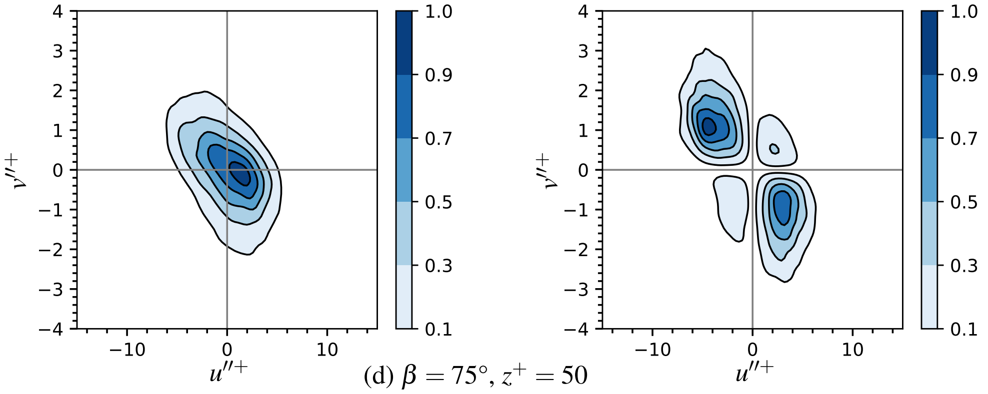

(d) $\beta = 75°$, $z^+ = 50$

Figure 5.61 The joint probability density function $P(u''^+, v''^+)$ (left) and covariance integrand $u''^+ v''^+ P(u''^+, v''^+)$ (right) at $y^+ = 20$, and $z^+ = 20$, 50, when $\beta = 0°, 75°$ at the phase time $\varphi = \pi/2$, giving $10, 30, 50, 70$ and 90% of the maximum probability level or covariance integrand.

a positive sign to $-\langle u''v''\rangle/u_\tau^2$. When $\beta = 75°$, the distributions of $P(u''^+, v''^+)$ at the two positions are similar to case ZMJ(off), having the highest probability in Q4 quadrant. From the plots of covariance integrand, it can be observed that the most contributions for $\langle u''v''\rangle$ are from Q4 quadrant and Q2 quadrant at the positions $(y_G^+ = 20, z^+ = 20)$ and $(y_G^+ = 20, z^+ = 50)$, respectively. This means that the ejections near the jet-exits and the sweeps near the middle of each sections are the most important fluid-motions for the Reynolds shear stress.

Figure 5.62 compares phase and space averaged profiles of the streamwise velocity $\langle u^+\rangle$ and Reynolds shear stress $-\langle u''v''\rangle/u_\tau^2$ at different phase time for case ZMJ($\beta = 75°$). The averaged profile of case ZMJ(off) is shown in the figure as well, highlighting the ZMJ effects. Figure 5.62b indicate that the profiles in the log-law regions are not different at different phase time. The profiles of Reynolds shear stress $-\langle u''v''\rangle/u_\tau^2$ in the log-law regions are quite closed to each other as shown in figure 5.62d. This means that the influence of ZMJ in the log-law region is not very different at different phase time. It is a good news for the turbulent modelling in the Reynolds averaged Navier-Stokes (RANS) simulations as mentioned at the end of the section 5.5. In the RANS simulation, the time step is relatively big. The result which is in a time-step of the RANS simulation can be treated as the time averaged result of the DNS simulation. A wall function can be designed to model the drag-reduction effects of ZMJ, which is similar to the modelling of the roughness wall.

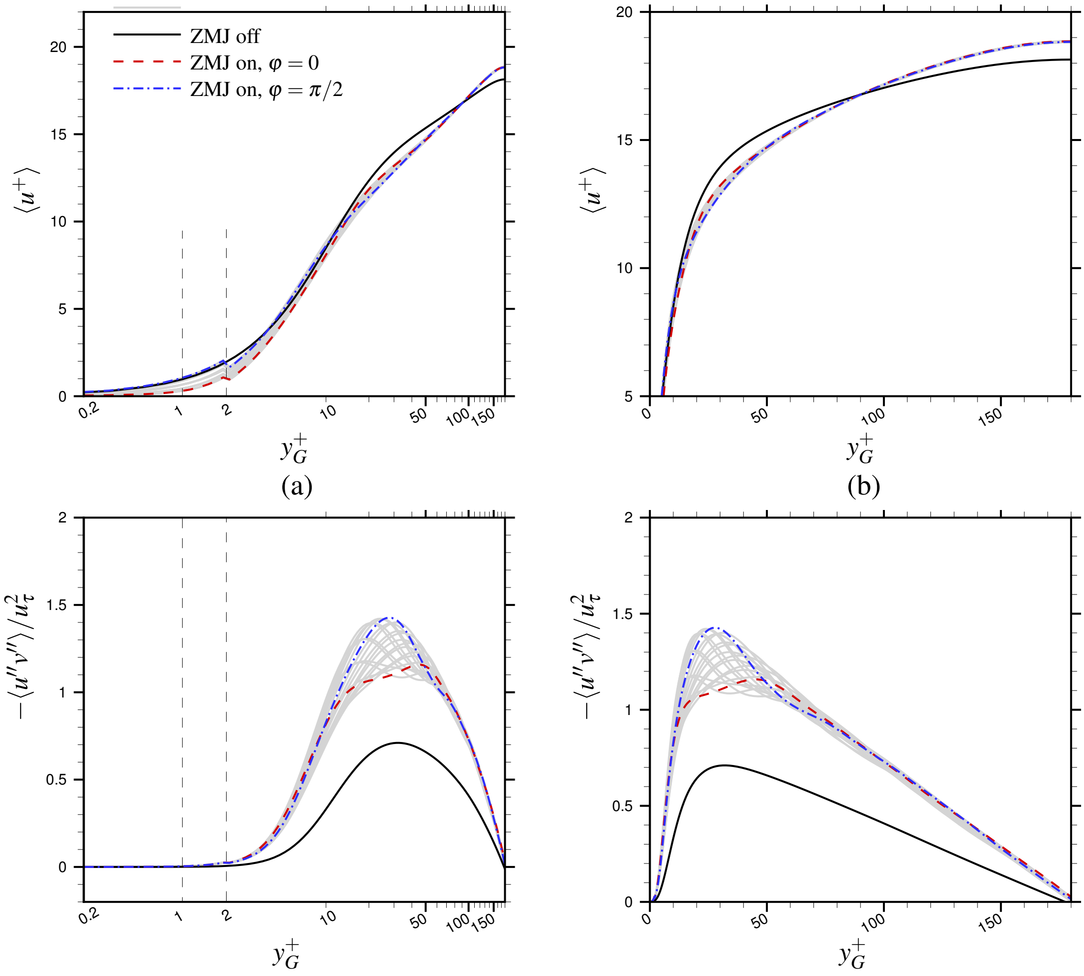

(a) (b)

(c) (d)

Figure 5.62 Comparisons of the phase and space averaged profiles at different phase time between cases ZMJ(off) and ZMJ($\beta = 75°$). The left figures are in inner-scale units to show the viscous sublayer, and the right figures are in outer-scale units to show the log-law regions. The grey lines are at the other phase time which are not listed in the line legend.

5.7 Detailed flow structures

In the previous studies, the results are averaged to statistically analyse the flow fields and to find out the mechanisms of the drag reduction. In this section, it will focus on the instantaneous flow to study the flow features. To show the differences of the instantaneous flow between increasing and decreasing the drag with ZMJ, the cases ZMJ($\beta = 0°$) and ZMJ($\beta = 75°$) are chosen to be compared with each other.

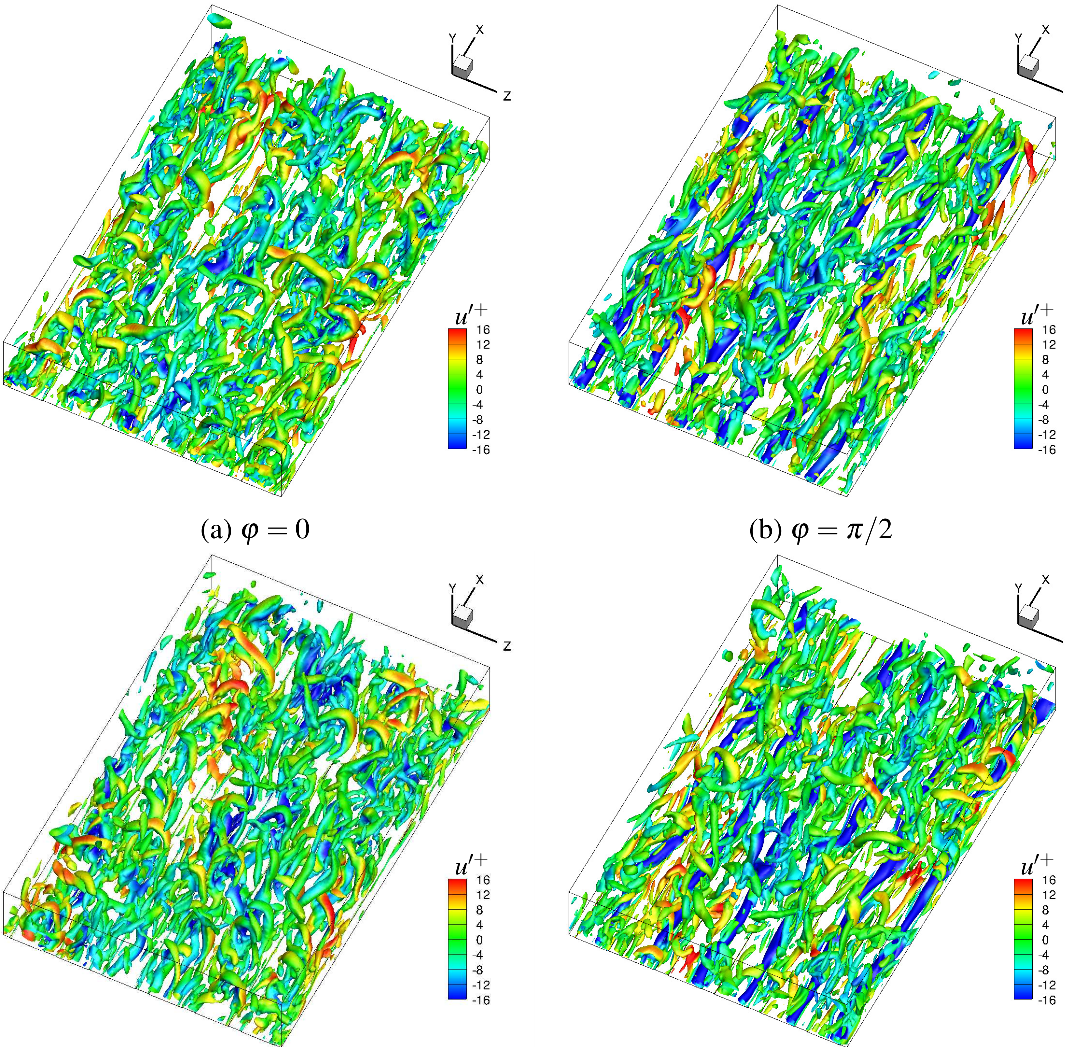

(a) $\varphi = 0$

(b) $\varphi = \pi/2$

(c) $\varphi = \pi$

(d) $\varphi = 3\pi/2$

Figure 5.63 In case ZMJ($\beta = 0°$), the iso-surfaces of $\lambda_2^+ = -2$ in the half channel at the different phase time $\varphi = 0,\ \pi/2,\ \pi,\ 3\pi/2$. The iso-surfaces are coloured by u'^+.

Figures 5.63 and 5.64 show the iso-surfaces of $\lambda_2^+ = -2$ in the half channel at different phase time for cases ZMJ($\beta = 0°$) and ZMJ($\beta = 75°$), respectively. The iso-surfaces are coloured by u'^{+} which is the total fluctuation of streamwise velocity. λ_2 method is an algorithm to detect the vortex core line, determining any point in the fluid whether this point is in the region of a vortex core. Additional vortices are generated by ZMJ in the channel flow. Comparing the figures, the vortex structures when $\beta = 0°$ are more than that when $\beta = 75°$. This is expected because the spanwise strength of ZMJ when $\beta = 0°$ is stronger than that when $\beta = 75°$. Figures 5.63b and 5.63d show that the blowing jet-exits generate the vortices and the sucking jet-exits discriminate the vortices.

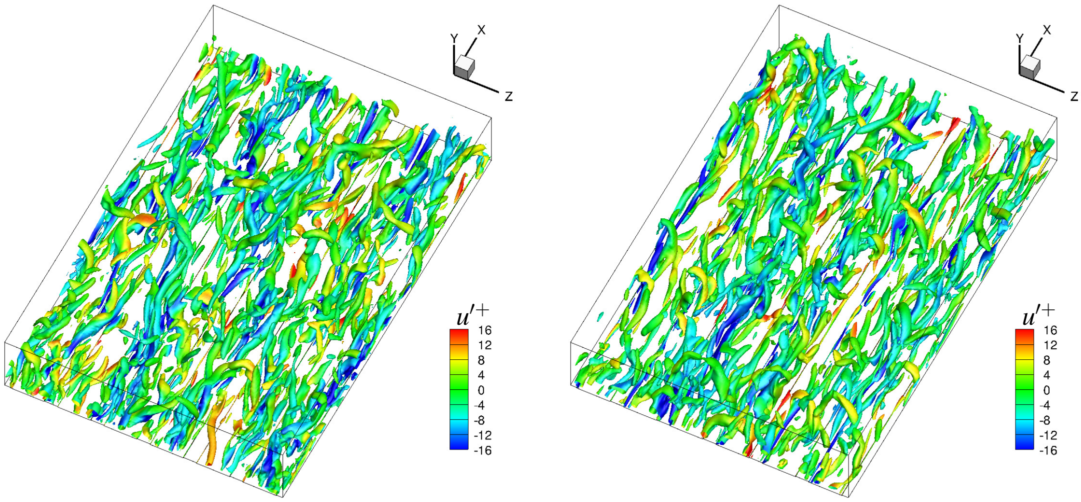

(a) $\varphi = 0$ (b) $\varphi = \pi/2$

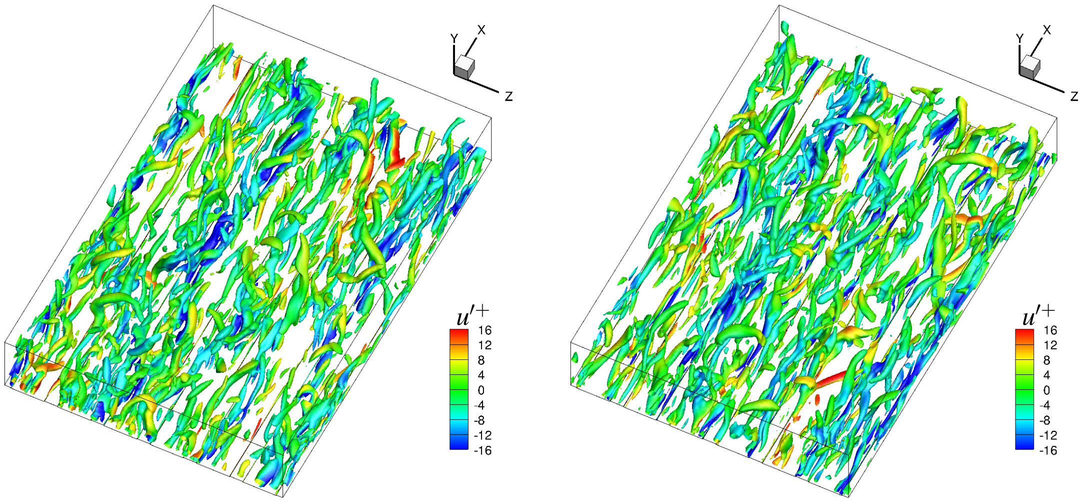

(c) $\varphi = \pi$ (d) $\varphi = 3\pi/2$

Figure 5.64 In case ZMJ($\beta = 75°$), the iso-surfaces of $\lambda_2^{+} = -2$ in the half channel at the different phase time $\varphi = 0$, $\pi/2$, π, $3\pi/2$. The iso-surfaces are coloured by u'^{+}.

Figures 5.65 and 5.66 represent the contour plots of the instantaneous streamwise-velocity u^+ in the $x-z$ plane at $y_G^+ = 5$ for cases ZMJ($\beta = 0°$) and ZMJ($\beta = 75°$), respectively. In order to study the jet effects on the streamwise velocity, the instantaneous results at different phase time are shown in the figures. Comparing the figures between two cases, most of the regions in case ZMJ($\beta = 0°$) has higher velocity than that in case ZMJ($\beta = 75°$). This is agreed with the studies of the time averaged results. In the figures, the spanwise direction of ZMJ is upwards in the positive direction of $z-$axis. Figure 5.65 shows that the high-velocity regions are most likely to cluster near the jet-exits, especially the sucking jet-exits. When the jet velocity increases, the regions are elongated on the sucking sides of ZMJ. When the jet velocity decreases, the regions are broken to be smaller. The distinctive feature of the flow patterns in figure 5.66 is the existence of highly elongated regions of negative velocity are generated by the blowing jet-exits. It needs to be emphasised that the jet velocity reaches its maximum at the phase time $\varphi = \pi/2$. When the jet velocity is around its maximum value, the negative-velocity regions continuously located adjacent to the blowing jet-exits. The regions are being broken and eliminated when the jet speed decreases below a certain level. In case ZMJ($\beta = 75°$), the sucking jet-exits also produce the high-velocity regions which are not as continuous as the negative-velocity regions.

Figures 5.67 and 5.68 show the total fluctuations of the streamwise velocity u'^+ in the $x-z$ plane at $y^+ = 5$ for cases ZMJ($\beta = 0°$) and ZMJ($\beta = 75°$), respectively. Figures 5.65 and 5.67 are based on the same results. Figures 5.66 and 5.68 are post processed from the same results as well. As shown in the figures, the low-speed regions are longer than the high-speed regions. The low-speed regions are created by the blowing jet-exits which eject the ZMJ into the channel. The high-speed regions are caused by the sucking jet-exits which bring down the fluid from the main flow. The fluctuations in ZMJ is quiet than that in the main flow, so the low-speed regions are more continuous than the high-speed regions. The figures also display that the long and strong low-speed regions when $\beta = 75°$ appear later than that when $\beta = 0°$. The reason is that the spanwise velocity of ZMJ in case ZMJ($\beta = 75°$) is smaller than that in case ZMJ($\beta = 0°$), so the low-speed regions are spread slower by ZMJ in case ZMJ($\beta = 75°$). Also, the low-speed regions in case ZMJ($\beta = 75°$) are damaged slower.

In figures 5.67 and 5.68, the low-speed regions can be distinguished near the blowing jet-exits, and the high-speed regions are located adjacent to the sucking jet-exits. To study the wall-normal movements of the low-speed or high-speed regions, the contour plots of u'^+ in the $y-z$ plane are displayed in figures 5.69 and 5.70. The figures correspond to the same flow fields in figures 5.67 and 5.68. Only the bottom half of the channel flow is shown in figures 5.69 and 5.70. The top half should be statistically symmetric with the bottom half.

Throughout the figures, it is easy to distinguish the vortex shape besides the blowing jet-exits. The shape is visually shown by the low-speed regions, because the vortices are generated by the countering jets which decrease the streamwise velocity of the fluid near the blowing jet-exits. From the beginning of the phase time, a small vortex is produced by each of the blowing jets, which grows up to be mixed with the vortices in the controlled channel until the end of the phase time.

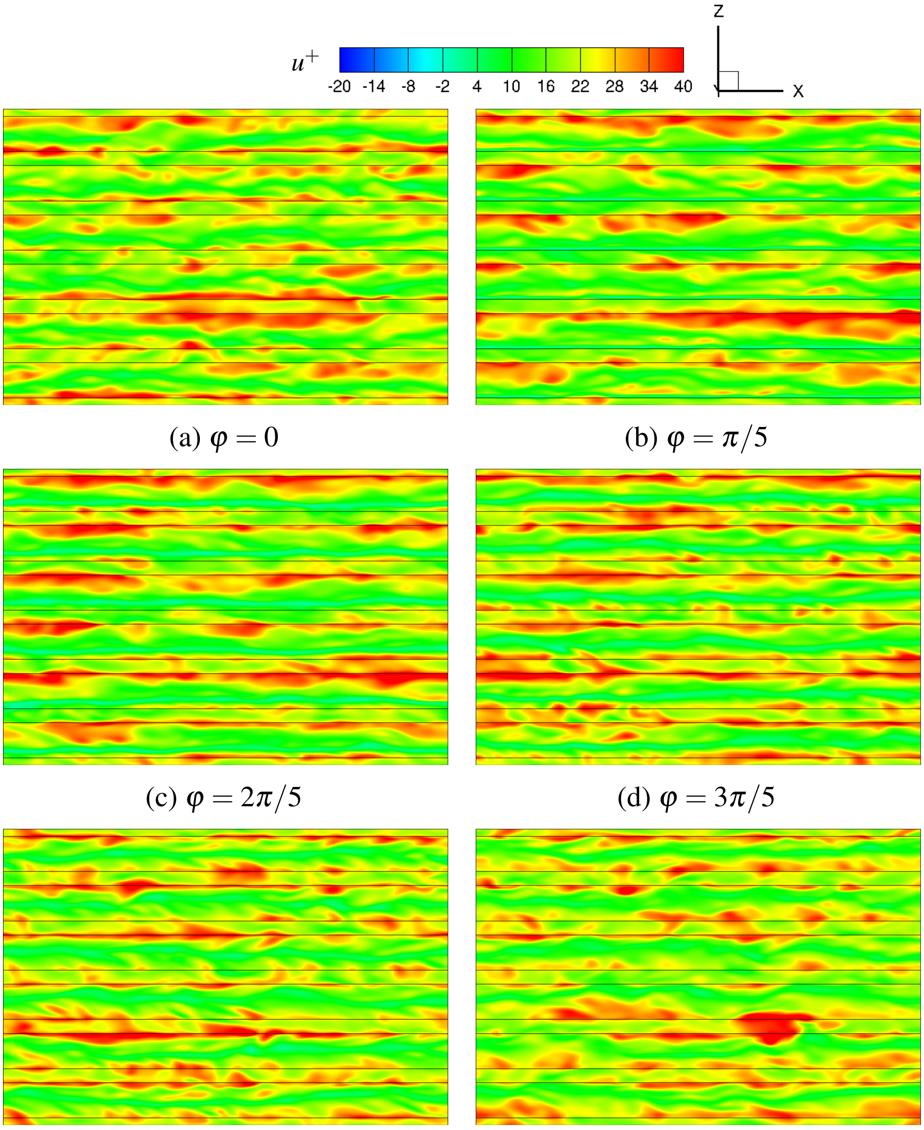

(a) $\varphi = 0$ (b) $\varphi = \pi/5$

(c) $\varphi = 2\pi/5$ (d) $\varphi = 3\pi/5$

(e) $\varphi = 4\pi/5$ (f) $\varphi = \pi$

Figure 5.65 In case ZMJ($\beta = 0°$), contours of the streamwise velocity u^+ in the $x - z$ plane at $y_G^+ = 5$ and the different phase time $\varphi = 0,\ \pi/5,\ 2\pi/5,\ 3\pi/5,\ 4\pi/5,\ \pi$. The black lines are the geometry edges.

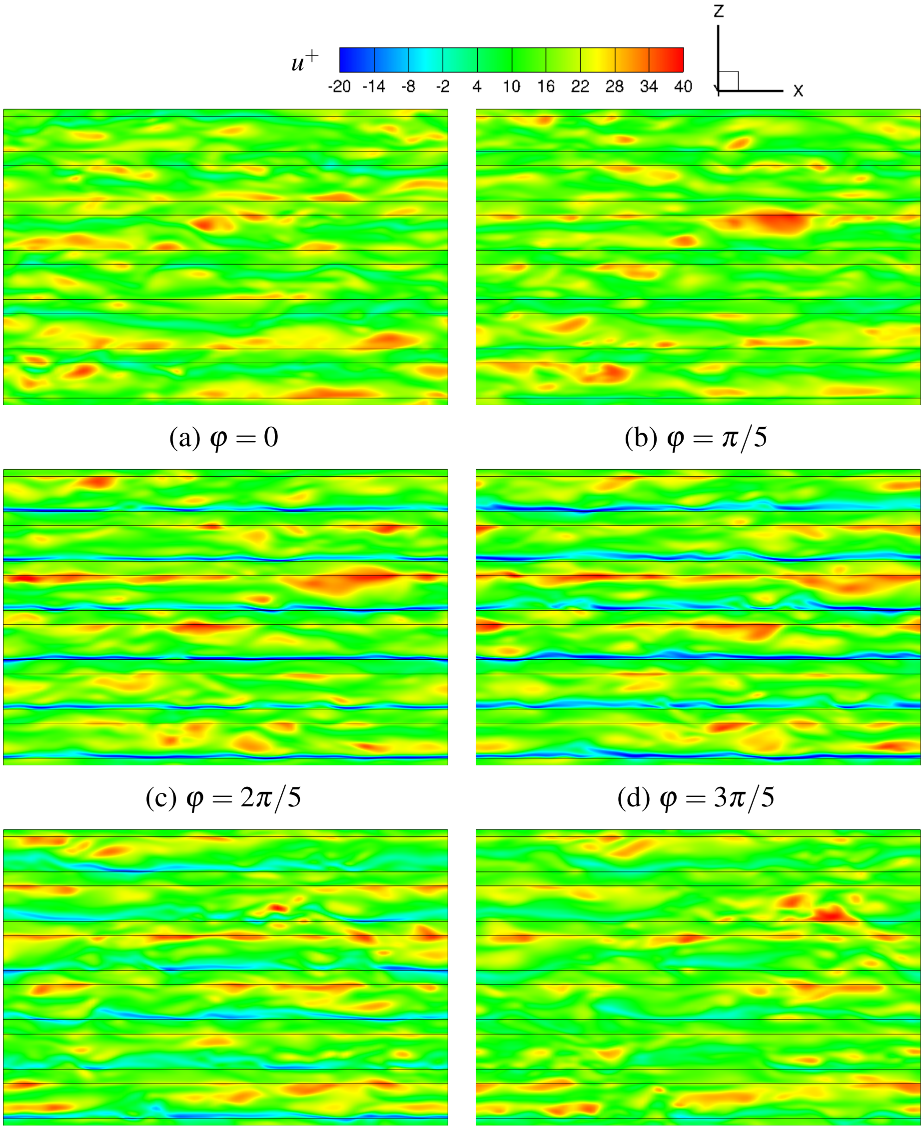

(a) $\varphi = 0$

(b) $\varphi = \pi/5$

(c) $\varphi = 2\pi/5$

(d) $\varphi = 3\pi/5$

(e) $\varphi = 4\pi/5$

(f) $\varphi = \pi$

Figure 5.66 In case ZMJ($\beta = 75°$), contours of the streamwise velocity u^+ in the $x-z$ plane at $y_G^+ = 5$ and the different phase time $\varphi = 0$, $\pi/5$, $2\pi/5$, $3\pi/5$, $4\pi/5$, π. The black lines are the geometry edges.

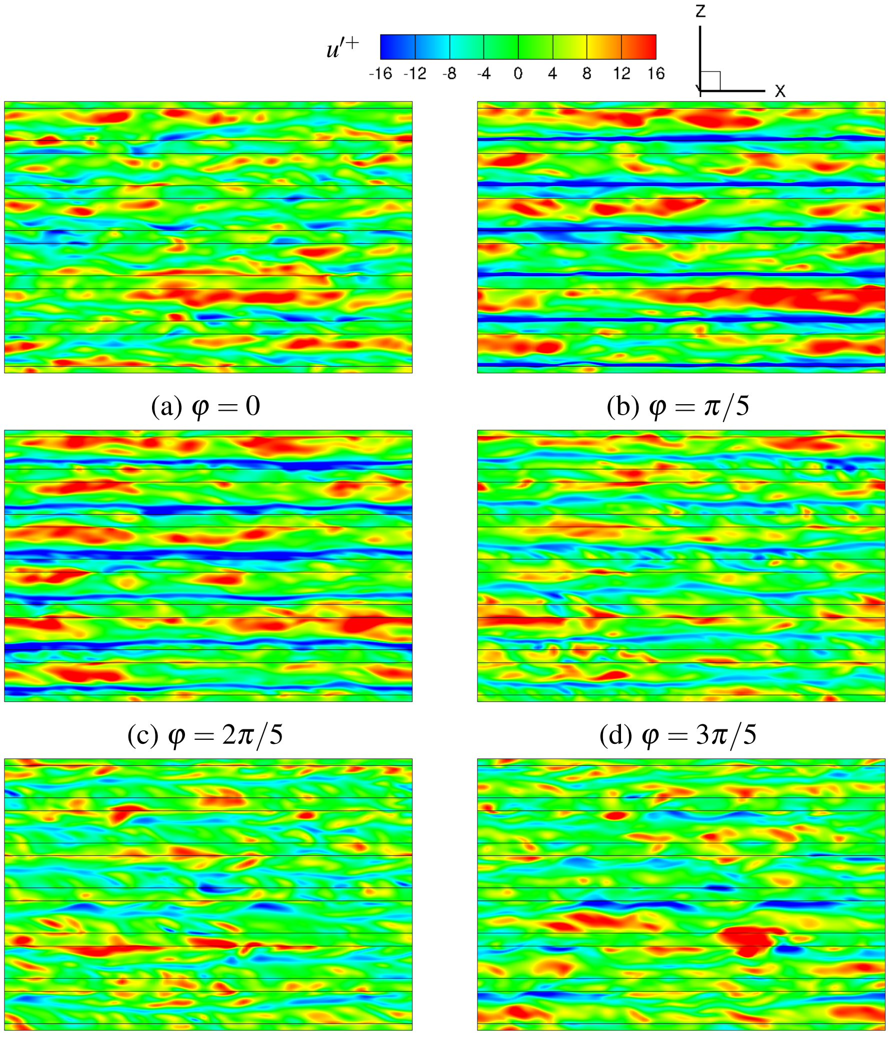

(a) $\varphi = 0$

(b) $\varphi = \pi/5$

(c) $\varphi = 2\pi/5$

(d) $\varphi = 3\pi/5$

(e) $\varphi = 4\pi/5$

(f) $\varphi = \pi$

Figure 5.67 In case ZMJ($\beta = 0°$), the contours of u'^+ in the $x-z$ plane at $y_G^+ = 5$ and at the different phase time $\varphi = 0$, $\pi/5$, $2\pi/5$, $3\pi/5$, $4\pi/5$, π. The black lines are the geometry edges.

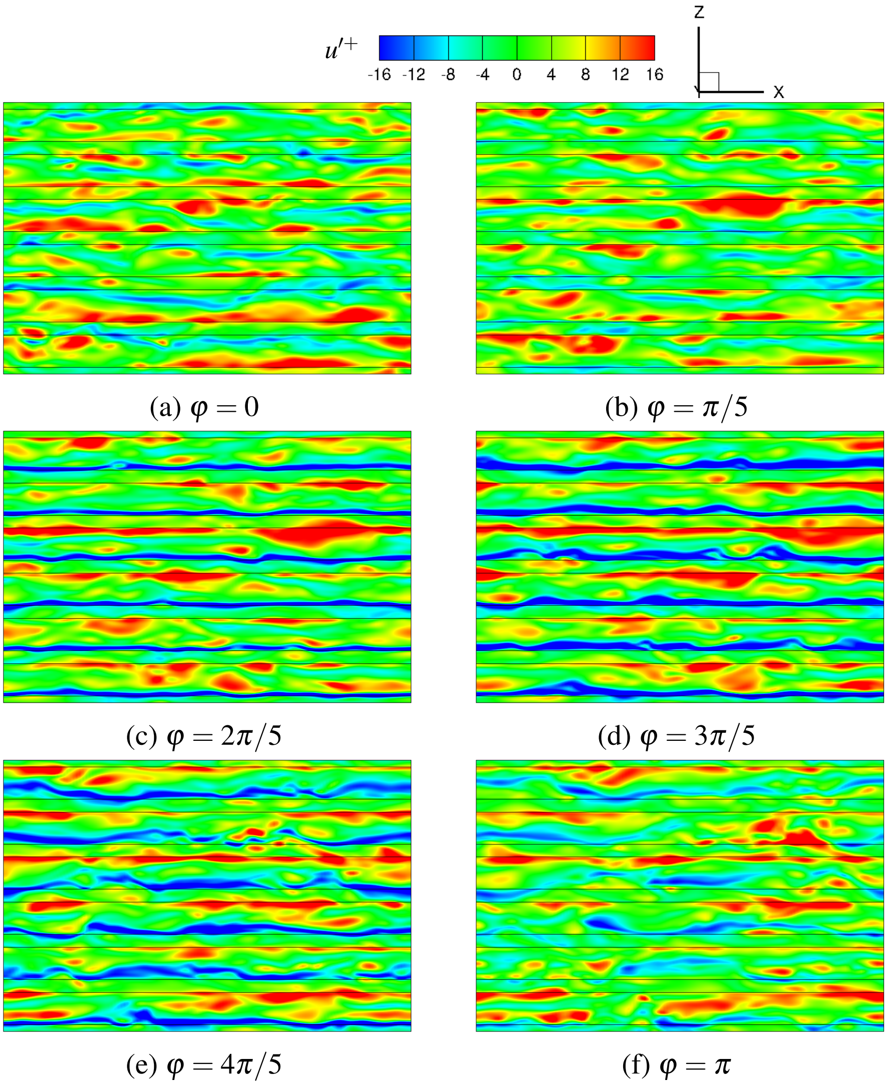

(a) $\varphi = 0$ (b) $\varphi = \pi/5$

(c) $\varphi = 2\pi/5$ (d) $\varphi = 3\pi/5$

(e) $\varphi = 4\pi/5$ (f) $\varphi = \pi$

Figure 5.68 In case ZMJ($\beta = 75°$), the contours of u'^+ in the $x - z$ plane at $y_G^+ = 5$ and at the different phase time $\varphi = 0$, $\pi/5$, $2\pi/5$, $3\pi/5$, $4\pi/5$, π. The black lines are the geometry edges.

Comparing figures 5.69 and 5.70, the size of the vortices generated by the blowing jet-exits in case ZMJ($\beta = 0°$) is bigger than that in case ZMJ($\beta = 75°$). Case ZMJ($\beta = 0°$) ejects the low-speed fluid higher than case ZMJ($\beta = 75°$), so that the peak position of the velocity fluctuations near the blowing jet-exits when $\beta = 0°$ is higher than that when $\beta = 75°$, as shown in figure 5.55b. Because the spanwise strength of ZMJ in case ZMJ($\beta = 0°$) is stronger than that in case ZMJ($\beta = 75°$). Throughout the figures, case ZMJ($\beta = 0°$) influences the spanwise and wall-normal directions stronger than case ZMJ($\beta = 75°$). The influence increases the Reynolds stresses and the friction drag, which is a drawback for the drag reduction. The strong influence of case ZMJ($\beta = 75°$) is more constrained near the jet-exits than that of case ZMJ($\beta = 0°$). The negative streamwise-velocity of ZMJ can produce the countering jets to significantly reduce the friction drag, so the drag reduction can be achieved when $\beta = 75°$.

Figure 5.71 shows the contour plots of u''^{+} and v''^{+} in the $y-z$ plane at the same streamwise position $x^{+} = 5$ and the same phase time $\varphi = \pi/2$. Only bottom half of the channel flow is displayed in the figures. In a big percentage of the region displayed, the correlation between u''^{+} and v''^{+} is negative. Some of the negative regions extend from the wall region to the central line of the controlled channel. In case ZMJ($\beta = 0°$), a positive correlation between u''^{+} and v''^{+} can be found near the blowing jet-exits. The interaction of the fluid near the blowing jet-exits is dominated by the blowing jet in case ZMJ($\beta = 0°$). When the jets interacts with the step corners, the vortices are generated. The vortices are different from the existed vortices in the main flow. The existed vortices prefer giving negative correlation to positive correlation, but the vortices caused by ZMJ prefer positive. There is a mixing effect between two kinds of vortices. Because the vortices caused by ZMJ in case ZMJ($\beta = 0°$) is strong enough to overcome the existed vortices. The correlation between u''^{+} and v''^{+} can be positive near the jet-exits. The joint probability density function $P(u''^{+}, v''^{+})$ of the point which is in the positive regions is shown in figure 5.61a. When ZMJ is on with $\beta = 75°$, the blowing jets in the spanwise direction is weaker than that when $\beta = 0°$. The blowing jet cannot create the strong vortices to overcome the mixing effects from the main flow. The negative correlation between u''^{+} and v''^{+} still dominates the regions near the blowing jet-exits.

In figure 5.72, the vortex regions $\lambda_2^{+} < -2$ are coloured with blue in the $y-z$ plane at $x^{+} = 5$ for case ZMJ($\beta = 0°$) and ZMJ($\beta = 75°$). The phase time is $\varphi = 0, \pi/2$. The contour lines of u''^{+} are shown in the figure to display the low-speed and high-speed regions. The solid lines denote the high-speed regions where are $(u''^{+} > 0)$, and the dashed lines show the low-speed regions where are $(u''^{+} < 0)$. From the figures, it is interesting to notice that the vortices are clustered in the low-speed regions, and between the high-speed and low-speed regions. The size of the vortices generated by ZMJ when $\beta = 75°$ is much smaller than that when $\beta = 0°$. The generated vortices are close to the wall at the phase time $\varphi = \pi/2$ when ZMJ is the strongest. At the phase time $\varphi = 0$, the vortices are brought away from the wall by the low-speed regions. The vortices in case ZMJ($\beta = 0°$) are more possible to be close to the channel centre than case ZMJ($\beta = 75°$).

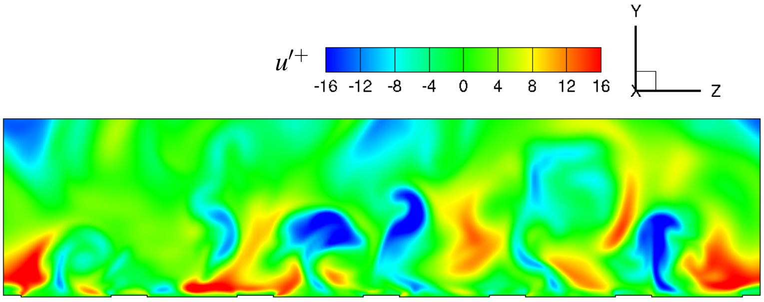

(a) $\varphi = 0$

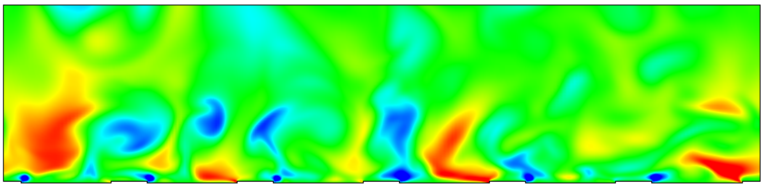

(b) $\varphi = \pi/5$

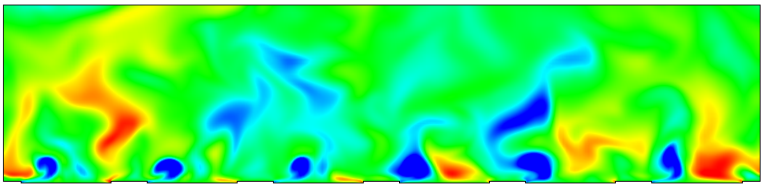

(c) $\varphi = 2\pi/5$

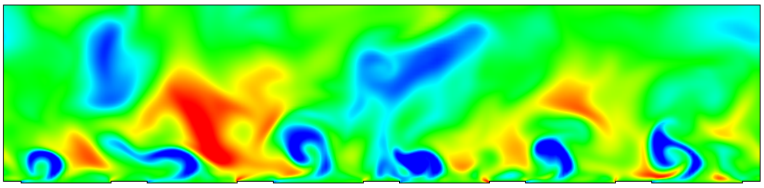

(d) $\varphi = 3\pi/5$

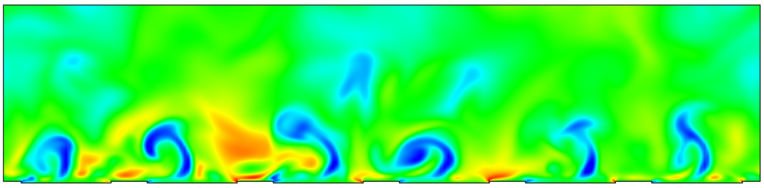

(e) $\varphi = 4\pi/5$

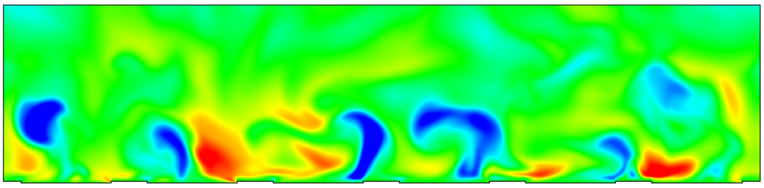

(f) $\varphi = \pi$

Figure 5.69 In case ZMJ($\beta = 0°$), the contours of u'^+ in the $y-z$ plane at $x^+ = 5$ and the different phase time $\varphi = 0$, $\pi/5$, $2\pi/5$, $3\pi/5$, $4\pi/5$, π.

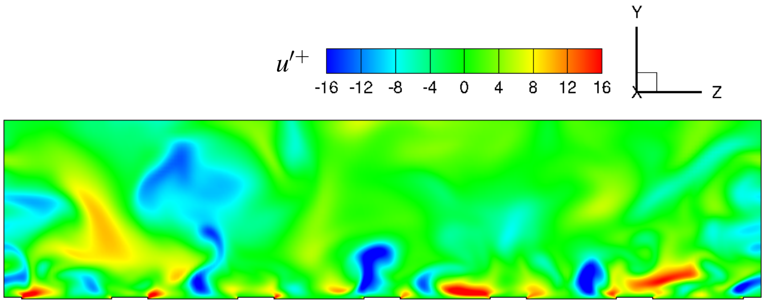

(a) $\varphi = 0$

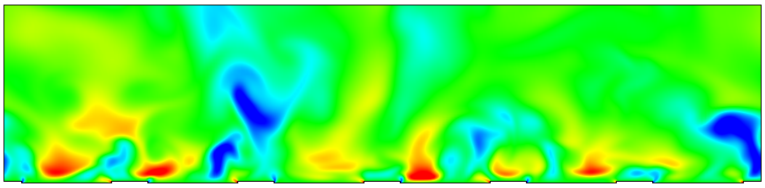

(b) $\varphi = \pi/5$

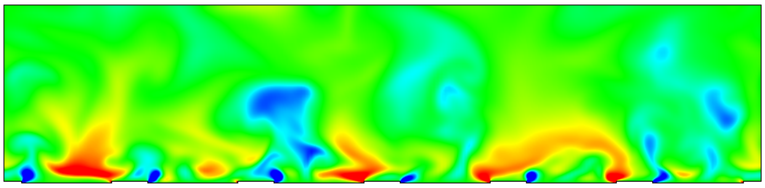

(c) $\varphi = 2\pi/5$

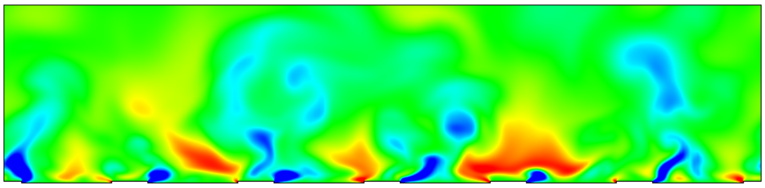

(d) $\varphi = 3\pi/5$

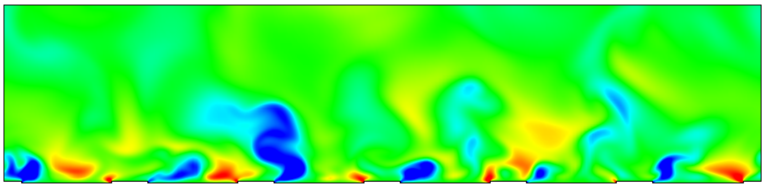

(e) $\varphi = 4\pi/5$

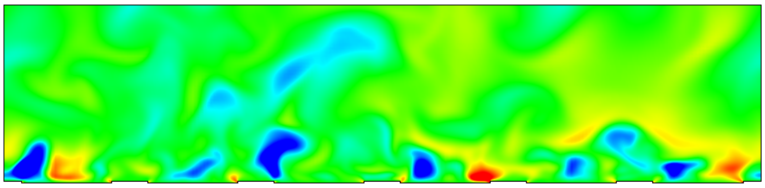

(f) $\varphi = \pi$

Figure 5.70 In case ZMJ($\beta = 75°$), the contours of u'^+ in the $y-z$ plane at $x^+ = 5$ and the different phase time $\varphi = 0,\ \pi/5,\ 2\pi/5,\ 3\pi/5,\ 4\pi/5,\ \pi$.

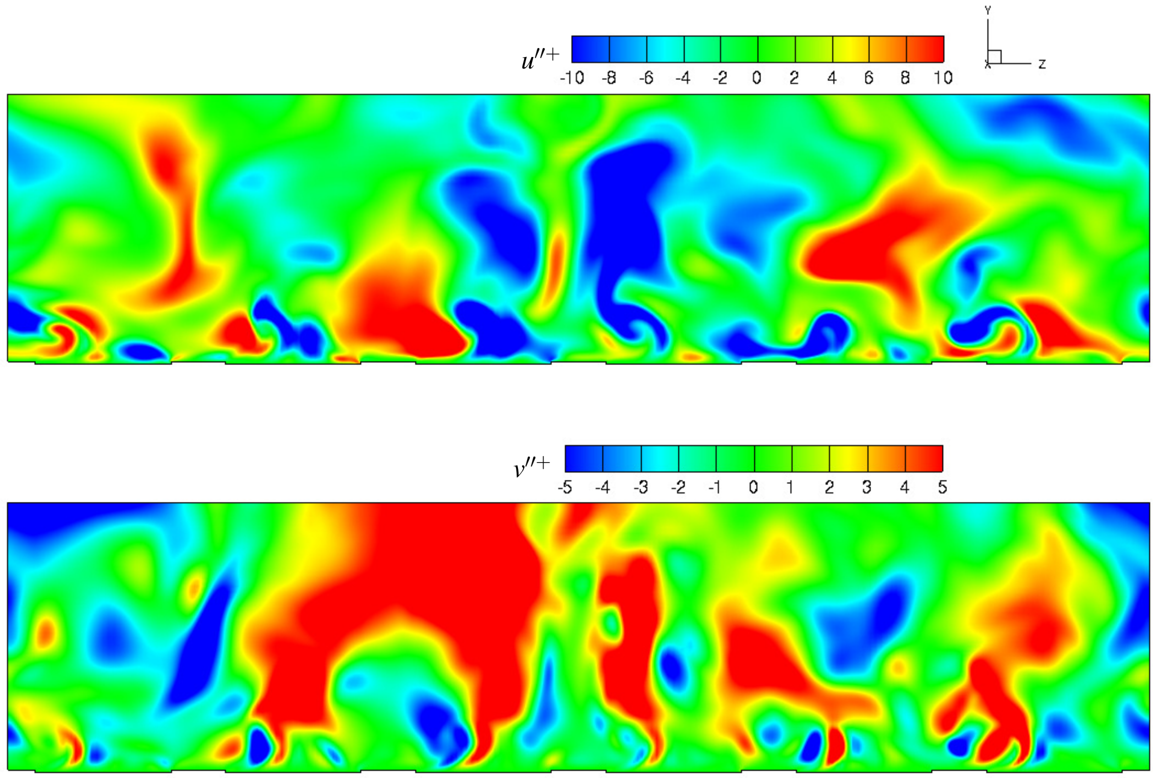

(a) $\beta = 0°$

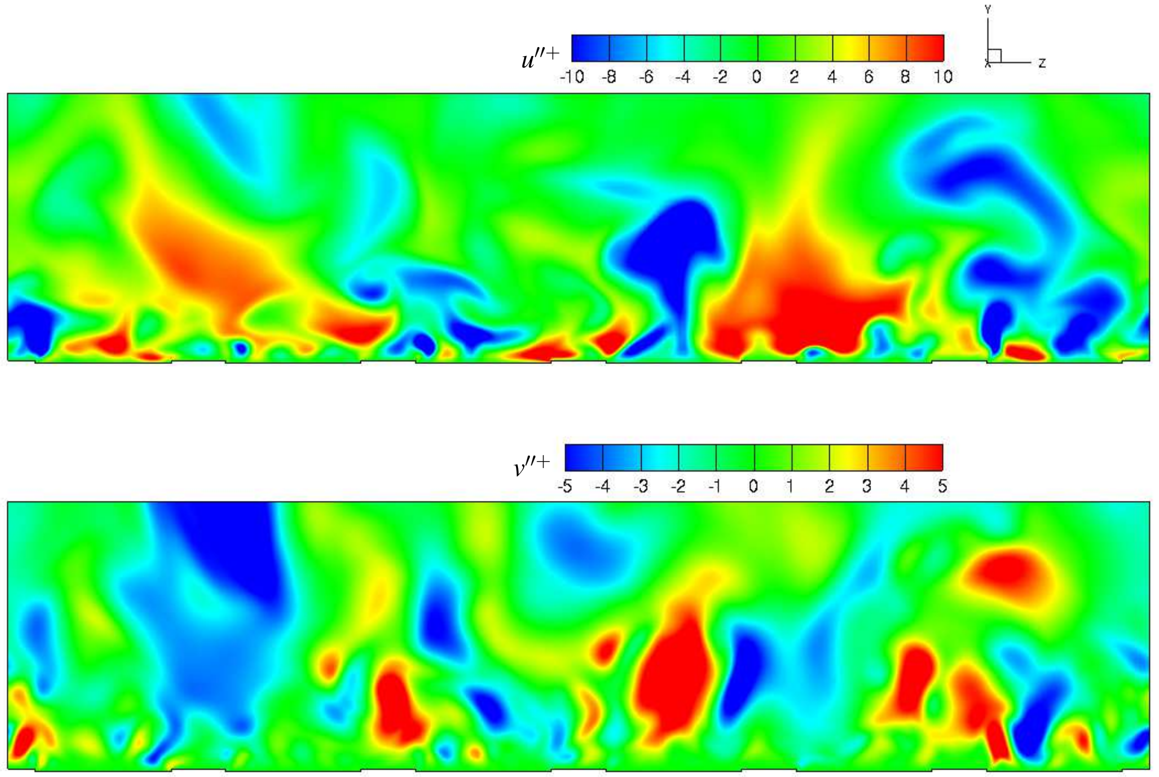

(b) $\beta = 75°$

Figure 5.71 In cases ZMJ($\beta = 0°$) and ZMJ($\beta = 75°$), the contours of u''^+ (top) and v''^+ (bottom) in the $y-z$ plane at $x^+ = 5$ and the same phase time $\varphi = \pi/2$.

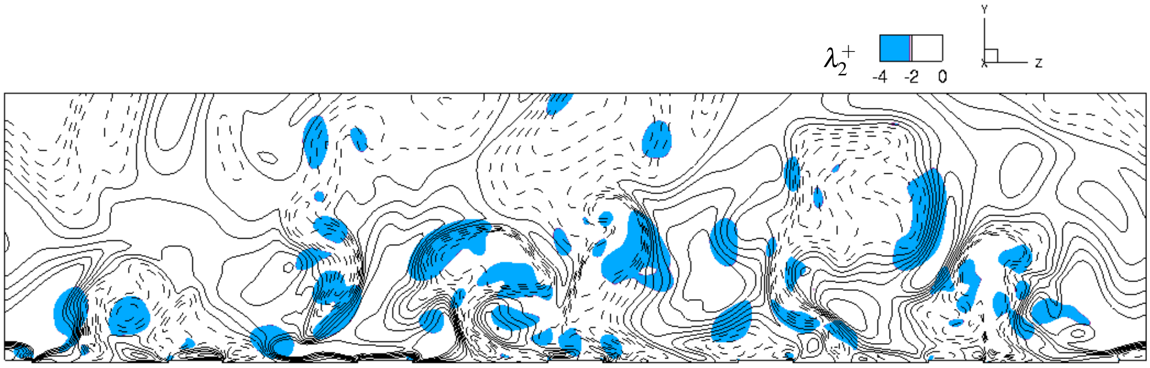

(a) $\beta = 0°$, $\varphi = 0$

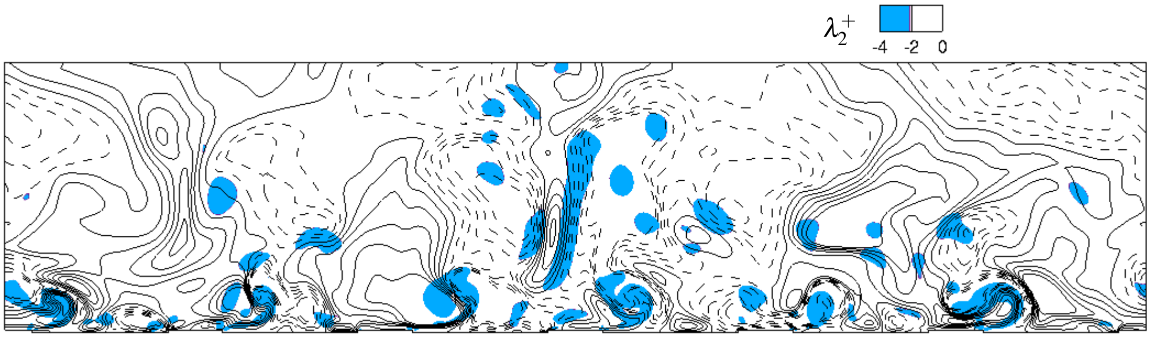

(b) $\beta = 0°$, $\varphi = \pi/2$

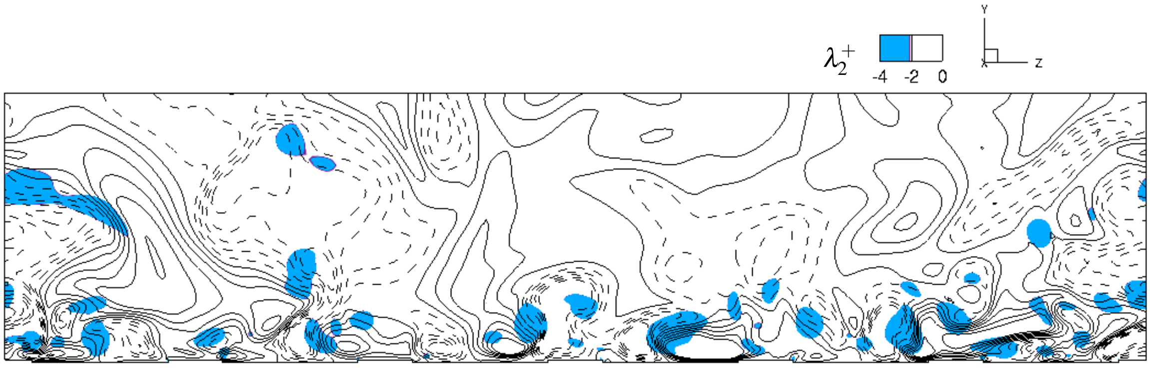

(c) $\beta = 75°$, $\varphi = 0$

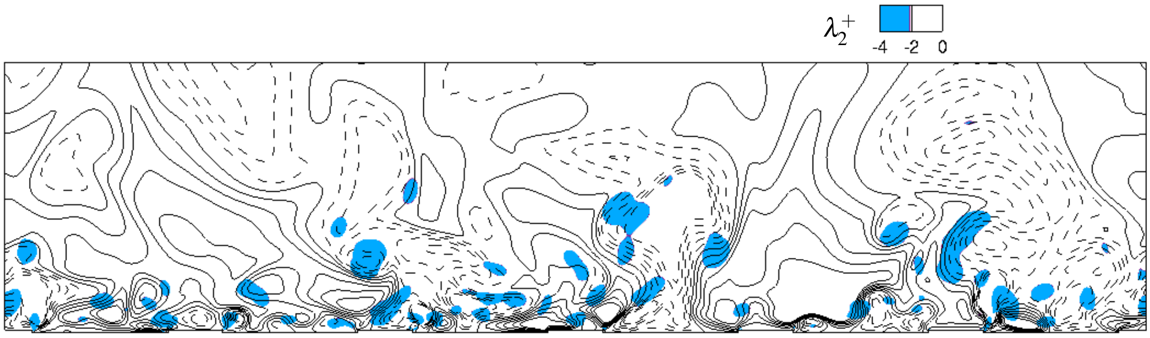

(d) $\beta = 75°$, $\varphi = \pi/2$

Figure 5.72 In cases ZMJ($\beta = 0°$) and ZMJ($\beta = 75°$), the contour lines of u''^+ in the $y-z$ plane at $x^+ = 5$ and the different phase time $\varphi = 0$, $\pi/2$. The solid lines are the positive values and the dashed lines are the negative values. The blue regions are the regions where $\lambda_2^+ < -2$.

5.8 Spectral analysis

In the controlled channel, since the flow is manipulated by ZMJ in the near-wall region, the turbulent kinetic energy of the channel flow should be significantly influenced, especially near the jet-exits. By studying the kinetic energy in the controlled channel, it can clearly show the transference of the energy from ZMJ to the channel flow. In this research, the total fluctuation of velocity has two parts, including periodic and pure turbulent parts. Both of them are related to the turbulent kinetic energy. In order to decompose the energy effects, the turbulent kinetic energy is divided into pure turbulent and periodic parts. The pure turbulent kinetic energy E_k^+ is computed as $E_k^+ = (u''^+)^2 + (v''^+)^2 + (w''^+)^2$. The periodic kinetic energy $\widetilde{E}_k^+$ is obtained by$\widetilde{E}_k^+ = (\widetilde{u}^+)^2 + (\widetilde{v}^+)^2 + (\widetilde{w}^+)^2$. In the following paragraphs, the distributions of E_k^+ and $\widetilde{E}_k^+$ from wall to the channel centre are investigated at two spanwise positions which are near the jet-exits $z^+ = 20$ and the middle of each sections $z^+ = 61$.

Figures 5.73, 5.74, 5.75, 5.76 and 5.77 show the evolutions of the kinetic energy distributions and the power spectral density (PSD) of E_k^+ and $\widetilde{E}_k^+$. In case ZMJ(off), there is no periodic energy input into the controlled channel. The periodic kinetic energy is zero, so there is not any plot of $\widetilde{E}_k^+$ for case ZMJ(off). In the contour plots of the evolutions, the kinetic energy distributions are computed from the instantaneous results along the wall-normal direction. The nondimensional time t^+ is the x-axis and the nondimensional hight y_L^+ is the y-axis in log-scale. Also, the figures represent the dominant frequencies of the nondimensional kinetic energy from wall to the channel centre with the PSD.

Comparing figures 5.73a and 5.73c, the evolutions of pure turbulent kinetic energy are quite similar at two spanwise positions in case ZMJ(off). The energy is low near wall and high in channel centre. Both of the PSD plots do not show any dominant frequency in figures 5.73b and 5.73d. This means the Energy fluctuations are pure noises without any pattern in case ZMJ(off).

As shown in figure 5.74, clear patterns can be found in the evolutions of pure turbulent kinetic energy at $z^+ = 20$ and 61 for case ZMJ($\beta = 0°$). The kinetic energy in case ZMJ($\beta = 0°$) is larger than that in case ZMJ(off). The ZMJ ejects kinetic energy into the near-wall regions and disturbs the fluid in its oscillating pattern. There are two wall-normal positions at where local peaks of the energy near the jet-exits appears, including $\log_{10}(y_L^+) = 0.2$ and 1.2. This means that the jets increase the energy of the fluid near the orifice of jet-exits by blowing and sucking. The first position of local peaks is formed. When the ZMJ blows, a region of shear flow is created between the main flow and the jets. The shear flow contains relatively low kinetic energy. Above the region of shear flow, the energy is increased by the jets as well to form the second position of local peaks. Figure 5.74c shows that there is only one wall-normal position of local peaks near the middle of each sections at $\log_{10}(y_L^+) = 1.4$.

This means that the ZMJ introduces extra energy into the channel near the middle of each sections. And the extra energy is mixed with the energy from the main flow, shifting the peak positions from $\log_{10}(y_L^+) = 1.2$ to 1.4.

The PSD plots of the energy also confirm the wall-normal positions of the local peaks. Figure 5.74b shows that the nondimensional frequency gap is 0.008 near the jet-exits. And the dominant frequency is 0.008, so the dominant period is 125 which equals the period of ZMJ. This means that the energy effects of blowing and sucking are not equal. The nondimensional frequency gap also is 0.008 near the middle of each sections, as shown in figure 5.74d. But the dominant frequency is 0.016 which is double of the frequency of ZMJ. This indicates that the energy effects from left and right sides of ZMJ are almost equal.

Figure 5.75 displays that case ZMJ($\beta = 75°$) has the similar phenomenon to case ZMJ($\beta = 0°$). The difference is that the strength of pure turbulent kinetic energy when $\beta = 75°$ is weaker than that when $\beta = 0°$. There is not any shear flow near the jet-exits to form the regions of low energy.

The evolutions and PSD of periodic kinetic energy are shown in figures 5.76 and 5.77. At $z^+ = 20$, the wall-normal position of local peaks is at $\log_{10}(y_L^+) = 0$ when $\beta = 0°$, and the position is at $\log_{10}(y_L^+) = 0.2$ when $\beta = 75°$. At $z^+ = 61$, the wall-normal position is at $\log_{10}(y_L^+) = 1.1$ for both $\beta = 0°$ and 75°. The energy during the blowing period is stronger than that during the sucking period, and the energy when $\beta = 0°$ is stronger than that when $\beta = 75°$. For all of the PSD plots in figures 5.76 and 5.77, the nondimensional frequency gap is 0.008. This indicate that the effects from a pair of ZMJ are not equal.

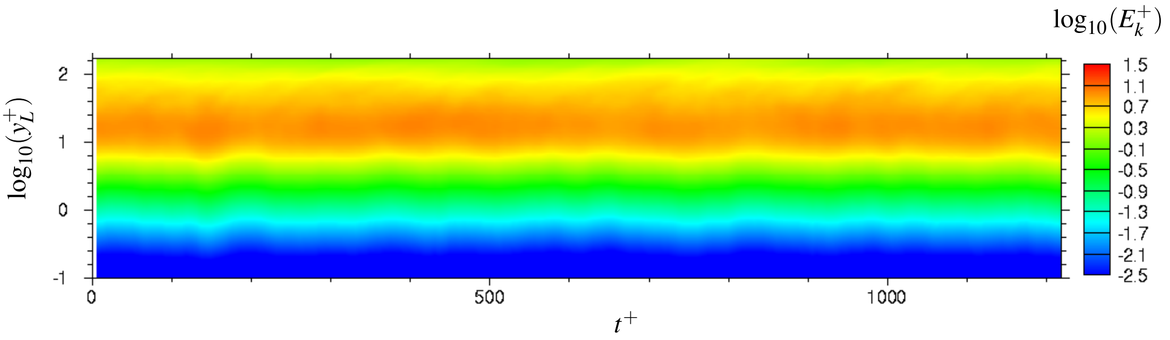

(a) The evolution of $\log_{10}(E_k^+)$ at $z^+ = 20$.

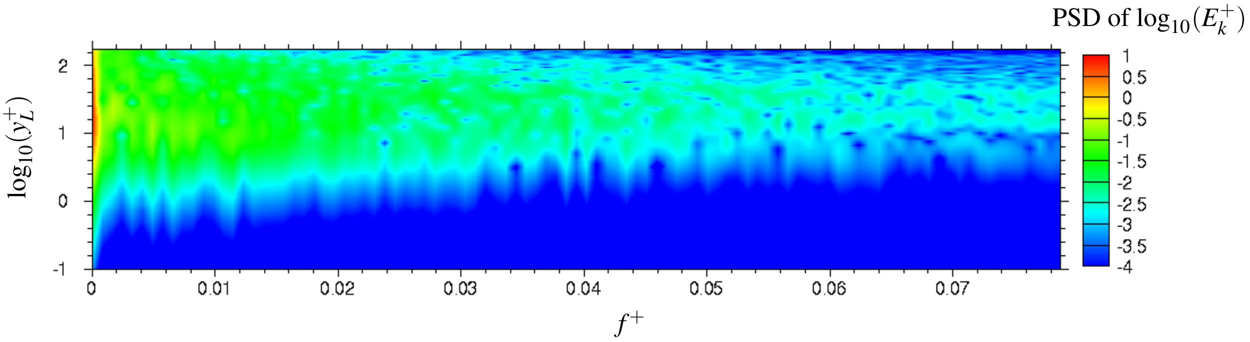

(b) The power spectral density (PSD) of $\log_{10}(E_k^+)$ at $z^+ = 20$.

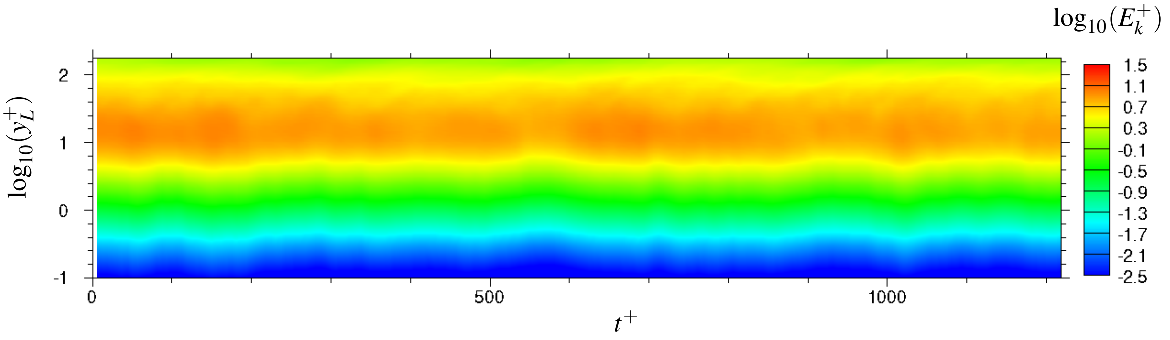

(c) The evolution of $\log_{10}(E_k^+)$ at $z^+ = 61$.

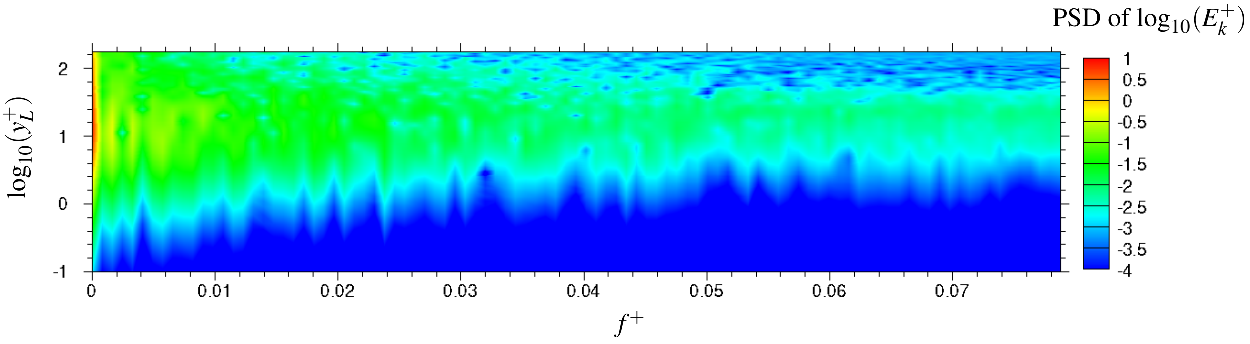

(d) The power spectral density (PSD) of $\log_{10}(E_k^+)$ at $z^+ = 61$.

Figure 5.73 In case ZMJ(off), the evolutions and the power spectral density (PSD) of $\log_{10}(E_k^+)$ are displayed at different spanwise positions $z^+ = 20$ and 61.

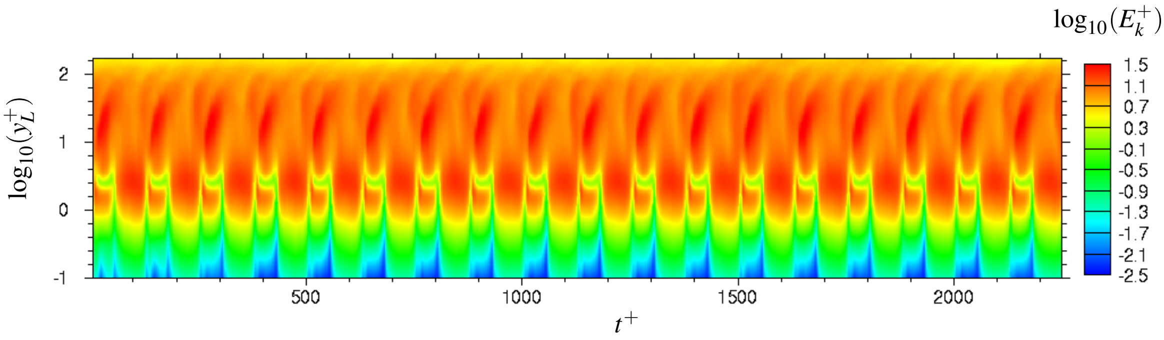

(a) The evolution of $\log_{10}(E_k^+)$ at $z^+ = 20$.

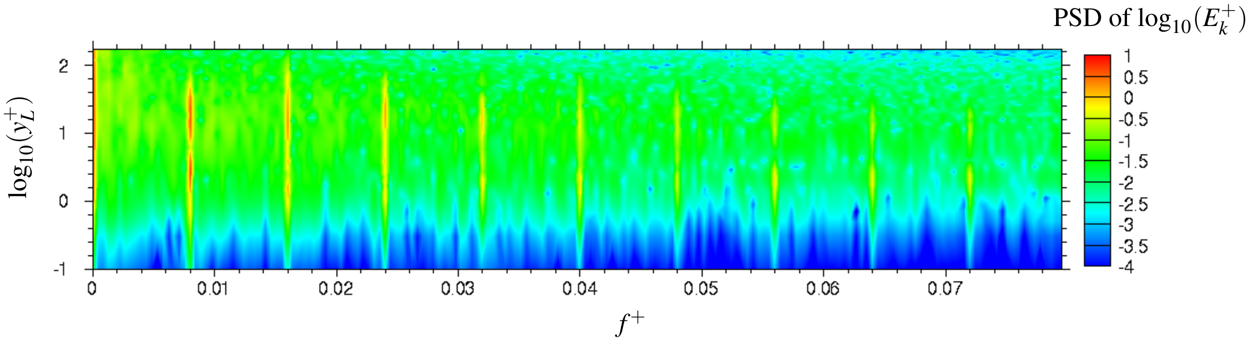

(b) The power spectral density (PSD) of $\log_{10}(E_k^+)$ at $z^+ = 20$.

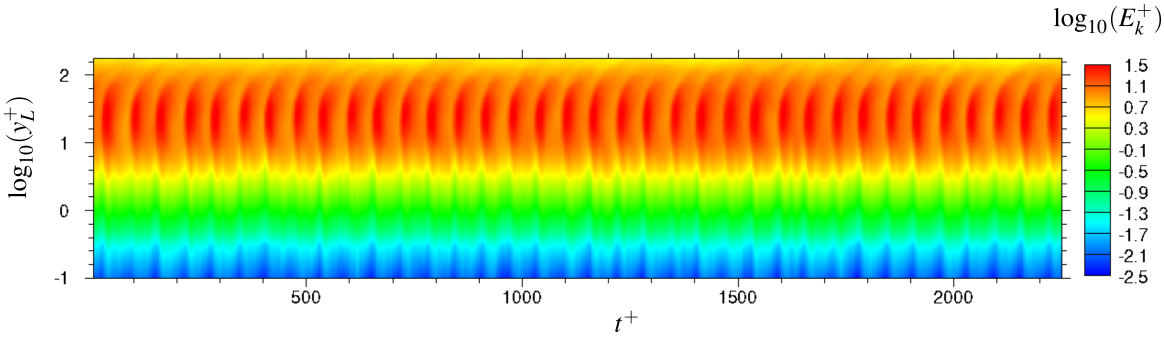

(c) The evolution of $\log_{10}(E_k^+)$ at $z^+ = 61$.

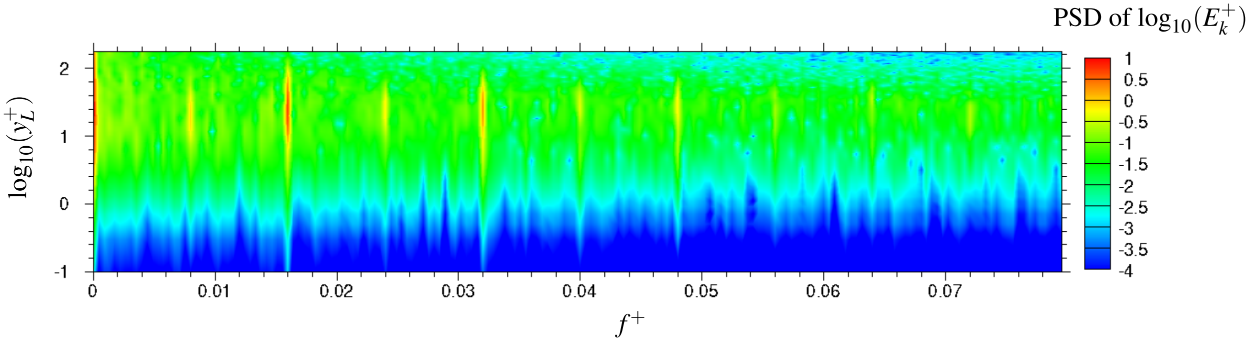

(d) The power spectral density (PSD) of $\log_{10}(E_k^+)$ at $z^+ = 61$.

Figure 5.74 In case ZMJ($\beta = 0°$), the evolutions and the power spectral density (PSD) of $\log_{10}(E_k^+)$ are displayed at different spanwise positions $z^+ = 20$ and 61.

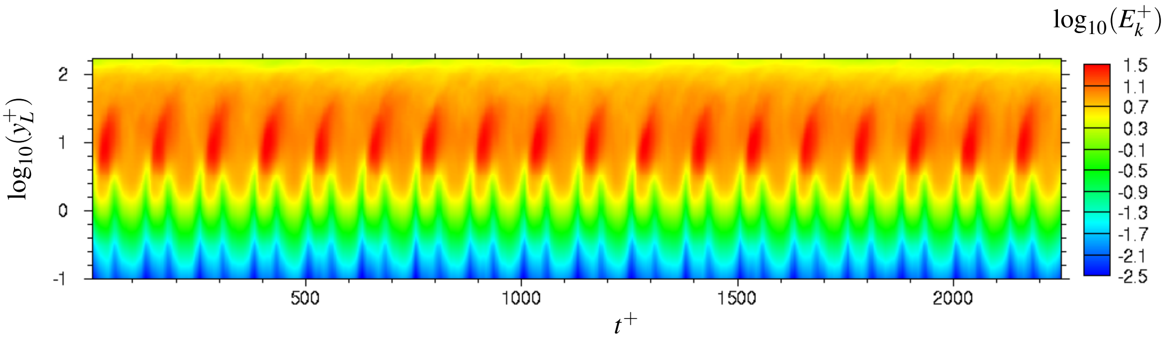

(a) The evolution of $\log_{10}(E_k^+)$ at $z^+ = 20$.

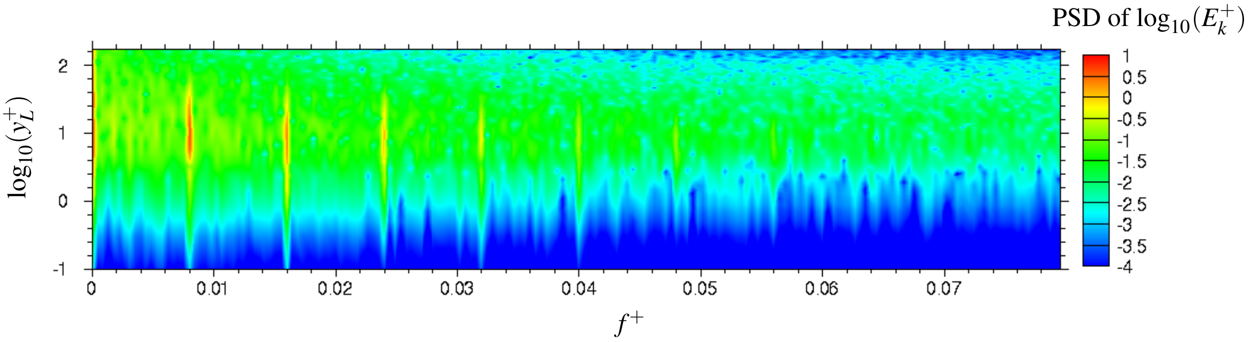

(b) The power spectral density (PSD) of $\log_{10}(E_k^+)$ at $z^+ = 20$.

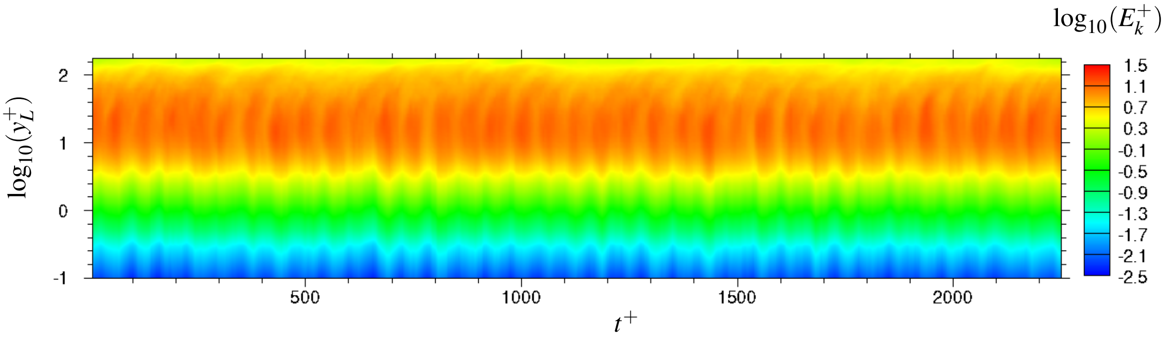

(c) The evolution of $\log_{10}(E_k^+)$ at $z^+ = 61$.

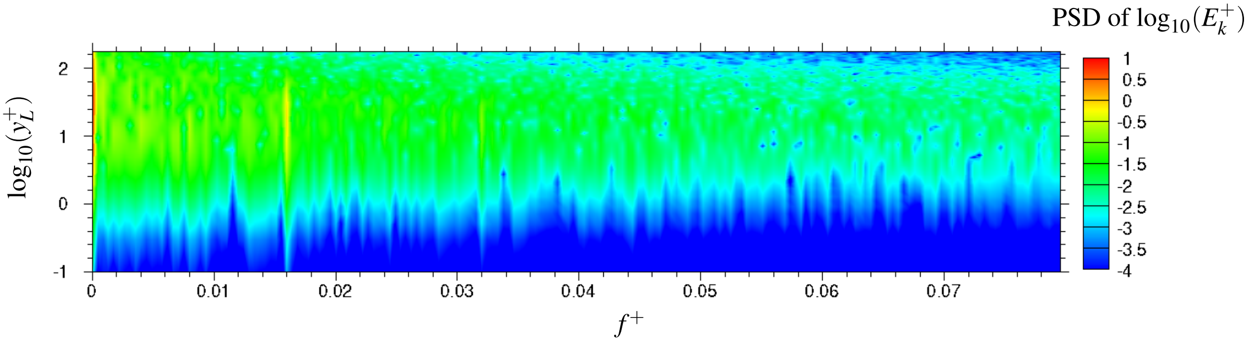

(d) The power spectral density (PSD) of $\log_{10}(E_k^+)$ at $z^+ = 61$.

Figure 5.75 In case ZMJ($\beta = 75°$), the evolutions and the power spectral density (PSD) of $\log_{10}(E_k^+)$ are displayed at different spanwise positions $z^+ = 20$ and 61.

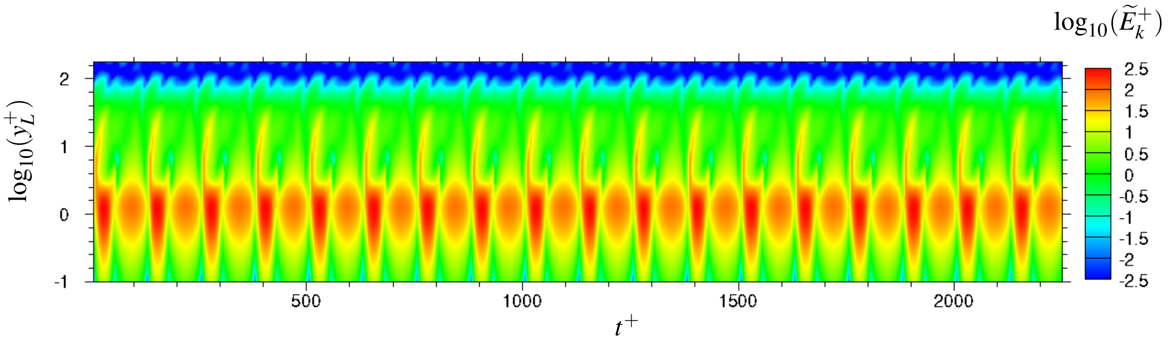

(a) The evolution of $\log_{10}(\widetilde{E}_k^+)$ at $z^+ = 20$.

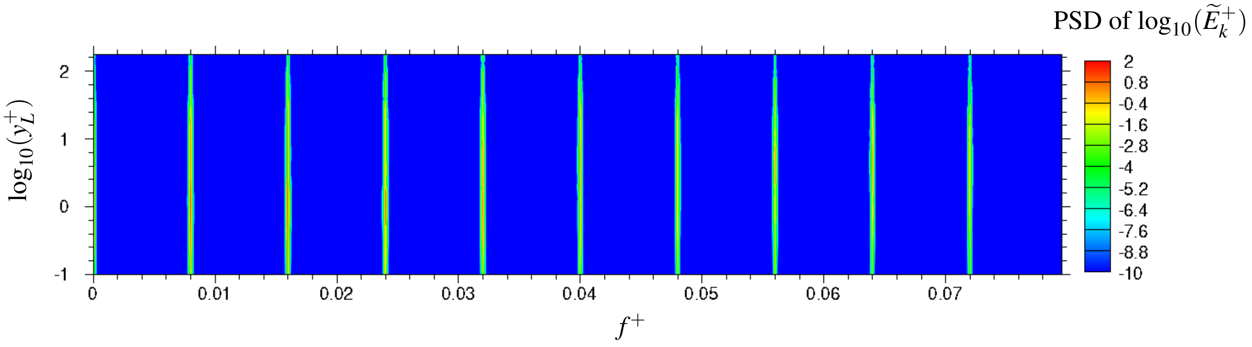

(b) The power spectral density (PSD) of $\log_{10}(\widetilde{E}_k^+)$ at $z^+ = 20$.

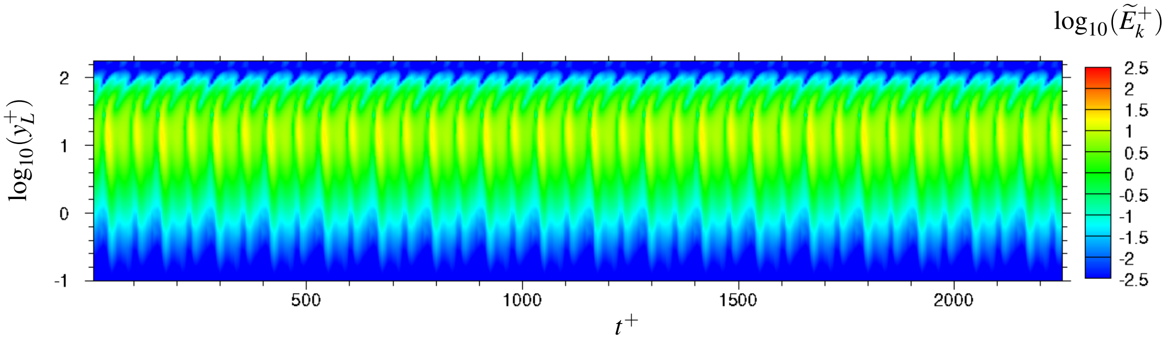

(c) The evolution of $\log_{10}(\widetilde{E}_k^+)$ at $z^+ = 61$.

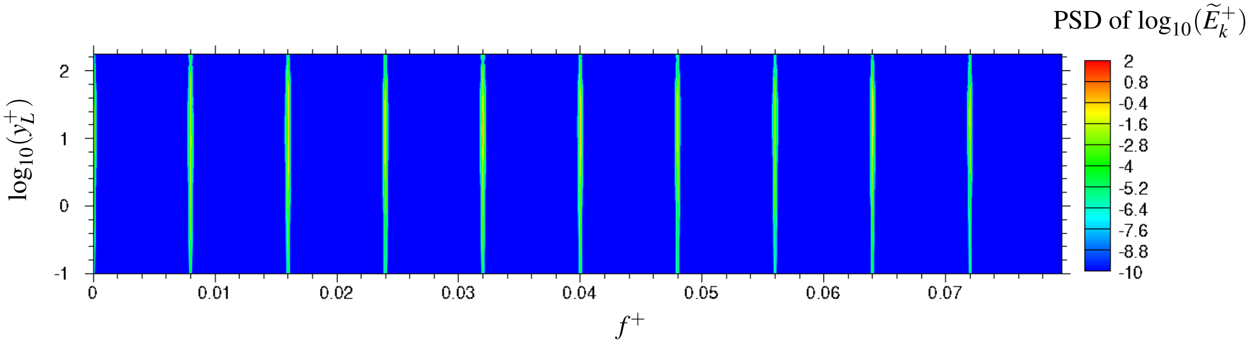

(d) The power spectral density (PSD) of $\log_{10}(\widetilde{E}_k^+)$ at $z^+ = 61$.

Figure 5.76 In case ZMJ($\beta = 0°$), the evolutions and the power spectral density (PSD) of $\log_{10}(\widetilde{E}_k^+)$ are displayed at different spanwise positions $z^+ = 20$ and 61.

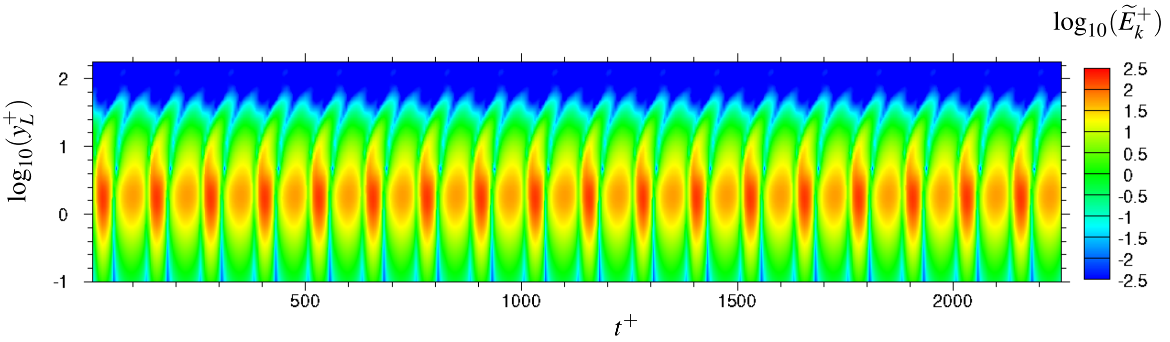

(a) The evolution of $\log_{10}(\widetilde{E}_k^+)$ at $z^+ = 20$.

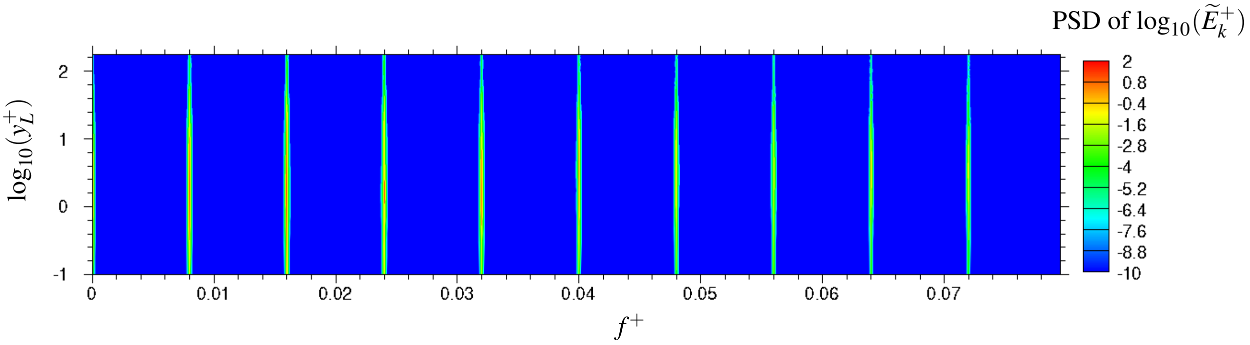

(b) The power spectral density (PSD) of $\log_{10}(\widetilde{E}_k^+)$ at $z^+ = 20$.

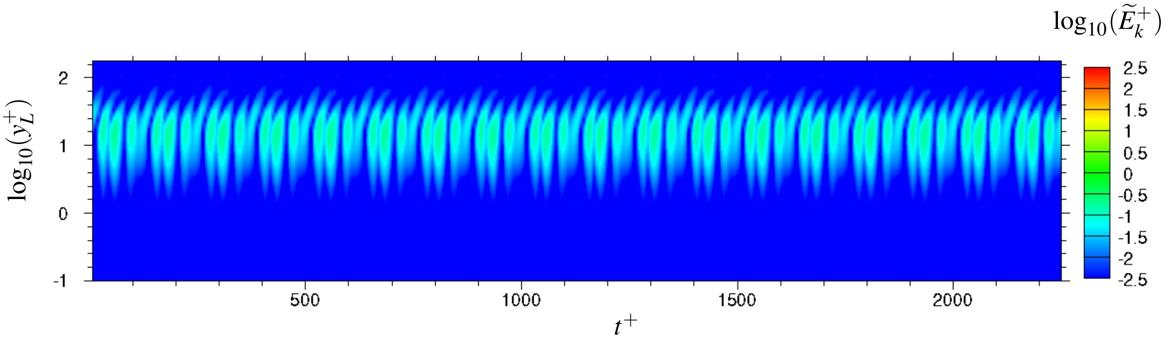

(c) The evolution of $\log_{10}(\widetilde{E}_k^+)$ at $z^+ = 61$.

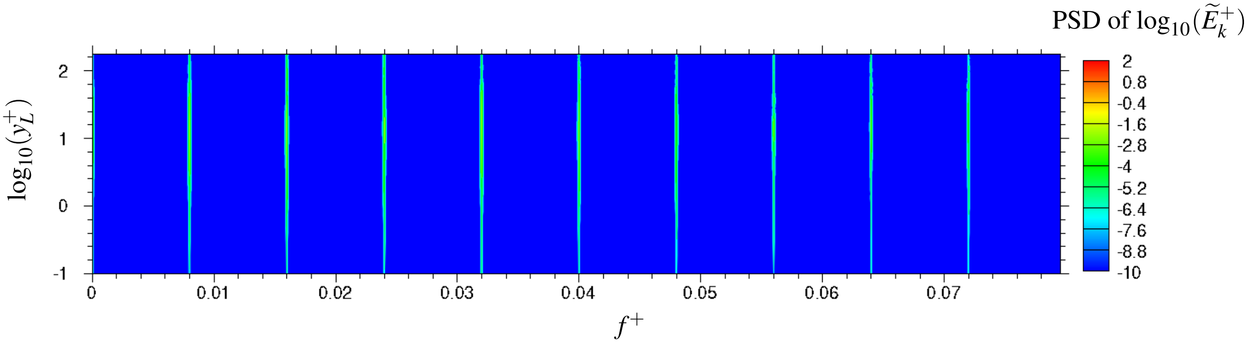

(d) The power spectral density (PSD) of $\log_{10}(\widetilde{E}_k^+)$ at $z^+ = 61$.

Figure 5.77 In case ZMJ($\beta = 75°$), the evolutions and the power spectral density (PSD) of $\log_{10}(\widetilde{E}_k^+)$ are displayed at different spanwise positions $z^+ = 20$ and 61.

Figure 5.78 and 5.79 show contours of the premultiplied one-dimensional energy spectrum of the streamwise velocity, $k_x\phi_{uu}/u_\tau^2$. The wavenumber in the streamwise direction is k_x, and $\phi_{uu} = \langle \hat{u}(k_x,y)\hat{u}^*(k_x,y)\rangle$. $\hat{u}$ is the Fourier coefficient of u. λ_x is the wavelength in the streamwise direction, which can be computed as $\lambda_x = 2\pi/k_x$. The streamwise kinetic energy contained in a streamwise wavelength λ_x is obtained by the spectral analysis.

In the smooth channel, the velocities are statistically same in the spanwise direction, so $k_x\phi_{uu}/u_\tau^2$ should be the same in the spanwise direction. Figure 5.78 shows the contour plot of $k_x\phi_{uu}/u_\tau^2$ for the smooth-channel case. Since the geometry is adapted in the controlled channel, the velocities in the spanwise direction are only statistically same at the same spanwise positions of each sections. In case ZMJ(off), four typical spanwise positions are chosen to study the effects of the steps on the streamwise kinetic energy, as shown in figure 5.79. Looking at the figures, all of the peaks are around the height of $y_L^+ = 15$ which is the location of the peaks of u'_{rms} in figure 5.10b. The figures show that the λ_x which contains the most of the streamwise kinetic energy in the controlled channel is smaller than that in the smooth channel. The small-scale velocity fluctuations are generated by the steps and brought up by the ejections, increasing the streamwise kinetic energy contained in $\lambda_x^+ = 710$. Figure 5.79 represents that all peak locations of $k_x\phi_{uu}/u_\tau^2$ are around $(y_L^+ = 15, \lambda_x^+ = 710)$ at the different spanwise positions in the controlled channel.

In the previous analysis, the ZMJ significantly disturbs the incoming flow and increases the velocity fluctuations. To understand the effect of ZMJ on the fluid motions, it is helpful to study the behaviour of the pre-multiplied spectra for the streamwise velocity $k_x\phi_{uu}/u_\tau^2$. It can tell the kinetic energy contained in the different wave lengths which are related to the

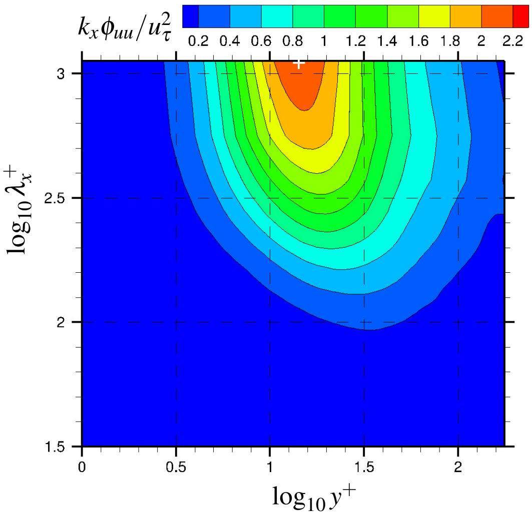

Figure 5.78 In the smooth channel, contours of the pre-multiplied spectra of the streamwise velocity $k_x\phi_{uu}/u_\tau^2$. The approximate location of the peak is denoted by $(+)$ symbol.

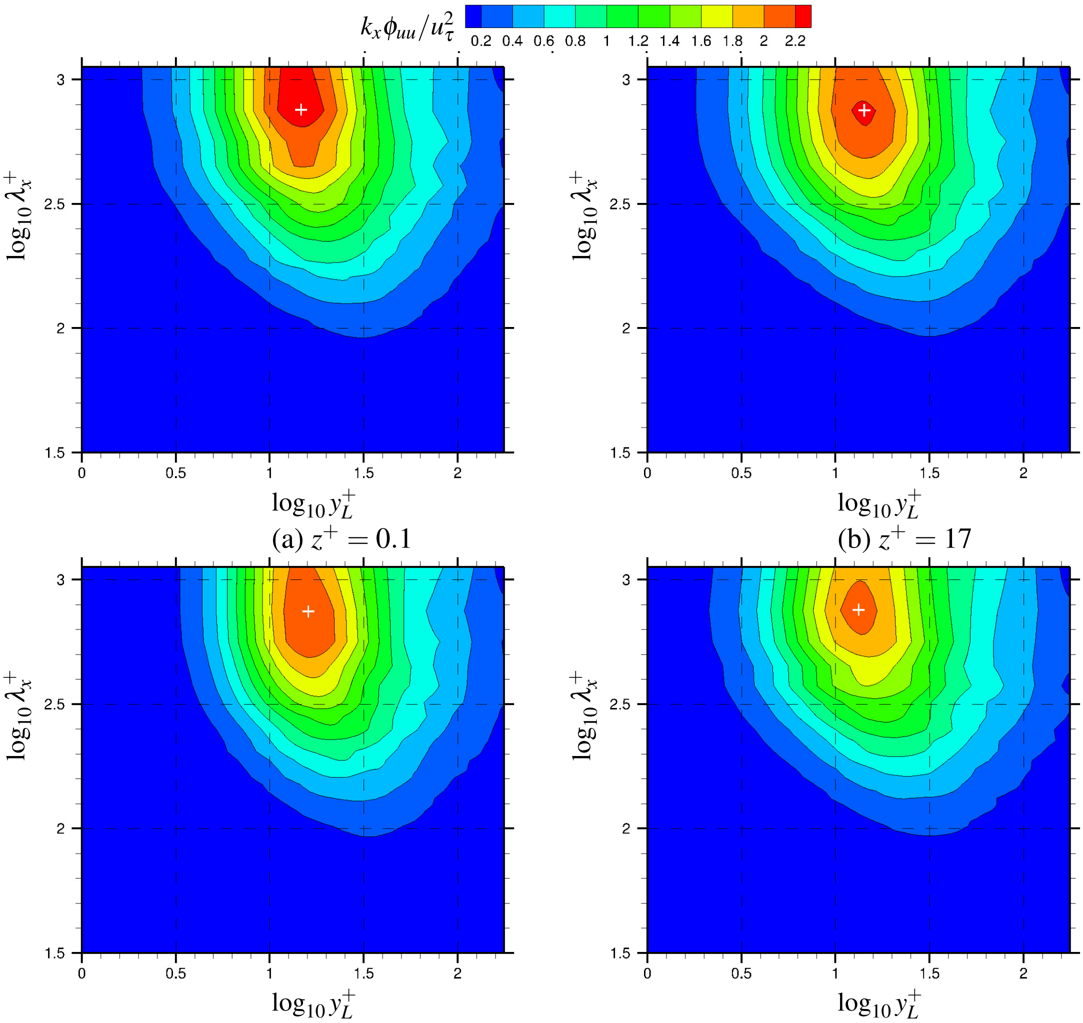

(a) $z^+ = 0.1$ (b) $z^+ = 17$

(c) $z^+ = 20$ (d) $z^+ = 62.83$

Figure 5.79 In case ZMJ(off), contours of the pre-multiplied spectra of the streamwise velocity $k_x\phi_{uu}/u_\tau^2$ at the different spanwise positions. The approximate locations of the peaks are denoted by $(+)$ symbols.

motion scales. In this research, because the Reynolds number is low, $Re_\tau = 180$, and the boundary layer thickness is limited by the channel height δ, there are not large-scale motions in the turbulent channel flow. It is interesting to study the small-scale motions which are influenced by ZMJ.

Figures 5.80 and 5.81 represent contour plots of $k_x\phi_{uu}/u_\tau^2$ at different spanwise positions in cases ZMJ($\beta = 0°$, $75°$). The difference of the pre-multiplied spectra when ZMJ is on or off can be distinguished by comparing the two figures with figure 5.79. The wavelengths that contain high kinetic energy in case ZMJ(on) is smaller than that in case ZMJ(off). This indicates that ZMJ injects kinetic energy into the small-scale motions $\lambda_x^+ < 600$.

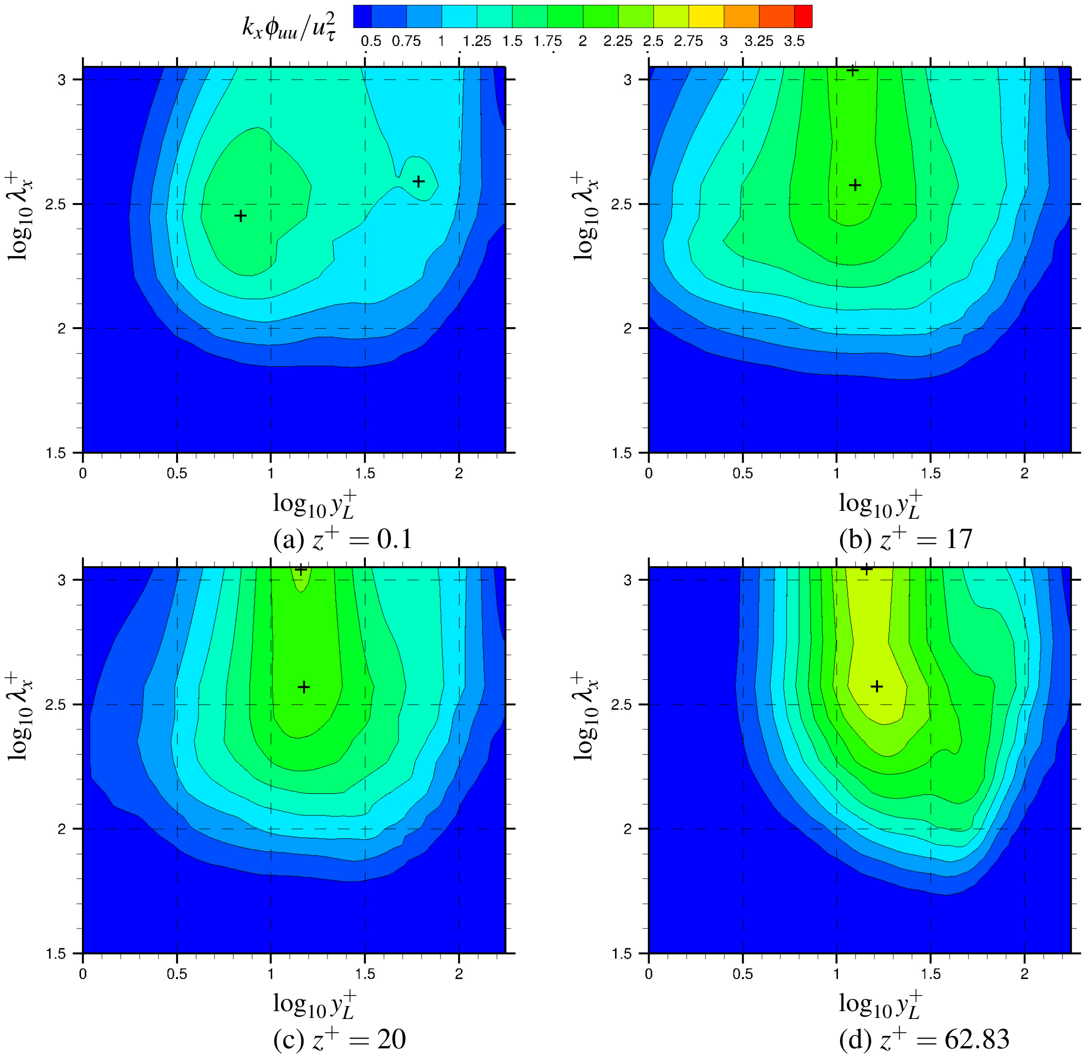

(a) $z^+ = 0.1$ (b) $z^+ = 17$ (c) $z^+ = 20$ (d) $z^+ = 62.83$

Figure 5.80 In case ZMJ($\beta = 0°$), contours of the pre-multiplied spectra of the streamwise velocity $k_x\phi_{uu}/u_\tau^2$ at the different spanwise positions. The approximate locations of the peaks are denoted by $(+)$ symbols.

Looking at figure 5.80, there are two peaks in the contour plots in case ZMJ($\beta = 0°$). At the spanwise positions, $z^+ = 20$, 62.83, the heights of peak locations are around $y_L^+ = 15$ which is the same as the case ZMJ(off). In figure 5.80b, the heights of peak locations are around $y_L^+ = 13$. The spanwise position of the peak is in region above the steps, having $y_G^+ = y_L^+ + 2$. If the heights are considered in a global view, the peak locations are at the same height $y_G^+ = 15$ when the spanwise positions are different, including $z^+ = 17$, 20, 62.83. Two local peaks are found in the contour plots at the three spanwise-positions. The two peak locations are around $\lambda_x^+ = 380$, 1131. When the wavelengths are in the range of

$380 \leq \lambda_x^+ \leq 1131$, the kinetic energy contained in the wavelengths is almost the same at the height $y_G^+ = 15$.

When $\beta = 0°$, the highest value of the kinetic energy is at $z^+ = 62.83$ in the middle of each sections, as displayed in figure 5.80. At the spanwise position $z^+ = 0.1$, unlike the others, two peaks happen at around ($y_L^+ = 7$, $\lambda_x^+ = 285$) and ($y_L^+ = 61$, $\lambda_x^+ = 393$). The peak which is at around ($y_L^+ = 7$, $\lambda_x^+ = 285$) is the global peak at $z^+ = 0.1$. The value of the peak is the lowest value among the global peaks of the four contour-plots. The time averaged motion of the fluid has already been shown in figure 5.19b. The ZMJ increases the energy contained in the small-scale motions $\lambda_x^+ < 316$, when the fluid is in region ($0 \leq y_G^+ \leq 3$, $17 \leq z^+ \leq 20$).

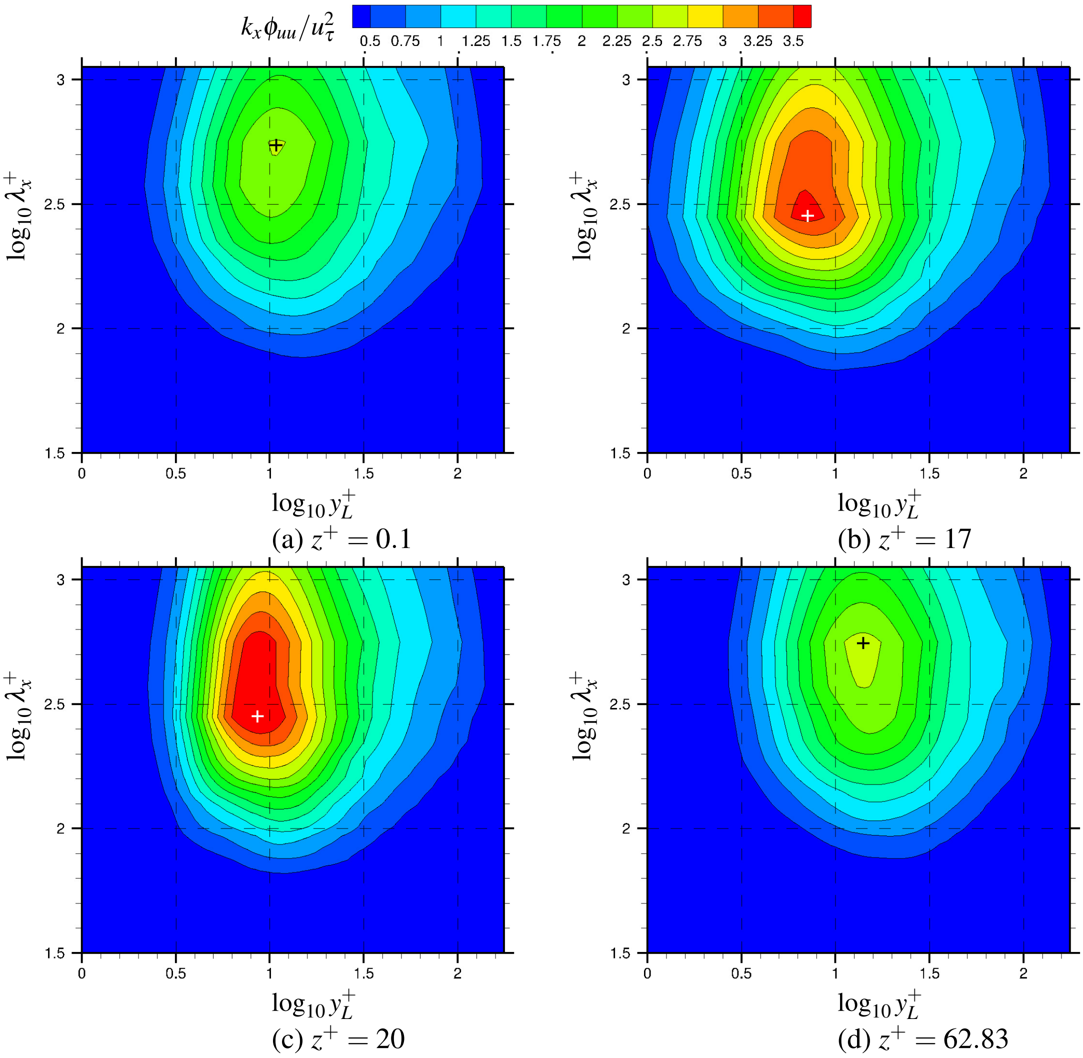

(a) $z^+ = 0.1$

(b) $z^+ = 17$

(c) $z^+ = 20$

(d) $z^+ = 62.83$

Figure 5.81 In case ZMJ($\beta = 75°$), contours of the pre-multiplied spectra of the streamwise velocity $k_x\phi_{uu}/u_\tau^2$ at the different spanwise positions. The approximate locations of the peaks are denoted by $(+)$ symbols.

This indicates that ZMJ generates small vortices near the jet-exits. The small vortices are brought upwards in the wall-normal direction and towards the middle of each sections in the spanwise direction by ZMJ. When the vortices are driven away from the jet-exits, the sizes of the vortices become bigger. The vortices increase all the energy that contained in the range $380 \leq \lambda_x^+ \leq 1131$ at around $y_G^+ = 15$. When the region is above $y_G^+ = 15$, the energy contained in the fluid begins to dissipate. The fluid follows the time averaged motion back to the side of each sections, the energy is dissipated relatively low. It is interesting to notice that the wavelength $\lambda_x^+ = 393$ contains the most energy rather than $\lambda_x^+ = 710$ at $z^+ = 0.1$. The controlled channel has the most energy in $\lambda_x^+ = 710$ with ZMJ off. There is a local peak at ($y_L^+ = 7$, $\lambda_x^+ = 285$). The reason is that the flow is incompressible, the fluctuations can propagate to the upstream as well. So, ZMJ can also increase the energy contained in the small-scale motions at the side of each sections.

The phenomenon in case ZMJ($\beta = 75°$) seems to be different from case ZMJ($\beta = 0°$), as shown in figure 5.81. There is only one peak at the different spanwise positions. The peak values when $\beta = 75°$ are bigger than that when $\beta = 0°$. Learning from reference [79], the relation between the streamwise turbulence intensity, $I_x = u''_{rms}/u_\tau = \sqrt{\overline{u''^2}^+}$, and the premultiplied energy spectra, $k_x\phi_{uu}/u_\tau^2$, can be described as

$$\overline{u''^2}^+ = \int \frac{k_x\phi_{uu}}{u_\tau^2} d(\log k_x) = -\int \frac{k_x\phi_{uu}}{u_\tau^2} d(\log \lambda_x) \tag{5.14}$$

Figure 5.55b has already shown that the streamwise turbulence intensity at ($y_G^+ > 3$, $z^+ = 20$) when $\beta = 75°$ is higher than that when $\beta = 0°$ at the phase time $\varphi = 0,\ \pi/2$. According to figure 5.81c, the small-scale motions in the range, $240 \leq \lambda_x \leq 650$, contribute the most to the streamwise turbulence intensity. At the spanwise positions $z^+ = 17$ and 20, case ZMJ($\beta = 75°$) disturbs the streamwise velocity more than case ZMJ($\beta = 0°$). Case ZMJ($\beta = 75°$) inputs more energy into the small-scale motions than case ZMJ($\beta = 0°$). This means that case ZMJ($\beta = 75°$) generates more small-scale vortices than case ZMJ($\beta = 0°$). The comparison of the vortex size between cases ZMJ($\beta = 0°$) and ZMJ($\beta = 75°$) has been displayed in figure 5.72. When the small-scale vortices move to either the middle or the sides of each sections, the vortex size expends to be bigger than that near the jet-exits, so the peak locations that are in either the middle or the sides of each sections locate at bigger wavelengths than that near the jet-exits.

5.9 Conclusions

In this chapter, the studies can be concluded with three parts, including global, time-averaged, and phase-averaged conclusions. The global conclusions are based on the analyses excluding time-averaged and phase-averaged analyses.

Global conclusions:

- The spanwise mesh-resolution near the jet-exits should be designed fine enough to accurately obtain the reduced skin-friction. The spanwise mesh-resolution $\Delta z^+ = 4.49$ is enough for a smooth channel, and it should be $\Delta z^+_{min} = 0.5$ near the jet-exits for the controlled channel.
- In case ZMJ(off), the skin friction of the controlled channel is only 0.24% different from that of the smooth channel. The step height is smaller than most of the length-scales of the flow structures, such as the low-speed regions and vortices structures. So, the flow structures are influenced limited.
- ZMJ can increase and decrease the skin friction of a turbulent channel flow by using different jet-angles. An estimated critical value between increasing and decreasing drag is $\beta = 50°$. The drag reaches the maximum when $\beta = 0°$. The maximum drag-reduction appears around $\beta = 75°$. Since no fluid is injected into main flow, influence of ZMJ is very little when $\beta = 90°$. Comparing to the smooth channel, the levels of gross drag reduction are -98.4%, 4.4% and 10.5% when the jet angles are 0°, 60° and 75°, respectively.
- The skin frictions periodically fluctuate due to the periodic character of ZMJ. When jet angle is 75°, the amplitude of skin friction is the largest among 0°, 60° and 75°. The frequency of 7776Hz appears in the skin-friction fluctuations of all jet angles. When jet angle is small such as $\beta = 0°$, other high frequencies 15552, 23328 and 31104Hz also play important roles.
- The vortices structures in case ZMJ($\beta = 0°$) are more dense than that in case ZMJ($\beta = 75°$). The small jet-angle can eject the vortices more possibly into the channel centre than the big jet-angle. Moreover, the spanwise length-scales of vortices structures generated by case ZMJ($\beta = 0°$) is larger than that by case ZMJ($\beta = 75°$).
- Long and continuous low-speed regions are created by the blowing jet-exits when the jet is strong. The low-speed and high-speed regions are elongated by ZMJ during

the period of increasing jet-velocity. The regions are broken by main flow during the period of decreasing jet-velocity.

- ZMJ significantly oscillates the fluid near the jet-exits. The fluid in the middle of each sections does not have the same dominant frequency as that near the jet-exits. ZMJ prefers ejecting energy into small length-scales of motions to actuating long length-scales of motions. The turbulent kinetic energy is mostly constrained in the near-wall region. Near the jet-exits, ZMJ with big jet-angle shifts the peak of turbulent kinetic energy closer to the wall.

Time-averaged conclusions:

- In case ZMJ(off), the gradients of averaged velocity profile are reduced at the step corner and in region above the steps, but the gradient is increased in the middle of each sections. The turbulent intensity in the middle of each sections is lower than that in the side of each sections. Comparing to the smooth channel, the absolute values of Reynolds shear stresses are increased by the steps, except two regions. One region is at $z^+ = 18.5$ and $y_L^+ < 20$, the other one is at $z^+ = 63$ and $y^+ > 20$.

- When ZMJ is on, a pair of vortices are induced by ZMJ in the near-wall region of a section. The averaged skin-frictions have three features in region above the steps. The first one is that the averaged skin-friction is proportional to the spanwise jet-velocity. The second one is that the averaged skin-friction increases from the sides of each sections to the jet-exits. The third one is that the averaged skin-friction in case ZMJ(on) is always bigger than that in case ZMJ(off). Between a pair of jet-exits, the averaged skin-frictions are reduced near the jet-exits when $\beta = 60°$ and 75°, but the skin friction is increased when $\beta = 0°$.

- The turbulent intensity and Reynolds shear stresses are significantly increased by ZMJ. The strengths of total fluctuations of spanwise and wall-normal velocities are proportional to spanwise periodic-velocity. The fluctuating strength of streamwise velocity depends on both streamwise and spanwise velocities of ZMJ. The streamwise jet-velocity decides the strength near the jet-exits, and the spanwise jet-velocity determines the strength away from the jet-exits. The distributions of root mean square of the velocity fluctuations are symmetric in a section. Reynolds shear stresses performs the same as the turbulent intensity. Because the distributions of Reynolds shear stresses $\overline{u'w'}$ and $\overline{v'w'}$ are symmetric but with opposite signs in a section, the mean-values of the Reynolds shear stresses of a section should be zero. The distributions of Reynolds shear stress $\overline{u'v'}$ are symmetric with the same signs in a section.

- ZMJ significantly increases the fluctuating ranges of streamwise and wall-normal velocities. By studying the JPDF of streamwise and wall-normal velocity fluctuations, it is found that the cross-correlation between the two fluctuations is proportional to the spanwise strength of ZMJ. The main contributions to Reynolds shear stress $\overline{u'v'}$ are always from ejection and sweep, giving negative values.

- The spanwise variations of profiles of the averaged streamwise-velocity, Reynold shear stress $\overline{u'v'}$, root mean square of streamwise and wall-normal velocities are huge in the viscous sublayer but small in the log-law region. The log-law regions can be found in the velocity profiles. Since the fluid motions are strongly interrupted by ZMJ, the Von Kármán constant κ is changed. A new wall function should be built to model the jet effects in the near-wall region.

Phase-averaged conclusions:

- The distributions of skin friction are strongly depend on the phase of ZMJ. The skin friction is increased near the sucking jet-exits but reduced near the blowing jet-exits. When jet angles are 60° and 75°, a overall drag-reduction can be obtained because the drag reduction is bigger than the drag increase. The peak values of skin friction appear at the phase time $\pi/2$ or $3\pi/2$. The peak values of jet angle 75° are the largest among 0°, 60° and 75°.

- The blowing jet can influence further than the sucking jet. The width of strongly influenced regions is proportional to the spanwise velocity of ZMJ. The gradient of phase averaged streamwise-velocity near the sucking jet-exits is proportional to the spanwise velocity as well.

- The variations of phase averaged profiles of streamwise velocity are big in viscous sublayer with all jet angles, even happens in buffer layer and part of log-law region when jet angle is 0°. The variations are small near the channel centre. The variation height is proportional to the spanwise velocity of ZMJ. The propagation speed of low streamwise-velocity acts the same as the variation height, depending on the spanwise velocity.

- Purely turbulent fluctuations of velocity are generated by the blowing jet-exits but eliminated by the sucking jet-exits. The phenomenon is the same for the Reynolds shear stresses given by these fluctuations. The region of strong strength of the pure turbulent intensity can be located higher when the spanwise jet-velocity is higher. The periodic velocity dominates the total velocity-fluctuations near the jet-exits. The pure turbulent fluctuations contribute most to the total velocity-fluctuations in the regions away from the jet-exits. The blowing jet-exits generate vortices which are eliminated by the sucking jet-exits.

- When the jet angle is small such as 0°, the blowing jet-exits generate a region of positive $\overline{u''v''}$ near the exits. However, the region does not exits in the case with big jet-angle such as 75°. The reason is that when the jet angle is small, the blowing jet make the fluid motions happen mostly in Q1 and Q3. This gives positive contributions to $\overline{u''v''}$. When the jet angle is big, the fluid motions in the main flow happen mostly in Q2 and Q4. This gives negative contributions to $\overline{u''v''}$.
- The big phase-variations of profiles of the averaged velocity and the Reynolds shear stress $\overline{u''v''}$ are near the wall below $y^+ = 80$.

Chapter 6

Behaviour of Zero Mass Jets by changing the frequency or speed

6.1 Flow conditions

In the previous chapter, a drag reduction can be achieved by adapting ZMJ. The drag reduction has been obtained by changing jet angle β. Except the angle, there are many parameters can be studied in the settings of the control method, as shown in figure 5.1. Without changing geometry, it is easy to test three parameters, including the jet angle β, the maximum jet speed W_{max}^{+} and the frequency f^{+}. In order to explore the unique control method, it is worthy to try the other two parameters except the jet angle β. Based on the previous analysis, the drag reduction is related to the strength of countering jet in the streamwise direction. The strength would be increased by increasing either W_{max}^{+} or f^{+}, so that either W_{max}^{+} or f^{+} is doubled to see the behaviour of the friction drag in the turbulent channel flow. In this chapter, only one parameter is changed at a time. This means that either the frequency or the jet speed is changed, the other parameters are kept the same as that in the previous chapter. Because the friction drag can be reduced with $\beta = 75°$, it is reasonable to start the study based on the successful parameters. If the frequency f^{+} is doubled, the period of ZMJ will be $T_{osc}^{+} = 62.5$. The maximum jet speed of the ZMJ will be doubled to be $W_{max}^{+} = 54$.

In this chapter, to simplify the case name, the case which has ($T^{+} = 125$, $W_{max}^{+} = 27$) will be called **baseline case**. The case which has ($T^{+} = 125$, $W_{max}^{+} = 54$) will be called **double-speed case**. The case which has ($T^{+} = 62.5$, $W_{max}^{+} = 27$) will be called **double-frequency case**.

6.2 Time averaged results

The evolutions of skin friction coefficients are shown in figure 6.1, comparing the cases ($T^+ = 125$, $W^+_{max} = 27$), ($T^+ = 125$, $W^+_{max} = 54$) and ($T^+ = 62.5$, $W^+_{max} = 27$). The time averaged skin-friction-coefficients are 1.31×10^{-3} and 6.59×10^{-3} for the double-speed case and the double-frequency case, respectively. The periodic characters of the coefficients can be observed in the results. Both increasing the jet speed and frequency of ZMJ can increase the effects of drag reduction. The best case of drag reduction in the previous chapter has a skin friction coefficient of 7.32×10^{-3}, and the best level of gross drag reduction is 10.5%. The level of gross drag reduction can be 84.0% by only doubling the jet speed of ZMJ, and it can be 19.4% by only doubling the frequency of ZMJ. Since the double-frequency case oscillates more frequently than the other two cases, the skin-friction of the double-frequency case fluctuates more frequently than the others as well. When the jet angle is $\beta = 75°$, the time period of the skin-friction fluctuation is the same as the time period of the ZMJ oscillation, which has been studied by the Fast Fourier Transform in section 5.5. The double-speed case has the highest amplitude of the skin-friction fluctuations in three cases, and double-frequency case has the lowest. This indicates that increasing the jet frequency can reduce the amplitude of the skin-friction fluctuations.

The distributions of time and space averaged skin-frictions in a section are shown in figure 6.2 with a very similar pattern. The friction drag is significantly reduced near the jet-exits, and it is increased in region above the steps and in the middle of each sections. In three cases,

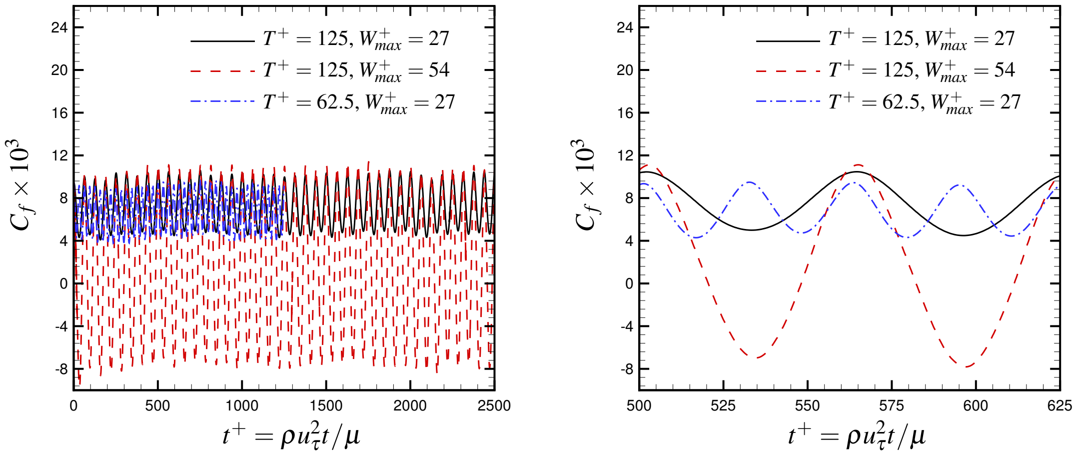

(a) The whole history

(b) Zooming in a short period

Figure 6.1 The evolutions of skin friction coefficients with different frequency and jet speed of ZMJ.

though the drag of double-speed case is increased the most in region above the steps, but the drag is reduced the most between the pair of jets. Overall, the drag of double-speed case is reduced the most. By increasing the jet frequency, the drag of double-frequency case is smaller than that of baseline case at all spanwise positions.

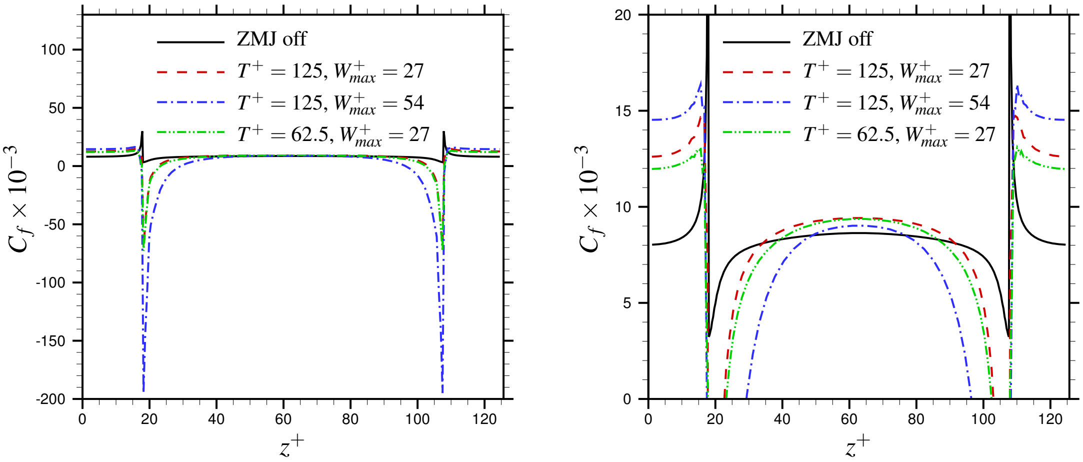

(a) Whole scale

(b) Narrow scale

Figure 6.2 Distributions of time and space averaged skin-friction-coefficients in a section for different cases, including the case ZMJ(off), the baseline case, the double-speed case and the double-frequency case.

Figure 6.3 shows the time and space averaged streamwise-velocity $\overline{u}^+$ in the $y-z$ plane, comparing the contour plots of the averaged streamwise-velocity. Looking at figures 5.22a, 5.22d, 6.3a and 6.3b, it is easy to notice that the contour lines between the pair of jets are lifted the most in the double-speed case, and the contour lines in region above the steps are brought down the most. Because the double-speed case has the highest spanwise jet-speed and forms the strongest motions of the vortices. The motions of the vortices which are shown in figure 5.19d cause the lift and drop of the contour lines. Comparing figure 5.25a, 5.25d, 6.3c and 6.3b with magnifying the fluid regions near the jet-exits, the double-speed case has the largest region of negative $\overline{u}^+$, and the negative region of double-frequency case is slightly larger than that of the baseline case. This indicates that increasing the jet speed is more effective than increasing the jet frequency to enlarge the regions in where the friction drag is reduced.

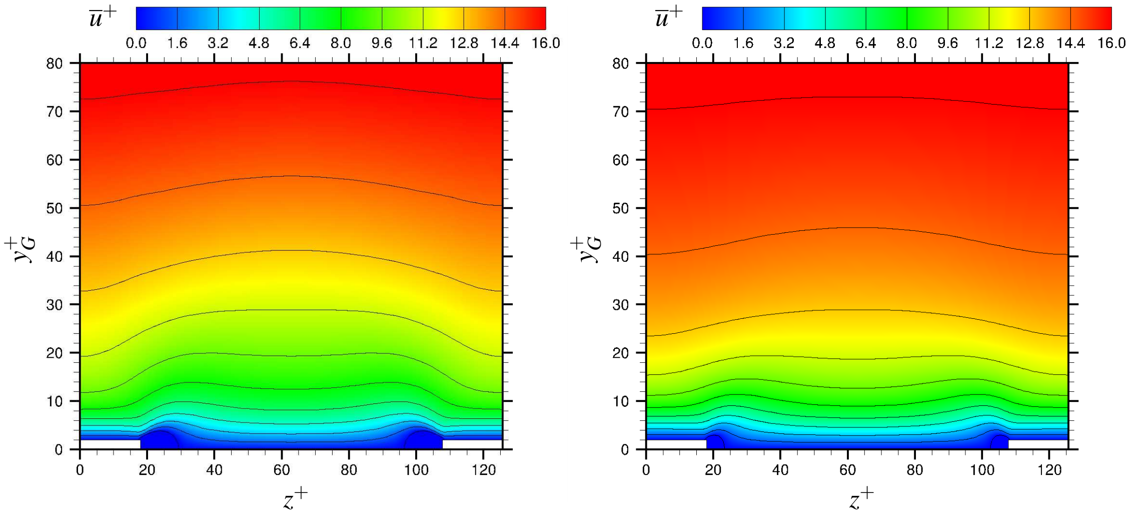

(a) $T^+ = 125$, $W_{max}^+ = 54$ (b) $T^+ = 62.5$, $W_{max}^+ = 27$

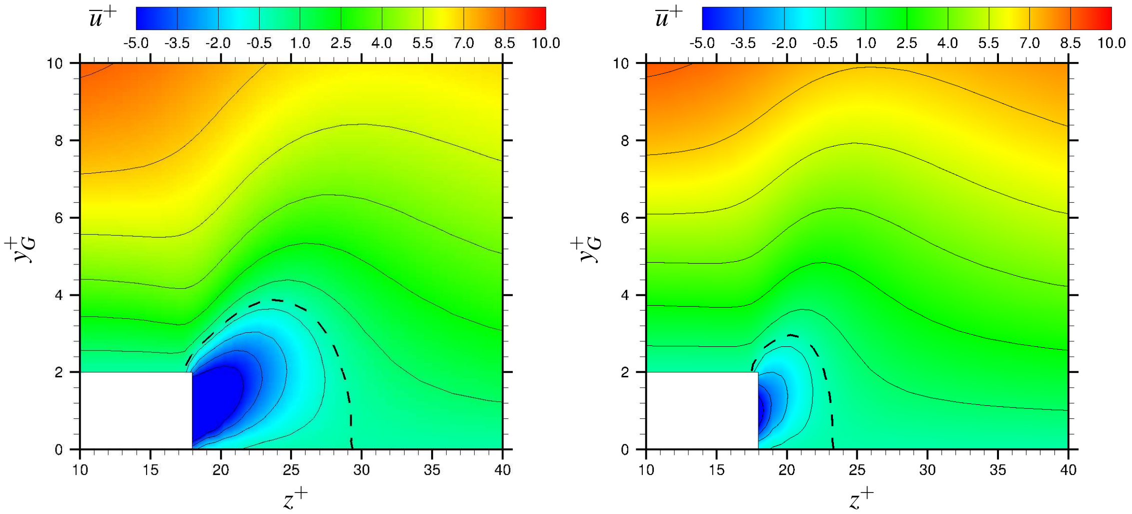

(c) $T^+ = 125$, $W_{max}^+ = 54$, zooming in (d) $T^+ = 62.5$, $W_{max}^+ = 27$, zooming in

Figure 6.3 The cross-stream ($y-z$ plane) view of time and space averaged streamwise-velocity $\overline{u}^+$ with contours. The top two show the regions near the bottom wall, and the bottom two magnify the regions near the jet-exits. The black dashed line is $\overline{u}^+ = 0$.

In figure 6.4, the profiles of time and space averaged streamwise-velocity of three cases are compared with the case ZMJ(off) at different spanwise positions, including $z^+ = 0.1$, 17, 20, 62.83. Comparing with the case ZMJ(off), the profiles of the cases ZMJ(on) are shifted at three positions. The reason has been discussed in section 5.5. As shown in the figures, the profile of double-speed case is shifted the most at shift ①, and the drag is reduced the most among the cases ZMJ(on). In the middle of each sections $z^+ = 62.83$, even either the jet-speed or the jet frequency is doubled, the averaged profiles are not changed much in the viscous sublayer.

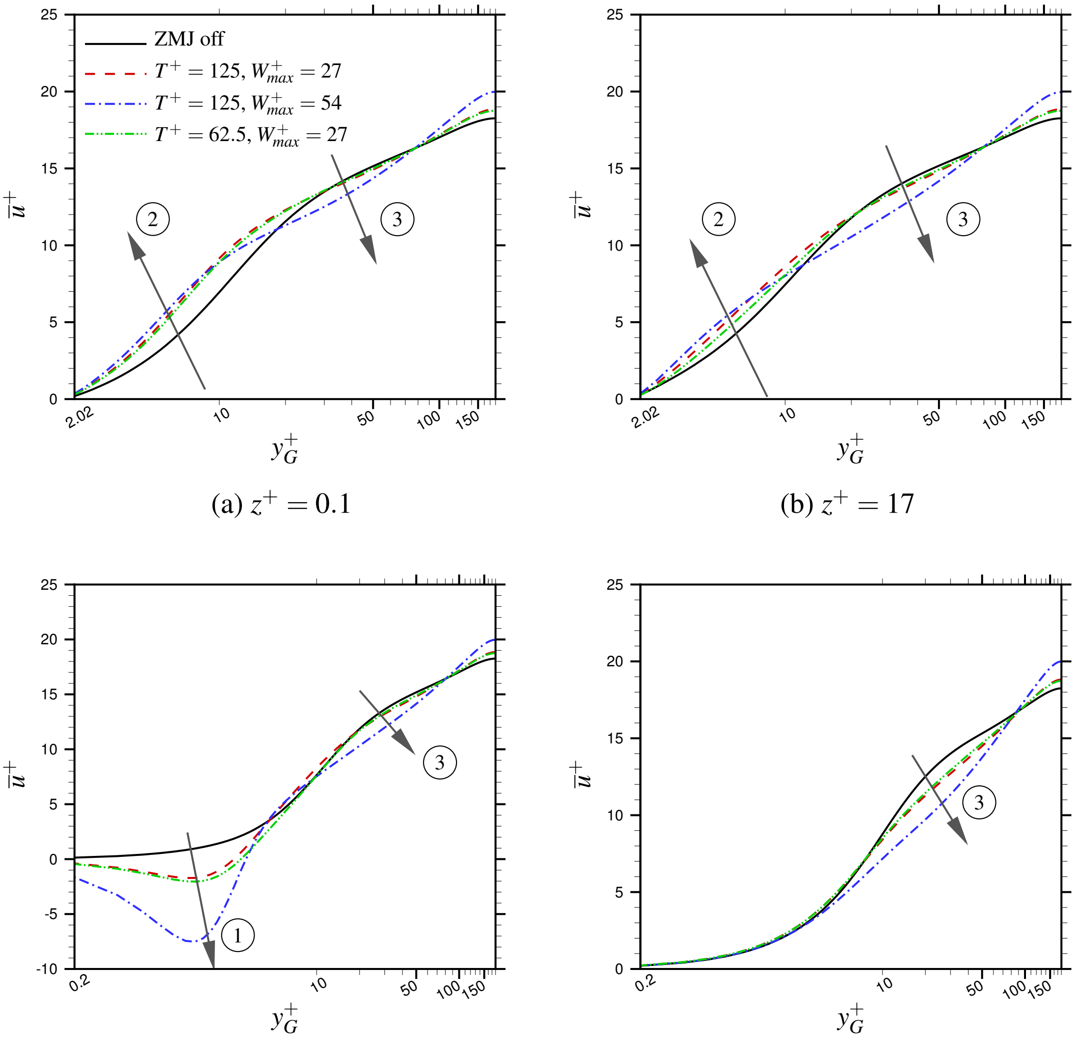

(a) $z^+ = 0.1$

(b) $z^+ = 17$

(c) $z^+ = 20$

(d) $z^+ = 62.83$

Figure 6.4 Comparisons of the time and space averaged streamwise-velocity profiles at the different spanwise positions.

Figure 6.5 shows the contour plots of u'_{rms}/u_τ and $-\overline{u'v'}/u_\tau^2$ in $y-z$ plane to compare the velocity fluctuations and Reynolds shear stress. The u'_{rms}/u_τ and $-\overline{u'v'}/u_\tau^2$ of the baseline case have already been shown in figure 5.31d and 5.38d, respectively. Comparing the contour plots of u'_{rms}/u_τ among three cases, it seems that increasing the jet frequency only slightly increases the streamwise-velocity fluctuations, but increasing the jet speed can significantly increase the fluctuations. The regions $u'_{rms}/u_\tau \geq 2.5$ when the jet speed is doubled are expended to be larger than that when the jet speed is $W^+_{max} = 27$. Looking at the Reynolds shear stress $-\overline{u'v'}/u_\tau^2$, it can be noticed that the Reynolds shear stress is reduced by increasing

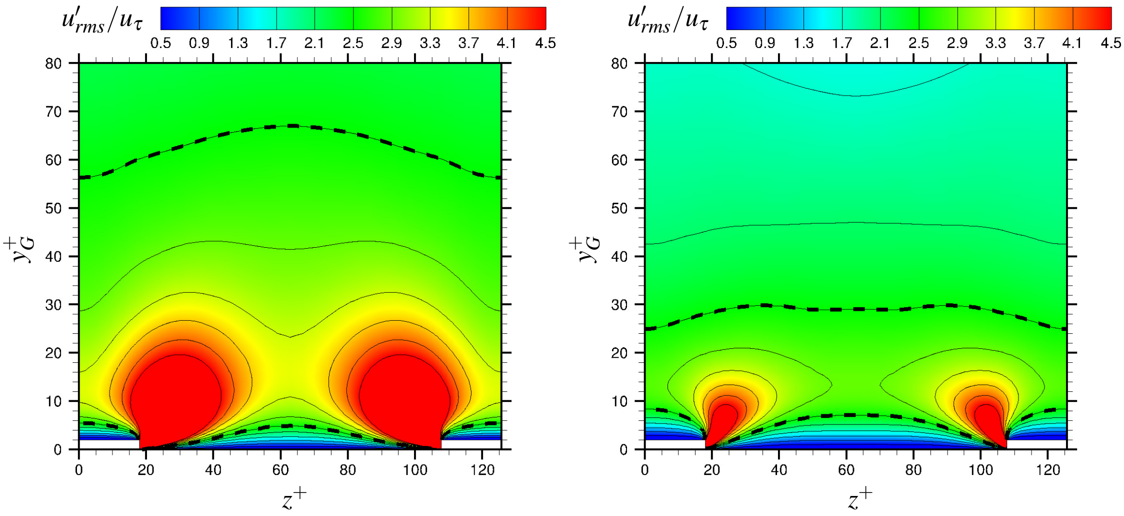

(a) $T^+ = 125$, $W^+_{max} = 54$ (b) $T^+ = 62.5$, $W^+_{max} = 27$

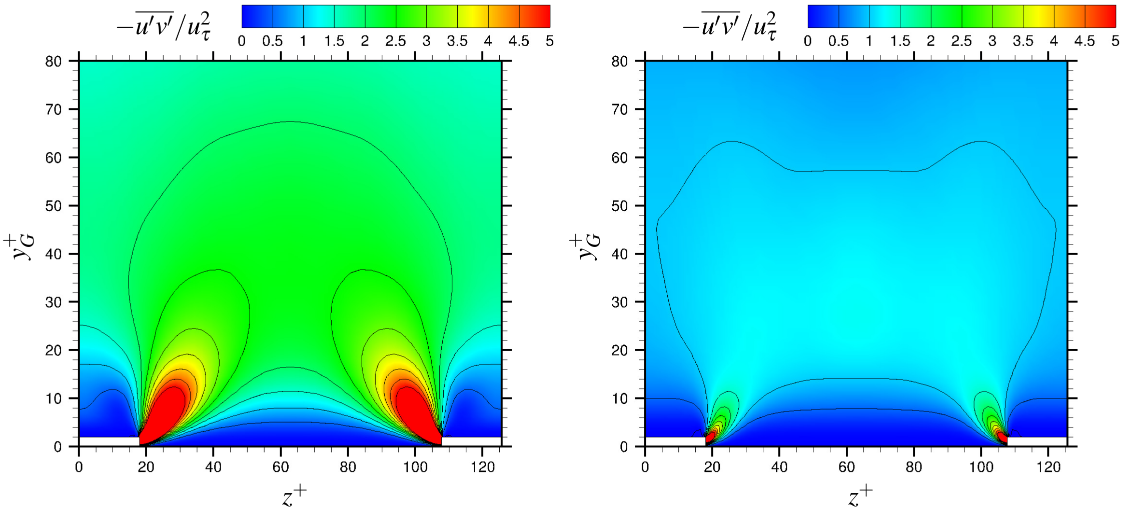

(c) $T^+ = 125$, $W^+_{max} = 54$ (d) $T^+ = 62.5$, $W^+_{max} = 27$

Figure 6.5 The cross-stream ($y-z$ plane) view of u'_{rms}/u_τ and $-\overline{u'v'}/u_\tau^2$ contours. The black dashed lines denote $u'_{rms}/u_\tau = 2.5$ in (a) and (b).

the jet frequency, and the Reynolds shear stress is significantly risen by increasing the jet speed. Among three cases, there are some similarities. The streamwise velocity-fluctuations are high in the regions where are close to the jet-exits because the fluctuating source is ZMJ. The Reynolds shear stresses are high near the jet-exits, but they are low near the walls.

As same as the previous chapter, to show the differences of the streamwise velocity-fluctuations and the Reynolds shear stress, figures 6.6 and 6.7 compare the profiles at different spanwise-positions. Both the streamwise velocity-fluctuations and the Reynolds

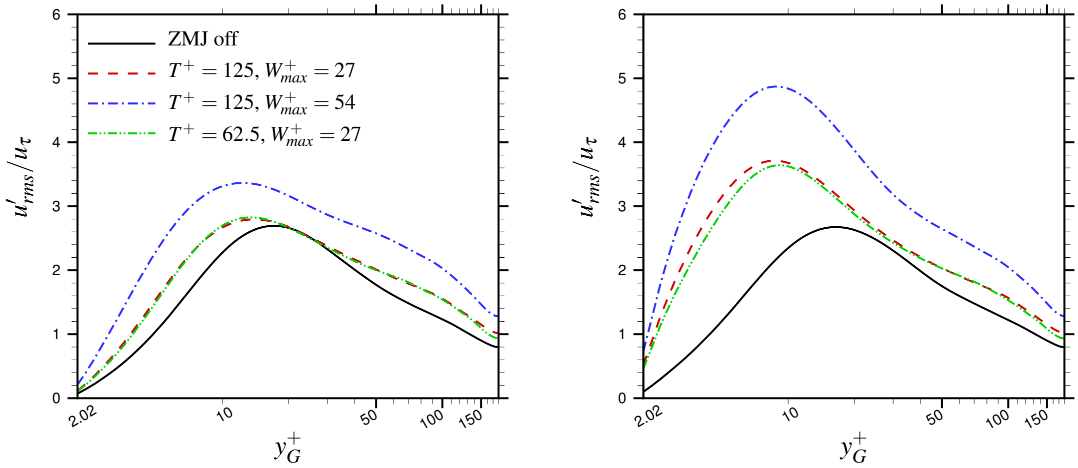

(a) $z^+ = 0.1$

(b) $z^+ = 17$

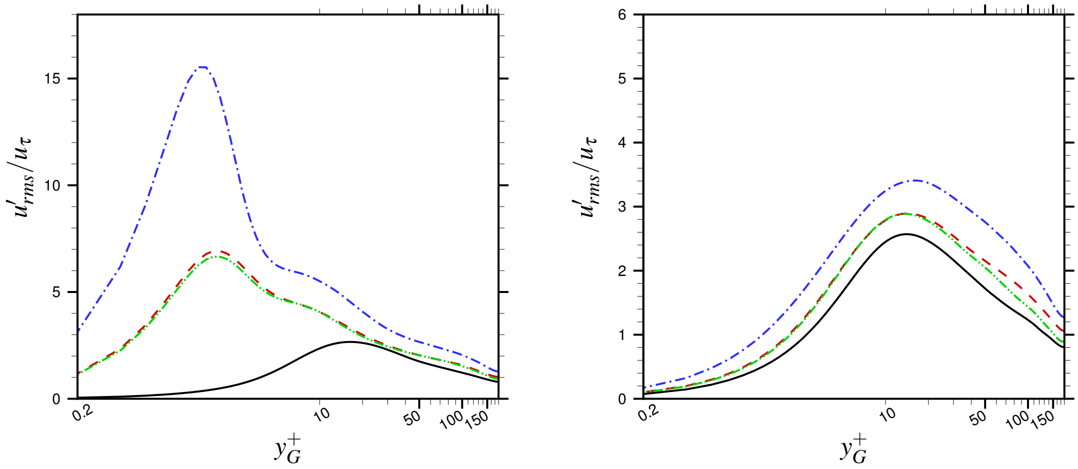

(c) $z^+ = 20$

(d) $z^+ = 62.83$

Figure 6.6 The comparisons of u'_{rms}/u_τ profiles at the different spanwise positions, covering the height ranges of a half channel. To clearly show the profile differences, the ranges of u'_{rms}/u_τ in (c) is different from (a), (b) and (d).

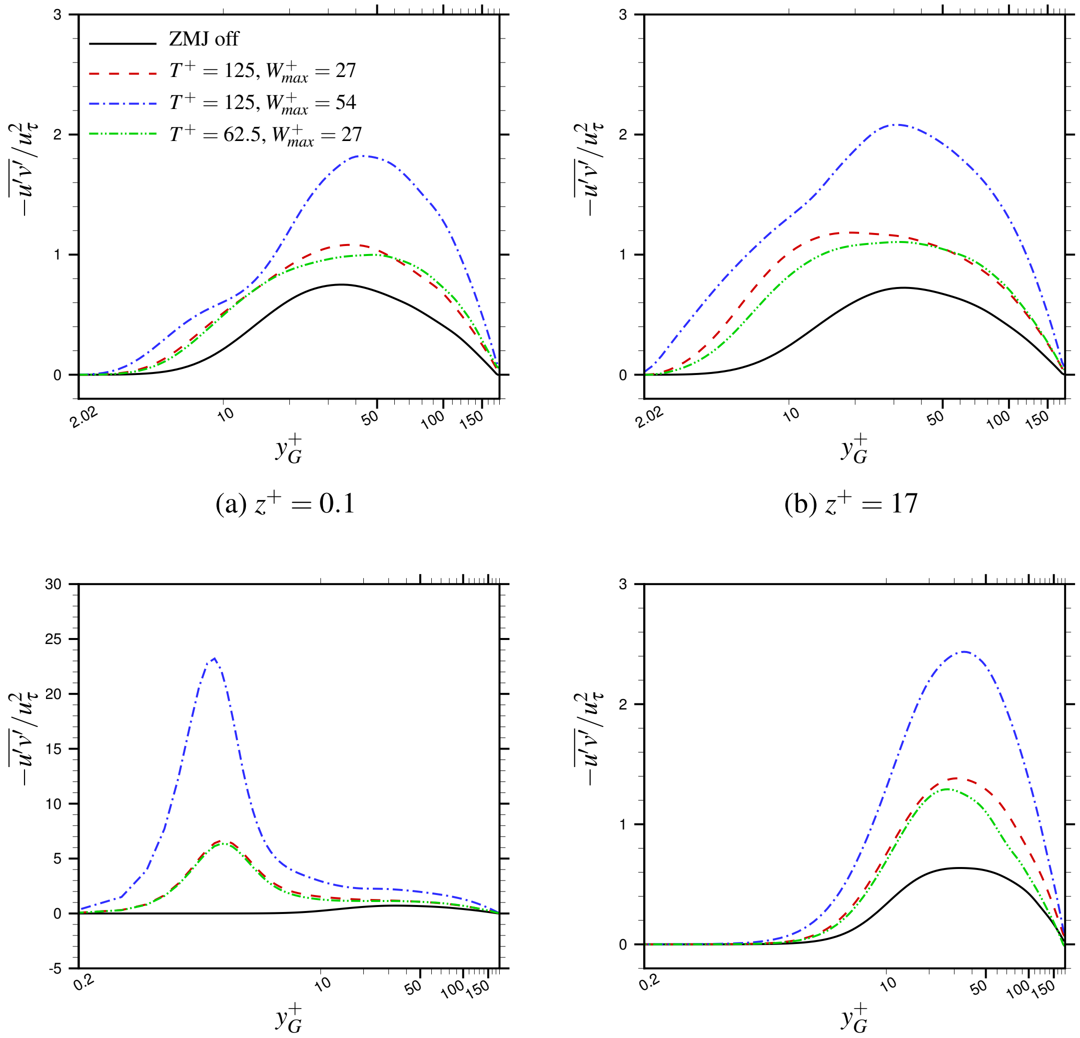

(a) $z^+ = 0.1$ (b) $z^+ = 17$

(c) $z^+ = 20$ (d) $z^+ = 62.83$

Figure 6.7 The comparisons of $-\overline{u'v'}/u_\tau^2$ profiles at the different spanwise positions, covering the height ranges of a half channel. To clearly show the profile differences, the ranges of u'_{rms}/u_τ in (c) is different from (a), (b) and (d).

shear stresses are increased from the walls to the channel centres by ZMJ, comparing to the case ZMJ(off). When ZMJ is on, both the streamwise velocity-fluctuations and the Reynolds shear stresses are significantly increased near the jet-exits at the regions ($y_G^+ \leq 10$, $z^+ = 20$). The double-speed case increases the most. It can be predicted that increasing the jet-speed always increases the streamwise velocity-fluctuations and the Reynolds shear stresses at different spanwise positions.

Comparing with the influence of the jet speed, the influence of the jet frequency seems to be more complicated. To investigate the influence of the jet frequency under the same jet speed, the baseline case and the double-speed case are compared. When the jet speed is fixed, figures 6.6b and 6.6c show that the fluctuations are slightly reduced in the regions $y_G^+ \leq 10$ by doubling the frequency, but the fluctuations are almost the same in the other regions. Figure 6.6a shows that the fluctuations are not changed in the sides of each sections from the walls to channel centres. Figure 6.7d represents that the fluctuations are reduced a bit by doubling the frequency when the height y_G^+ is bigger than 20. When the jet frequency is increased, figures 6.7a and 6.7b represent that the Reynolds shear stresses are reduced when $y_G^+ < 60$, but the Reynolds shear stresses are increased in the regions $y_G^+ > 60$ in region above the steps. The Reynolds shear stresses are always reduced from the walls to the channel centres between the pair of jets by doubling the jet frequency.

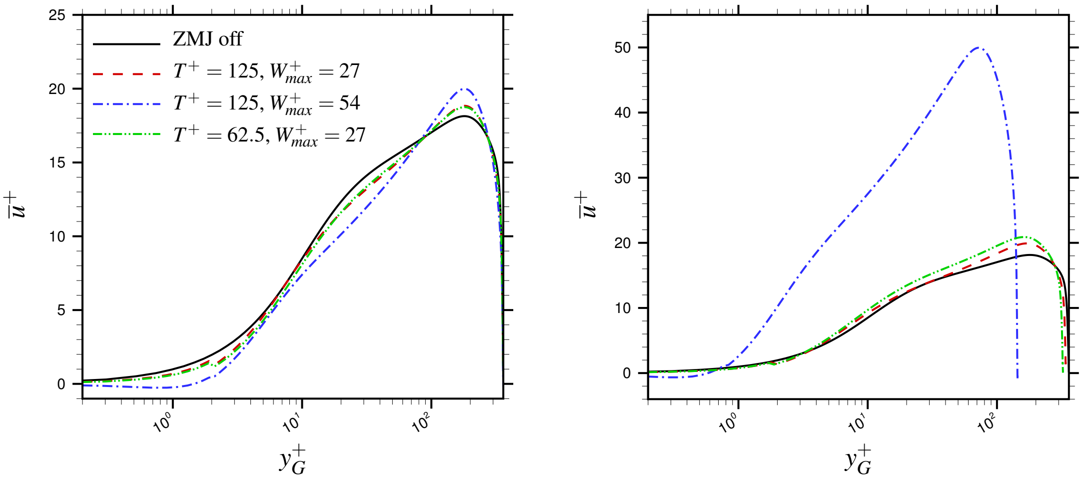

(a) u_τ (b) $u_{\tau.l}$

Figure 6.8 The logarithmic profiles of the averaged streamwise-velocity which are nondimensionalized by u_τ obtained from the smooth channel, and $u_{\tau.l}$ computed from the local results.

As the discussion in the end of section 5.5, the averaged streamwise-velocity profile in the log-law region can be twisted by ZMJ, and the Von Kármán constant is changed. Figure 6.8 shows the streamwise-velocity profiles which are time and space averaged without regarding the variations in the streamwise and spanwise directions. Figure 6.8a uses the friction velocity u_τ obtained from the result of smooth channel to do the nondimensionalization of velocity and wall-distance. Figure 6.8b employs the local friction-velocity $u_{\tau.l}$ computed from the result of each case. In figure 6.8a, the velocity gradient of the double-speed case is the highest in the log-law region among the cases, and the velocity gradients of the baseline case and double-frequency case are almost the same. In the log-law region, the cases ZMJ(on) have bigger velocity gradients than the case ZMJ(off). The Von Kármán constant κ and constant A for the general logarithmic equation 5.9 can be obtained from figure 6.8b by fitting the profiles in the log-law regions, as shown in table 6.1. The information is useful for the RANS simulations of the drag reduction with ZMJ.

Table 6.1 The values of the parameters in the general logarithmic equation 5.9 for different cases.

ZMJ	T^+	W^+_{max}	κ	A
off	–	–	0.41	5.8
on	125	27	0.26	0.7
on	125	54	0.08	−2.2
on	62.5	27	0.26	1.8

6.3 Phase averaged results

The time and space averaged flow fields of the double-speed and double-frequency cases are studied in the previous section. In this section, the flow fields will be phase and space averaged to see the behaviour of doubling either the jet speed or the jet frequency.

Figure 6.9 displays the contours of the phase and space averaged streamwise-velocities in the $y-z$ for the double-speed and double-frequency cases, when the phase time is $\varphi = \pi/2$. The baseline case in the same condition is already shown in figure 5.50e. Three cases have very similar averaged flow fields. A separation zone $\langle u^+ \rangle \leq 0$ is near the left jet-exits that is blowing, and the viscous sublayer is compressed near the right jet-exits that is sucking. The double-speed case has the largest separation zone among three cases, and the viscous sublayer is compressed the most. Increasing the jet frequency reduces the size of the separation zone, and the viscous sublayer of the double-frequency case is compressed the lest in three cases. The shape of the region $\langle u^+ \rangle \leq 9.6$ depends on both the jet mass and the jet frequency.

At the phase time $\varphi = \pi/2$, the distributions of phase and space averaged skin-friction-coefficients are compared in figure 6.10. The averaged distributions of the double-speed and double-frequency cases are very similar with that of the baseline case. When the phase time is $\varphi = \pi/2$, a region of drag-reduction appears near the left jet-exits, and the drag is increased near the right jet-exits. Because the reducing amount of the drag is more than the increasing amount, so the overall drag is reduced. As discussed in the previous chapter, the distributions of the skin friction coefficients are related to the gradients of the averaged streamwise-velocity. In three cases, the largest region of drag reduction near the left jet-exits is the double-speed case. The drag near the right jet-exits is increased the most in the double-speed case as well. The double-frequency case has a smaller region of drag reduction than the baseline case. The increased drag of the double-frequency case near the right jet-exits is smaller than the baseline case as well. The phenomenon is the related to the averaged flow fields.

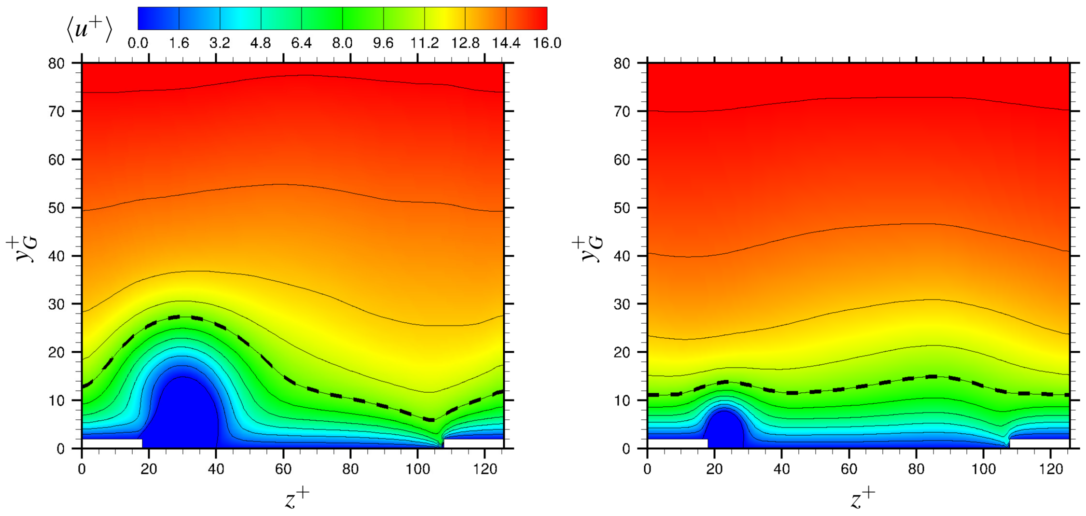

(a) $T^+ = 125$, $W^+_{max} = 54$ (b) $T^+ = 62.5$, $W^+_{max} = 27$

Figure 6.9 The contours of cross-stream ($y - z$ plane) view of phase and space averaged streamwise-velocities, when the phase time is $\varphi = \pi/2$. The dashed lines denote $\langle u^+ \rangle = 9.6$.

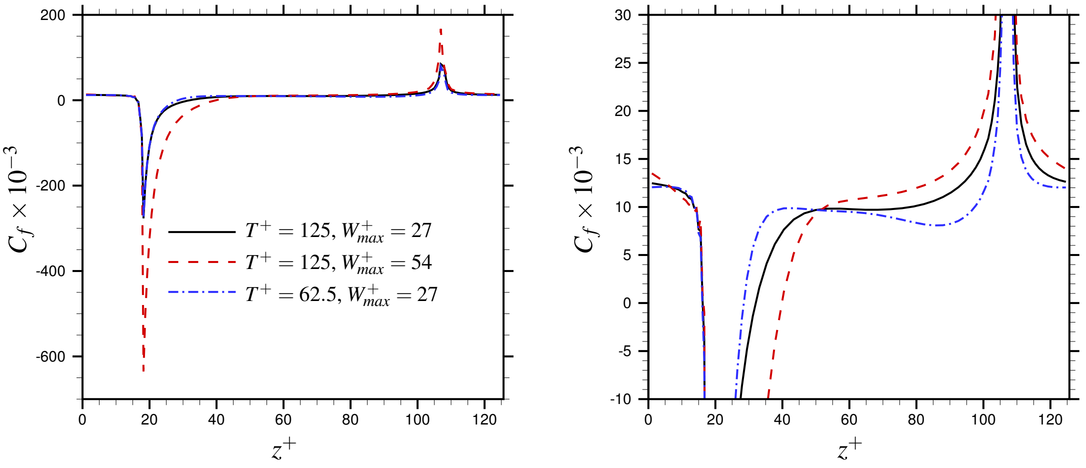

(a) Whole scale (b) Narrow scale

Figure 6.10 Comparison of the phase and space averaged distributions of skin-friction-coefficients at the phase time $\varphi = \pi/2$.

The phase and space averaged streamwise velocity at the spanwise position $z^+ = 20$ where is near the left jet-exits plays a very important role on the drag reduction, so the velocity profiles through a period of ZMJ is put together to show the variations in the contour plots, as shown in figures 6.11a and 6.11b. Since the drag at $z^+ = 20$ is reduced the most at $\varphi = \pi/2$ and is increased the most at $\varphi = 3\pi/2$ as discussed before, the velocity profiles of three cases are compared to represent the difference in figures 6.11c and 6.11d. Comparing figures 5.51e, 6.11a and 6.11b, all three cases have separation from $\varphi = \pi/10$ to $\varphi = \pi$. In the figures, the difference is that the minimum value of the averaged streamwise-velocity of

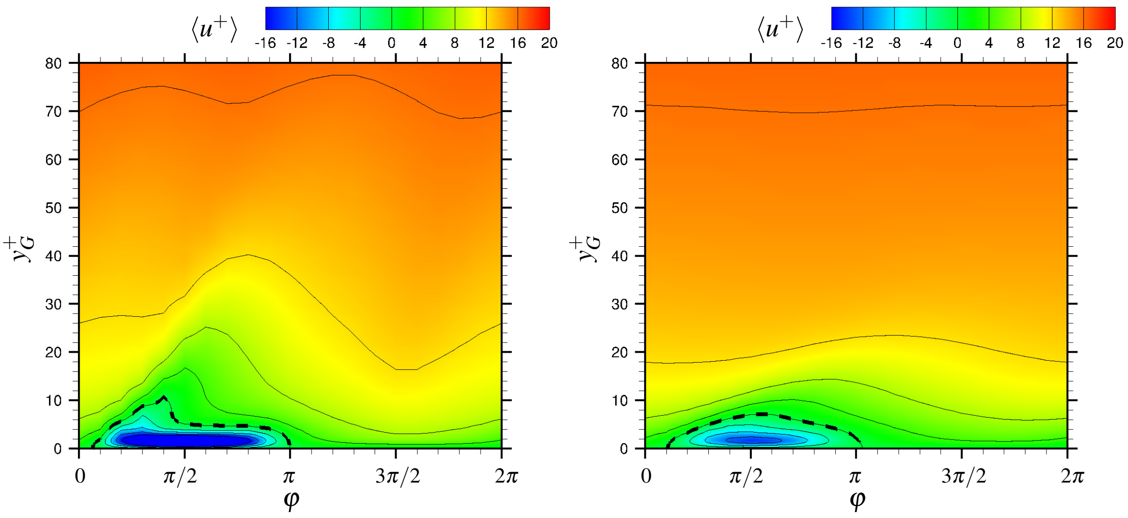

(a) The contours of $T^+ = 125$, $W_{max}^+ = 54$ (b) The contours of $T^+ = 62.5$, $W_{max}^+ = 27$

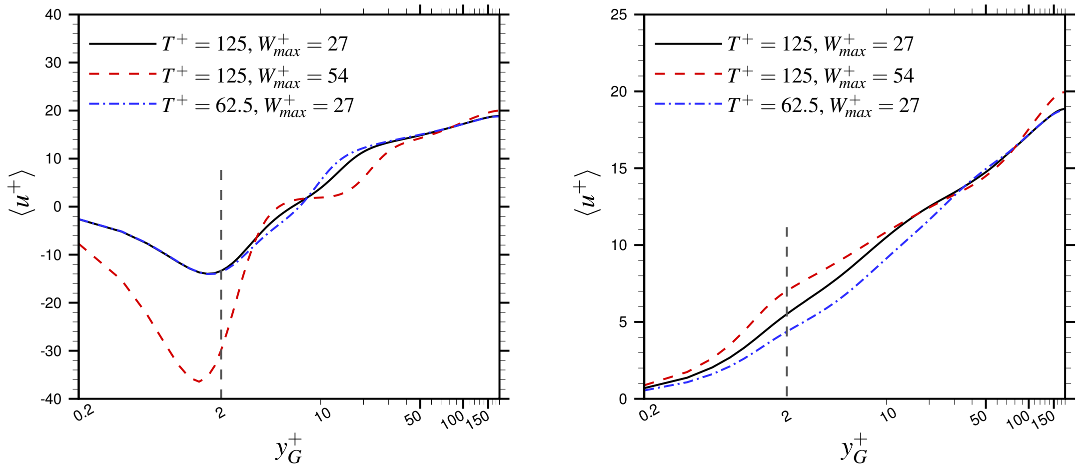

(c) $\varphi = \pi/2$ (d) $\varphi = 3\pi/2$

Figure 6.11 The contours and profiles of the phase and space averaged streamwise-velocity at the spanwise position $z^+ = 20$. The black dashed lines denote $\langle u^+ \rangle = 0$.

the double-speed case is the smallest among three cases, because the countering jet of the double-speed case is the strongest. Figure 6.11c shows that the double-speed case has the lowest gradient of the averaged streamwise-velocity near wall at $\varphi = \pi/2$, and the profiles of the averaged streamwise-velocity in the region $y_G^+ \leq 2$ are not affected by the change of the jet frequency. At $\varphi = 3\pi/2$, the double-speed case has the biggest gradient of the averaged streamwise velocity, and the double-frequency has the lowest gradient in the regions where $y_G^+ \leq 2$, representing in figure 6.11d.

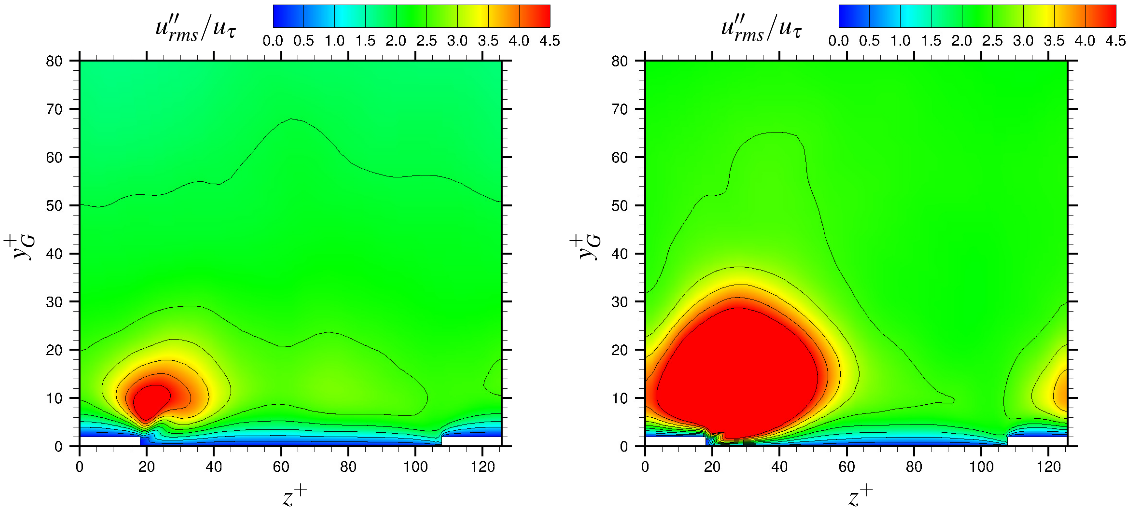

(a) $T^+ = 125$, $W_{max}^+ = 27$ (b) $T^+ = 125$, $W_{max}^+ = 54$

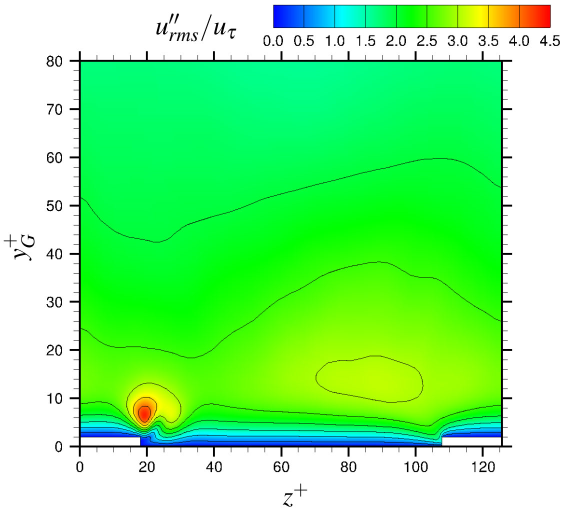

(c) $T^+ = 62.5$, $W_{max}^+ = 27$

Figure 6.12 Contours of u''_{rms}/u_τ in the cross-stream ($y-z$ plane) view at $\varphi = \pi/2$. The left jet-exits is blowing and the right jet-exits is sucking.

Figure 6.12 compares the root-mean-square of the pure turbulent fluctuations of the streamwise velocity in the $y-z$ plane at the phase time $\varphi = \pi/2$. The fluid is being blown out from the left jet-exits and is being sucked in from the right jet-exits. The similarity is that the fluctuations are generated by the blowing jet-exits and cancelled by the sucking jet-exits. Increasing the jet speed can enlarge the region of high fluctuations, but increasing the jet frequency shrinks the region. The reason is that increasing the jet speed enlarges the influence strength of ZMJ. Increasing the jet frequency reduces the spreading time for the fluctuations. Since the right jet-exits of the double-frequency case dose not sucks in the pure

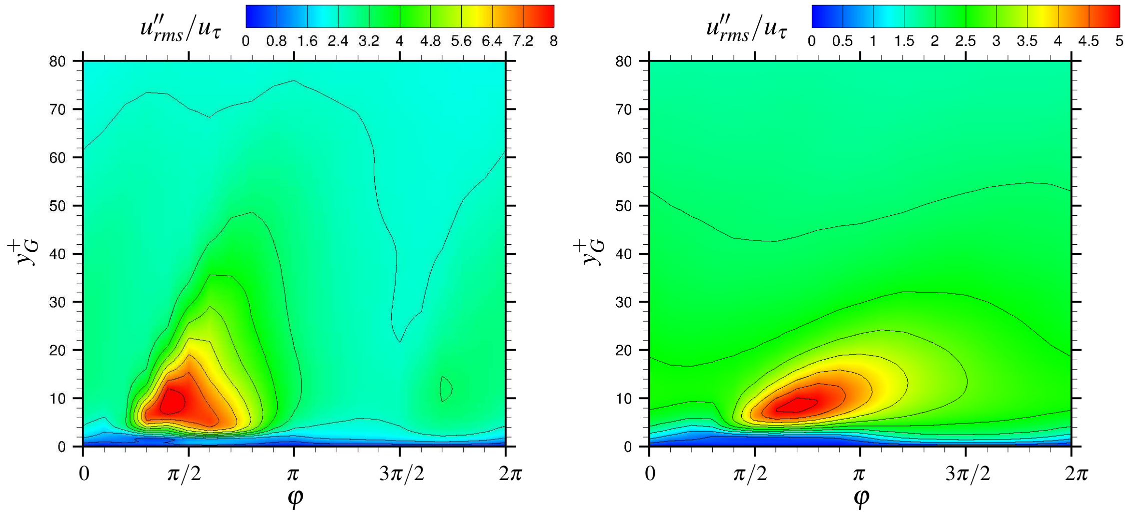

(a) The contours of $T^+ = 125$, $W^+_{max} = 54$ (b) The contours of $T^+ = 62.5$, $W^+_{max} = 27$

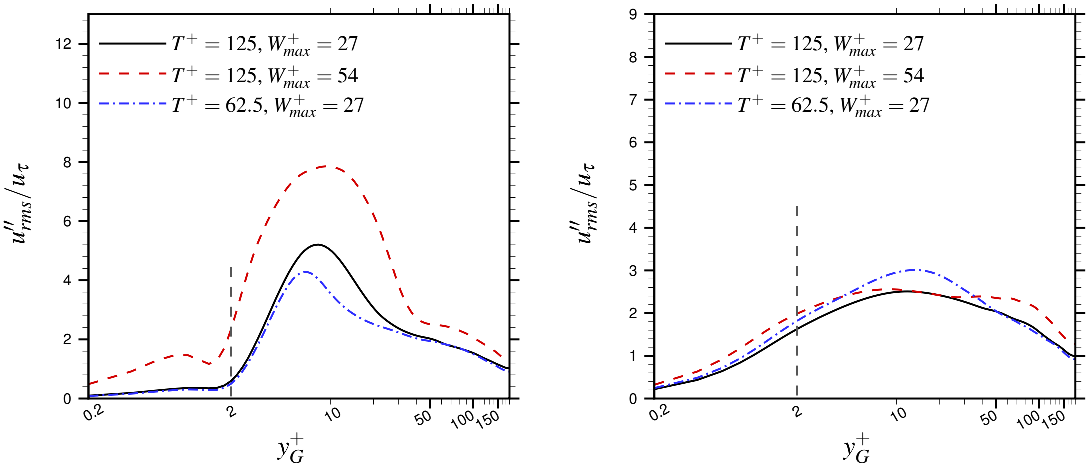

(c) $\varphi = \pi/2$ (d) $\varphi = 3\pi/2$

Figure 6.13 The contours and profiles of the root mean square of pure turbulent velocity-fluctuations in the streamwise direction, u''_{rms}/u_τ, at the spanwise position $z^+ = 20$.

velocity-fluctuations enough at $\varphi = \pi/2$, there is a local zone of high fluctuations near the right jet-exits.

Putting the profiles of u''_{rms}/u_τ from different phase time together like $\langle u^+ \rangle$, figure 6.13 shows the contour and profile plots at the spanwise position $z^+ = 20$. Comparing figures 5.53a, 6.13a and 6.13b, the peaks of u''_{rms}/u_τ happen around the same height $y_G^+ = 10$ for all the three cases, but the peaks appear at the different phase time. The double-speed case has the earliest phase time at $\varphi = 2\pi/5$. The second place is the baseline case which is at $\varphi = 3\pi/5$. The double-frequency case is at $\varphi = 7\pi/10$, taking the last place. Figures 6.13c and 6.13d compare the profiles of u''_{rms}/u_τ at the spanwise position $z^+ = 20$ at $\varphi = \pi/2$ and $\varphi = 3\pi/2$, respectively. At $\varphi = \pi/2$, the double-speed case always has the highest values of u''_{rms}/u_τ across the half channel among the three cases. This indicates that the double-speed case has the highest turbulence level. The double-frequency case and the baseline case have the similar values of u''_{rms}/u_τ in the region $y_G^+ \leq 2$ or the log-law region $y_G^+ \geq 60$. In the buffer layer, the double-frequency case has smaller values of u''_{rms}/u_τ than the baseline case. At $\varphi = 3\pi/2$, the double-frequency case has the highest peak value around the height $y_G^+ = 12$. In the region $y_G^+ \leq 2$ and the log-law region $y_G^+ \geq 60$, the double-speed case has the highest values of u''_{rms}/u_τ among the three cases. In these two regions, the values are similar between the double-frequency and baseline cases.

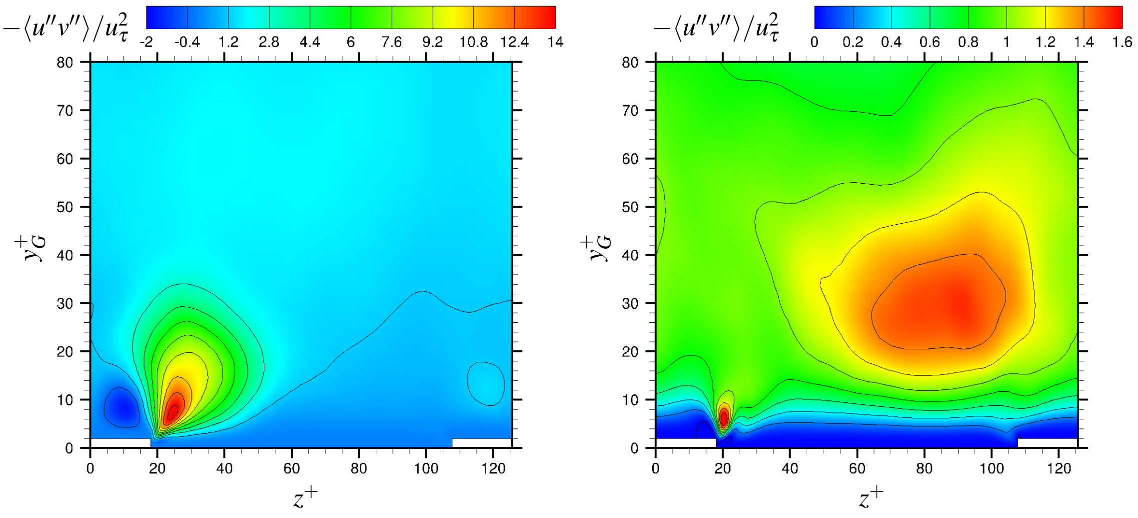

(a) $T^+ = 125$, $W_{max}^+ = 54$

(b) $T^+ = 62.5$, $W_{max}^+ = 27$

Figure 6.14 The contours of the Reynolds shear stress, $-\langle u''v'' \rangle/u_\tau^2$, in the $y - z$ plane when the phase time is $\varphi = \pi/2$.

Figure 6.14 shows the contour plots of the Reynolds shear stress, $-\langle u''v'' \rangle/u_\tau^2$, in the $y - z$ plane for the double-speed case and double-frequency case, when the phase time is $\varphi = \pi/2$. To compare the Reynolds shear stresses of three cases, it needs to look at figures

5.60b and 6.14. The Reynolds shear stresses are high near the blowing jet-exits and are relatively low near the sucking jet-exits. The phenomenon is quite similar to u''_{rms}/u_τ. In the double-frequency case, there is a local high region of $-\langle u''v''\rangle/u_\tau^2$ in the right region of a section, because the fluid which contains the high Reynolds shear stress is not sucked enough into the right jet-exits.

Figure 6.15 shows the contour plots of the Reynolds shear stress at the spanwise position $z^+ = 20$, representing the Reynolds shear stress in a period. The peak of the double-frequency case happens at $\varphi = 7\pi/10$ which is later than that of the baseline case and the double-speed

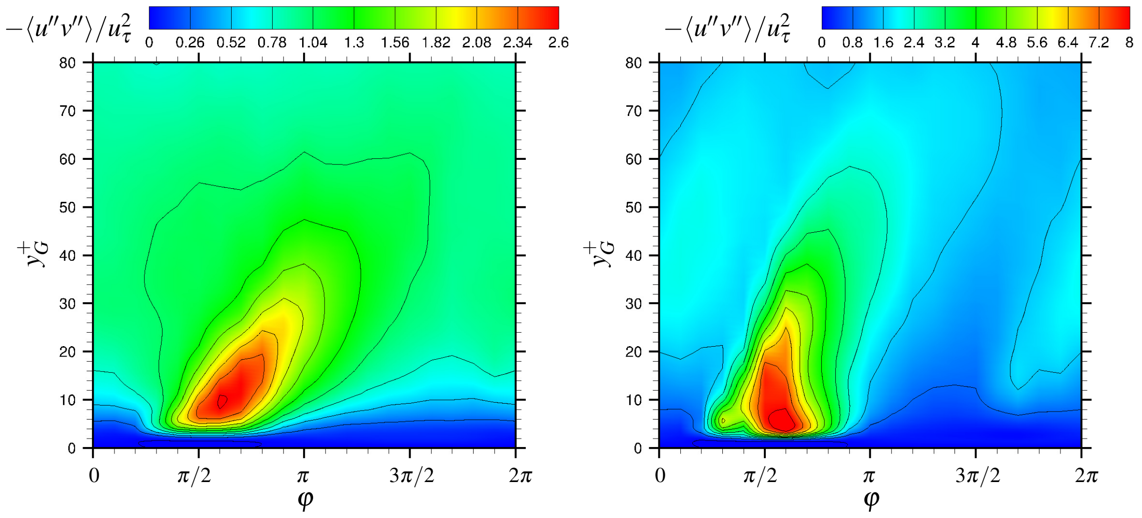

(a) The contours of $T^+ = 125$, $W^+_{max} = 27$ (b) The contours of $T^+ = 125$, $W^+_{max} = 54$

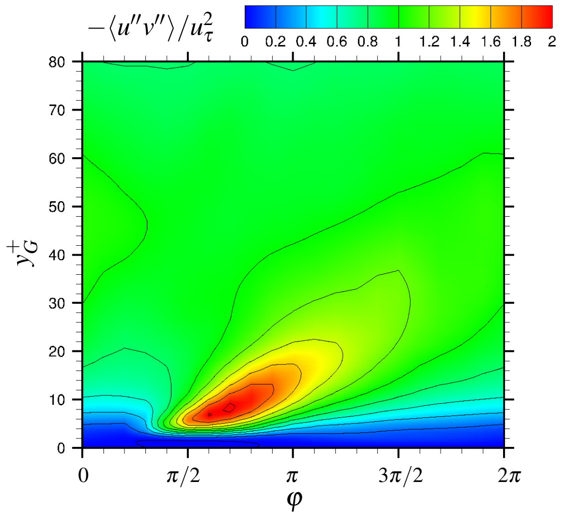

(c) The contours of $T^+ = 62.5$, $W^+_{max} = 27$

Figure 6.15 Contours of the Reynolds shear stress, $-\langle u''v''\rangle/u_\tau^2$, at the spanwise position $z^+ = 20$.

case. $\varphi = 3\pi/5$ is the phase time for the peaks of the baseline and double-speed cases. The peak of the double-speed case appears around $y_G^+ = 4.6$ which is the closest to the wall. The peak position of the double-frequency case is around $y_G^+ = 8.3$, and the peak of the baseline case is located around $y_G^+ = 9.5$. It means that both increasing either the jet-speed or the jet-frequency can bring down the peak position of the Reynolds shear stress.

Figure 6.16 compares the profiles of the Reynolds shear stress, $-\langle u''v''\rangle/u_\tau^2$, at the spanwise position $z^+ = 20$. When $\varphi = \pi/2$, the double-speed case has a negative value of $-\langle u''v''\rangle/u_\tau^2$ around $y_G^+ = 1$, and the value increases into positive. The Reynolds shear stress of the double-speed case is the highest among the three cases above $y_G^+ = 2$. The Reynolds shear stress of the double-frequency case is the lowest in region $2 \leq y_G^+ \leq 60$. When $\varphi = 3\pi/2$, the double-speed case changes the value of $-\langle u''v''\rangle/u_\tau^2$ to be positive below $y_G^+ = 1$ and reduces the peak value from 8 to 1.8. The peak value of the double-speed case is still the highest among three cases. The Reynolds shear stress of the double-frequency case is stronger than that of the baseline case when the wall distance is blow $y_G^+ = 40$.

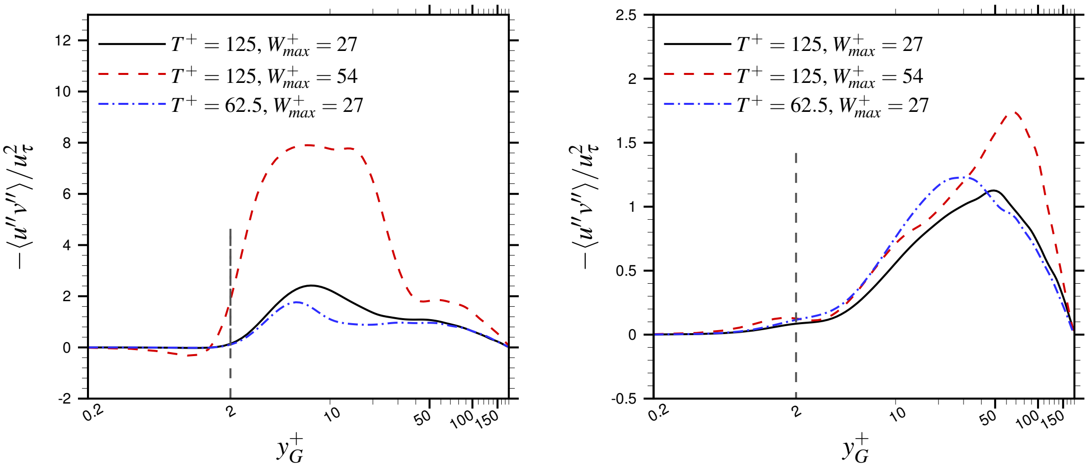

(a) $\varphi = \pi/2$

(b) $\varphi = 3\pi/2$

Figure 6.16 The profiles of the Reynolds shear stress, $-\langle u''v''\rangle/u_\tau^2$, at the spanwise position $z^+ = 20$.

6.4 Detailed flow structures

In this subsection, the flow structures will be compared in details among the three cases. Figure 6.17 shows the iso-surfaces of $\lambda_2^+ = -2$ in the half channel at the different phase time $\varphi = 0$ and $\pi/2$, representing the flow structures of the double-speed case and the double-frequency case. The total fluctuation of streamwise velocity u'^+ is employed to colour the iso-surfaces. The baseline case is shown in figure 5.64. Comparing three cases, the double-speed case has the highest density of vortices in the flow field, and the double-frequency case is the lowest. This confirms that the double-speed case disturbs the fluid the most and has the highest turbulence level. The double-frequency case has the lowest turbulence level.

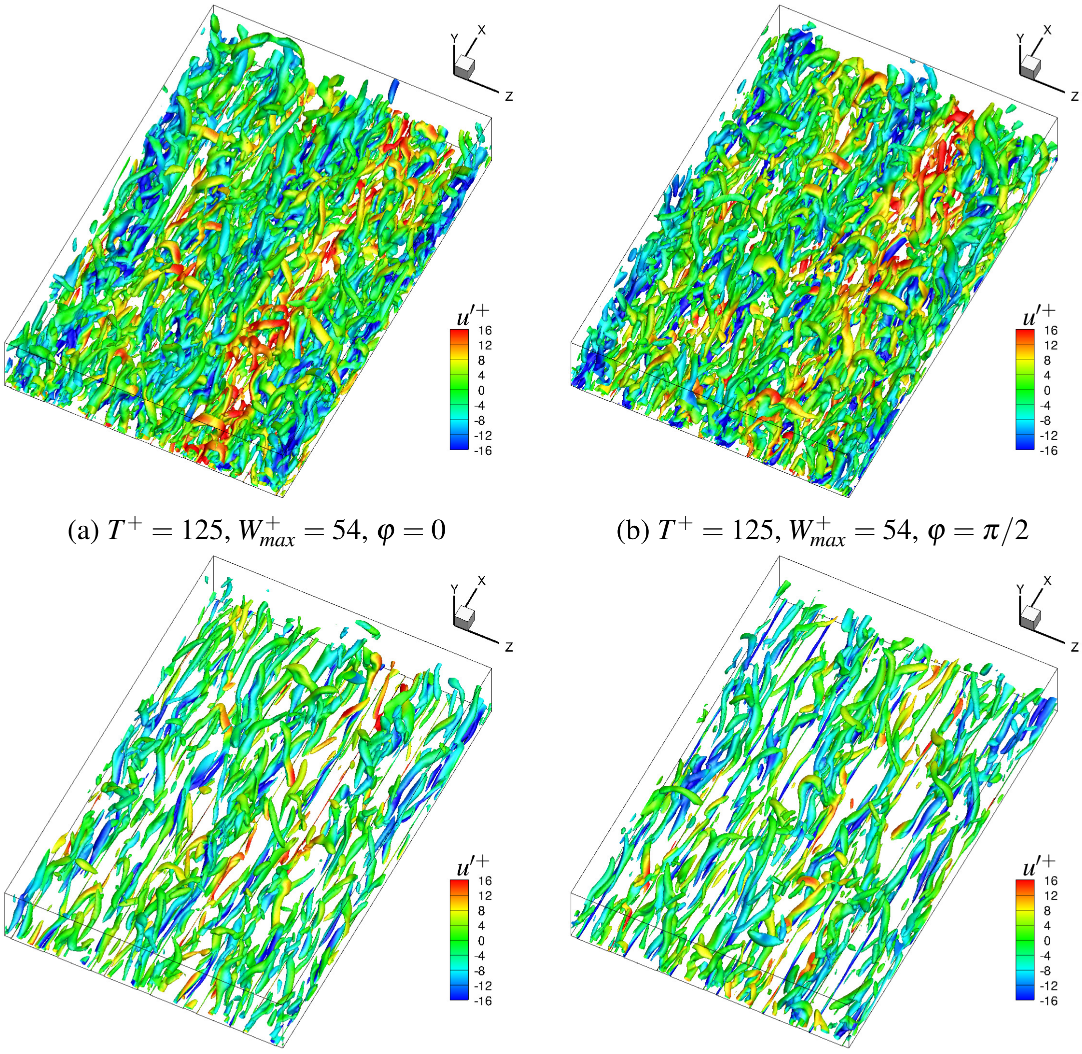

(a) $T^+ = 125$, $W^+_{max} = 54$, $\varphi = 0$ (b) $T^+ = 125$, $W^+_{max} = 54$, $\varphi = \pi/2$

(c) $T^+ = 62.5$, $W^+_{max} = 27$, $\varphi = 0$ (d) $T^+ = 62.5$, $W^+_{max} = 27$, $\varphi = \pi/2$

Figure 6.17 When the jet angle is $\beta = 75°$, the iso-surfaces of $\lambda_2^+ = -2$ in the half channel are shown at the different phase time $\varphi = 0$, $\pi/2$, comparing the flow structures between the double-speed case and the double-frequency case. The iso-surfaces are coloured by u'^+.

Figures 6.18 and 6.19 represent the total fluctuations of the streamwise-velocity in the $x - z$ plane at $y^+_G = 5$ for the double-speed case and the double-frequency case, respectively. The baseline case is shown in figure 5.68. In the figures, when $\varphi = 2\pi/5$, the low-speed regions are the most continuous among the different phase time. At $\varphi = 2\pi/5$, the double-speed case has the biggest width of the regions $u'^{+} \leq -16$, and the double-frequency has the smallest width. At $\varphi = 4\pi/5$, the lengths of the regions $u'^{+} \leq -16$ in the double-speed case tend to be the shortest, and that in the double-frequency case have a tendency to be the longest. The figures show that the velocity fluctuations in the double-speed case are the fiercest, and those in the double-frequency case are the gentlest. In conclusion, it is clear that increasing the jet speed raises the velocity fluctuations, and increasing the jet frequency reduces the velocity fluctuations.

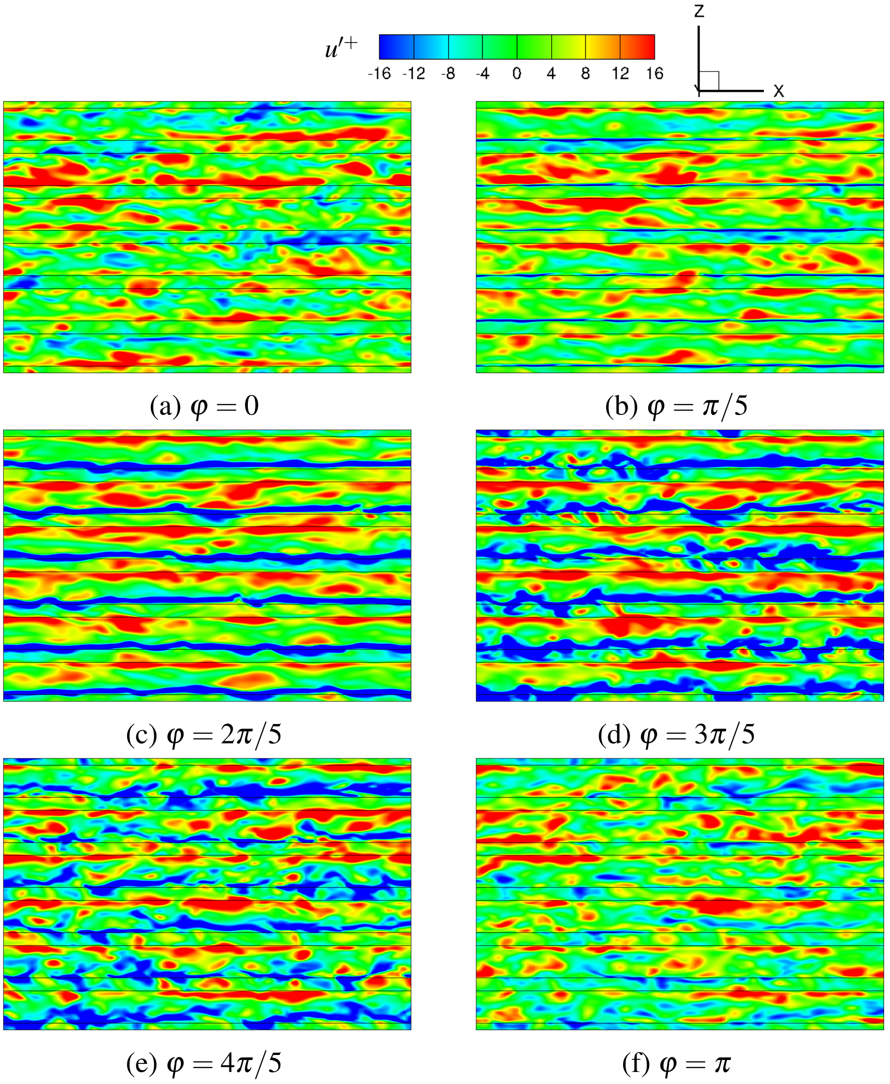

(a) $\varphi = 0$ (b) $\varphi = \pi/5$

(c) $\varphi = 2\pi/5$ (d) $\varphi = 3\pi/5$

(e) $\varphi = 4\pi/5$ (f) $\varphi = \pi$

Figure 6.18 When $T^{+} = 125$ and $W^{+}_{max} = 54$, the contours of u'^{+} in the $x-z$ plane at $y^{+}_{G} = 5$ and at the different phase time $\varphi = 0$, $\pi/5$, $2\pi/5$, $3\pi/5$, $4\pi/5$, π. The black lines are the geometry edges.

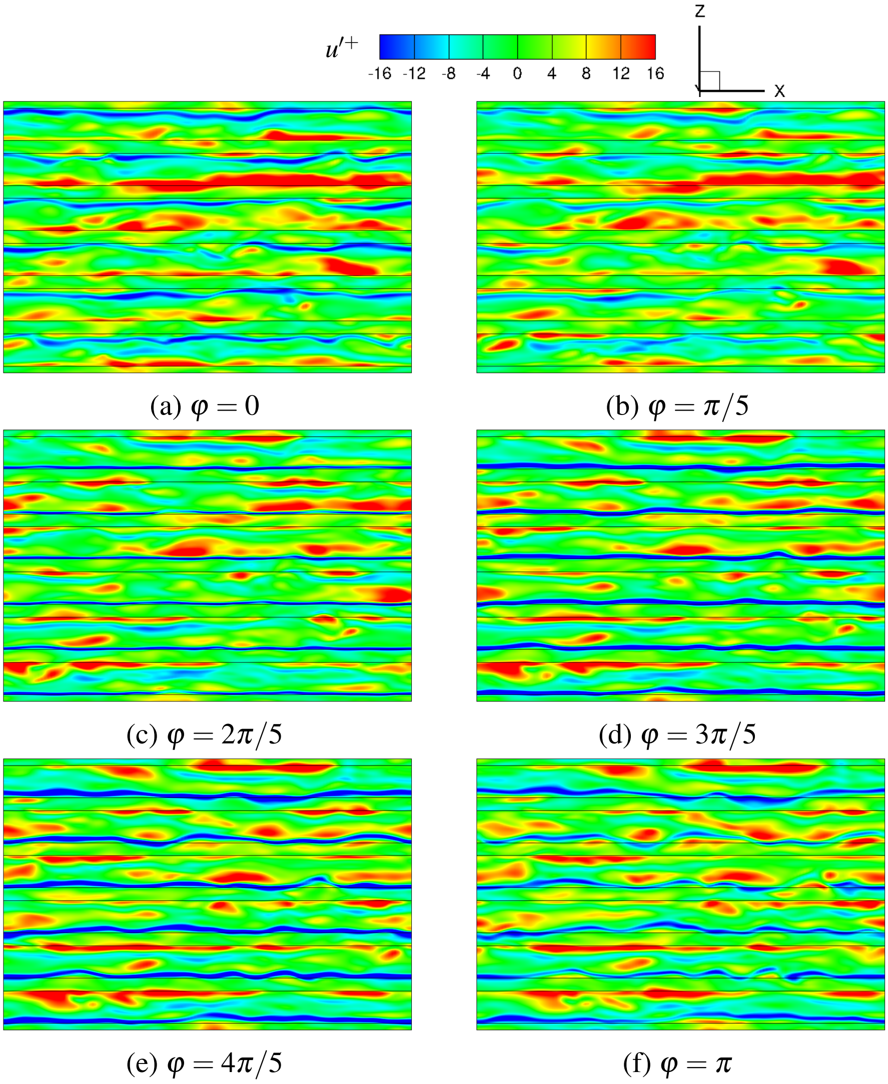

(a) $\varphi = 0$

(b) $\varphi = \pi/5$

(c) $\varphi = 2\pi/5$

(d) $\varphi = 3\pi/5$

(e) $\varphi = 4\pi/5$

(f) $\varphi = \pi$

Figure 6.19 When $T^+ = 62.5$ and $W^+_{max} = 27$, the contours of u'^+ in the $x - z$ plane at $y^+_G = 5$ and at the different phase time $\varphi = 0,\ \pi/5,\ 2\pi/5,\ 3\pi/5,\ 4\pi/5,\ \pi$. The black lines are the geometry edges.

Figure 6.20 shows the interactions between the vortices and the low-speed regions in the bottom half of the channel for the double-speed case and the double-frequency case. The baseline case is shown in figures 5.72c and 5.72d. Comparing the figures, it can be found that the vortices are clustered in the low-speed regions, and between the low-speed regions and high-speed regions as discussed before. The double-speed case generates the most vortices, and the double-frequency case produces the lest. The vortices of the double-speed case tend to be brought the highest, and the vortices of the double-frequency case have a tendency to be kept the lowest.

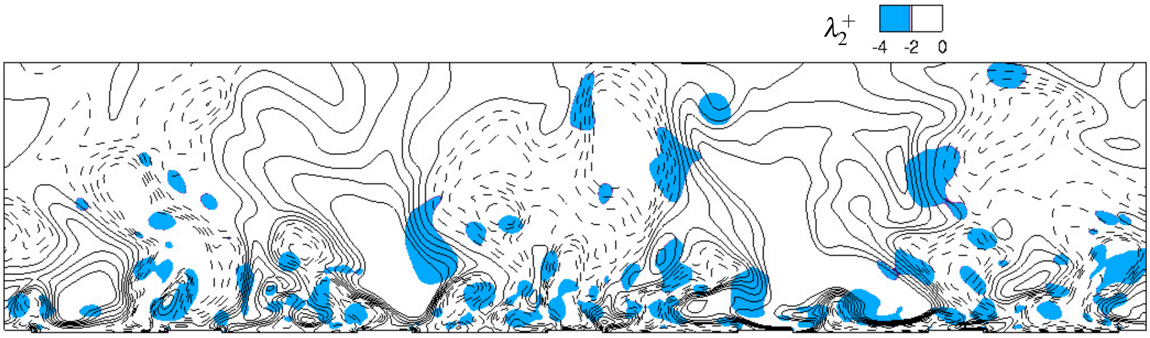

(a) $T^+ = 125$, $W^+_{max} = 54$, $\varphi = 0$

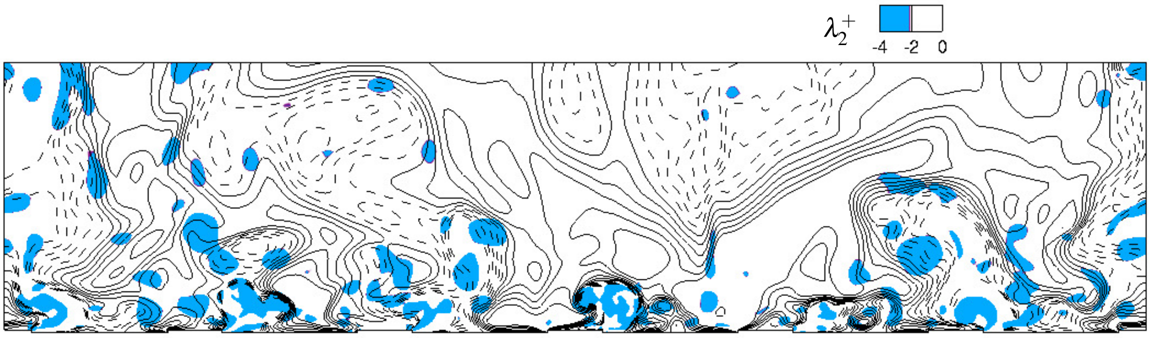

(b) $T^+ = 125$, $W^+_{max} = 54$, $\varphi = \pi/2$

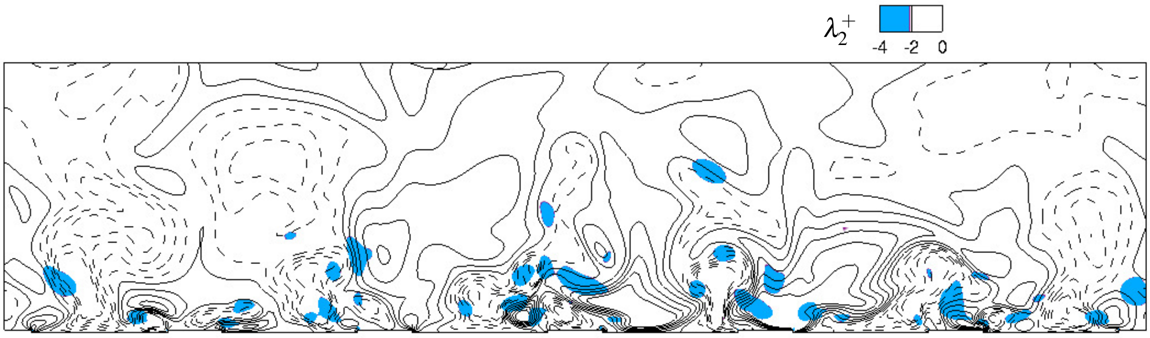

(c) $T^+ = 62.5$, $W^+_{max} = 27$, $\varphi = 0$

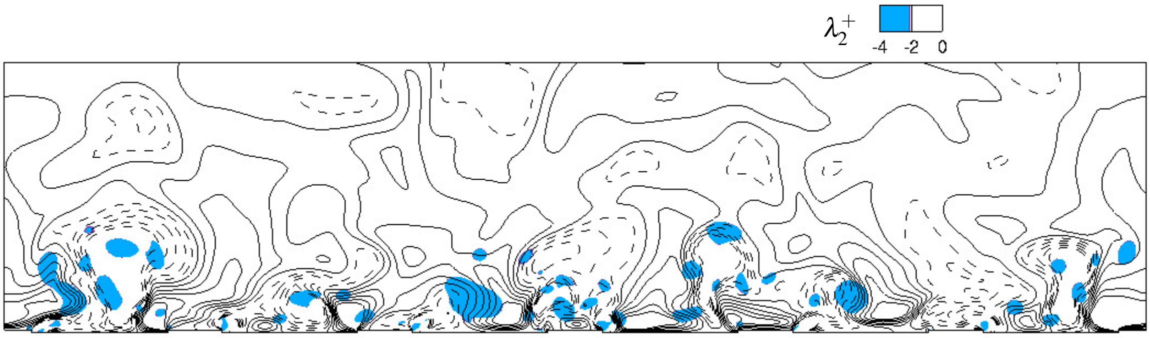

(d) $T^+ = 62.5$, $W^+_{max} = 27$, $\varphi = \pi/2$

Figure 6.20 The contour lines of u''^+ in the $y-z$ plane at $x^+ = 5$ and the different phase time $\varphi = 0$, $\pi/2$ for the double-speed case and the double-frequency case. The solid lines are the positive values and the dashed lines are the negative values. The blue regions are the regions where $\lambda_2^+ < -2$.

6.5 Spectral analysis

The spectra analysis is employed to study the turbulence in the double-speed case and the double-frequency case as the same as the discussion in subsection 5.8.

The evolutions of pure turbulent kinetic energy distributions and the power spectral density (PSD) of E_k^+ for the double-speed case and the double-frequency case are shown in figures 6.21 and 6.22, respectively. Figure 5.75 displays the evolutions and the PSD for the baseline case. It can be observed that the phenomena are similar among three cases. The evolutions of three cases have the same pattern at $z^+ = 20$ and 61. The dominant frequencies are the same among three cases. The differences is the fluctuating strength. The double-speed case has the strongest strength and the highest peak-values of the PSD among three cases. The double-frequency case has the weakest strength and the lowest peak-values of the PSD among three cases. Figures 6.23 and 6.24 show the evolutions of periodic kinetic energy distributions and the power spectral density (PSD) of $\widetilde{E}_k^+$ in the double-speed case and the double-frequency case. Comparing to the baseline case in figure 5.77, the similarity and difference of $\widetilde{E}_k^+$ among three cases are the same as that of E_k^+. Except the strength of $\widetilde{E}_k^+$, the phenomena are similar among three cases.

Figures 6.25 and 6.26 show the contour plots of the premultiplied one-dimensional energy spectrum of the streamwise velocity $k_x\phi_{uu}/u_\tau^2$ for the double-speed case and the double-frequency case, respectively. The baseline case is shown in figure 5.81. As shown in the figures, even either the jet speed or the jet frequency is increased, only one peak can be found at different spanwise positions when $\beta = 75°$. Comparing the figures between the baseline case and the double-speed case, the peak values of $k_x\phi_{uu}/u_\tau^2$ increase when the jet speed increases. Comparing the figures between the baseline case and the double-frequency case, the peak values of $k_x\phi_{uu}/u_\tau^2$ are slightly influenced by the changing of the jet frequency.

Comparing figures 5.81a, 6.25a and 6.26a which are at the spanwise position $z^+ = 0.1$, changing the jet speed influences the peak positions, but increasing the jet frequency slightly affect the peak positions. The peak of the double-speed case locates at smaller length-scales than that of the other two cases. This happens at $z^+ = 62.83$ as well. It reveals that the double-speed case can spread the small-scale motions further than the baseline case and the double-frequency case. The abilities of spreading the small-scale motions are the same between the baseline case and the double-frequency case. Comparing figures 5.81b, 6.25b and 6.26b, the peak position at $z^+ = 17$ is not influenced by changing the jet speed, but it is affected by changing the jet frequency. The peak of the double-frequency case appears at the longer length-scales than that of the other two. This happens at $z^+ = 20$ as well. The kinetic energy of the double-frequency case is injected into the longer length-scales of motions than that of the baseline case and the double-speed case. It indicates that increasing the jet frequency can produce longer length-scales of motions.

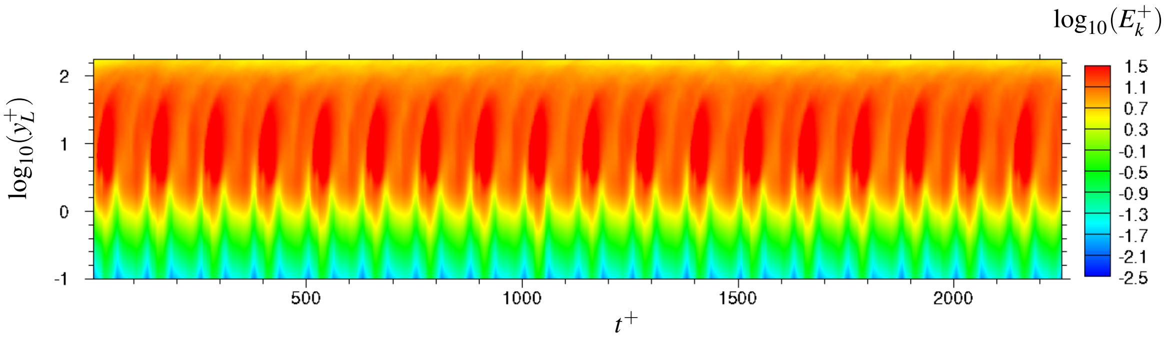

(a) The evolution of $\log_{10}(E_k^+)$ at $z^+ = 20$.

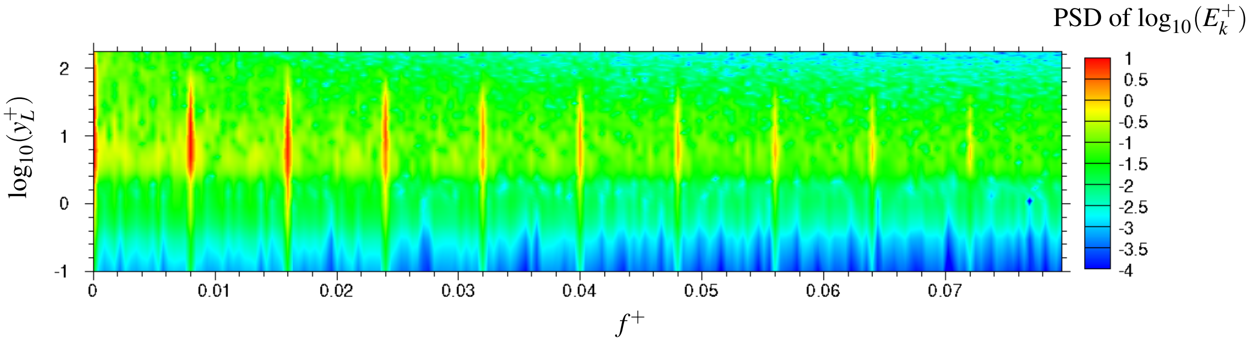

(b) The power spectral density (PSD) of $\log_{10}(E_k^+)$ at $z^+ = 20$.

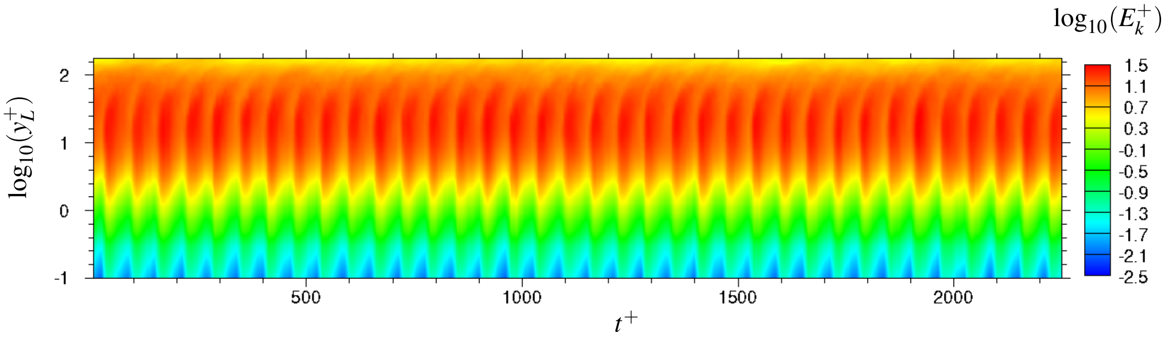

(c) The evolution of $\log_{10}(E_k^+)$ at $z^+ = 61$.

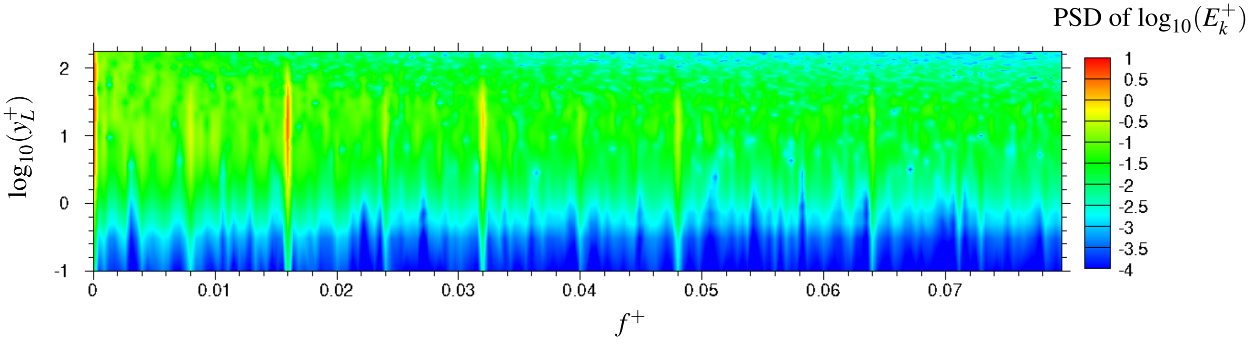

(d) The power spectral density (PSD) of $\log_{10}(E_k^+)$ at $z^+ = 61$.

Figure 6.21 When $T^+ = 125$, $W_{max}^+ = 54$, the contours of the evolutions and the power spectral density (PSD) of E_k^+ at the different spanwise positions $z^+ = 20$ and 61.

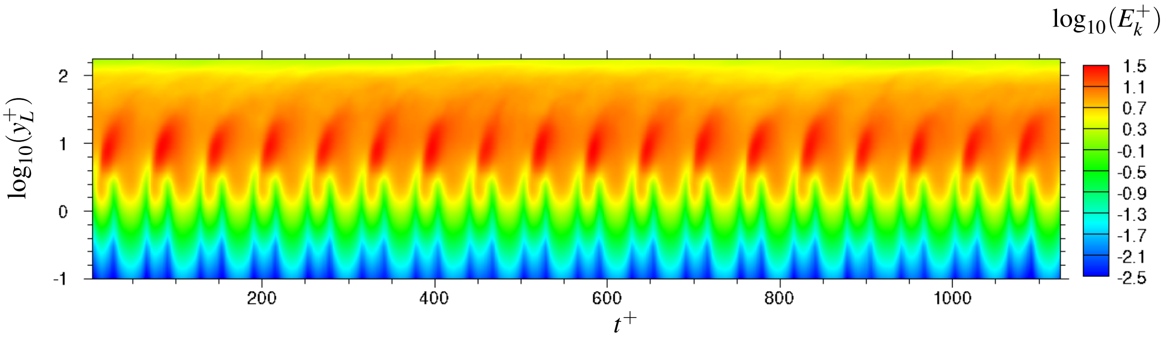

(a) The evolution of $\log_{10}(E_k^+)$ at $z^+ = 20$.

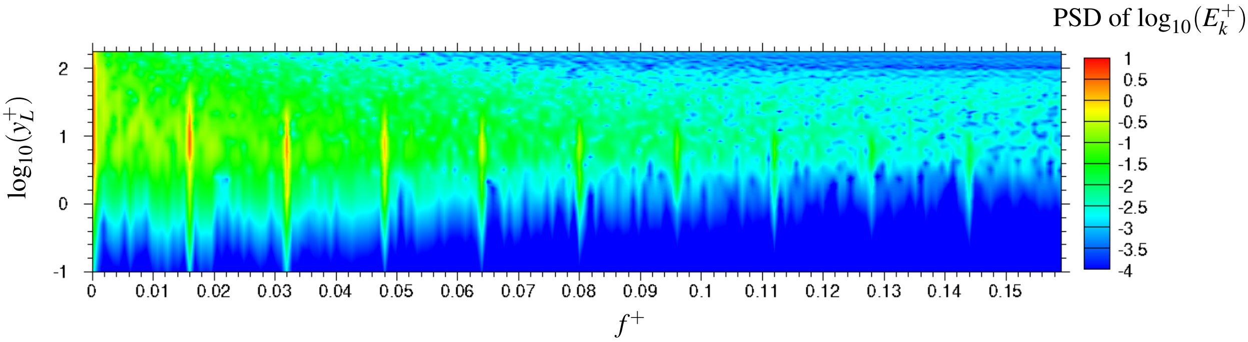

(b) The power spectral density (PSD) of $\log_{10}(E_k^+)$ at $z^+ = 20$.

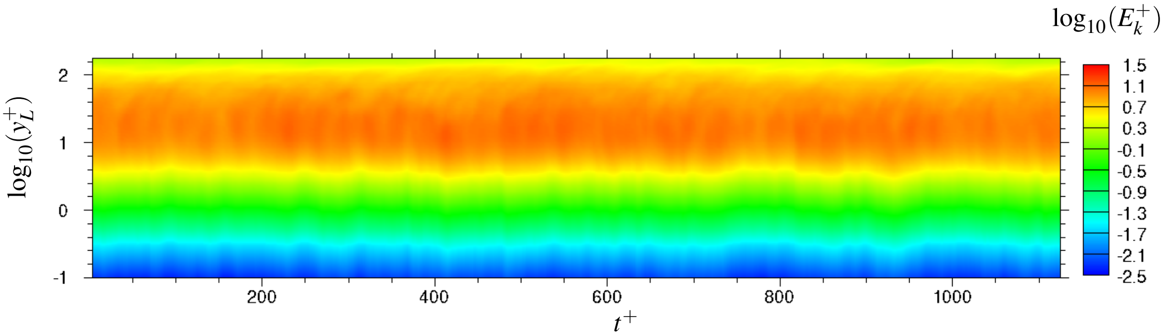

(c) The evolution of $\log_{10}(E_k^+)$ at $z^+ = 61$.

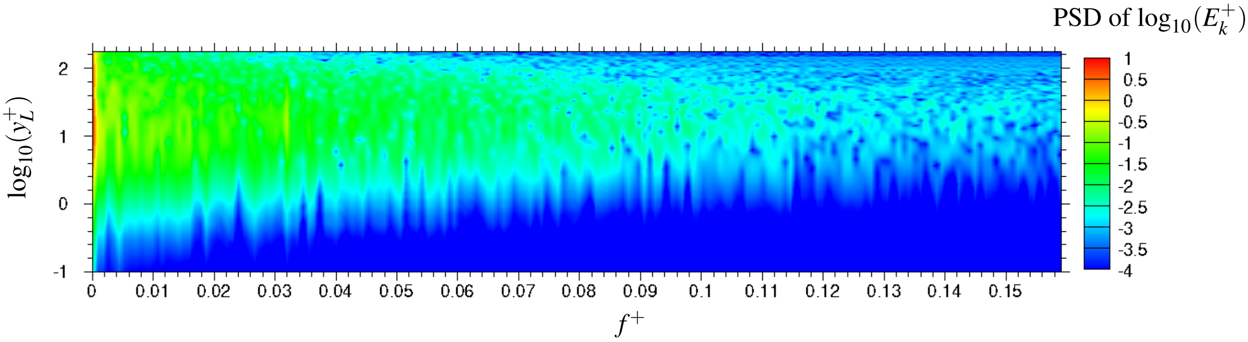

(d) The power spectral density (PSD) of $\log_{10}(E_k^+)$ at $z^+ = 61$.

Figure 6.22 When $T^+ = 62.5$, $W_{max}^+ = 27$, the contours of the evolutions and the power spectral density (PSD) of E_k^+ at the different spanwise positions $z^+ = 20$ and 61.

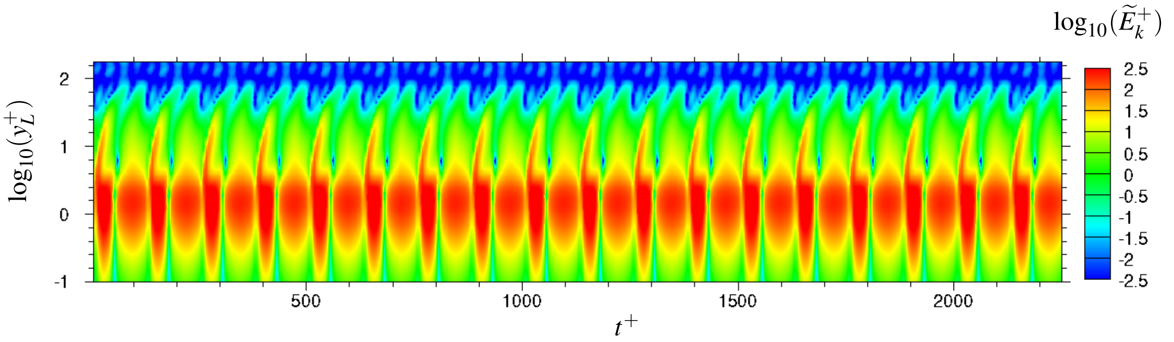

(a) The evolution of $\log_{10}(\widetilde{E}_k^+)$ at $z^+ = 20$.

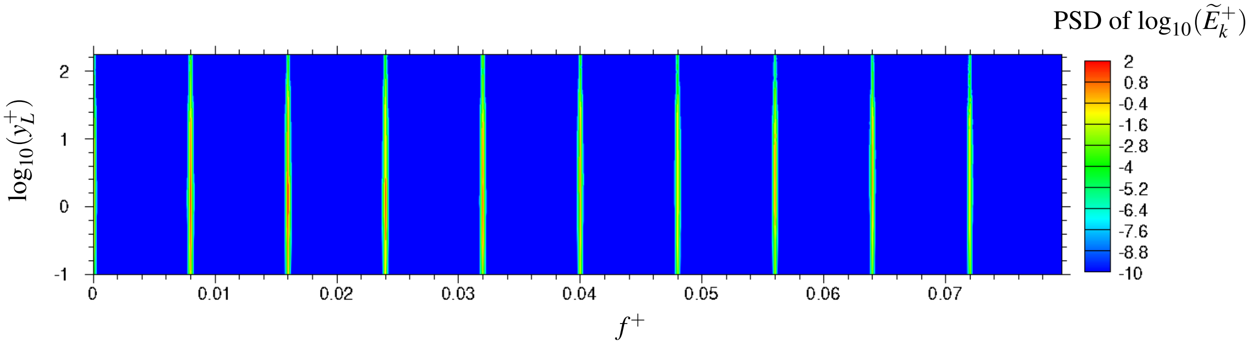

(b) The power spectral density (PSD) of $\log_{10}(\widetilde{E}_k^+)$ at $z^+ = 20$.

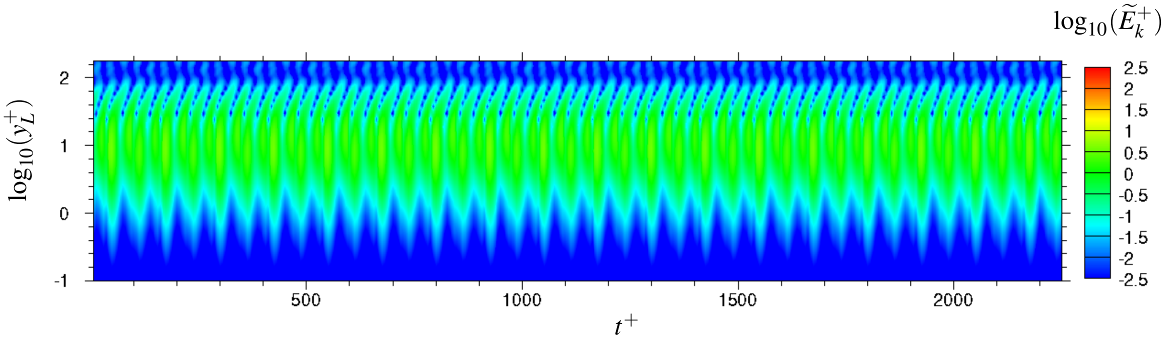

(c) The evolution of $\log_{10}(\widetilde{E}_k^+)$ at $z^+ = 61$.

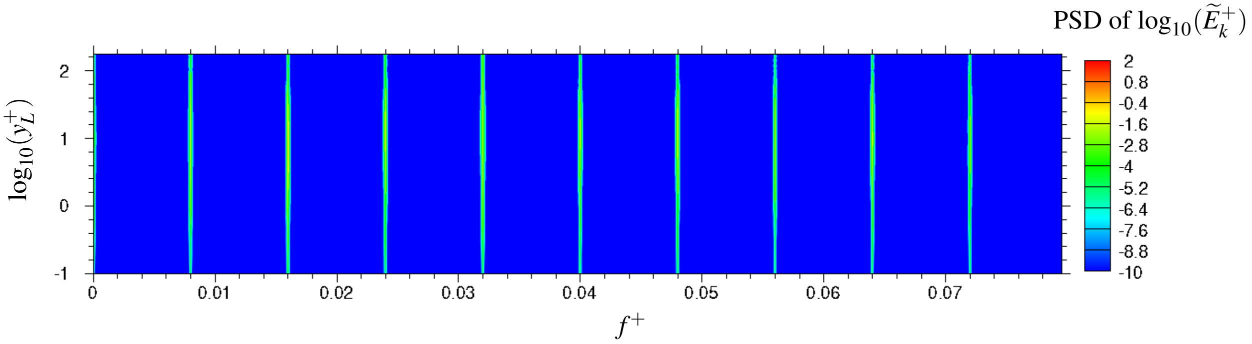

(d) The power spectral density (PSD) of $\log_{10}(\widetilde{E}_k^+)$ at $z^+ = 61$.

Figure 6.23 When $T^+ = 125$, $W_{max}^+ = 54$, the contours of the evolutions and the power spectral density (PSD) of $\log_{10}(\widetilde{E}_k^+)$ at the different spanwise positions $z^+ = 20$ and 61.

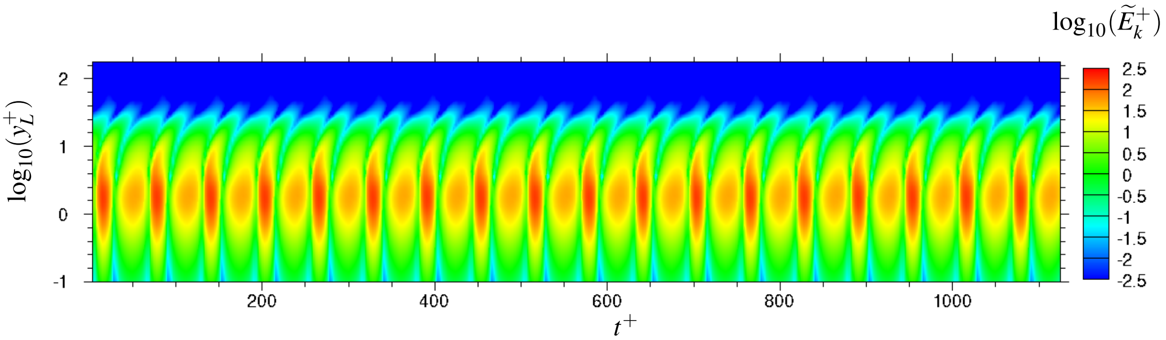

(a) The evolution of $\log_{10}(\widetilde{E}_k^+)$ at $z^+ = 20$.

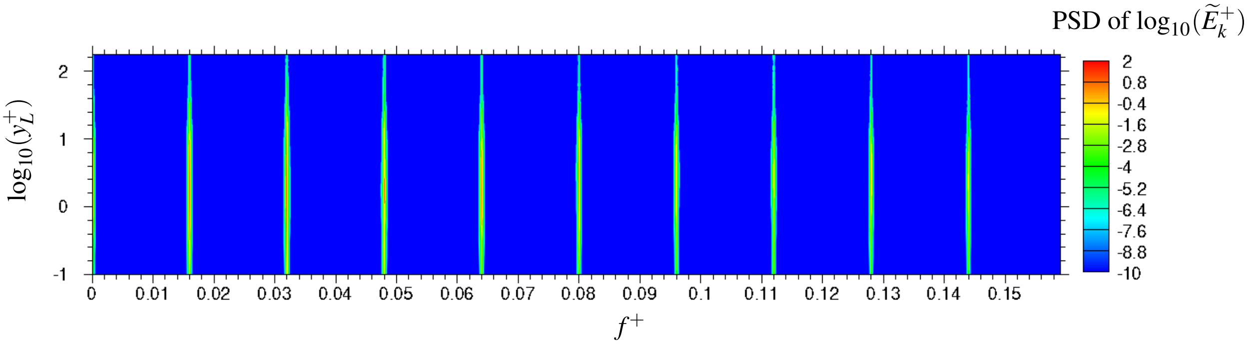

(b) The power spectral density (PSD) of $\log_{10}(\widetilde{E}_k^+)$ at $z^+ = 20$.

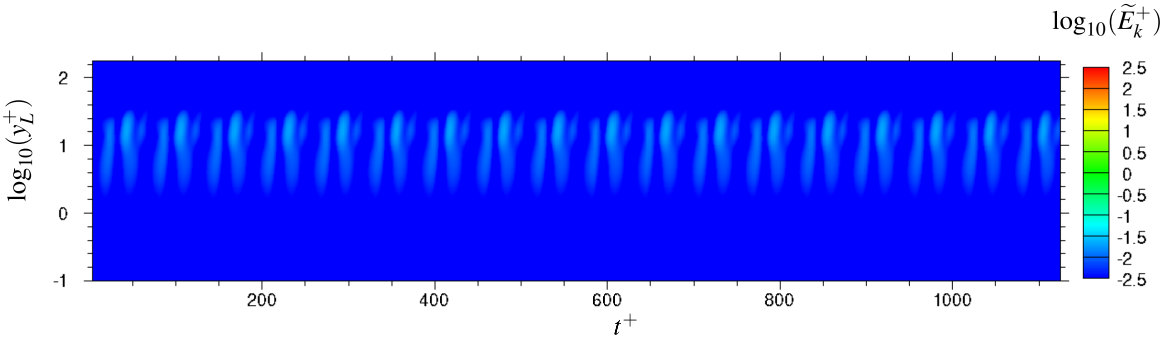

(c) The evolution of $\log_{10}(\widetilde{E}_k^+)$ at $z^+ = 61$.

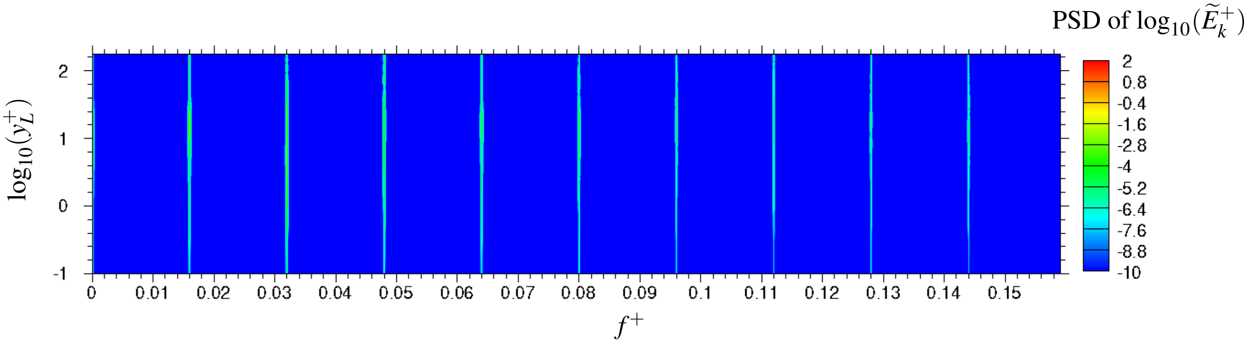

(d) The power spectral density (PSD) of $\log_{10}(\widetilde{E}_k^+)$ at $z^+ = 61$.

Figure 6.24 When $T^+ = 62.5$, $W_{max}^+ = 27$, the contours of the evolutions and the power spectral density (PSD) of $\log_{10}(\widetilde{E}_k^+)$ at the different spanwise positions $z^+ = 20$ and 61.

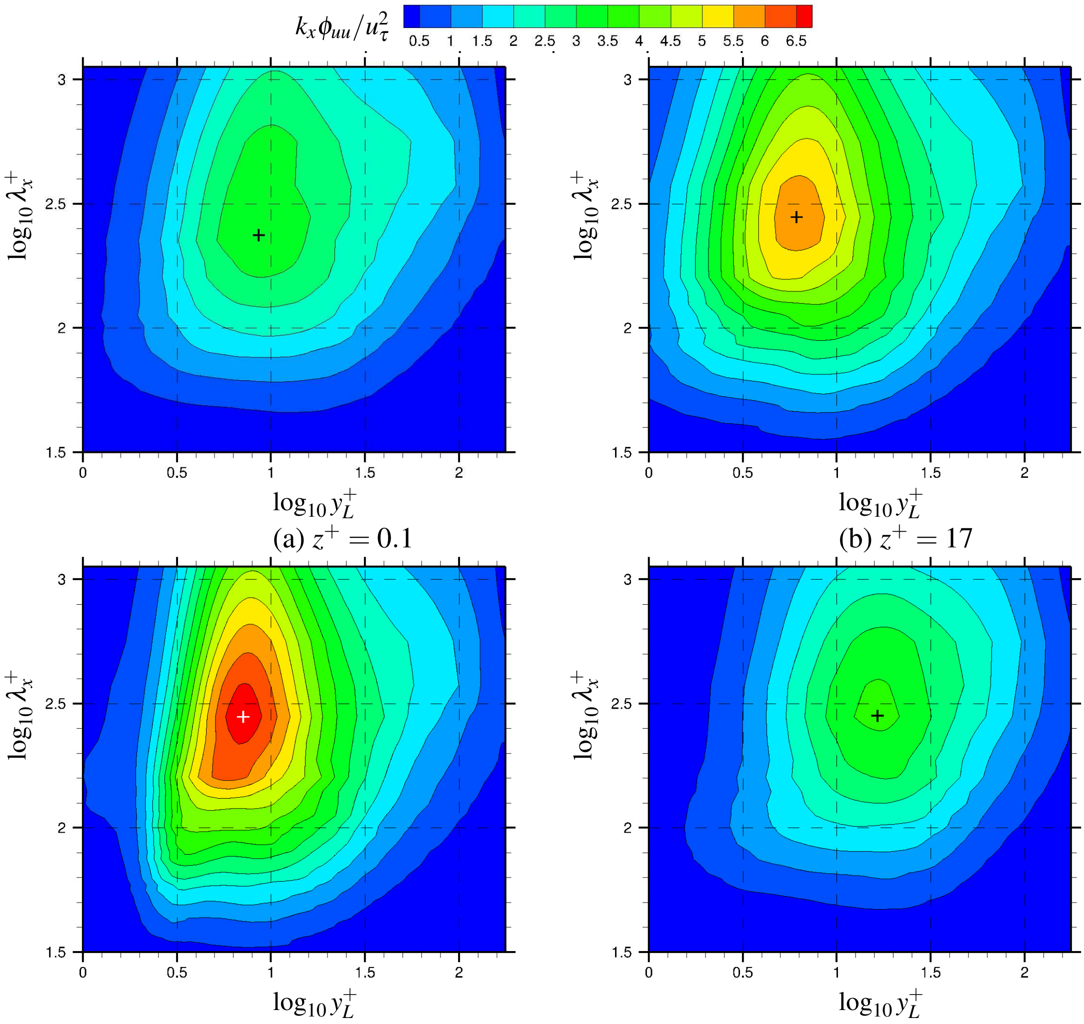

(a) $z^+ = 0.1$

(b) $z^+ = 17$

(c) $z^+ = 20$

(d) $z^+ = 62.83$

Figure 6.25 When $T^+ = 125$, $W_{max}^+ = 54$, contours of the pre-multiplied spectra of the streamwise velocity $k_x\phi_{uu}/u_\tau^2$ at the different spanwise positions. The approximate locations of the peaks are denoted by $(+)$ symbols.

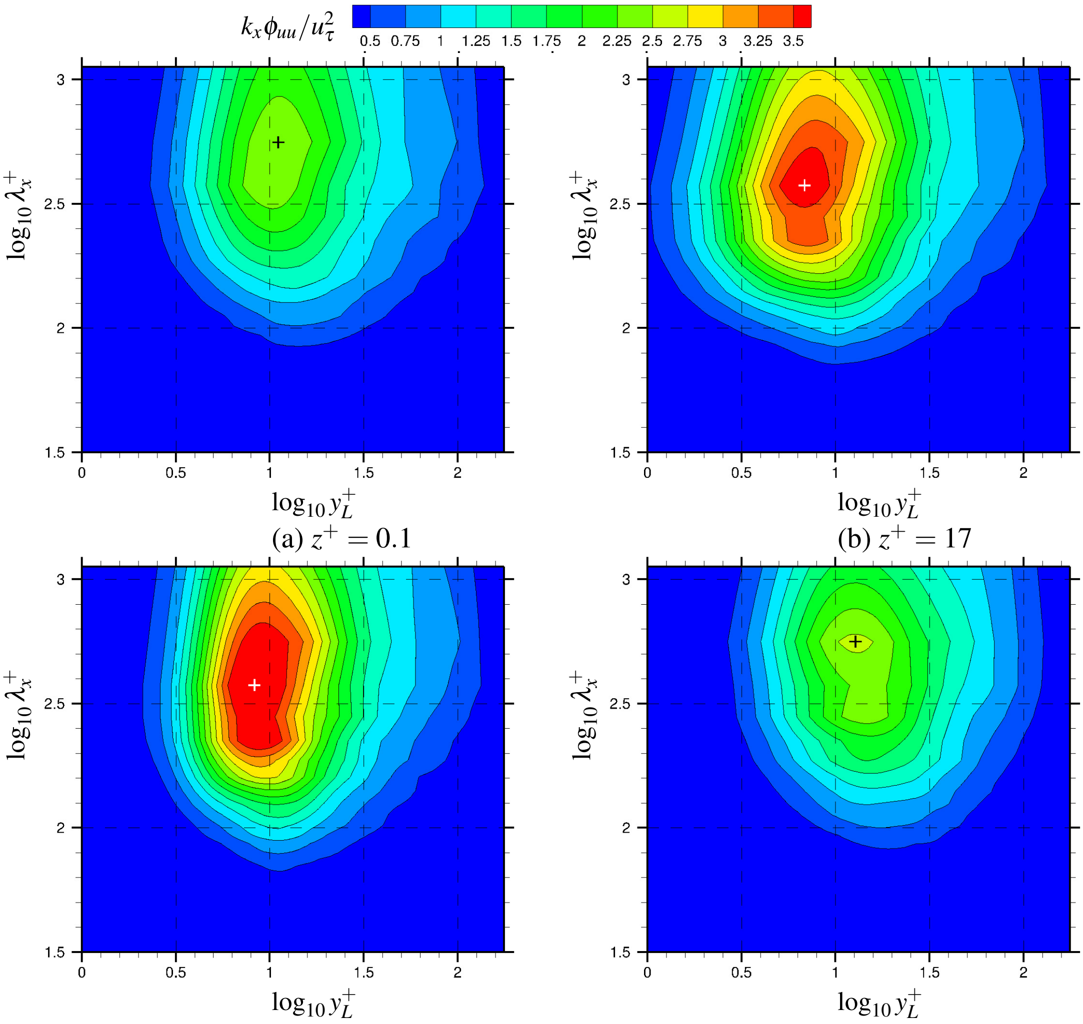

(a) $z^+ = 0.1$ (b) $z^+ = 17$

(c) $z^+ = 20$ (d) $z^+ = 62.83$

Figure 6.26 When $T^+ = 62.5$, $W_{max}^+ = 27$, contours of the pre-multiplied spectra of the streamwise velocity $k_x\phi_{uu}/u_\tau^2$ at the different spanwise positions. The approximate locations of the peaks are denoted by $(+)$ symbols.

6.6 Power performance

For the practical application of the active control method, not only the level of gross drag reduction (DR) is very important, but also the net power saving N. In a turbulent channel flow, it has

$$N_p = DR - P_{sp}/P_0 \tag{6.1}$$

where P_0 is the power used to drive the flow in a smooth channel, and P_{sp} is the power spent on the active control. In this research, the jet speed on the jet-exits can be computed as

$$U(y,t) = W_{max} \sin\left(\frac{2\pi}{T_{osc}}t\right)\left[1-\left(\frac{2y-\delta_{jet}}{\delta_{jet}}\right)^2\right] \tag{6.2}$$

where, $y \in [0, \delta_{jet}]$ is the height from the bottom wall, and t is the instant time.

Let

$$Y = \frac{2y-\delta_{jet}}{\delta_{jet}} \tag{6.3}$$

and

$$\tilde{t} = \frac{2\pi}{T_{osc}}t \tag{6.4}$$

Equation 6.2 can be simplified as

$$U(y,t) = W_{max}\left(\sin\tilde{t}\right)\left(1-Y^2\right) \tag{6.5}$$

If the energy is fully spent on driving the fluid and the energy loss is not considered, the power spent on ZMJ can be estimated by the kinetic energy contained by the fluid at the jet-exits. For a single jet-exit, the power is

$$P_{sp.1} = \frac{1}{T_{osc}}\int_0^{T_{osc}}\int_0^{\delta_{jet}} \frac{1}{2}\rho L_x \cos\beta \left|U(y,t)\right|^3 dydt \tag{6.6}$$

Substituting equation 6.5 into equation 6.6,

$$\begin{aligned} P_{sp.1} &= \frac{1}{T_{osc}}\int_0^{T_{osc}}\int_0^{\delta_{jet}} \frac{1}{2}\rho L_x \cos\beta \left|W_{max}\left(\sin\tilde{t}\right)\left(1-Y^2\right)\right|^3 dydt \\ &= \frac{1}{8\pi}\rho L_x \cos\beta W_{max}^3 \delta_{jet}\int_0^{2\pi}\int_{-1}^{1}\left|\sin\tilde{t}\right|^3\left(1-Y^2\right)^3 dYd\tilde{t} \\ &= \frac{1}{8\pi}\rho L_x \cos\beta W_{max}^3 \delta_{jet}\int_0^{2\pi}\left|\sin\tilde{t}\right|^3\int_{-1}^{1}\left(1-Y^2\right)^3 dYd\tilde{t} \end{aligned} \tag{6.7}$$

In equation 6.7,

$$\begin{aligned}
&\int_{-1}^{1}\left(1-Y^2\right)^3 dY\\
=&\int_{-1}^{1}\left(1-3Y^2+3Y^4-Y^6\right) dY\\
=&(Y-\frac{3}{3}Y^3+\frac{3}{5}Y^5-\frac{1}{7}Y^7)\Big|_{-1}^{1}\\
=&\frac{32}{35}
\end{aligned} \tag{6.8}$$

Substituting equation 6.8 into equation 6.7,

$$\begin{aligned}
P_{sp.1} &= \frac{1}{8\pi}\rho L_x \cos\beta W_{max}^3 \delta_{jet}\int_0^{2\pi}\frac{32}{35}\left|\sin\tilde{t}\right|^3 d\tilde{t}\\
&= \frac{8}{35\pi}\rho L_x \cos\beta W_{max}^3 \delta_{jet}\int_0^{\pi}\left(\sin\tilde{t}\right)^3 d\tilde{t}\\
&= \frac{8}{35\pi}\rho L_x \cos\beta W_{max}^3 \delta_{jet}\left(-\cos\tilde{t}+\frac{1}{3}\left(\cos\tilde{t}\right)^3\right)\Big|_0^{\pi}\\
&= \frac{8}{35\pi}\rho L_x \cos\beta W_{max}^3 \delta_{jet}\times\frac{4}{3}\\
&= \frac{32}{105\pi}\rho L_x \cos\beta W_{max}^3 \delta_{jet}
\end{aligned} \tag{6.9}$$

Because there are N_d jet-exits on the walls, the power per unit area for ZMJ is

$$P_{sp.A} = \frac{2N_d P_{sp.1}}{2L_x Lz} = \frac{32 N_d \delta_{jet}}{105\pi L_z}\rho W_{max}^3 \cos\beta \tag{6.10}$$

In a smooth channel, the force required to drive the flow is

$$F = 2\tau_{wall} L_x L_z = C_{f0}\rho U_b^2 L_x L_z \tag{6.11}$$

where C_{f0} is the skin friction coefficient in the smooth channel. The power per unit area required to drive the flow is

$$P_{0.A} = \frac{F U_b}{2L_x L_z} = \frac{1}{2}C_{f0}\rho U_b^3 \tag{6.12}$$

The power ratio is computed as

$$\frac{P_{sp}}{P_0} = \frac{P_{sp.A}}{P_{0.A}} = \frac{64 N_d \delta_{jet}\cos\beta}{105\pi L_z C_{f0}}\left(\frac{W_{max}}{U_b}\right)^3 \tag{6.13}$$

In equation 6.13, it indicates that the power ratio is proportional to the number of devices N_d, the jet-exit height δ_{jet}, the jet angle β, and the maximum jet-velocity W_{max}. The ratio W_{max}/U_b is crucial to the power ratio. Although increasing the jet speed can reduce the drag, the extra power required by ZMJ cancels out the benefits by saving the power from drag reduction. The net power saving is reduced by doubling the jet speed. Since the power ratio is not related to the jet frequency, increasing the jet frequency can save the net power.

By substituting the parameters into equation 6.13, the power performances for different cases can be obtained, as displayed in table 6.2. In the results, the net power saving is not ideal. None of them has a positive saving. Too much power demanded by ZMJ in these cases. More jobs need to be done to find a case that can give a positive net power saving by changing the parameters of the control method.

Table 6.2 The power performance for different cases.

case name	T^+	W^+_{max}	$DR(\%)$	$P_{sp}/P_0(\%)$	$N_p(\%)$
baseline	125	27	10.5	102.2	-91.7
double-speed	125	54	84.0	817.4	-733.4
double-frequency	62.5	27	19.4	102.2	-82.8

6.7 Wall pressure fluctuation

In order to be a practical application, the pressure fluctuation on walls is an important factor to be considered. If the pressure fluctuation is huge, it is hard to find a suitable material to build the structure. In this section, the characters of wall pressure fluctuation are investigated.

The triple decomposition can be used to analyse the pressure fluctuation as well, giving periodic part and pure turbulent part. Figure 6.27 shows the root mean square of pressure fluctuation on wall in a section. As the periodic velocity oscillates fiercely near the jet-exits, it is expected that the periodic pressure-fluctuation is high there. The pure turbulent pressure-fluctuation on the steps is high near the jet-exits. The strength of pressure fluctuations in case ZMJ(off) is always smaller than that in case ZMJ(on). The jet speed increases, the strength of both periodic and pure turbulent fluctuations increases. The jet frequency increases, the strength both periodic and pure turbulent fluctuations decreases. The peak values of periodic fluctuations are bigger than that of pure turbulent fluctuations, but the values of periodic fluctuations are smaller than that of pure turbulent fluctuations in the middles of steps and sections.

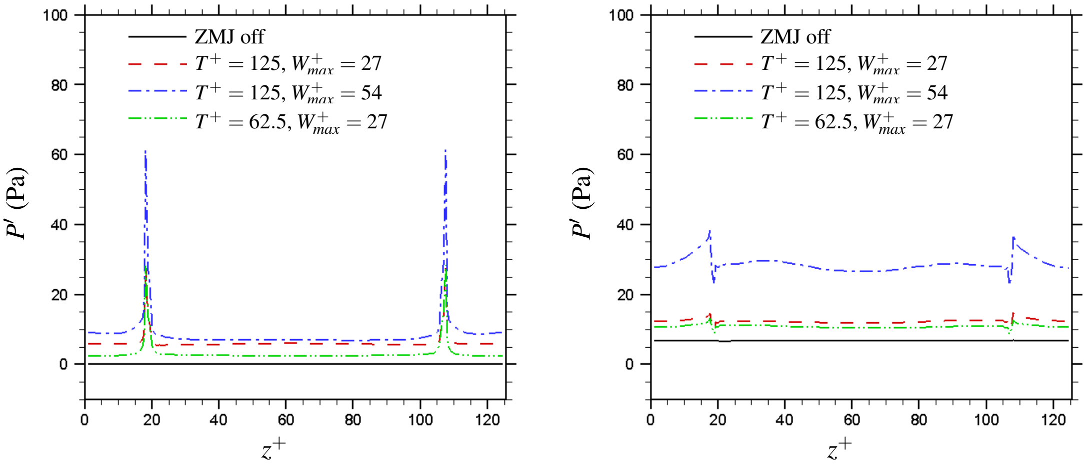

(a) Periodic pressure-fluctuation (b) Pure turbulent pressure-fluctuation

Figure 6.27 Root mean square of pressure fluctuations on wall in a section.

Figures 6.28 and 6.29 displays the evolutions and the power spectral density of total pressure-fluctuations on wall at $x^+ = 0.1$ in a section for four cases, including case ZMJ(off), the baseline case, the double-speed case and the double-frequency case. There is no dominating frequency in the case ZMJ(off). The baseline case is dominated by two frequencies, including $f^+ = 0.008$ and 0.016. The frequency of $f^+ = 0.008$ only dominates the positions near jet-exits. There are two jet-exits in a section. Since $f^+ = 0.008$ is the frequency of ZMJ, a part strength of P' near the jet-exits is only given by one side of jet-exits. The frequency of $f^+ = 0.016$ given by both sides of jet-exits influences the whole section. When the jet speed is doubled, there are still two dominating frequencies. The frequency of $f^+ = 0.008$ still only dominates the positions near jet-exits. But the frequency of $f^+ = 0.016$ cannot dominate the middle of a section. In the double-frequency case, the frequency of $f^+ = 0.008$ is still there, but the frequency of $f^+ = 0.016$ is too weak to find.

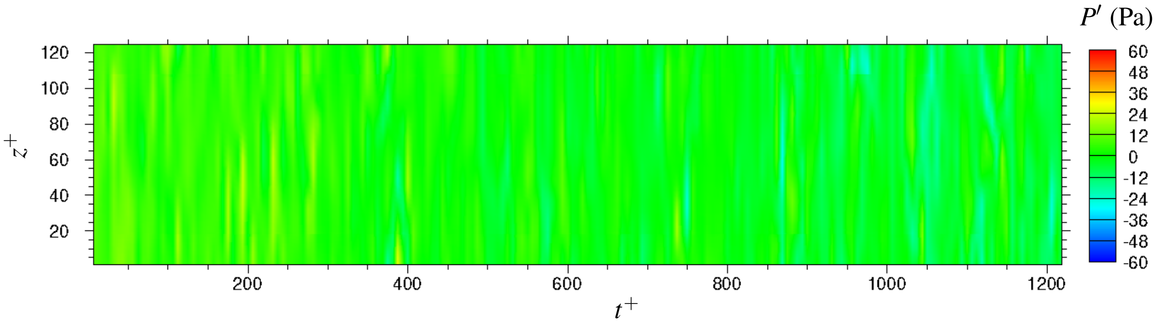

(a) The evolution of pressure in case ZMJ(off).

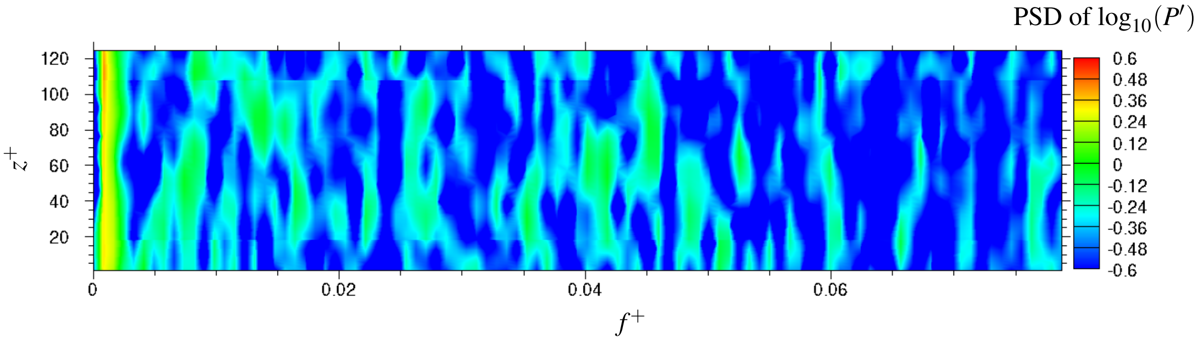

(b) The power spectral density of $\log_{10}(P')$ in case ZMJ(off).

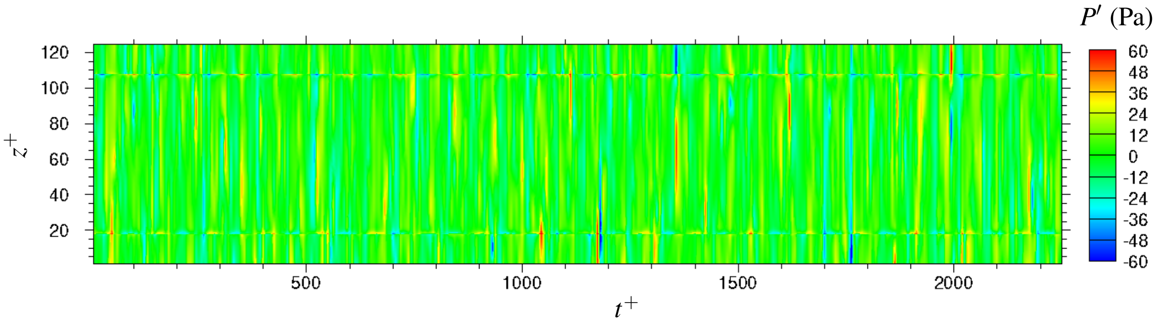

(c) The evolution of pressure in the baseline case.

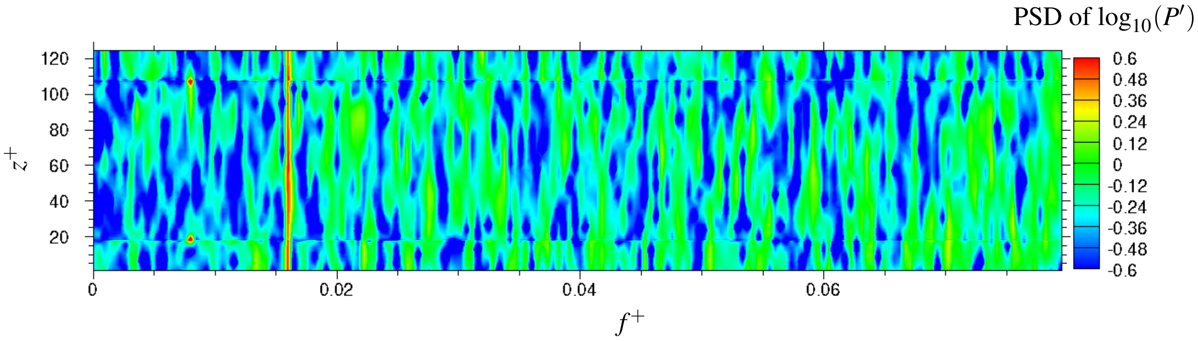

(d) The power spectral density of $\log_{10}(P')$ in the baseline case.

Figure 6.28 The evolutions and the power spectral density (PSD) of total pressure-fluctuations P' are displayed at $x^+ = 0.1$ for case ZMJ(off) and the baseline case.

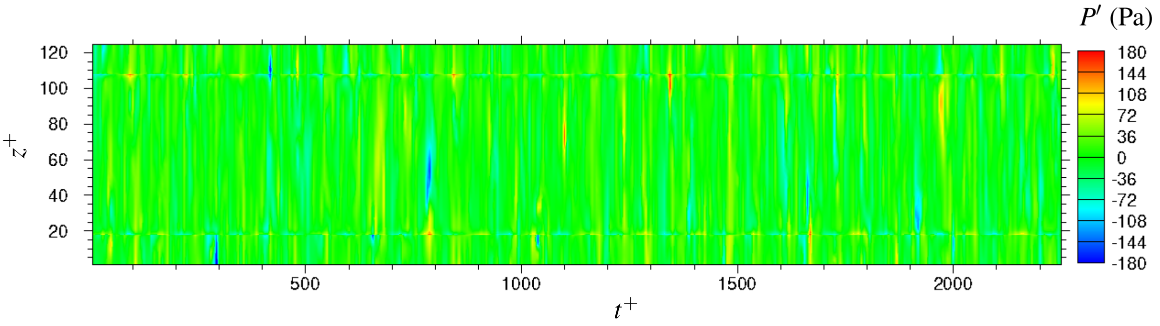

(a) The evolution of pressure in the double-speed case.

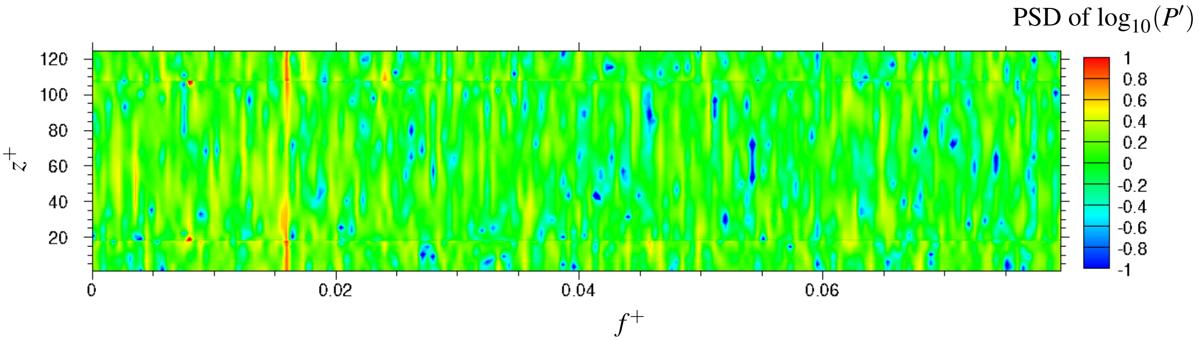

(b) The power spectral density of $\log_{10}(P')$ in the double-speed case.

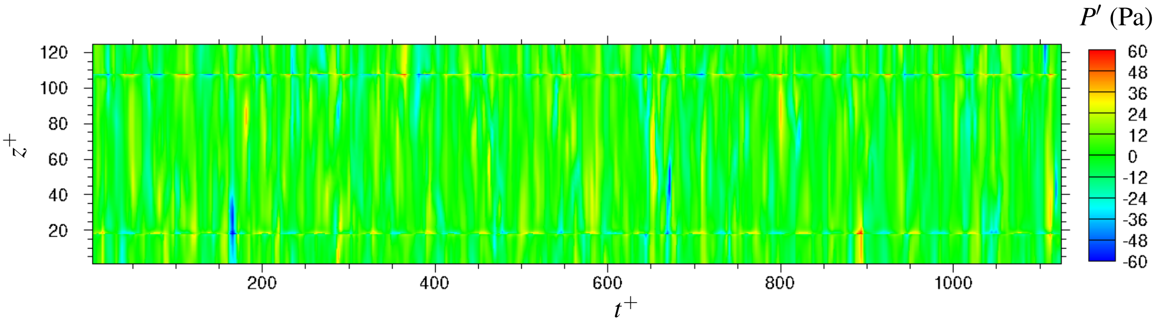

(c) The evolution of pressure in the double-frequency case.

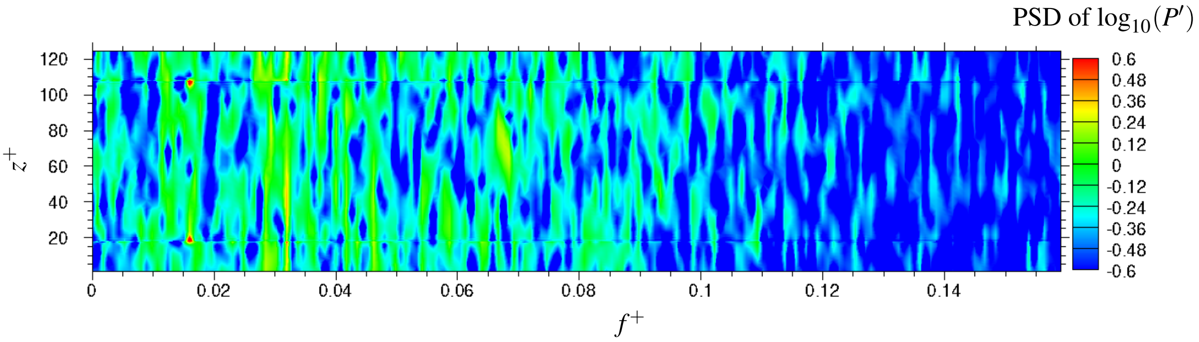

(d) The power spectral density of $\log_{10}(P')$ in the double-frequency case.

Figure 6.29 The evolutions and the power spectral density (PSD) of total pressure-fluctuations P' are displayed at $x^+ = 0.1$ for the double-speed case and the double-frequency case.

6.8 Conclusions

By doubling either the frequency or speed of ZMJ, and fixing the other parameters of the best case of drag reduction in the previous chapter, the behaviour of ZMJ is studied. Conclusions are made and listed as below.

Global conclusions:

- Baseline case, double-speed case and double-frequency case can bring down the skin friction coefficients of smooth channel from 8.18×10^{-3} to be 7.32×10^{-3}, 1.31×10^{-3} and 6.59×10^{-3}, respectively. Increasing either jet speed or jet frequency can improve the effects of drag reduction. The levels of gross drag reduction are 10.5%, 84.0% and 19.4% in baseline case, double-speed case and double-frequency case, respectively. The fluctuation amplitude of skin friction is increased by doubling jet speed, but is reduced by doubling jet frequency.
- The density of vortices structures is the highest in double-speed case and is the lowest in double-frequency case. Vortices structures of double-speed case are the most possibly ejected into the channel centre. The spanwise length-scales of vortices structures are similar among the three cases.
- All the three cases have similar evolutions and dominant frequencies of the turbulent kinetic energy near blowing jet-exits. None of them has an apparent frequency of the energy in the middle of each sections.
- Double-speed case ejects the most turbulent kinetic energy into the channel flow among these three cases. The energy peaks are shifted by changing jet speed and frequency, comparing to baseline case. Increasing jet speed can shift the energy peak into the shorter length-scale motions in the sides and middle of each sections. More energy is ejected into the longer length-scale motions near the jet-exits by increasing jet frequency.

Time-averaged conclusions:

- Comparing to baseline case, doubling jet speed increases the skin friction in region above the steps but reduces the skin friction between a pair of jet-exits. The skin frictions are reduced by doubling jet frequency both in region above the steps and region between a pair of jet-exits, comparing to baseline case. The width of separation region is significantly increased by doubling the speed, and slightly increased by doubling the frequency.

- The regions of high streamwise velocity-fluctuations and Reynolds shear stress $\overline{u'v'}$ are significantly enlarged by the increase of jet speed and slightly reduced by the increase of jet frequency.
- In the log-law regions, the Von Kármán constant of double-frequency case is the same as that of baseline case. But this constant is much bigger than that of double-speed case.

Phase-averaged conclusions:

- Near blowing jet-exits, the width of separation zone is the narrowest in double-frequency case and is the widest in double-speed case among the three cases. Near sucking jet-exits, the skin-friction is the highest in double-speed case and is the lowest in double-frequency case.
- The pure turbulent fluctuations of streamwise velocity generated by blowing jet-exits is the strongest in double-speed case and the weakest in double-frequency case. The fluctuations created by blowing jet-exits in double-speed case can be canceled the most in the three cases by sucking jet-exits. Double-frequency case can cancel the lest. The propagation speed of the fluctuations is increased by the increase of jet speed but reduced by the increase of jet frequency.
- The Reynolds shear stress $-\overline{u''v''}$ generated by blowing jet-exits is crucial in double-speed case. There are two peak regions of the Reynolds shear stress in double-frequency case. One is produced by blowing jet-exits, and the other one is left on the side of sucking jet-exits. The propagation speed of the Reynolds shear stress is the fastest in double-speed case and the lowest in double-frequency case among three cases. The Reynolds shear stress $-\overline{u''v''}$ under jet-exits height can be negative near blowing jet-exits. The peak values of $-\overline{u''v''}$ in double-speed case are always the highest near blowing and sucking jet-exits. The peak value of double-frequency case is smaller than that of baseline case near blowing jet-exits, whereas the result is opposite near sucking jet-exits. The Reynolds shear stresses in the regions of $y^+ < 2$ and $y^+ > 60$ are similar between baseline case and double-frequency case.

Chapter 7

Conclusions

7.1 Summary

This research has investigated a novel active flow control method called ’zero mass jets’ using direct numerical simulation. The computations are simulated by the in-house code named ’SHEFFlow’ using the 5^{th} order MUSCL scheme. Parts of this study have been published in reference [130]. A paper about the drag-reduction mechanisms is being written for Journal of Fluid Mechanics. The detailed conclusions have been written at the ends of chapters 4, 5, 6. The major findings from these chapters are presented here and the future works is discussed.

7.2 Major findings

It is shown in chapter 4 that a low-order unstructured solver is easy to have high-order abilities by adding the high-order MUSCL schemes, though the mesh should be structured for the high-order part. This provides the solver with an advantage. The unstructured solver can simulate parts of a flow field by high order. These simulations can be done with a structured or hybrid mesh. For a complicated geometry, the high-order parts can be allocated around the concerned areas. The unconcerned areas can be covered by unstructured mesh and solved by low-order. This approach saves computing resources.

The skin friction can be increased or reduced by ZMJ in a fully developed turbulent channel flow at Reynolds number $Re_\tau = 180$. A fluctuating character of the skin friction is strongly related to the oscillating character of ZMJ. The designed step-height is small and hardly influence the skin friction. In all cases, the turbulent intensity and Reynolds shear stresses are significantly increased by ZMJ, comparing to smooth channel. The spanwise jet-velocity mainly influences the fluctuating strengths of streamwise and spanwise velocities in the channel flow. The streamwise velocity fluctuations near jet-exits depend on both streamwise and spanwise jet-speed. The oscillating jet is the main source of the streamwise velocity fluctuations near jet-exits, and the spanwise jet-speed decides the propagation of the fluctuations. Far away from jet-exits, the streamwise fluctuations depend on the spanwise jet-velocity.

Chapter 5 studies the flow control method by changing jet angle. It is found that the skin frictions in region above the steps are always increased by ZMJ and is proportional to spanwise jet-speed. Between a pair of jet-exits in a section, an apparent flow separation near jet-exits can be induced by the countering jets when jet direction is against the main flow. The area of the separation regions depends on both spanwise and streamwise jet-speed. The drag can be significantly reduced in the separation regions. In the middle of each sections, the distance between a pair of jet-exits is too wide to have the drag reduction, even the drag is slightly increased. It seems that the drag reduction can be improved by decreasing the width of the steps and the distance between a pair of jet-exits.

Chapter 6 shows that both increasing jet speed and frequency can enhance the reduction of skin friction. The fluctuating amplitude of skin friction is enlarged by increasing jet speed and reduced by increasing jet frequency. The reasons of improving drag reduction are different between those two. The reason of double-speed case is that the separation regions are significantly enlarged and the velocity gradients are reduced because the countering jet speed is increased. The reason of double-frequency case is that the skin friction in region above the steps are relatively reduced comparing to baseline case. Blowing jet-exits produces smaller area of separation region, but sucking jet-exits also increases less skin friction.

Kinetic energy is ejected into main flow by ZMJ. The energy near jet-exits are monitored and analysed with power spectrum density. When jet angle is big, oscillating character of ZMJ is kept near jet-exits. The flow that is away from jet-exits does not have an apparent frequency. It's also found that ZMJ tends to influence the small length-scales of motions. Comparing with smooth channel, the peaks of turbulent kinetic energy in controlled channel are shifted to the smaller length-scales.

ZMJ significantly influences the fluid motions in the log-law region. Comparing with smooth channel, the time averaged profile in the region is not only shifted, but also twisted. The Von Kármán constant is changed by ZMJ. New wall functions should be developed to model the turbulence in the near-wall region of controlled channel.

Through the direct numerical simulations of zero mass jets in this thesis, a potential method of drag reduction is found to improve the performance of wings or fuselages in the future.

7.3 Future work

The followings are the potential research directions in the future.

- There are still several parameters of the control device need to be investigated.
- This research accurately obtained flow structures and suggested some values of the Von Kármán constant by DNS. New wall functions for the control method can be developed for RANS based on these data. Some RANS can be carried out for a design to predict the controlling effects.
- SHEFFlow is a compressible solver. The control method can be tested in a compressible flow by changing the 5^{th} order MUSCL scheme to be a WENO scheme.
- The control method should be tested by a open boundary layer flow or even a two-dimensional aerofoil at low Reynolds number.
- The net saving energy has not been investigated in details due to the lack of simulating the cavity flow.
- The steps are straight in the streamwise direction, and the jets oscillate in the same phase in this research. According to the research of traveling waves, the controlling effects may be improved by using sinusoidal steps and oscillating the jet in different phase.

References

[1] Abe, Y., Nonomura, T., and Fujii, K. (2015). Spatial growth of the spanwise disturbance induced by a synthetic jet on separation control over an airfoil. *53rd AIAA Aerospace Sciences Meeting*.

[2] Agostini, L. and Leschziner, M. (2014). On the influence of outer large-scale structures on near-wall turbulence in channel flow. *Physics of Fluids*, 26(7):075107.

[3] Agostini, L. and Leschziner, M. (2016a). On the validity of the quasi-steady-turbulence hypothesis in representing the effects of large scales on small scales in boundary layers. *Physics of Fluids*, 28(4):045102.

[4] Agostini, L. and Leschziner, M. (2016b). Predicting the response of small-scale near-wall turbulence to large-scale outer motions. *Physics of Fluids*, 28(1):015107.

[5] Agostini, L. and Leschziner, M. (2018). The impact of footprints of large-scale outer structures on the near-wall layer in the presence of drag-reducing spanwise wall motion. *Flow, Turbulence and Combustion*, pages 1–25.

[6] Agostini, L., Leschziner, M., and Gaitonde, D. (2016). Skewness-induced asymmetric modulation of small-scale turbulence by large-scale structures. *Physics of Fluids*, 28(1):015110.

[7] Agostini, L., Touber, E., and Leschziner, M. (2015). The turbulence vorticity as a window to the physics of friction-drag reduction by oscillatory wall motion. *International Journal of Heat and Fluid Flow*, 51:3–15.

[8] Agostini, L., Touber, E., and Leschziner, M. A. (2014). Spanwise oscillatory wall motion in channel flow: drag-reduction mechanisms inferred from dns-predicted phase-wise property variations at $Re_\tau = 1000$. *Journal of Fluid Mechanics*, 743:606–635.

[9] Akhavan, R., Jung, W., and Mangiavacchi, N. (1993). Turbulence control in wall-bounded flows by spanwise oscillations. In *Advances in Turbulence IV*, pages 299–303. Springer.

[10] Arik, M., Weaver, S. E., Seeley, C. E., and Utturkar, Y. V. (2011). Method and apparatus for reducing acoustic noise in a synthetic jet. US Patent 8,006,917.

[11] Arik, M., Weaver, S. E., Seeley, C. E., and Utturkar, Y. V. (2014). Method and apparatus for reducing acoustic noise in a synthetic jet. US Patent 8,752,775.

[12] Baron, A. and Quadrio, M. (1996). Turbulent drag reduction by spanwise wall oscillations. *Applied Scientific Research*, 55(4):311–326.

[13] Bernardini, M. and Pirozzoli, S. (2011). Inner/outer layer interactions in turbulent boundary layers: a refined measure for the large-scale amplitude modulation mechanism. *Physics of Fluids*, 23(6):061701.

[14] Billson, M., Eriksson, L. E., and Davidson, L. (2004). Jet noise modeling using synthetic anisotropic turbulence. In *10th AIAA/CEAS Aeroacoustics Conference*, page 3028.

[15] Blackwelder, R. F. and Eckelmann, H. (1979). Streamwise vortices associated with the bursting phenomenon. *Journal of Fluid Mechanics*, 94(3):577–594.

[16] Bradshaw, P. and Pontikos, N. (1985). Measurements in the turbulent boundary layer on an 'infinite'swept wing. *Journal of Fluid Mechanics*, 159:105–130.

[17] Brereton, G. J. and Hwang, J. L. (1994). The spacing of streaks in unsteady turbulent wall-bounded flow. *Physics of Fluids*, 6(7):2446–2454.

[18] Capizzano, F., Catalano, P., Marongiu, C., and Vitagliano, P. L. (2005). U-rans modelling of turbulent flows controlled by synthetic jets. In *35th AIAA Fluid Dynamics Conference and Exhibit*, page 5015.

[19] Choi, J.-I., Xu, C. X., and Sung, H. J. (2002). Drag reduction by spanwise wall oscillation in wall-bounded turbulent flows. *AIAA journal*, 40(5):842–850.

[20] Choi, K. S., DeBisschop, J. R., and Clayton, B. R. (1998). Turbulent boundary-layer control by means of spanwise-wall oscillation. *AIAA journal*, 36(7):1157–1163.

[21] Corino, E. R. and Brodkey, R. S. (1969). A visual investigation of the wall region in turbulent flow. *Journal of Fluid Mechanics*, 37(1):1–30.

[22] Dandois, J., Garnier, E., and Sagaut, P. (2007). Numerical simulation of active separation control by a synthetic jet. *Journal of Fluid Mechanics*, 574:25–58.

[23] Driver, D. M. and Hebbar, S. K. (1987). Experimental study of a three-dimensional, shear-driven, turbulent boundary layer. *AIAA journal*, 25(1):35–42.

[24] Eto, K., Kondo, Y., Fukagata, K., and Tokugawa, N. (2018). Friction drag reduction on a clark-y airfoil using uniform blowing. In *2018 Flow Control Conference*, page 3374.

[25] Flores, O. and Jiménez, J. (2010). Hierarchy of minimal flow units in the logarithmic layer. *Physics of Fluids*, 22(7):071704.

[26] Fukagata, K., Iwamoto, K., and Kasagi, N. (2002). Contribution of reynolds stress distribution to the skin friction in wall-bounded flows. *Physics of Fluids*, 14(11):L73–L76.

[27] Fukagata, K., Kobayashi, M., and Kasagi, N. (2010). On the friction drag reduction effect by a control of large-scale turbulent structures. *Journal of Fluid Science and Technology*, 5(3):574–584.

[28] Gad-el-Hak, M. (2000). *Flow Control : passive, active, and reactive flow management*. Cambridge University Press.

[29] García-Mayoral, R. and Jiménez, J. (2011). Drag reduction by riblets. *Philosophical Transactions of the Royal Society of London A: Mathematical, Physical and Engineering Sciences*, 369(1940):1412–1427.

[30] Germano, M., Piomelli, U., Moin, P., and Cabot, W. H. (1991). A dynamic subgrid-scale eddy viscosity model. *Physics of Fluids A: Fluid Dynamics*, 3(7):1760–1765.

[31] Glezer, A. and Amitay, M. (2002). Synthetic jets. *Annual Review of Fluid Mechanics*, 34(1):503–529.

[32] Golubev, V. V., Sansone, M., Nguyen, L. D., and Mankbadi, R. R. (2015). Numerical study of synthetic-jet actuation effect on airfoil leading and trailing edge noise. *53rd AIAA Aerospace Sciences Meeting.*

[33] Grek, G., Kozlov, V., and Titarenko, S. (1996). An experimental study of the influence of riblets on transition. *Journal of Fluid Mechanics*, 315:31–49.

[34] Head, M. and Bandyopadhyay, P. (1981). New aspects of turbulent boundary-layer structure. *Journal of Fluid Mechanics*, 107:297–338.

[35] Hetsroni, G., Zakin, J., and Mosyak, A. (1997). Low-speed streaks in drag-reduced turbulent flow. *Physics of Fluids*, 9(8):2397–2404.

[36] Hutchins, N. and Marusic, I. (2007a). Evidence of very long meandering features in the logarithmic region of turbulent boundary layers. *Journal of Fluid Mechanics*, 579:1–28.

[37] Hutchins, N. and Marusic, I. (2007b). Large-scale influences in near-wall turbulence. *Philosophical Transactions of the Royal Society of London A: Mathematical, Physical and Engineering Sciences*, 365(1852):647–664.

[38] Hwang, H. G. and Lee, J. H. (2018). Secondary flows in turbulent boundary layers over longitudinal surface roughness. *Physical Review Fluids*, 3(1):014608.

[39] Ishibashi, Y. and Miyaji, K. (2015). Detached-eddy simulations of synthetic jets for high-angles-of-attack airfoils. *Journal of Aircraft*, 52(1):168–175.

[40] Iwamoto, K., Kasagi, N., and Suzuki, Y. (2004). Dynamical roles of large-scale structures in turbulent channel flow. *Computational Mechanics, WCCM VI in conjunction with APCOM*, 4:5–10.

[41] Jeromin, L. (1970). The status of research in turbulent boundary layers with fluid injection. *Progress in Aerospace Sciences*, 10:65–189.

[42] Jiménez, J. and Moin, P. (1991). The minimal flow unit in near-wall turbulence. *Journal of Fluid Mechanics*, 225:213–240.

[43] Johansson, A. V., Alfredsson, P. H., and Kim, J. (1991). Evolution and dynamics of shear-layer structures in near-wall turbulence. *Journal of Fluid Mechanics*, 224:579–599.

[44] Jung, W., Mangiavacchi, N., and Akhavan, R. (1992). Suppression of turbulence in wall-bounded flows by high-frequency spanwise oscillations. *Physics of Fluids A: Fluid Dynamics (1989-1993)*, 4(8):1605–1607.

[45] Kametani, Y. and Fukagata, K. (2011). Direct numerical simulation of spatially developing turbulent boundary layers with uniform blowing or suction. *Journal of Fluid Mechanics*, 681:154–172.

[46] Kametani, Y., Fukagata, K., Örlü, R., and Schlatter, P. (2015). Effect of uniform blowing/suction in a turbulent boundary layer at moderate reynolds number. *International Journal of Heat and Fluid Flow*, 55:132–142.

[47] Kametani, Y., Fukagata, K., Örlü, R., and Schlatter, P. (2016). Drag reduction in spatially developing turbulent boundary layers by spatially intermittent blowing at constant mass-flux. *Journal of Turbulence*, 17(10):913–929.

[48] Kamnis, S. and Kontis, K. (2004). Numerical studies on the application of synthetic jets for the active control of subsonic flow configurations. In *24 th AIAA Aerodynamic Measurement Technology and Ground Testing Conference*.

[49] Karniadakis, G. and Choi, K. S. (2003). Mechanisms on transverse motions in turbulent wall flows. *Annual Review of Fluid Mechanics*, 35(1):45–62.

[50] Kim, H., Kline, S., and Reynolds, W. (1971). The production of turbulence near a smooth wall in a turbulent boundary layer. *Journal of Fluid Mechanics*, 50(1):133–160.

[51] Kim, J., Moin, P., and Moser, R. (1987). Turbulence statistics in fully developed channel flow at low Reynolds number. *J. Fluid Mech*, 177:133–166.

[52] Kim, K. H. and Kim, C. (2005). Accurate, efficient and monotonic numerical methods for multi-dimensional compressible flows: Part i: Spatial discretization. *Journal of Computational Physics*, 208(2):527–569.

[53] Kim, S. H. and Kim, C. (2009). Separation control on naca23012 using synthetic jet. *Aerospace Science and Technology*, 13(4-5):172–182.

[54] Kline, S. J., Reynolds, W., Schraub, F., and Runstadler, P. (1967). The structure of turbulent boundary layers. *Journal of Fluid Mechanics*, 30(4):741–773.

[55] Kornilov, V. (2015). Current state and prospects of researches on the control of turbulent boundary layer by air blowing. *Progress in Aerospace Sciences*, 76:1–23.

[56] Kotapati, R. B., Mittal, R., and Cattafesta Iii, L. N. (2007). Numerical study of a transitional synthetic jet in quiescent external flow. *Journal of Fluid Mechanics*, 581:287–321.

[57] Kral, L. D. (2000). Active flow control technology. *ASME FED, Technical Brief*, pages 1–28.

[58] Kral, L. D., Donovan, J. F., Cain, A. B., and Cary, A. W. (1997). Numerical simulation of synthetic jet actuators. *AIAA paper*, 1824:1997.

[59] Laadhari, F., Skandaji, L., and Morel, R. (1994). Turbulence reduction in a boundary layer by a local spanwise oscillating surface. *Physics of Fluids (1994-present)*, 6(10):3218–3220.

[60] Lagraa, B., Labraga, L., and Mazouz, A. (2004). Characterization of low-speed streaks in the near-wall region of a turbulent boundary layer. *European Journal of Mechanics-B/Fluids*, 23(4):587–599.

[61] Lee, C. Y. and Goldstein, D. B. (2002). Two-dimensional synthetic jet simulation. *AIAA journal*, 40(3):510–516.

[62] Lee, M. K., Eckelman, L. D., and Hanratty, T. J. (1974). Identification of turbulent wall eddies through the phase relation of the components of the fluctuating velocity gradient. *Journal of Fluid Mechanics*, 66(1):17–33.

[63] Leschziner, M. A. and Lardeau, S. (2011). Simulation of slot and round synthetic jets in the context of boundary-layer separation control. *Philosophical Transactions of the Royal Society of London A: Mathematical, Physical and Engineering Sciences*, 369(1940):1495–1512.

[64] Li, C. G., Tsubokura, M., and Onishi, K. (2014). Feasibility investigation of compressible direct numerical simulation with a preconditioning method at extremely low mach numbers. *International Journal of Computational Fluid Dynamics*, 28(6-10):411–419.

[65] Lilly, D. K. (1992). A proposed modification of the germano subgrid-scale closure method. *Physics of Fluids A: Fluid Dynamics*, 4(3):633–635.

[66] Liu, P., Duan, H., Chen, J., and He, Y. (2010). Numerical study of suction-blowing flow control technology for an airfoil. *Journal of aircraft*, 47(1):229–239.

[67] Liu, X., Xuan, L., Xia, Y., and Luo, H. (2017). A reconstructed discontinuous galerkin method for the compressible navier-stokes equations on three-dimensional hybrid grids. *Computers & Fluids*, 152:217–230.

[68] Lozano-Durán, A. and Jiménez, J. (2014). Effect of the computational domain on direct simulations of turbulent channels up to re_τ= 4200. *Physics of Fluids*, 26(1):011702.

[69] Mahfoze, O., Laizet, S., and Wynn, A. (2018). Bayesian optimisation of intermittent wall blowing for drag reduction of a spatially evolving turbulent boundary.

[70] Martens, S., Saddoughi, S. G., and Early, K. S. (2006). Method and apparatus for noise attenuation for gas turbine engines using at least one synthetic jet actuator for injecting air. US Patent 7,055,329.

[71] Marusic, I., Mathis, R., and Hutchins, N. (2010). Predictive model for wall-bounded turbulent flow. *Science*, 329(5988):193–196.

[72] Mathis, R., Hutchins, N., and Marusic, I. (2009a). Large-scale amplitude modulation of the small-scale structures in turbulent boundary layers. *Journal of Fluid Mechanics*, 628:311–337.

[73] Mathis, R., Monty, J. P., Hutchins, N., and Marusic, I. (2009b). Comparison of large-scale amplitude modulation in turbulent boundary layers, pipes, and channel flows. *Physics of Fluids*, 21(11):111703.

[74] Mickley, H. and Davis, R. (1957). Momentum transfer for flow over a flat. *LATE WITH BLOWING, NACA TN*, 4017.

[75] Mittal, R. and Moin, P. (1997). Suitability of upwind-biased finite difference schemes for large-eddy simulation of turbulent flows. *AIAA journal*, 35(8):1415–1417.

[76] Mittal, R., Rampunggoon, P., and Udaykumar, H. (2001). Interaction of a synthetic jet with a flat plate boundary layer. *AIAA paper*, 2773(200):1.

[77] Moin, P. (1982). Numerical simulation of wall-bounded turbulent shear flows. In *Eighth International Conference on Numerical Methods in Fluid Dynamics*, pages 55–76. Springer.

[78] Moin, P., Shih, T.-H., Driver, D., and Mansour, N. (1990). Direct numerical simulation of a three-dimensional turbulent boundary layer. *Physics of Fluids A: Fluid Dynamics (1989-1993)*, 2(10):1846–1853.

[79] Monty, J. and Chong, M. (2009). Turbulent channel flow: comparison of streamwise velocity data from experiments and direct numerical simulation. *Journal of Fluid Mechanics*, 633:461–474.

[80] Mori, E., Quadrio, M., and Fukagata, K. (2017). Turbulent drag reduction by uniform blowing over a two-dimensional roughness. *Flow, Turbulence and Combustion*, 99(3-4):765–785.

[81] Moser, R. D., Kim, J., and Mansour, N. N. (1999). Direct numerical simulation of turbulent channel flow up to $Re_\tau = 590$. *Physics of fluids*, 11(4):943–945.

[82] Negi, P. S., Mishra, M., and Skote, M. (2015). Dns of a single low-speed streak subject to spanwise wall oscillations. *Flow, Turbulence and Combustion*, 94(4):795–816.

[83] Noguchi, D., Fukagata, K., and Tokugawa, N. (2016). Friction drag reduction of a spatially developing boundary layer using a combined uniform suction and blowing. *Journal of Fluid Science and Technology*, 11(1):JFST0004–JFST0004.

[84] Oldaker, D. and Tiederman, W. (1977). Spatial structure of the viscous sublayer in drag-reducing channel flows. *The Physics of Fluids*, 20(10):S133–S144.

[85] Peet, Y., Sagaut, P., and Charron, Y. (2008). Turbulent drag reduction using sinusoidal riblets with triangular cross-section. *AIAA paper*, 3745.

[86] Pope, S. B. (2001). Turbulent flows.

[87] Qin, N. and Xia, H. (2008). Detached eddy simulation of a synthetic jet for flow control. *Proceedings of the Institution of Mechanical Engineers, Part I: Journal of Systems and Control Engineering*, 222(5):373–380.

[88] Quadrio, M. and Ricco, P. (2003). Initial response of a turbulent channel flow to spanwise oscillation of the walls. *Journal of Turbulence*, 4(7):1–23.

[89] Quadrio, M. and Ricco, P. (2004a). Critical assessment of turbulent drag reduction through spanwise wall oscillations. *Journal of Fluid Mechanics*, 521:251–271.

[90] Quadrio, M. and Ricco, P. (2004b). Critical assessment of turbulent drag reduction through spanwise wall oscillations. *Journal of Fluid Mechanics*, 521:251–271.

[91] Quadrio, M., Ricco, P., and Viotti, C. (2009). Streamwise-travelling waves of spanwise wall velocity for turbulent drag reduction. *Journal of Fluid Mechanics*, 627:161–178.

[92] Quadrio, M., Viotti, C., and Luchini, P. (2007). Skin-friction drag reduction via steady streamwise oscillations of spanwise velocity. In *Advances in Turbulence XI*, pages 659–661. Springer.

[93] Rathnasingham, R. and Breuer, K. S. (1997). System identification and control of a turbulent boundary layer. *Physics of Fluids*, 9(7):1867–1869.

[94] Rathnasingham, R. and Breuer, K. S. (2003). Active control of turbulent boundary layers. *Journal of Fluid Mechanics*, 495:209–233.

[95] Ravi, B., Mittal, R., and Najjar, F. (2004). Study of three-dimensional synthetic jet flow fields using direct numerical simulation. *AIAA paper*, 51:61801.

[96] Ricco, P. and Quadrio, M. (2008). Wall-oscillation conditions for drag reduction in turbulent channel flow. *International Journal of Heat and Fluid Flow*, 29(4):891–902.

[97] Rizzetta, D. P., Visbal, M. R., and Stanek, M. J. (1999). Numerical investigation of synthetic-jet flowfields. *AIAA journal*, 37(8):919–927.

[98] Robinson, S. K. (1991). Coherent motions in the turbulent boundary layer. *Annual Review of Fluid Mechanics*, 23(1):601–639.

[99] Roe, P. (1986). Characteristic-based schemes for the euler equations. *Annual review of fluid mechanics*, 18(1):337–365.

[100] Rumsey, C., Gatski, T., Sellers, W., Vatsa, V., and Viken, S. (2004). Summary of the 2004 cfd validation workshop on synthetic jets and turbulent separation control. In *2nd AIAA Flow Control Conference*, page 2217.

[101] Sankaran, R., Sokolov, M., and Antonia, R. (1988). Substructures in a turbulent spot. *Journal of Fluid Mechanics*, 197:389–414.

[102] Saravi, S. S. and Cheng, K. (2013). A review of drag reduction by riblets and micro-textures in the turbulent boundary layers. *European Scientific Journal*, 9(33).

[103] Sareen, A., Deters, R. W., Henry, S. P., and Selig, M. S. (2014). Drag reduction using riblet film applied to airfoils for wind turbines. *Journal of Solar Energy Engineering*, 136(2):021007.

[104] Šarić, S., Jakirlić, S., Djugum, A., and Tropea, C. (2006). Computational analysis of locally forced flow over a wall-mounted hump at high-*Re* number. *International journal of heat and fluid flow*, 27(4):707–720.

[105] Schetz, J. A. and Nerney, B. (1977). Turbulent boundary layer with injection and surface roughness. *AIAA Journal*, 15(9):1288–1294.

[106] Schlatter, P. and Örlü, R. (2010). Quantifying the interaction between large and small scales in wall-bounded turbulent flows: a note of caution. *Physics of fluids*, 22(5):051704.

[107] Singh, D. K., Jain, A., and Paul, A. R. (2016). Active flow control on naca23012 airfoil using combined action of synthetic jet and continuous jet. In *Proceedings of 6th International and 43rd National Conference on Fluid Mechanics and Fluid Power (FMFP-2016)*, pages 15–17.

[108] Skote, M. (2011). Turbulent boundary layer flow subject to streamwise oscillation of spanwise wall-velocity. *Physics of Fluids (1994-present)*, 23(8):081703.

[109] Skote, M. (2014). Scaling of the velocity profile in strongly drag reduced turbulent flows over an oscillating wall. *International Journal of Heat and Fluid Flow*, 50:352–358.

[110] Smith, C. and Metzler, S. (1983). The characteristics of low-speed streaks in the near-wall region of a turbulent boundary layer. *Journal of Fluid Mechanics*, 129:27–54.

[111] Smith, D., Amitay, M., Kibens, V., Parekh, D., and Glezer, A. (1998). Modification of lifting body aerodynamics using synthetic jet actuators. In *36th AIAA Aerospace Sciences Meeting and Exhibit*, page 209.

[112] Spalart, P. and Allmaras, S. (1992). A one-equation turbulence model for aerodynamic flows. In *30th aerospace sciences meeting and exhibit*, page 439.

[113] Stanek, M., Raman, G., Ross, J., Odedra, J., Peto, J., Alvi, F., and Kibens, V. (2002). High frequency acoustic suppression-the role of mass flow & the notion of superposition. In *8th AIAA/CEAS Aeroacoustics Conference & Exhibit*, page 2404.

[114] Stanek, M., Ross, J., Odedra, J., and Peto, J. (2003). High frequency acoustic suppression-the mystery of the rod-in-crossflow revealed. In *41st Aerospace Sciences Meeting and Exhibit*, page 7.

[115] Sumitani, Y. and Kasagi, N. (1995). Direct numerical simulation of turbulent transport with uniform wall injection and suction. *AIAA journal*, 33(7):1220–1228.

[116] Tang, Z. Q., Jiang, N., Zheng, X. B., and Wu, Y. H. (2016). Bursting process of large- and small-scale structures in turbulent boundary layer perturbed by a cylinder roughness element. *Experiments in Fluids*, 57(5):79.

[117] Tani, I. (1988). Drag reduction by riblet viewed as roughness problem. *Proceedings of the Japan Academy. Ser. B: Physical and Biological Sciences*, 64(2):21–24.

[118] Touber, E. and Leschziner, M. A. (2012). Near-wall streak modification by spanwise oscillatory wall motion and drag-reduction mechanisms. *Journal of Fluid Mechanics*, 693:150–200.

[119] Utturkar, Y., Holman, R., Mittal, R., Carroll, B., Sheplak, M., and Cattafesta, L. (2003). A jet formation criterion for synthetic jet actuators. In *41st Aerospace Sciences Meeting and Exhibit*, page 636.

[120] Vanderwel, C. and Ganapathisubramani, B. (2015). Effects of spanwise spacing on large-scale secondary flows in rough-wall turbulent boundary layers. *Journal of Fluid Mechanics*, 774.

[121] Vanderwel, C., Stroh, A., Kriegseis, J., Frohnapfel, B., and Ganapathisubramani, B. (2019). The instantaneous structure of secondary flows in turbulent boundary layers. *Journal of Fluid Mechanics*, 862:845–870.

[122] Viotti, C., Quadrio, M., and Luchini, P. (2009). Streamwise oscillation of spanwise velocity at the wall of a channel for turbulent drag reduction. *Physics of Fluids (1994-present)*, 21(11):115109.

[123] Wallace, J. M. (2016). Quadrant analysis in turbulence research: history and evolution. *Annual Review of Fluid Mechanics*, 48:131–158.

[124] Wallace, J. M., Eckelmann, H., and Brodkey, R. S. (1972). The wall region in turbulent shear flow. *Journal of Fluid Mechanics*, 54(1):39–48.

[125] Walsh, M. J. (1983). Riblets as a viscous drag reduction technique. *AIAA journal*, 21(4):485–486.

[126] Walsh, M. J., Sellers III, W. L., and Mcginley, C. B. (1989). Riblet drag at flight conditions. *Journal of Aircraft*, 26(6):570–575.

[127] Wang, Z. J., Fidkowski, K., Abgrall, R., Bassi, F., Caraeni, D., Cary, A., Deconinck, H., Hartmann, R., Hillewaert, K., Huynh, H. T., et al. (2013). High-order cfd methods: current status and perspective. *International Journal for Numerical Methods in Fluids*, 72(8):811–845.

[128] Weiss, J. M. and Smith, W. A. (1995). Preconditioning applied to variable and constant density flows. *AIAA journal*, 33(11):2050–2057.

[129] Xia, H. and Qin, N. (2005). Dynamic grid and unsteady boundary conditions for synthetic jet flow. *AIAA*, 106:2005.

[130] Xie, F., Pérez Muñoz, J. D., and Qin, N. (2018). High-order simulation of zero mass jets for reduction of turbulent skin friction. In *7th European Conference on Computational Fluid Dynamic*.

[131] Yao, J., Chen, X., and Hussain, F. (2018). Drag control in wall-bounded turbulent flows via spanwise opposed wall-jet forcing. *Journal of Fluid Mechanics*, 852:678–709.

[132] You, D. and Moin, P. (2006). Large-eddy simulation of flow separation over an airfoil with synthetic jet control. *Center for Turbulence Research Annual Research Briefs*, pages 337–346.

[133] You, D., Wang, M., and Moin, P. (2006). Large-eddy simulation of flow over a wall-mounted hump with separation control. *AIAA journal*, 44(11):2571–2577.

[134] Yudhistira, I. and Skote, M. (2011). Direct numerical simulation of a turbulent boundary layer over an oscillating wall. *Journal of Turbulence*, (12):N9.

[135] Zhang, C. and Chernyshenko, S. I. (2016). Quasisteady quasihomogeneous description of the scale interactions in near-wall turbulence. *Physical Review Fluids*, 1(1):014401.

[136] Zhang, W. and Samtaney, R. (2015). A direct numerical simulation investigation of the synthetic jet frequency effects on separation control of low-*Re* flow past an airfoil. *Physics of Fluids (1994-present)*, 27(5):055101.